Synthesis Of High-Entropy-Alloy-Based Magnetic Alloys By Mechanical Alloying

by

Anuj Rathi

A thesis submitted in partial fulfillment
of the requirements for the degree of
Master of Science in Engineering
(Mechanical Engineering)
in the University of Michigan-Dearborn
2018

Master's Thesis Committee:

Assistant Professor Tanjore V. Jayaraman, Chair

Professor Pravansu Mohanty

Associate Professor German Reyes-Villanueva

ACKNOWLEDGMENTS

I would first like to express my sincere gratitude to my thesis advisor Dr. Tanjore V. Jayaraman for his continuous support. The door to Dr. Jayaraman's office was always open whenever I ran into a trouble spot or had questions about my research and/or writing. He consistently steered me in the right the direction whenever he thought I needed it. I would also like to thank Dr. Pravansu Mohanty and Dr. German Reyes-Villanueva for sparing their time to evaluate my thesis and for being a part of the thesis committee.

I would like to thank the Mechanical Engineering Department, College of Engineering and Computer Science at the University of Michigan in Dearborn for their support in completing my thesis and the Department of Material Science and Engineering at The University of Michigan at Ann Arbor for providing access to some of their equipment. I would also like to thank Tim Chambers, Ying Qi, Chris Cristian, and Erik Kirk for their assistance with equipment and safety training.

Finally, I must express my very profound gratitude to my parents Mr. Dinesh Kumar Rathi and Mrs. Madhu Rathi, and to my sisters Mrs. Purvi Rathi and Mrs. Aditi Rathi for providing me with unfailing support and continuous encouragement throughout my years of study and through the process of researching and writing this thesis. This accomplishment would not have been possible without them. Thank you!

TABLE OF CONTENTS

LIST OF FIGURES

LIST OF TABLES

ABSTRACT

The objective of this thesis work was to synthesize high-entropy based magnetic alloys and investigate the phase evolution during the synthesis and thermal treatments. A thorough literature review was performed on magnetic high-entropy alloys. The ternary iron-cobalt-nickel alloys ($Fe_{33.33}Co_{33.33}Ni_{33.33}$, $Ni_{40}Co_{30}Fe_{30}$, $Fe_{40}Co_{30}Ni_{30}$, $Co_{40}Fe_{30}Ni_{30}$, and $Fe_{46}Co_{34}Ni_{20}$) and the quaternary iron-cobalt-nickel-silicon alloys $(Fe_{40}Co_{30}Ni_{30})_{0.9}Si_{0.1}$ were synthesized by mechanical alloying, followed by structural characterization of phase evolution by x-ray diffraction (XRD), scanning electron microscopy (SEM) and magnetic characterization by magnetometry.

The $Fe_{33.33}Co_{33.33}Ni_{33.33}$ alloy was formed after mechanical alloying for ~9 hours. The lattice parameter of the face-centered-cubic (f.c.c) alloy was ~0.3591 nm and the crystallite size was ~12 nm. The SEM revealed particle size (D_{90}) ~15.9 µm. The alloy exhibited decent magnetic properties having saturation magnetization (M_S) of ~136 ± 3 Am^2/kg and coercivity (H_C) of ~2.4 kA/m at room temperature. After the thermal treatment, *Ms* increased by ~14% and *Hc* decreased by 60%. Among the $Ni_{40}Co_{30}Fe_{30}$, $Fe_{40}Co_{30}Ni_{30}$, and $Co_{40}Fe_{30}Ni_{30}$ alloys, the Fe-rich alloy mechanically alloyed for 12 hours showed superior magnetic properties. The *Ms* was ~148 ± 3 Am^2/kg and the *Hc* was ~4.3 kA/m. The lattice parameter, crystallite size, and D_{90} was ~0.3574 nm, ~8 nm, and ~5.5 µm, respectively. Thermal treatment of the Fe-rich alloy improved its magnetic properties. It increased *Ms* by 10% and decreased *Hc* by 25%. The $Fe_{46}Co_{34}Ni_{20}$ showed the best magnetic properties among all, the *Ms* was ~167 ± 2 Am^2/kg and the *Hc* was ~3.3 kA/m. Lastly, in the case of $(Fe_{40}Co_{30}Ni_{30})_{0.9}Si_{0.1}$ alloy, the *Ms* decreased by ~10% and the *Hc* increased by ~40% compared to $Fe_{40}Co_{30}Ni_{30}$ alloy.

A systematic study of magnetic properties of the iron-cobalt-nickel alloys is likely to provide the necessary foundation for the development of high-entropy based magnetic alloys by further alloying additions.

Chapter 1 INTRODUCTION

Magnetism is a phenomenon by which a material asserts an attractive or repulsive force on other materials. Some metals like iron, steel and other naturally occurring minerals are well known examples that exhibit magnetic properties. They are categorized as diamagnetic, paramagnetic, ferromagnetic, ferrimagnetic, and antiferromagnetic materials based on how they get influenced to one degree or the other by the presence of a magnetic field [1].

The macroscopic magnetic properties of a material are a consequence of interaction of an external magnetic field and the magnetic dipole moments in the constituent atoms. The net magnetic moment for an atom is the sum of the contributions from the spin and orbital moment of each of its electrons. When an external magnetic field is applied, the electron orbital motion changes in opposite direction and this is called diamagnetism. Paramagnetic materials have permanent atomic dipole which gets aligned in the direction of the external magnetic field. Since the magnetization is relatively small, both of these materials are considered to be non-magnetic. Ferromagnetic materials have high magnetization for example in Fe, $CoFe_2O_4$, $SmCo_5$, Ni etc. The atomic magnetic dipole moments are coupled and mutually aligned with the moments of the adjacent atoms. When these adjacent atom spin moments are found anti parallel then the cancellation of the spin moments is termed as antiferromagnetism. If all the moments do not cancel each other then it might cause some permanent magnetization because of the incomplete spin moment cancellation (**Figure 1**). This is called ferrimagnetism [1].

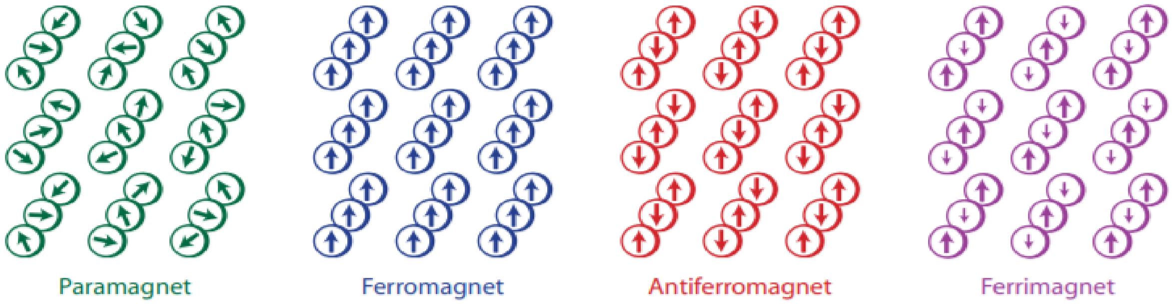

Figure 1. Alignment of magnetic moments in four principle classes of magnetism [2]

Chapter 2 LITERATURE REVIEW AND BACKGROUND

1. Magnetic Materials

A material that responds to magnetic field is called a magnetic material. The magnetic field is responsible for the push and pull on other ferromagnetic materials [3]. The magnetic materials are broadly classified into two categories, soft and hard magnetic materials. Soft magnetic materials can be magnetized with a low external magnetic field and when the field is removed, the material comes back to its state of low residual magnetism. The range of coercivity is from 0.0002 kA/m to ~0.4 kA/m [4]. However, the hard-magnetic materials retain large amount of residual magnetization and coercivity the is between ~10 kA/m (125 Oe) to ~1000 kA/m (12 kOe)

1.1 Soft Magnetic Materials

Materials with high permeability, low coercivity, and low hysteresis loss; and which can be used to amplify the flux density generated by a magnetic field are known as soft magnetic materials. With time, the properties are improving i.e. coercivity is reducing, permeability is increasing, and hysteresis losses are decreasing. All this is accomplished by reducing anisotropy and reducing domain in wall pinning. Impurity content greatly affects the wall pinning [4]. Few examples of soft magnetic materials are FeSi alloys, NiFe alloys and ferrites.

1.2 Hard Magnetic Materials

These materials are highly resistant to demagnetizing field. Materials with coercivity greater than ~10 kA/m are considered in this category. When an external magnetic field is applied, the material tends to retain the magnetic properties because of its high magneto-crystalline anisotropy. Ferromagnetic metals like Fe and Co are alloyed with high anisotropic materials to increase coercivity to form hard magnetic materials [4]. Current research progress focusses on improving the magnetic properties of materials like cobalt rare earth alloys ($SmCo_5$ and/or Sm_2Co_{17}) and neodymium-iron-boron ($Nd_2Fe_{14}B$), iron platinum, and hard ferrites (SrO-Fe_2O_3 or BaO-$6Fe_2O_3$) to improve their magnetic properties.

1.3 Properties of Ferromagnetic Materials

Magnetization of a material is dependent on the applied magnetic field. When magnetic field is applied, magnetization increases proportionally and then the change in magnetization slows down. Ultimately, magnetization reaches its saturation value. Now as the field is reduced, the magnetization does not retrace the original path. A hysteresis effect is produced in which magnetization lags behind applied magnetic field, as shown in **Figure 2(a).**

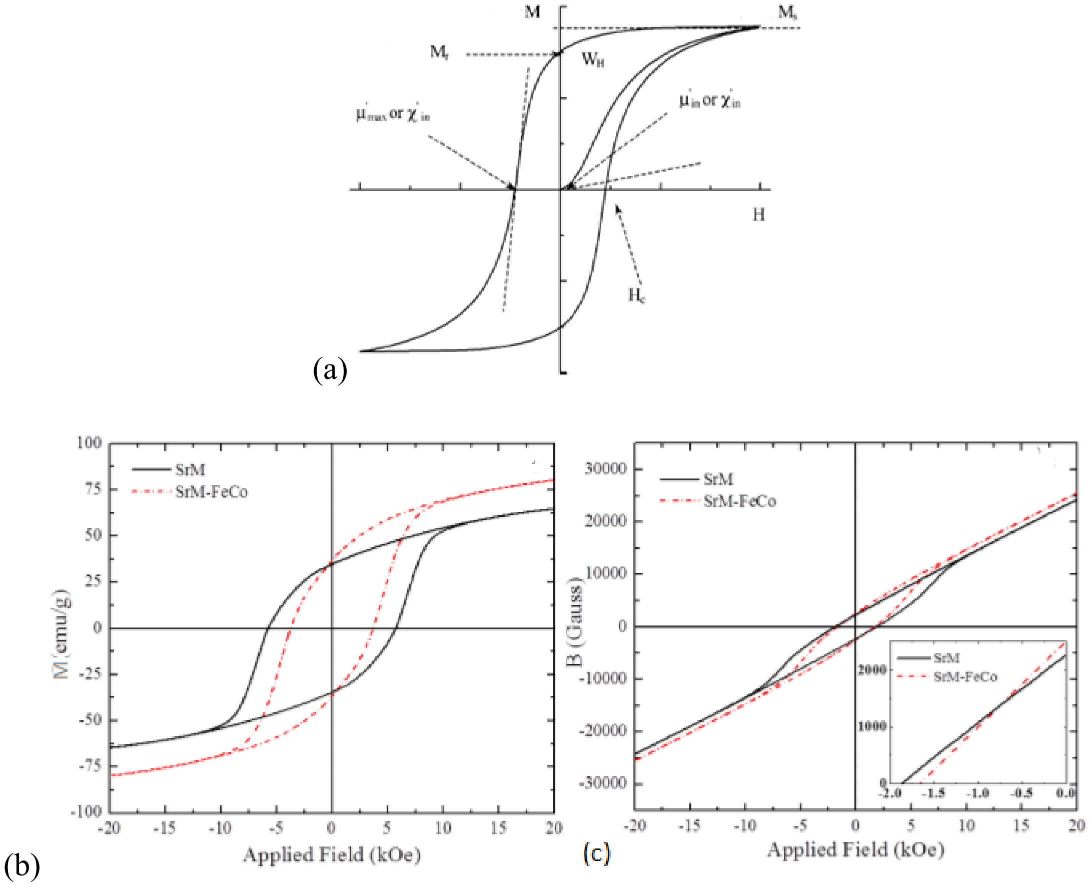

Figure 2. (a) Magnetic properties of materials as defined on the M_H plane of Magnetization M versus magnetic field H. These include coercivity H_C, remanence B_R (M_R), hysteresis loss W_H, initial permeability μ_{in} (initial susceptibility χ_{in}), maximum differential permeability μ_{max} (maximum differential susceptibility χ_{max}) and saturation flux density B_S (saturation magnetization Ms) (b) M-H curve of $SrFe_{12}O_{19}$ or SrM (c) B-H curve of SrM [5]

1.3.1 Saturation Magnetization (M_S)

Saturation magnetization is the maximum value of magnetization reached during application of external field, as shown in **Figure 2(a)**. There has been a little progress in improving the M_S of materials in last 100 years. The highest magnetization available is in bulk magnetic material is B_S = 2.43 T which is achieved in iron-cobalt alloy with 35% cobalt [4]. Neodymium-iron-boron (NdFeB) has B_S = 1.6 Tesla. The minimum value of M_S goes down to as low as zero. The remanence is dependent on the saturation magnetization, and for this reason the permanent magnets should have high M_S.

1.3.2 Coercivity (H_C)

Coercivity is defined as either the field at which magnetization M becomes zero or the field at which magnetic flux density B in the material is zero, as shown in **Figure 2(a).** For example, the intrinsic coercivity of NdFeB is typically 1.1 MA/m and for samarium-cobalt it is typically 0.69 MA/m. This is one of the factors to distinguish between hard and soft magnetic materials.

1.3.3 Permeability (μ)

It indicates how much magnetic induction B is generated by the material in a given magnetic field strength H. Permeability can also be defined as the ratio of magnetic induction to external magnetic field, B/H. This definition refers to normal permeability when the material is in a "cyclic" magnetic state [6]. The range of permeability is from 1,000,000 in amorphous materials to as low as 1.1 in permanent magnets. It is known that initial permeability and coercivity are inversely proportional to each other [4].

1.3.4 Remanence (M_R)

Remanence is the maximum residual magnetization that can be obtained in a closed loop configuration in which there is no demagnetizing field, as shown in **Figure 2(a)**. To be a source of magnetic field, the permanent magnet should have relatively high magnetization even after removal of external magnetic field. Therefore, the combination of high remanence and high coercivity is required for permanent magnet [4].

1.3.5 Hysteresis Loss (W_H)

Hysteresis refers to a damping phenomenon of two conjugate quantities like stress and strain, magnetic field and magnetic induction, etc lag behind each other, thus damping some of the energy and heating up the lattice [6]. The area enclosed by the hysteresis loop on the B-H plane is called the hysteresis loss. The loss increases with increase in magnetic field to the maximum. This is also related to coercivity, the lesser the coercivity, lesser is the hysteresis loss [4]. The proof of magnetic hysteresis appears in the fourth quadrant of B-H curve.

2. High-Entropy Alloys (HEAs)

Conventional alloys were all based on one or at the most two principle elements. With time the demand of materials with different type of properties were emerging and to satisfy these demands minor elements were added accordingly. Other approach, to fulfill demand, was to employ novel production methods like mechanical alloying, rapid solidification, thermochemical treatments. Even after such improvements, all the demands are not yet fulfilled like better elevated-temperature strength, light material with better strength and toughness, high electrical resistance [7]. Thus, to overcome these issues a new category of alloy was developed called multi-principal-element alloys.

The initial study of multi-principal-element alloys (MPEAs) began in 1970's as an undergraduate thesis. Later in 2002 the study was refined and was presented in a conference and was subsequently published. In 1996, the research work on HEAs began as a series of thesis leading to 5 publications in 2004 [8]. It was believed that multi-principal-element alloys formed complicated and brittle microstructure until 1995 when Yeh et al. suggested that alloys system with five or more principal elements would poses higher mixing entropy [7]. HEAs are of great interest of research because of vast properties exhibited by it along with large number of possible compositions which has wide spectrum of functional uses.

High-Entropy Alloys are defined as alloys with five or more principal elements in equiatomic or equimolar ratio. However, to make HEAs vaster, the percentage range of each principal element has been set from 35 to 5 at.% [9]. This has led to number of simple crystal structure HEAs with extraordinary properties.

The concept of High-Entropy Alloys depends on the equation of Gibbs' Free Energy

$$G = H - TS \tag{1}$$

To reach an equilibrium state, a system should attain the minimum Gibbs' Free Energy (G) (kJ/mol) under constant temperature and pressure. Thus, enthalpy (H) (J) and entropy (S) (J/K) of the system have direct effect on determination of equilibrium at a given temperature. During the manufacturing of an alloy, the free energy changes from elemental state to different state. Thus, now we get the differences in the free energy (ΔG_{mix}), enthalpy (ΔH_{mix}) and entropy (ΔS_{mix}) and the relation between three are as follows

$$\Delta G_{mix} = \Delta H_{mix} - T\Delta S_{mix} \tag{2}$$

We can use the Boltzmann's equation for the entropy change as applied to the mixing entropy

$$\Delta S_{mix} = R \ln (n) \tag{3}$$

where R (8.31 J/mol.K) is gas constant. From the **Figure 3**, we can see that by increasing the number of elements in the system, the mixing entropy also increases. From equation (3), for binary to five element alloys have mixing entropy of 5.76 and 13.37 respectively. This in turn decreases the mixing free energy(ΔG_{mix}).

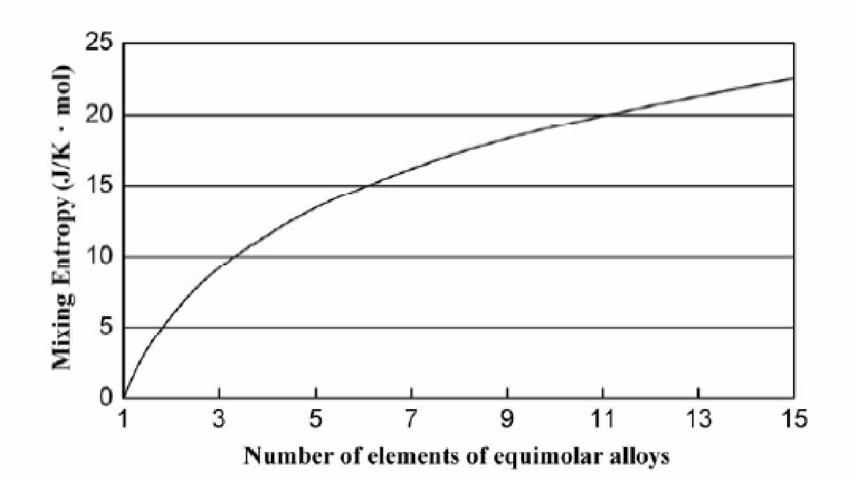

Figure 3. The entropy of mixing as a function of the number of elements for equimolar alloys [7]

The limit on the number of elements is set from five to thirteen. The lower limit is five so that the mixing entropy is high enough to form solid solution phase by counter balancing mixing enthalpy. The upper limit is set to 13 elements as the curve goes almost parallel to x-axis and thus we do not see much change in mixing enthalpy. The elements in HEAs need not be in equimolar ration and can be between 5 and 35 atomic percentage and in this way, we can have more number of possible combinations. These combinations can further be broadened by allowing equimolar combination of elements. The mixing entropy of the multi-principal-element alloys should be greater than $1.61R$ to be a HEA, as shown in **Figure 4** [7].

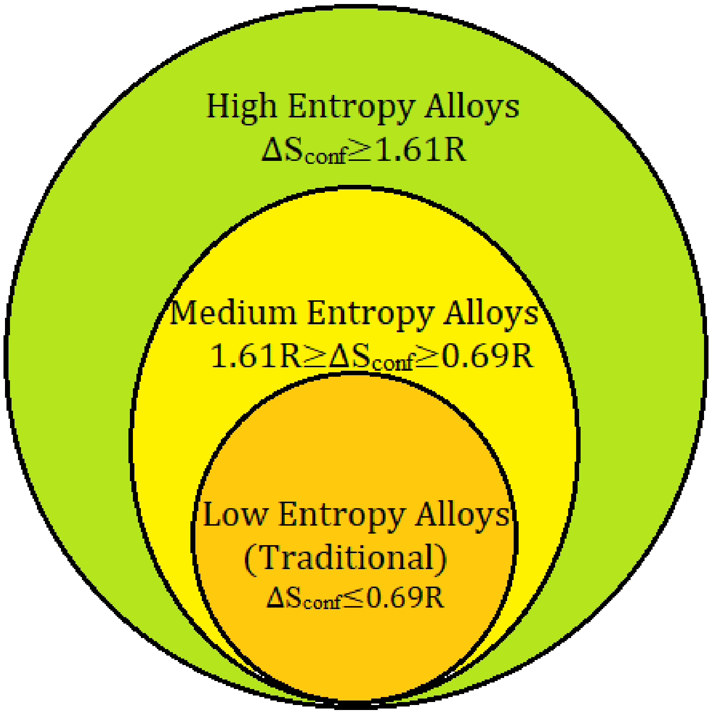

Figure 4. Division of alloys according to the mixing entropy [7]

The multi-principal-element alloys were expected to exhibit brittleness and complex manufacturing process and challenging analysis. Nonetheless, they showed better stability because of their large mixing entropies. Following Boltzmann's hypothesis on relationship between entropy and system complexity, the configurational entropy per mole, ΔS_{conf}, during the formation of a solid solution from n elements with equimolar fractions may be calculated from the following equation [9].

$$\Delta S_{conf} = -k \ln w = -R \left(\frac{1}{n}\ln\frac{1}{n} + \frac{1}{n}\ln\frac{1}{n} + \ldots + \frac{1}{n}\ln\frac{1}{n}\right) = -R \ln\frac{1}{n} = R \ln n \qquad (4)$$

Where k is Boltzmann's constant, w is the number of ways of mixing and R is the gas constant: 8.314 J/mol.K. By Richard's rule, the entropy change in fusion of most of metals are only empirically equal to R at their melting point. ΔS_{conf} value for equimolar alloys of 3 elements is 1.10R which increases to 1.61R and 2.57R for 5 and 13 element solid solution, respectively. In fact, if we consider other factors like vibrational, electronic and magnetic randomness, the entropy change of mixing will be much higher than calculated. The resulting ΔS_{conf} for strong intermetallic compounds of NiAl and TiAl is 1.38R and 2.06R respectively which are in the same range as the entropy changes in a system with more than five elements. This indicates that higher the mixing entropy, lower is the tendency of ordering and segregation. Thus, it can be said that alloys with higher number of principal elements will more easily yield the formation of random solid solution during solidification except for those with large heat of formation like ceramics [9].

Based on the name "High-Entropy Alloys" we can also define these alloys on the basis of their configurational molar entropy. The Boltzmann's equation (Eq. 4) gives us the simple way to calculate configurational entropy and if it is greater than $1.61R$, then we can call it a HEA. According to some researchers only equimolar alloys are HEAs while some consider entropy concept to define HEA and thus sometimes they contradict. For example, an alloy with 5% A, 5% B, 20% C, 35% D, and 35% E is an HEA according the composition-based definition, but the entropy of the alloy is $1.36R$ (which is $< 1.61R$) and thus cannot be considered an HEA (based on Boltzmann's equation). Thus, as compromise, some have suggested to consider an alloy is an HEA if the configurational entropy is near to $1.5R$. This excludes a small number of HEAs on the composition-based definition and any alloy having less than 5 principal elements [8]. Also, as shown in **Figure 5,** for a ternary system if the ΔS_{conf} is greater than 8.5 J/mol.K (1.01R) then it is considered as high-entropy alloy.

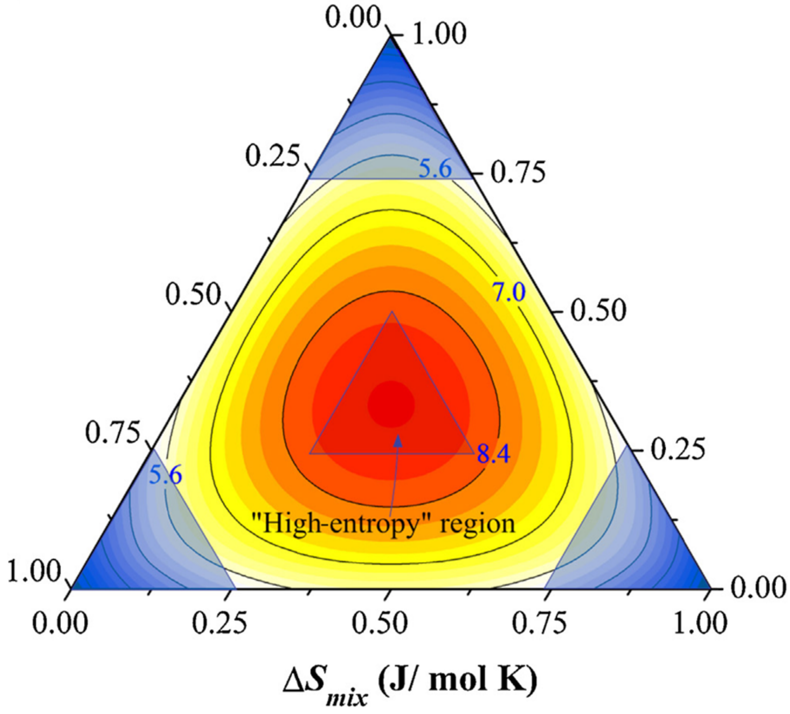

Figure 5. The contour plot of ΔS_{mix} (J/mol K) on a schematic ternary alloy system. The blue corner regions indicate the conventional alloys based on one or two principal elements, whereas the red center region indicates the 'high-entropy' region [10]

There are four types of effect [7] seen by mixing of multi principal elements:

1. High-Entropy Effect

Contrary to what was expected, HEAs were found to form of only few or sometime even single solid solution phase which is the result of the high mixing entropies. The number of phases formed are much lesser as predicted by the Gibbs' phase rule. Thus, higher the mixing entropies, more is the solubility among elements and prevents phase separation.

2. Lattice Distortion Effect

The conventional crystal structure was based on one or two elements but with introduction of HEAs, this concept has been extended to multi elemental structures. Such a structure with all the atoms of different elements will always be distorted because of their difference in atomic size. **Figure 6** shows body centered cubic structure (BCC) and face centered cubic structure (FCC) crystal structure incorporating five different elements. With such huge difference in atomic size, the lattice is expected to collapse into an amorphous structure because to retain such a structure huge lattice distortion energy is required. These distortion in lattice causes the change in thermal, mechanical, electrical, and magnetic properties of composition and is known as 'lattice distortion effect'.

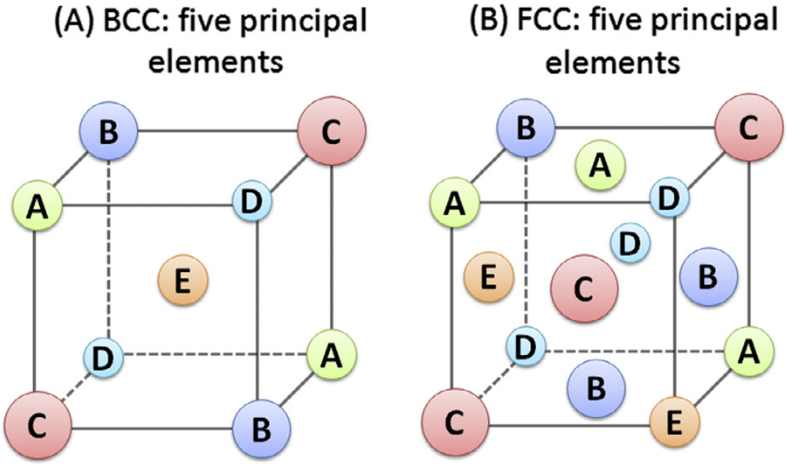

Figure 6. BCC and FCC crystal structure with five principal elements [11]

3. Sluggish Diffusion Effect

In order to acquire equilibrium partitioning among the phases, cooperative diffusion of elements is required during phase transformation. In combination with lattice distortion, the atomic movement is hindered and limits the effective diffusion rate of HEAs. In conventional HEAs, the phase separation during cooling is often inhibited at higher temperatures and therefore delayed until lower temperatures [7]. Because of this the as-cast structures of HEAs often have nano-precipitates in the matrix. This also causes higher recrystallisation temperatures and activation energy of deformed HEAs. This tendency to form nanocrystalline or amorphous structures may be exploited to promote the mechanical, physical, and chemical properties of alloys.

4. Cocktail Effects

Now that HEAs are multi-principal-element alloys, they exhibit composite effect coming from the basic features and interactions among all the elements. HEAs can be viewed as an atomic scale composite, like if oxidation resistant materials are used such as Al, Cr and Si, then the composite also gets oxidation resistance at higher temperatures. Similarly, with addition of Al which has strong bonding with other elements and thus the overall strength of composite is increased. Thus, as per the required properties, the principal elements may vary to give desired properties to composite. “The ‘cocktail’ effect reminds us to remain open to non-linear, unexpected results that can come from unusual combinations of elements and microstructures in the vast composition space of MPEAs” [8].

HEAs have a vast pool of different combinations of mutually miscible metallic elements. If we consider 13 such elements with 5 to 13 other elements in equimolar ratios, we can design a total of 7099 HEAs.

$$C_5^{13} + C_6^{13} + C_7^{13} + C_7^{13} + C_8^{13} + C_9^{13} + C_{10}^{13} + C_{11}^{13} + C_{12}^{13} + C_{13}^{13} = 7099$$

where C_n^m is the number of combinations of m items taken n at a time. However, if consider the 89 metallic elements in periodic table, then the number of HEAs that can be designed becomes countless even if we exclude some of the incompatible elements.

2.1 Major Alloy Families

There are a number of compositions available for HEAs and following are the alloy families of these composition.

2.1.1 3d Transition Metal HEAs

By far the most commonly used elements for HEAs or complex, concentrated alloys (CCAs) are Al, Co, Cr, Cu, Fe, Mn, Ni, Ti, and V, as shown in **Figure 7**. For an alloy to be in this family, it must have at least 4 out of 9 of the above elements. These alloys can be considered as an extension of stainless steel and superalloys. For example, austenitic (FCC), duplex (FCC + BCC) and precipitation hardened stainless steels all have 3 principal elements-Fe-Cr-Ni [8].

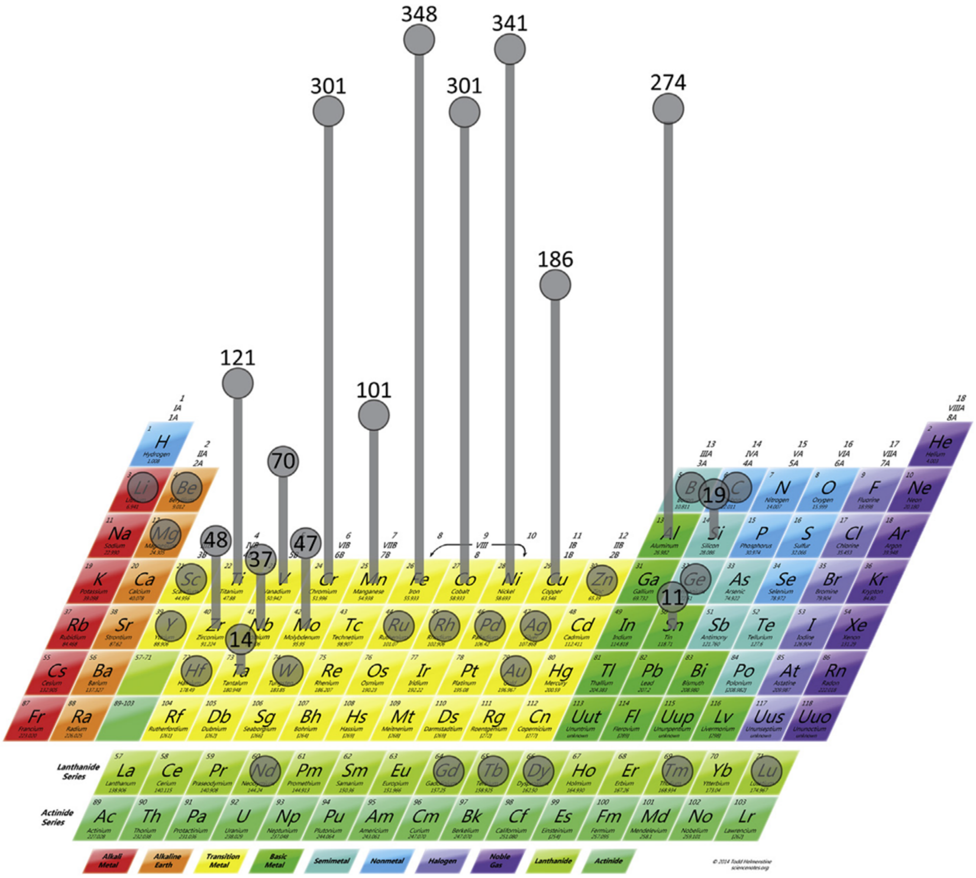

Figure 7. The frequency with which elements are used in the 408 multi-principal-element alloys (MPEAs) of this assessment. The vertical lines are proportional to the number of alloys [8]

2.1.2 Refractory Metal HEAs

The refractory metal HEAs family consists of alloys having at least 4 of the 9 following elements: Cr, Hf, Mo, Nb, Ta, Ti, V, W, and Zr, plus Al, as shown in **Figure 8** [8]. Compared to

3d transition family, this family is studied less. Only 29 refractory HEAs were reported by mid-2015. However, some of the refractory elements (Ir, Os, Re, Rh, Ru) have not yet been studied and they offer new possibilities. The objective of refractory HEAs is to develop high temperature structural metals. It offers wide range of elemental properties such as melting temperature as (2128-3695K), density (4.5-19.5 g/cm^3) and elastic moduli (68-411 GPa for Young's Modulus).

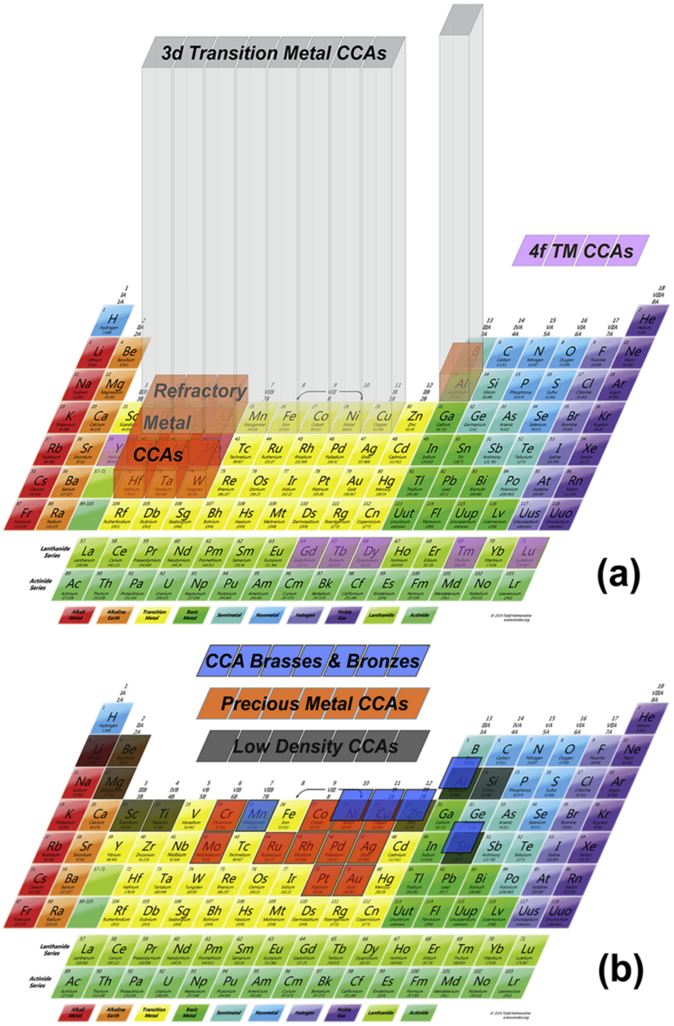

Figure 8. Six of the seven CCA families illustrated by element groupings. (a) 345 3d transition metal CCAs, 29 refractory metal CCAs and 2 lanthanide (4f) transition metal CCAs. (b) 7 light metal CCAs, as well as precious metal CCAs and CCA brasses and bronzes. The heights of boxes in (a) are proportional to the number of alloys in the two major families. Alloys containing B, C and N are not shown [8]

2.1.3 Other Alloy Families

Recently, several new families have been introduced (**Figure 9**). This third family shows the growing need of new type of alloys with low density for aerospace and transportation purpose.

It is based on the following elements: Al, Be, Li, Mg, Sc, Si, Sn, Ti and Zn. With the broad range of boiling and melting point of such alloys, the processing also becomes difficult. Thus, careful selection of primary alloy is needed in primary processing.

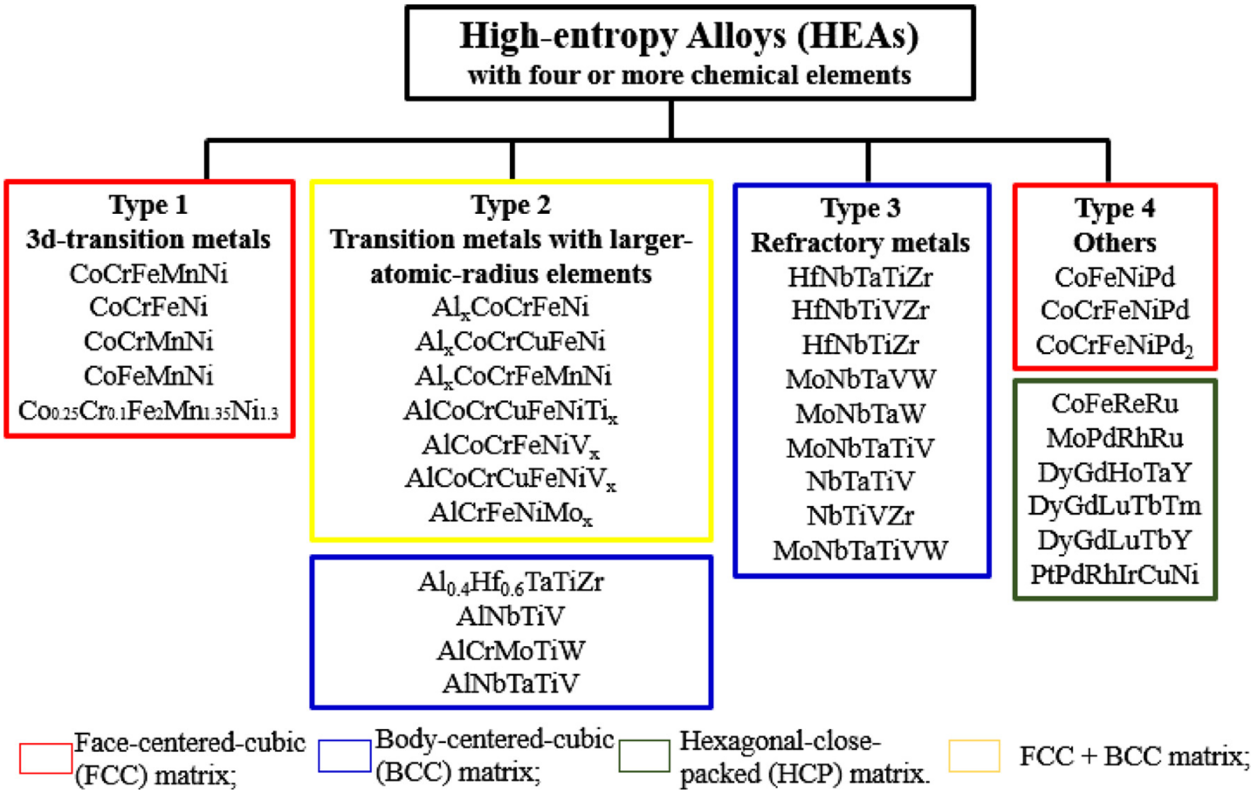

Figure 9. The classifications of high-entropy alloys (HEAs) [12]

2.2 Properties

The vast range of compositions also increases the number of composites to be characterized. There are new challenges in establishing relationships between compositions, microstructure, and properties. Even a small adjustment in one element can bring a drastic change in microstructure and properties, even if they belong to same family, since the elements are more concentrated in MPEAs than in conventional alloys. The production method and post-process thermos-mechanical treatment influences the microstructure of the alloy. Even the defects such as cast segregation, dendritic microstructures, and residual stresses me influence the results [8].

2.2.1 Structural Properties

2.2.1 a) High Temperature Mechanical Properties

The four effects discussed earlier- high-entropy, sluggish effect, lattice distortion and cocktail effects are all in favor of high temperature applications. For example, at high temperature, high-entropy enhances phase and microstructural stability. Sluggish effect slows down structure recovery and thus improves high temperature resistance. Similarly, lattice distortion leads to high friction and makes it difficult for dislocation motion.

For FCC HEAs, FeCoNiCrMn has been studied for high-temperature [13] [14]. The study revealed that the alloy was able to withstand one-month aging at 950°C and remained a single phase with no precipitation of any second phase. This indicates the good microstructural and phase stability of HEAs.

Tensile test of this FCC HEA with different grain size was also performed at different temperatures (**Figure 10)** and the results indicated that the HEAs are not good for tensile loads at high temperature. It is kind of expected because such monolithic pure metals lack the strengthening mechanism at high temperature. To make the HEAs good at tensile properties, precipitates or second phase elements must be added to the matrix to form barriers to the dislocation. Some studies are going on Mn and Cr precipitates formation, especially in samples that deformed at a higher temperature and lower strain rates, presumably after long exposure to heat. Thus, to come up with high performance heat resistant alloys is very difficult because of the challenges of excellent mechanical strength, resistance to thermal creep deformation, good surface stability and resistance to corrosion.

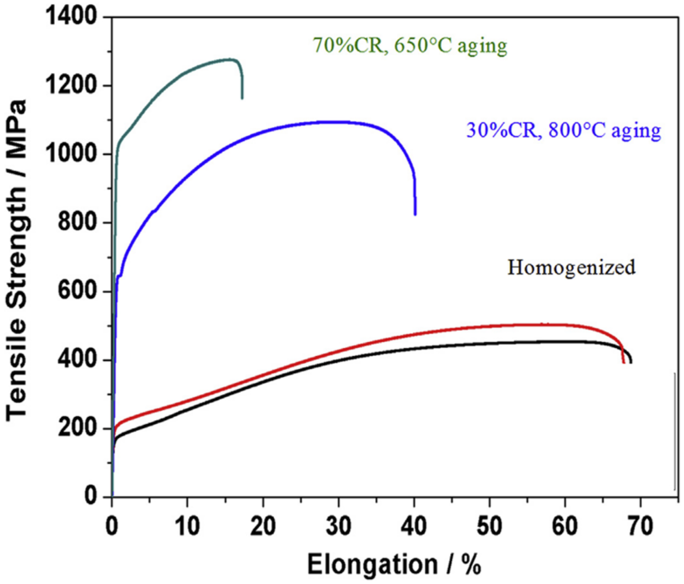

Figure 10. Tensile properties of the FeCoNiCr HEA with precipitation hardening resulted from addition of Ti and Al [13]

2.2.2 Functional Properties

Most of the functional properties are based on the 3d transition metal alloy family. Following are the thermal, electrical, and magnetic properties of alloys.

2.2.2 a) Thermal Properties

$Al_xCoCrFeNi$ ($0<x<2$) and $Al_xCrFe_{1.5}MnNi_{0.5}Mo_y$ ($x=0.3$, 0.5; $y=0$, 0.1) systems were studied for thermal properties. First system was annealed at 1273 K and then water quenched while the second system was studied in as-cast condition. The influence of temperature is opposite to what is observed for pure metals but is similar to stainless steel and superalloys. With increasing Al content, the thermal conductivity decreases within single phase region. This can be explained by the concept that single phase BCC alloy (high Al content) have almost double the thermal conductivity of single phase FCC alloys (low Al content). These behaviors are analyzed using lattice distortions and an increased phonon mean free path due to thermal expansion of lattice at high temperatures.

2.2.2 b) Electrical Properties

$Al_xCoCrFeNi$ ($0<x<2$) alloys shows an electrical resistivity ranging from 100 to 200 μΩ-cm. The electrical resistivity is linearly dependent on temperature [8]. With the increase in Al content, the microstructure transforms from FCC to FCC+BCC to BCC. With some experimental data we have an equation to define the resistivity of FCC and BCC phase.

$$\rho_{BCC} = 107 + 1.43(c_{Al}) \qquad \rho_{FCC} = 107 + 5.50(c_{Al}) \tag{5}$$

where c_{Al} is the Al concentration in atomic percentage. The electrical resistivity of the BCC phase is lower than the FCC phase for the same composition. This transition from BCC to FCC microstructure also defines the reason of a non-monotonic dependence of electrical resistivity on Al content. An MPEA of refractory elements was studied since they are low temperature superconductors [15] [8]. In a zero-magnetic field, the electrical resistivity of single-phase BCC $Hf_8Nb_{33}Ta_{34}Ti_{11}Zr_{14}$ decreases from 46 μΩ-cm to ~36 μΩ-cm with a decrease in temperature from 300 K to ~8 K, and then sharply drops to zero at $T_C = 7.3$ K. The lattice parameter and Debye temperature of the alloy obey a rule of mixtures of the pure elements, so that the elements are concluded to distribute randomly in the lattice.

2.2.2 c) Magnetic Properties

The alloys studied for magnetic properties mostly contains Fe, Co, and Ni. FeCoNi is a ferromagnetic solid solution (SS) alloy with FCC crystal structure and saturation magnetization (M_S) of 151 Am^2/kg [8]. M_S for pure Fe is 218 Am^2/kg and for Ni is 55 Am^2/kg. With addition of Al in AlxFeCoNi, the FCC structure transforms to FCC + BCC/B2. The alloy remains ferromagnetic with addition of Al but the Ms decreases to 102 Am^2/kg. With the addition of Al and Si to $(AlSi)_X$FeCoNi ($0<x<0.8$), at $x=0.2$ gives good M_S, coercivity, electrical resistivity, strain, and yield strength without fracture that makes the alloy an attractive soft magnetic material. Similarly, some alloys show ferromagnetic material for specific range of temperature and then turns paramagnetic beyond the range due to changing alloy phases. The magnetic properties of alloys are influenced by composition through the fraction of magnetic element present. The manufacturing process and post-manufacturing processes like annealing also influence the magnetic properties through the phases formed. Heat treating a material might change the phase of a material resulting in change in magnetic properties.

The HEAs show excellent mechanical and electrochemical properties which make them promising candidate for refractory materials, corrosion resistant materials etc. Recently it has been discovered that HEAs also possess excellent magnetic properties. They are perfect candidate for soft magnetic materials which require high saturation magnetization, electrical resistivity, and malleability, in addition with low coercivity. There are number of ferromagnetic materials that are forms HEAs and the topological disorientation and chemical randomness may increase the electrical resistivity. Also, these HEAs form simple crystalline structure which helps increasing malleability. But there are very few HEAs that can meet all the above requirements. Let us consider FeCoNi$(AlSi)_X$ ($0 \leq x \leq 0.8$), with the increase in value of x, the magnetization goes down, the resistivity goes up and the coercivity firstly increases and then decreases, as shown in **Figure 11**. So, we need to find an optimum value of *x* for which the three properties are good enough [16].

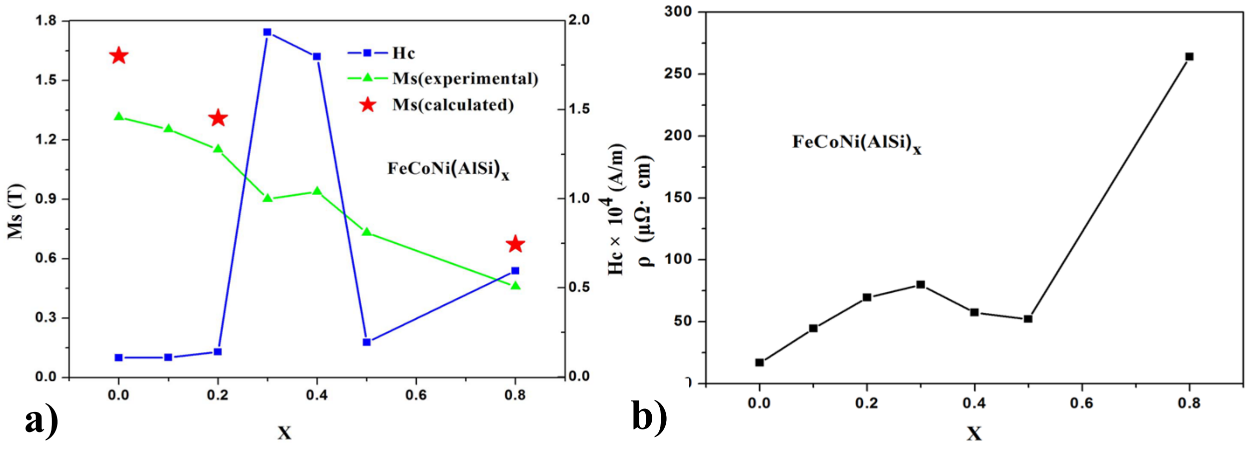

Figure 11. (a) Magnetic properties of FeCoNi(AlSi)x (0≤x≤0.8) alloys (*Hc* and *Ms* represent the coercivity and saturation) (b) The electrical resistivity (r) of FeCoNi(AlSi)x alloys obtained at room temperature [16]

In the similar way, many compositions have been synthesized to get the best possible magnetic properties. Most of the alloys were prepared using casting and some of them were also heat treated before testing. **Table 1** shows the list of HEAs that has been studied for magnetic properties.

Table 1. Comparison of magnetic properties of high-entropy alloys. *Ms* denotes saturated magnetization and *Hc* for coercivity

Alloy	Phase	Synthesis Process	*Ms*		*Hc*	Ref.
			T	Am^2/kg	kA/m	
FeCoNi	FCC	As-Cast	1.32		0.99	[16]
FeCoNiCrCu(Ti)$_{0\text{-}0.5}$	FCC	As-Cast		0.333-1.505	≈0	[17]
FeCoNiCuCr(Ti)$_{0.5\text{-}1}$	FCC	As-Cast		1.368-1.511	≈0	
FeCoNiCrCuAl	BCC	As-Cast		38.178	3.58	[18]
FeCoNiCrCuAl	FCC	Cast+Annealed		16.08	1.19	
FeCoNiCrAl$_{0\text{-}2}$	FCC & FCC+BCC	Cast+ Homogenised	0.05-0.38		0.04-1.42	[19]
FeCoNi(SiAl)$_{0\text{-}0.8}$	FCC & FCC+BCC & BCC	As-Cast	0.5-1.25		1.05- 19	[16]
FeNiCoCrPd$_2$	FCC	As-Cast		34		[20]
FeNiCoCrPd	FCC	As-Cast		33		
FeCoMnNi	FCC	As-Cast		18.14	0.12	[21]
FeCoMnNiAl	BCC	As-Cast		147.86	0.63	
FeCoMnNiSn	CO2MnSn	As-Cast		80.29	3.43	

FeCoMnNiCr	FCC	As-Cast		1.39	10.80	
FeCoMnNiGa	FCC+BCC	As-Cast		80.43	0.91	
$Fe_{25}Co_{25}Ni_{25}(PCB)_{25}$		As-Cast	0.71-0.86		0.001-0.004	[22]
$CuFeMnNiTi(Sn)_{0-1}$		As-Cast		0.34-15.81	4.85-24.7	[23]
AlBFeNiSi(Nb)		Mechanical Milling		1-50	15.87-30.11	[24]
$FeCoNi(CuAl)_{0-1.2}$	FCC & FCC+BCC & BCC	Cast+ Annealed		72-132	12.89	[25] [26]
$FeCoNi(MnAl)_{0-2}$	FCC & FCC+BCC & BCC	As-Cast		51.9-132.2	0.27-0.73	[27]
FeCoNiSiB	FCC	Melt Spinning	0.98-1.1		0.002-0.006	[28]
$FeCoNiCr_X$ X=Sn, Ga, Pd, Mn, Ti, Al	FCC & FCC+BCC & BCC	As-Cast		0.5- 38		[29]
FeCoNiMnX X=Sn, Ga, Al	FCC & FCC+BCC & BCC	As-Cast		80-148		[29]
$Fe_{25}Co_{25}Ni_{25}(PCBSi)_{25}$		Melt Spinning	0.86-0.8		0.8- 2.1	[30]
$FeCoNi(CuAl)_{0.8}Ga_x$ $0 \leq x \leq 0.08$	FCC & BCC	As-Cast		78.6-82.8	0.36-0.69	[31]
$FeCoNiAl_{0.4}Si_x$ $0.1 \leq x \leq 0.5$	FCC & BCC	Mechanical Milling + Annealed		112-124	8.83-12.73	[32]
FeCoNiN		Sol-gel spin coating	0.003-0.009		51.09-56.98	[33]

2.3 Microstructure and Phase Stability

The addition of elements to HEA increases the configurational entropy and sometimes it may cause the transition of phase from single to multiphase, depending on the element added and its amount. This can be explained by HEA $Al_XCoCrFeNi$ ($0<x<3$), where all the elements are equiatomic apart from Al. With increasing Al content, the phase transform M_S from FCC (at $x>0.5$) to mixed FCC + BCC and then back to single phase BCC (at $x = 2.8$). The recrystallisation kinetic are slow because of the sluggish diffusion in HEAs. This sometimes result in nanosized precipitates [13]. In **Figure 12,** the Υ-δ differentiates HEA from solid solutions, intermetallic compounds, and metallic glass.

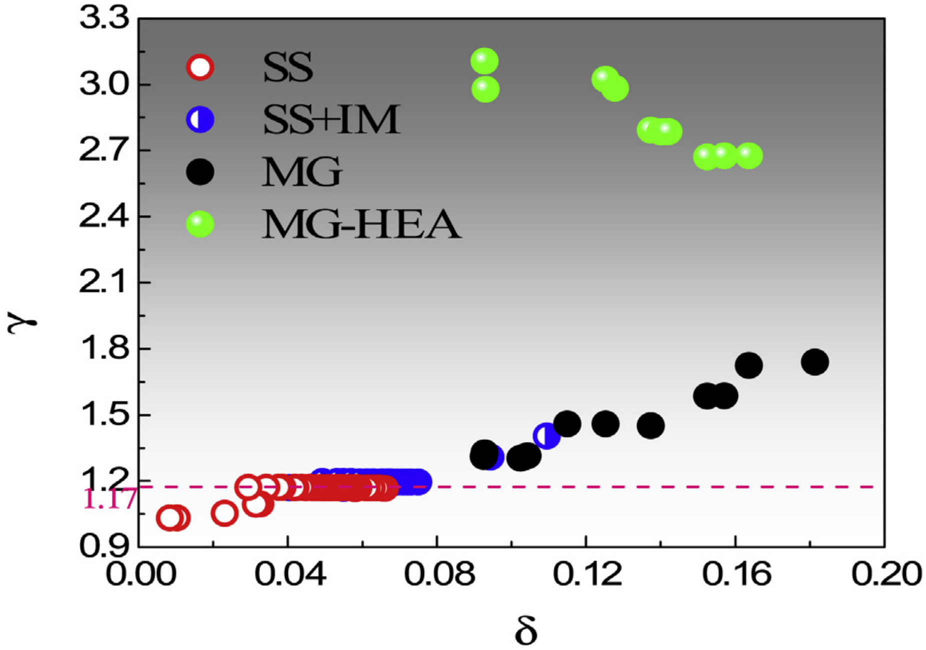

Figure 12. ϒ-δ plot of representative as-cast HEAs. The SS, SS + IM, MG and MG-HEA indicate solid solution, solid solution plus intermetallics, metallic glass and highentropy metallic glass, respectively [13]

Now the question arises, if HEAs with 5 or more elements with some configurational entropy can form single phase alloy. Wu et al. [34] [13] researched if the combinations of elements of single phase FCC quinary HEA FeCoNiMnCr were also single-phase FCC. They cast all the quaternary, ternary and binary possible combinations and found that only quaternary FeNiCoCr, FeNiCoMn, NiCoCrMn, the ternary alloys FeCoNi, FeNiCr, FeNiMn, FeCoCr and NiCoMn and the binary alloys FeNi and NiCo were all single-phase FCC. All the other combinations were either multiphase or has a different crystal structure. Thus, it proves that single phase alloy is not just determined by the number of elements but also the type of alloying element being added. Also, many times because the size of particles goes down to tens of nano particle, it becomes difficult for X-ray Diffraction (XRD) to pick up the two phases of the alloy. For example, in AlCoCrCuFeNi and AlCoCrFeNi, the second phase particles are very small to be distinguished by the XRD. However, by atomic scale structural and high resolution Transmission Electron Microscopy (TEM) and atom probe tomography often reveals the nano-scale phase separation caused by local chemical ordering. For example, CoCrFeCuNiAl$_{0.5}$ HEA can be considered a single-phase FCC alloy according to XRD. However, under high-resolution TEM, the atomic image taken using a high angle annular dark field detector shows obvious structural and chemical variations. The phase separation in this case is because of depletion of Cu from the HEA lattice because formation of simple FCC phase by Cu uphill diffusion is kinetically easier than that of $L1_2$ phase formation. The potential strengthening of HEAs is highly affected by the observation of phase separation and nanoprecipitation.

2.4 Strengthening Mechanisms

When moving dislocations interact with crystalline defect, hardening or strengthening of crystalline solid occurs [13]. Depending upon the type of defects, hardening mechanism are traditionally divided into four categories: solid solution hardening, which is associated with four point defects in crystal; strain hardening, which is associated with line defects in the crystal; grain boundary hardening, which is associated with planar defects in the crystal; and precipitation and/or dispersion hardening, which is associated with volumetric defects in the crystal [13]. Each of them operates individually and simultaneously to the overall strength of the crystal, σ_t, which can be defined as

$$\sigma_t = \sigma_f + \sigma_{ss} + \sigma_{sh} + \sigma_{pt} + \sigma_{gb}$$

where the subscripts *ss* stands for solid solution, *sh* for strain hardening, *pt* for precipitation/dispersion, *gb* for grain boundary, and σ_f represents the intrinsic or frictional strength of the crystal. The four concepts of hardening are summarized on the basis of available data.

2.4.1 Strain Hardening

It was found that for single phase FCC FeCrNiCoMn was relatively soft as-cast, cold working significantly increased the strength. As shown in **Figure 13**, 50% of cold working can increase the yield strength by a factor of 5. However, the plastic instability develops immediately once the yielding is cold rolled over 50% which indicates the edge of plastic strain limit of the alloy.

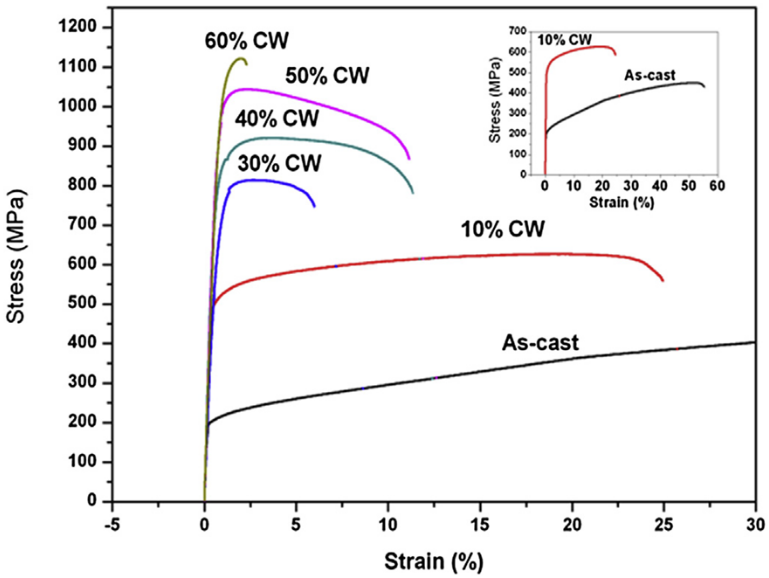

Figure 13. Mechanical properties of the FeCoNiCrMn HEA as a function of cold rolling [13]

2.4.2 Grain Boundary Hardening

There is not much research done on the effect of grain size on the yield strength. According to one of the research on 70% cold rolled FCC-FeCoNiCrMn and then annealed the samples at 850-950 °C to produce various grain size. Subsequently microhardness test was performed and it was found that *kHP* = 677 MPa-(μm)-1/2, where *kHP* is the hall petch coefficient. For conventional alloy value of *kHP* is about 600 MPa-(μm)-1/2, which is slightly lesser than the above alloy [13]. FCC-FeCoNiCr was also cold rolled to 90% reduction and then annealed at 900 °C for various durations of time to get different grain sizes. The *kHP* for this alloy came out to be 900 MPa-(μm)-1/2, apparently much higher than the conventional alloys. The reason for high strength FCC-FeCoNiCrMn can be the large number of twins present in the composition which may contribute to the strengthening while in contrast FCC-FeCoNiCr contains negligible twins. Therefore, grain refinement can be considered as an effective strengthening mechanism in HEAs.

2.4.3 Solid-solution Hardening

For conventional alloys we have formula for calculating strength. It is based on the dislocations in a solvent matrix locally distorted by solute atoms. But in HEAs it's hard to differentiate between solute and solvent.

It is noted that the overall strength of HEA is higher than the individual elements. For example, yield strength of fully-annealed pure Ni is 150MPa which is lower than the fully homogenized FCC-FeCoNiCrMn which is 200 MPa [13] [35]. Many efforts have been put in to propose a mathematical relation to rationalize the increase in strength, so called the solid-solution effects in HEAs but the inherent problem of solute and solvent encounters it. This area of solid solution is yet to be explored. However, it was recently found that the presence of interstitial atoms in a BCC-HEA caused a dramatic hardening [13].

2.4.4 Precipitation Hardening

There have been reports on the observation of age hardening in some HEAs, for example, a mixed FCC + BCC $CuCr_2Fe_2NiMn$ [36] [13], a mixed FCC + BCC $Al_{0.3}CrFe_{1.5}MnNi_{0.5}$ and single-phase BCC $Al_{0.5}CrFe_{1.5}MnNi_{0.5}$ [37] [13]. The strength increases by about 2-3 times and the aging temperature is around 600-800 °C. The strengthening phases were identified to be tetragonal $Cr_5Fe_6Mn_8$ phase in BCC-$Al_{0.5}CrFe_{1.5}MnNi_{0.5}$ alloys and $Cr_5Fe_6Mn_8$ (ρ phase) in $CuCr_2Fe_2NiMn$. Compared to conventional alloys, these precipitates were relatively bulky (>micron size). The precipitates in traditional hardened alloys are very fine particles (~nm). Furthermore, microstructural kinetics such as size, shape and distribution and the feature of precipitate are not yet clearly identified. In short, we can say that the nature of age hardening, till date, is largely unclear [13].

2.5 Prospects of HEAs

HEAs is a new class of alloys consisting of several principal elements in the crystal lattice. They cannot be called a solid solution without clear identification of solute and solvent. Thus, theories of solid solutions cannot be applied on HEAs. Since there are five or more principal elements in HEAs thus it is hard to determine a solute or solvent and thus we need to come up with a new theory for HEAs. In addition to this, with such multiple elements, the crystallographic lattice of HEAs containing multiple primary elements with different atomic sizes and chemical properties is severely distorted, and thus the creation, interaction and movement of all kinds of crystal defects, e.g. Vacancy, dislocation, stacking fault and grain boundary etc., are expected to be different from those in conventional alloys. So, a novel characterization technique, advanced computational method with extensive research is needed to come up with a relationship between microstructure and mechanical properties of HEAs [13].

To understand the strengthening in HEAs, we have to characterize the lattice distortion and its effects on defect energies. However, measuring lattice distortion and calculating lattice distortion energy is still a challenging task at this moment.

In HEAs, it does not matter if segregation occurs or not in order to lower overall energy. A distorted lattice with high energy level and a larger lattice friction already has a large effect on the mobility of dislocations, cross slip ability of screw dislocations, and twinning tendency which influence deformation behaviors and thus the deformation structure. For all these dynamic behaviors, grain size hardening, twinning induced strain hardening, ductility, creep and fatigue initiation and propagation all need to be assessed and investigated in the future [13].

For high temperature applications, the HEAs must have Reduced lattice diffusion. The BCC structure generally has a relatively higher self-diffusion rate than the close packed FCC and HCP structures. One of the key factor for high temperature deformation behavior is lattice diffusion. To maintain high phase stability and to keep the excellent creep properties, we have to slow down the lattice diffusion behavior [13]. The pure metals are not strong enough at high temperatures and thus we need to include a strengthening technique for effective strengthening. Till date, precipitation hardening seems to be the most promising method of high temperature strengthening. Also, at high temperatures the grain boundaries tend to be weak regions at high temperature and thus needs to be properly controlled. The BCC HEAs shows strong resistance to high temperature softening and substantial microstructure stability. However, under long time of high temperature exposure needs to be improved. Cr, Al or Si can be considered for such problems. If an HEA contain expensive raw material such as Nb, Hf, Ta, W, Zr and V, then cost is an inevitable issue because of the equimolar ratios of components. Thus, FCC HEAs containing Fe, Co, Ni, Cr and Mn are much cheaper. Cost reduction is also a big challenge for HEAs.

3. Mechanical Alloying

Ball milling or mechanical alloying is a technique to produce ultrafine materials. It is widely used in ceramic and metal processing industries. It consists of repeated fracture, mixing and cold welding of a fine blend of metal, oxide and alloy particles resulting in size reduction and may also include chemical reactions [38]. Ball milling is used to prepare nanostructured materials for study because nanostructured materials behave in different way than the bulk materials.

However, the processing parameter and machine construction is being optimized to obtain powder with desired size and performance characteristics.

There are two different terms used in high energy ball mills. Mechanical Alloying (MA) describes the process when two or more powders are milled together. In this process the material is transferred into each other to obtain homogeneous alloy. On the other hand, milling of uniform composition powder such as pure metals, intermetallic, where material transfer is not required for homogenization, is called Mechanical Milling (MM).

This powder metallurgical process is used for the preparation of alloys which cannot be produced using conventional techniques. Mechanical milling involves use of compressive force and shear force to effect particle size reduction of bulk materials. A vial or a jar containing milling balls and powder is vigorously shaken to obtain the nanostructure. The size of the particle depends on milling speed, type of milling equipment, size of milling balls and ball to charge ratio.

Various experiments were conducted using different equipment, milling speed and ball to powder ratio (BPR) [39] [40]. The powder was taken out after selected interval to analyze the change in size and shape of powder sample. The experiment which used pure iron powder in Pulverisette-5 planetary ball mill with 20:1 BPR and 230rpm as milling speed for 80 hours run resulted in grain size of up to 6nm [40]. The conclusion is that MA is an effective method to produce nanometer powders of pure elements, as shown in **Figure 14.**

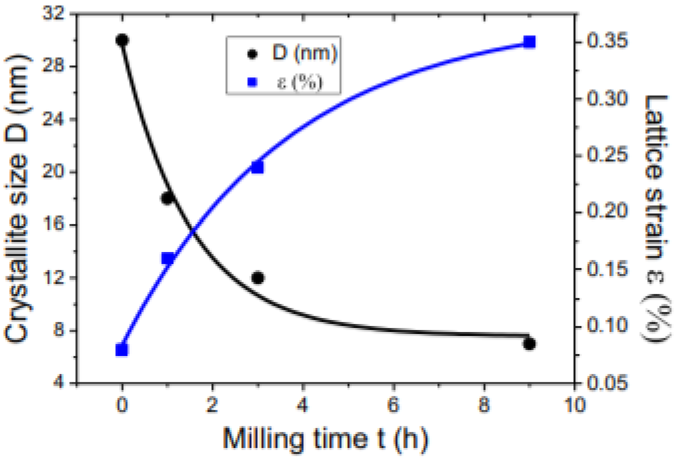

Figure 14. Reduction in crystallite size and increase in strain as a function of milling time [41]

In the early stages of milling the particles are soft and have tendency to weld together and form larger particles. A broad range of particles are sizes are developed, with some as large as three times bigger than the initial particle size. With continued deformation, the particles get work hardened and fracture by a fatigue failure mechanism or by the fragmentation of fragile flakes. A schematic of ball-powder-ball collision is shown in **Figure 15.** Now the tendency to fracture and reduce size of particles dominates over cold welding. After that the particle size remains the same but the continued impact of grinding balls steadily refines the structure as shown in **Figure 16**.

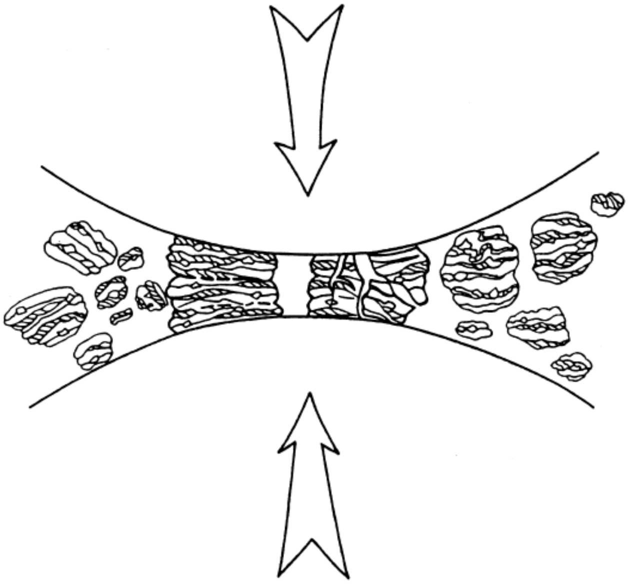

Figure 15. Ball-powder-ball collision of powder mixture during mechanical alloying. [42]

The efficiency of the ball mill is less than 1%. The remaining energy is lost in the form of heat, and small amount is utilized in elastic and plastic deformation of powder particles. After milling for certain period of time, a steady state equilibrium is attained between cold welding and fracturing. The smaller particles are able to withstand the impact loads. At this stage the powder becomes homogeneous and it reaches saturation hardness due to accumulation of strain energy.

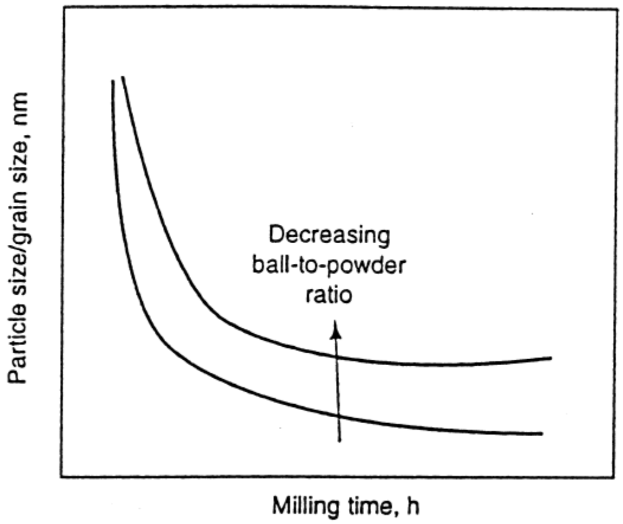

Figure 16. Refinement of particle and grain sizes with milling time. Rate of refinement increases with higher milling energy, ball-to-powder weight ratio, lower temperature, etc. [40]

3.1 Types of Mills

Different types of high-energy milling equipment are available according to different capacity, efficiency of milling and additional arrangements like cooling, heating, etc. Following are some of the mills available.

3.1.1 SPEX Shaker Mills

These kinds of mills are mostly used in laboratory for milling about 10-20 g of the powder at a time. These mills (**Figure 17(a))** may have one or two vials option to mill at one time. The vial (**Figure 17(b))** is clamped and swung back and forth several thousands of times in a minute. The back and forth is combined with lateral movements of the end of the vial so that the vial appears to be moving in a figure 8 or infinity sign. With every swing of vial, the ball impact against each other and the end of the vial causing both the milling and mixing of the sample. The amplitude (about 5 cm) and speed (about 1200 rpm) of the clamp motion, the ball velocities are high (in order of 5 m/s) and consequently causing unusually high impact [42].

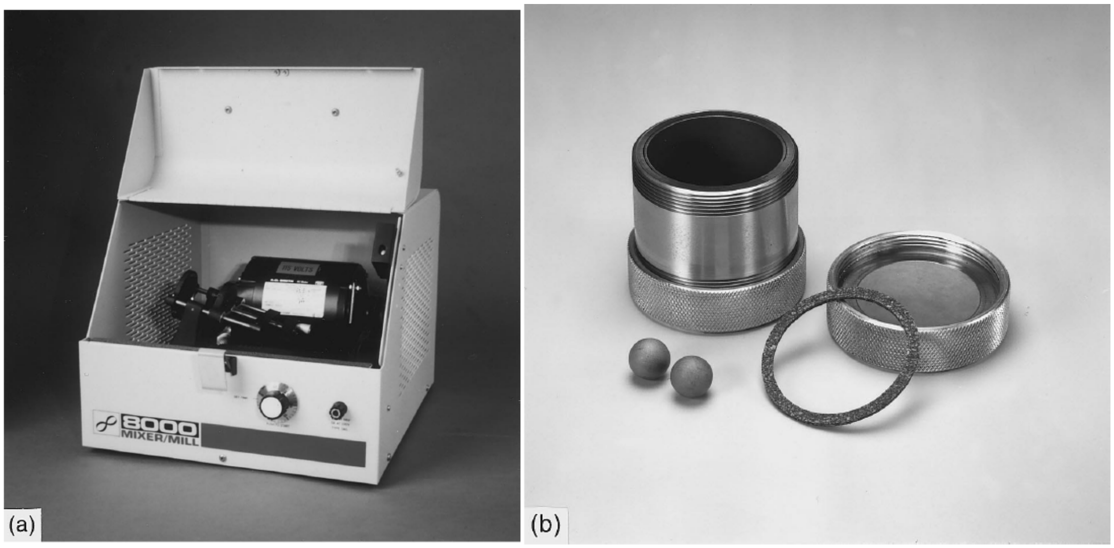

Figure 17. (a) SPEX 8000 mixer/mill in the assembled condition. (b) Tungsten carbide vial set consisting of the vial, lid, gasket, and balls. Courtesy of SPEX CertiPrep, Metuchen, NJ [42]

3.1.2 Planetary Ball Mills

Planetary ball mill (referred to as Pulverisette) is a popular mill for conducting MA experiments. These are manufactured in Germany. As the name suggests, the vials move like the planet system. These are arranged on a rotating support disk and a special drive mechanism causing them to rotate around their own axes. The centrifugal force produced by the vial rotating motion and the force produced by rotating disk both act on the vial contents, consisting of material to be ground and the grinding balls, as shown in **Figure 18**. The vials and the supporting disk rotate in opposite direction, causing the centrifugal force to act in opposite direction. This causes the balls to run down the inside of the vial causing the friction effect followed by the material being ground and grinding balls lifting off and travelling freely through the inner chamber of the vial, colliding against the opposing inside wall and causing the impact effect [42].

Even though the linear velocity of the balls in planetary mills is higher than SPEX, the frequency of impact is much more in SPEX mills. Hence, Fritsch Pulverisette are lower energy mills compared to SPEX mills.

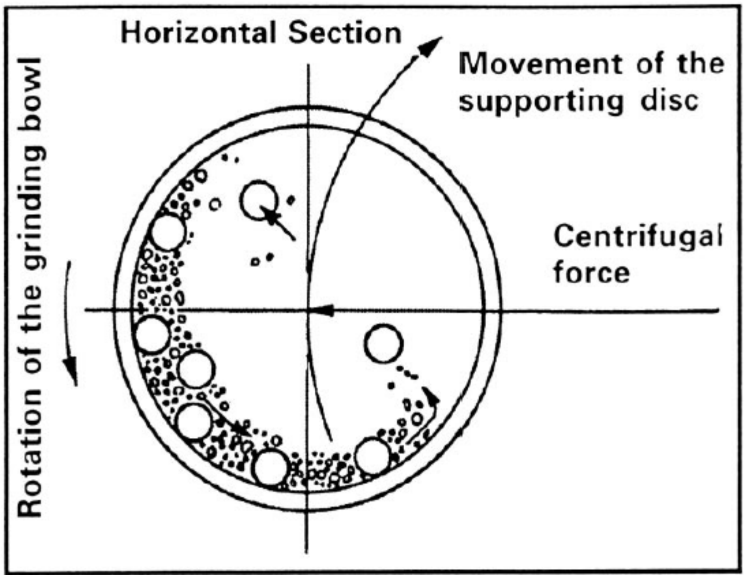

Figure 18. Schematic depicting the ball motion inside the ball mill. Courtesy of Gilson Company, Inc., Worthington, OH [42].

3.1.3 Attritor Mills

These conventional ball mills consist of horizontal drum half-filled with small steel balls. With the rotation of the drum, the balls drop on the powder that is being ground. The grounding rate can be increased with higher speed of drum rotation. However, if the speed of the drum is increased beyond a limit then the centrifugal force becomes more than the gravity forces causing the balls to be pinned to the walls of drum and the grinding option stops. An attritor has a vertical drum with series of impellers inside it. They are progressively set to 90 degrees to each other and the impeller energizes the ball charge, causing the powder size reduction because of impact between balls and container. Some size reduction is because of interparticle collisions and by ball sliding. The velocity of the grinding is much lower (about 0.5 m/s) than any other mills [42].

3.1.4 Commercial Mills

These mills are much larger in size and can process several hundred pounds of powder at a time. MA for commercial production is carried out in ball mills of up to about 3000 lbs capacity. The milling time is inversely proportional to the energy of mill. For comparison purpose, 20 minutes of milling in SPEX is equivalent to 20 hours of milling in a low-energy mill of the type Invicta BX 920/2 [42]. The **Figure 19** shows the time required by different mils to reach the same particle size.

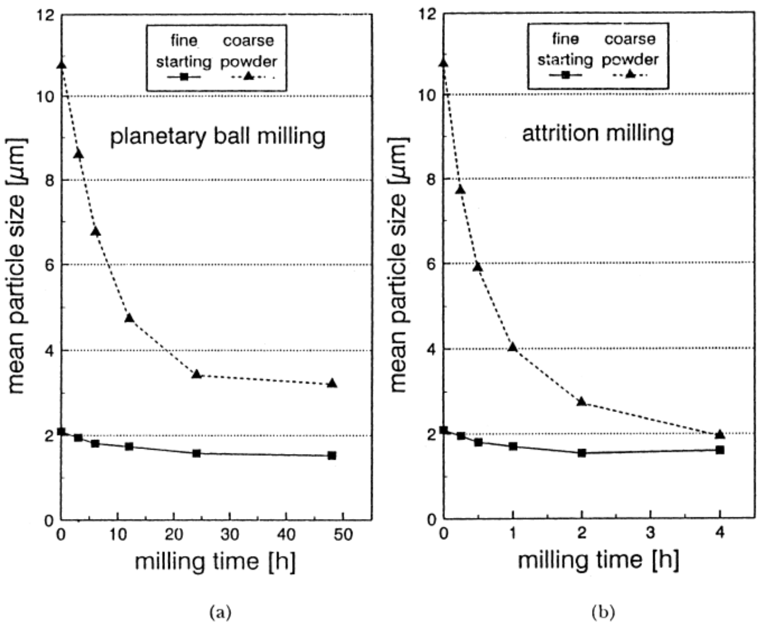

Figure 19. Time to reach similar particle sizes during milling of TiB_2 powder in (a) planetary ball mill and (b) attritor [42]

3.1.5 Special New Design Mills

According to new requirements, there are some specialized mills coming up in the market. These include the rod mills, vibrating frame mills, cryogenic mills and uni-ball-mills. Some issues of sample getting contaminated because of erosion of container was solved by designing a friction free mechanical grinder. It had seven steel rods arranged in hexagonal motif with one rod in the center. The device moves up and down with an amplitude of 3.5 mm and frequency of 25 Hz [42]. It is claimed to have a low contamination of the milled powder. **Table 2** shows the capacities of various mills.

Table 2. Typical capacities of the different types of mills [42]

Mill Type	Sample Weight
Mixer Mills	Up to 2 × 20 g
Planetary Mills	Up to 4 × 250 g
Attritors	0.5-100 kg
Uni-ball Mills	Up to 4 × 2000 g

3.2 Process variables

Mechanical alloying is a complex process with 10 important process variables. These variables are required to be optimized to obtain the maximum efficiency. Some of the variables are dependent on each other, like optimum time of milling depends on type of mill, size of mill, size of grinding medium, temperature of milling, BPR etc. Following are the process variables.

3.2.1 Type of Mill

As discussed above, there are different mills available in market with different capacity, speed of operation, and their ability to control the operation by varying the temperature of milling [42]. Depending on the type of powder, quantity of powder and final constitution required, a suitable mill can be selected.

3.2.2 Milling Container

The grinding vessel, vial or the jar used for milling is important since the inner walls may get eroded during the impacts of balls with the wall and cause contamination. The whole chemistry may change if the vial material is different from the powder. Hardened steel, tool steel, hardened chromium steel, tempered steel, stainless steel, WC-Co, WC-lined steel and bearings are the most common types of materials being used for grinding vessel [42]. The shape of the container is also important, especially the design of the container. We get both flat and round-ended SPEX mill containers.

3.2.3 Milling Speed

It cannot be always said that higher the speed, more the energy input into the powder. It depends on the design of mill which may have certain limitations to highest speed that can be employed. As discussed earlier, in conventional mills the balls get pinned to the balls at very high speeds. Therefor the speed should be kept below the critical speed so that the balls fall from the highest possible height to produce maximum collision energy.

Also, with increase in speed of mill, the temperature of the vial also rises. This may be advantageous in cases where diffusion is required to promote homogenization. But, in some cases this increased temperature may accelerate the transformation process and result in the decomposition of supersaturated solid solutions.

3.2.4 Milling Time

This is the most important parameter of milling. It is so chosen to achieve a steady state between fracturing and cold welding of the powder particles. It depends on the type of mill being used, BPR, temperature of milling, intensity of milling. Contamination is also one factor for deciding the milling time because more the milling time, the probability of contamination increases. Thus, it is preferred to keep the time just for the required duration and not any longer.

3.2.5 Grinding Medium

Hardened steel, tool steel, hardened chromium steel, tempered steel, stainless steel, WC-Co and bearings are the most common types of materials being used for grinding vessel [42]. The density of the balls needs to be high to create enough impact force on the powder. The material of vessel and grinding media are always desired to be of same material to prevent cross contamination. However, as in the case of grinding vessel, some special materials are used for the grinding medium and these include copper [43], titanium [44], niobium [45], zirconia [46], etc.

It has been reported that the final constitution of the powder is dependent upon the size of grinding medium used. The size of the grinding medium influences the milling efficiency because bigger the balls, more will be its weight and higher will be the impact energy to the powder particles. It has also been predicted that the highest collision energy is obtained if balls with different diameter is used [47]. The powder forms a coating on the grinding media and on grinding vessel. This is advantageous because it prevents any further contamination from the vessel or the balls. But, at the same time, the thickness of the coating should be kept minimum to avoid formation of heterogenous final product. It has been reported that the combination of small and big balls reduces the cold welding and the amount of powder being coated on the surface of balls [48]. Although we do not have any specific reason for this. Also, with the same size balls it has been found that the balls tend to follow a well-defined path. Thus, to make the path more random, different size balls must be used.

3.2.6 Ball-to-powder Weight Ratio

The ratio of weight of the balls to powder (BPR) or sometimes referred to as charge ratio (CR), is also a critical variable in the milling process. For study purpose, the ratio has been varied from 1:1 [49] to 220:1 [50] and it has been found that 10:1 is the most commonly used ratio while milling the powder in small scale mill such as SPEX mill. But with higher scale, the ratio may go up to as high as 100:1. The higher the BPR shorter is the time required to reach a particular phase of the powder being milled. It is also found that with ‘soft’ conditions (low BPR and low rotation speed) of MA produce metastable phases whereas ‘hard’ conditions produce equilibrium phases.

3.2.7 Extent of Filling the Vial

To increase the impact energy transferred to the vial, the balls should fall from higher height. Thus, the balls must have enough room to move around freely in the vial. If the quantity is kept very less than the rate of production falls drastically and if the vials is filled in large quantity, then the balls do not get space to move around. Thus, care has to be taken by not filling the vial more than 50% of its total space.

3.2.8 Milling Atmosphere

Contamination is the major effect of atmosphere of vial. The vial is usually filled with inert gas such as argon or helium to prevent oxidation of material. The loading and unloading of vial is usually carried out in oxygen-free argon glove boxes. Hydrogen environment causes formation of hydrides, nitrogen environment forms nitrides and air forms oxides and nitrides in the powder. Thus, care has to be taken during milling regarding atmosphere of vial.

3.2.9 Process Control Agent (PCA)

Due to heavy plastic deformation of powder particles during milling, they get cold welded to each other. But there should be a balance maintained between cold welding and fracturing of the particles for true alloying. A PCA act as a lubricant or surfactant which reduces this effect of cold welding in powders. The PCAs are generally organic compounds which can be solid, liquid or gaseous. The PCA gets coated on the powder particles and thus minimizes cold welding, inhibiting agglomeration.

The PCA used in a milling process varies from 1-5 wt% of total powder charge. The most common PCAs are stearic acid, ethanol, methanol and hexane. Most of these PCAs decompose during milling, interact with the powder and form compounds and gets incorporated in the form of inclusions or dispersoids into the powder. These hydrocarbons may also result in formation of carbides and oxides in powder which are uniformly dispersed in the matrix. This may increase the strength and hardness of material. The hydrogen generally escapes as gas, but some research says that it acts as catalyst for the formation of amorphous phase [51]. PCAs sometimes may affect the final phase formation too.

The quantity and nature of PCA used and the type of powder milled determine the final shape, size and purity of the powder particles. If large quantity of PCA is taken then the particle size may reduce by 2-3 orders of magnitude.

Finally, we can say that there is no universal PCA. PCA selection depends on (1) cold welding characteristics of the powder particles (2) chemical and thermal stability of PCA (3) amount of powder and grinding medium used.

3.2.10 Temperature of Milling

Since the milling involve diffusion processes in the formation of alloy phase irrespective of whether the final product is solid, solution, intermetallic, nanostructure or an amorphous phase, temperature is expected to have a significant effect on alloying.

The temperature is either controlled by dripping nitrogen on the milling container or electrically heating the milling vial. It was found that the root mean square (*rms*) strain in the material was lower and the grain size larger for materials milled at higher temperature [52]. The solid solubility was reported to decrease at higher temperatures. There is a conflict of how the temperature variation affect amorphization.

Chapter 3 MOTIVATION

A saturation in the options available (and the current market) in developing conventional alloy-based magnetic materials and, the rising demand in developing novel magnetic materials was the motivation to devise an alloy-design strategy based on high-entropy alloys, for improved magnetic properties. The HEAs, in the past, were investigated for their mechanical properties; however, the studies on magnetic properties is currently gaining attention. Looking at the future manufacturing approach, powder materials and processing is expected to dominate. Mechanical alloying, a solid state material synthesis technique provides an opportunity to synthesize novel alloys comprising metastable phases. This motivated to perform a systematic study of iron-cobalt-nickel alloy synthesis using mechanical alloying and characterize its magnetic properties from low-temperature to elevated temperatures. Such a study is likely to provide the necessary foundation for the development of high-entropy based magnetic alloys by further alloying additions.

Chapter 4 EXPERIMENTAL PROCEDURE

1. Procedure for Synthesis

1.1 Equiatomic FeCoNi $\Delta S_{mix} \approx 9.1$ J/mol.K (1.1*R*)

A blend of three powders- Fe (Alfa Aesar, <10micron, 99.9+% purity), Co (Alfa Aesar, -325 mesh, 99.5% purity) and Ni (Acros Organcis, -325 mesh, 99.9% purity) were taken in equiatomic ratio (33.33 at%) and poured in a hardened steel vial. Around 2-3% stearic acid as process control agent (PCA) and 5 hardened steel balls of 12 mm diameter were put together along with the powders and the vial was closed in argon chamber (<0.1% oxygen). The vial was then clamped in a SPEX Sample Prep 8000D Mixer/Mill and the alloying is performed for 3, 6, 9, 12, 15 and 18 hours for each sample, giving a break of 30 minutes after every 3 hours of run. Each run had 5 g of blended powder, keeping the ball to mass ratio to be 8:1.

1.2 Nominal composition considering $\Delta S_{mix} \approx 9$ J/mol.K (1.09*R*)

To check the behavior of FeCoNi composition, one of the three principal elements was kept higher than the other. The at% of Fe:Co:Ni = 40:30:30, 30:40:30 and 30:30:40 were taken in a hardened steel vial. 3-4% Stearic acid as process control agent (PCA) and 5 hardened steel balls of 12 mm diameter were put together along with the powders and the vial was closed in argon chamber (<0.1% oxygen). The vial was then clamped in a SPEX Sample Prep 8000D Mixer/Mill and the alloying is performed for 2, 3, 6, 9 and 12 hours for each sample, giving a break of 30 minutes after every 3 hours of run. Each run had 5 g of blended powder, keeping the ball to mass ratio to be 8:1.

1.3 Nominal composition with minimum $\Delta S_{mix} \approx 8.7$ J/mol.K (1.05*R*)

To figure out properties of a FeCoNi HEA with maximum possible Fe, the at% of Fe:Co:Ni was kept to be 46:34:20. The blend was poured in a hardened steel vial with 3% stearic acid and 5 hardened steel balls of 12 mm diameter. The vial was closed in argon chamber (<0.1% oxygen). The vial was then clamped in a SPEX Sample Prep 8000D Mixer/Mill and the alloying is performed for 9 hours, giving a break of 30 minutes after every 3 hours of run. Each run had 5 g of blended powder, keeping the ball to mass ratio to be 8:1.

1.4 Nominal composition considering $\Delta S_{mix} \approx$ 10.12-10.85 J/mol.K (1.22*R*-1.31*R*)

It was figured out that at% Fe:Co:Ni = 40:30:30, mechanically alloyed for 9 hours is the single-phase alloy with best magnetic properties of all. So, a 5gm sample of same composition of FeCoNi was prepared in oxygen in the similar manner. Keeping the at% of FeCoNi:Si = 95.8:4.2, 4.9 gm of FeCoNi alloy and 0.1 gm of Si is physically mixed together mixed in a hardened steel vial. 5 hardened steel balls of 12 mm diameter were used, maintaining the ball to powder ratio as 8:1. The vial was closed in open atmosphere with ~1% stearic acid, the alloy was milled for 1 hour, 3 hours in SPEX Sample Prep 8000D Mixer/Mill, and 2 alloys were prepared. In the similar manner, another alloy with nominal composition of 90:10 was also prepared. All the three alloys were tested for magnetics and structural properties.

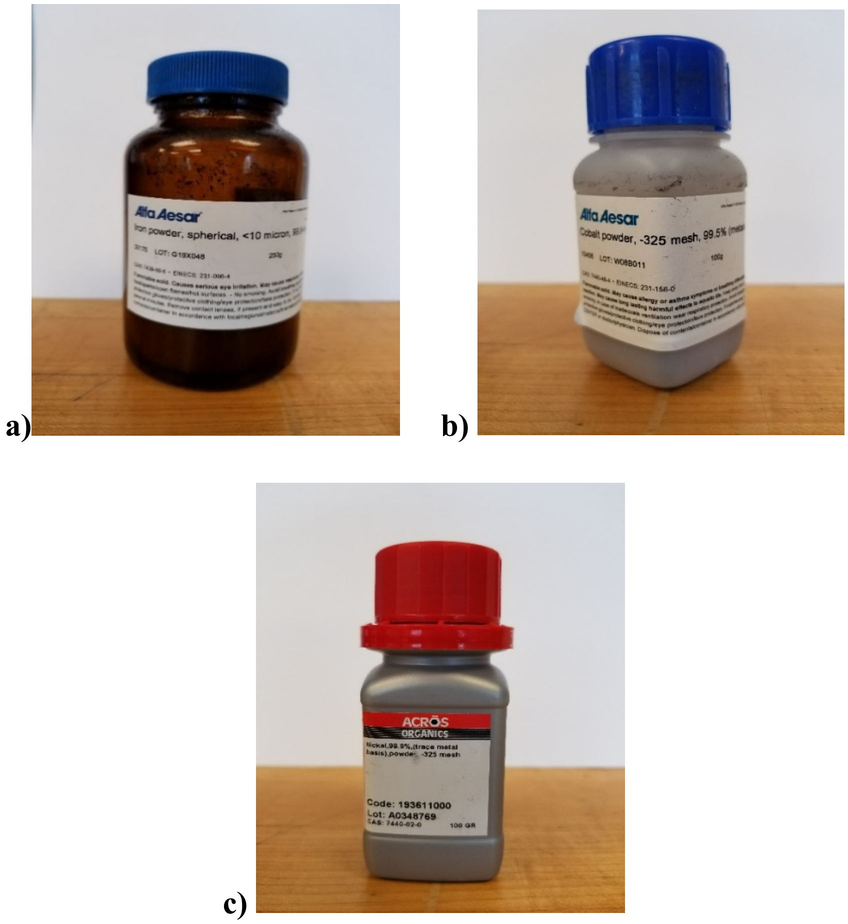

Figure 20. Elemental Powders a) Fe powder 99.9% purity b) Co powder 99.5% purity c) Ni powder99.9% purity

Figure 21. SPEX Sample Prep 8000D Mixer/Mill high energy ball mill

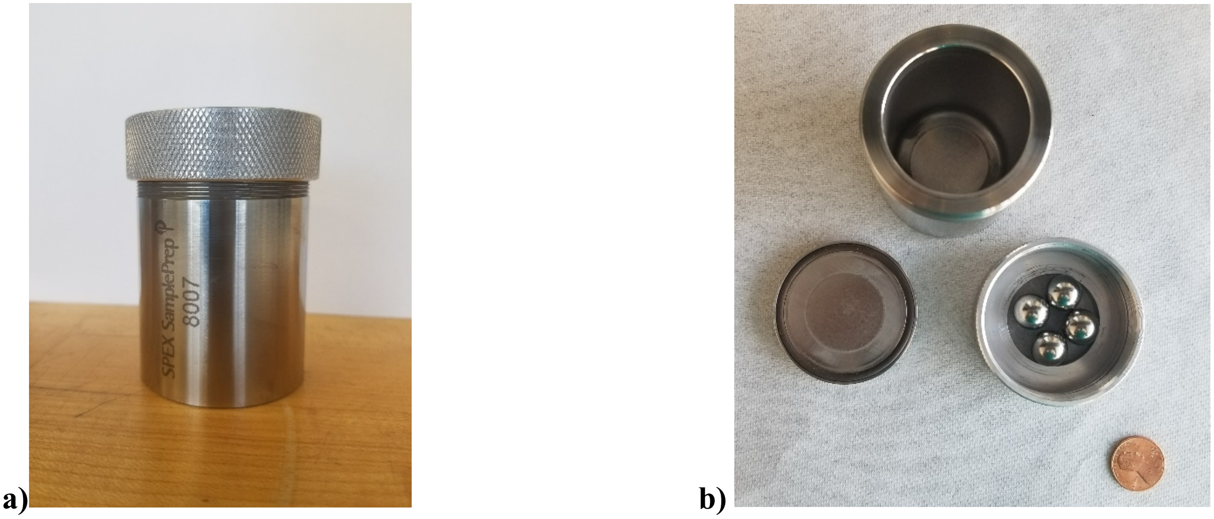

Figure 22. a) SPEX 8007 Stainless Steel vial b) Open vial with all components and stainless-steel balls placed next to a cent coin for reference

Depending on the total number of hours of alloying, the legs were created. Each leg was kept either 3 hours or 2 hours with a 30 minutes of cooling period after each run. This not only helps the vial (and the powder) to cool down but also reduces the load on the SPEX Mill. The temperature of the vial was noted down after every leg. After the run was over, the vial was allowed to cool down overnight (> 6hours). Once the sample was prepared by mechanical alloying, the vial was opened in the argon chamber (with <0.1% oxygen). The powder sticking to the walls of vial were all scrapped out and mixed well with the remaining powder in the vial. The powder was transferred equally in two glass vials, as shown in **Figure 23**. The sample in the big vial was used for the testing purpose while the small vial was kept in in argon chamber untouched as backup in case the sample in bigger vial gets oxidized. The sample in smaller vial was tested after 2 months to check the stability of the alloy. Once all the tests were over, the best sample of the composition was selected and was milled in oxygen environment.

Figure 23. Two types of glass vial used for sample storage.

2. Experimental Parameters

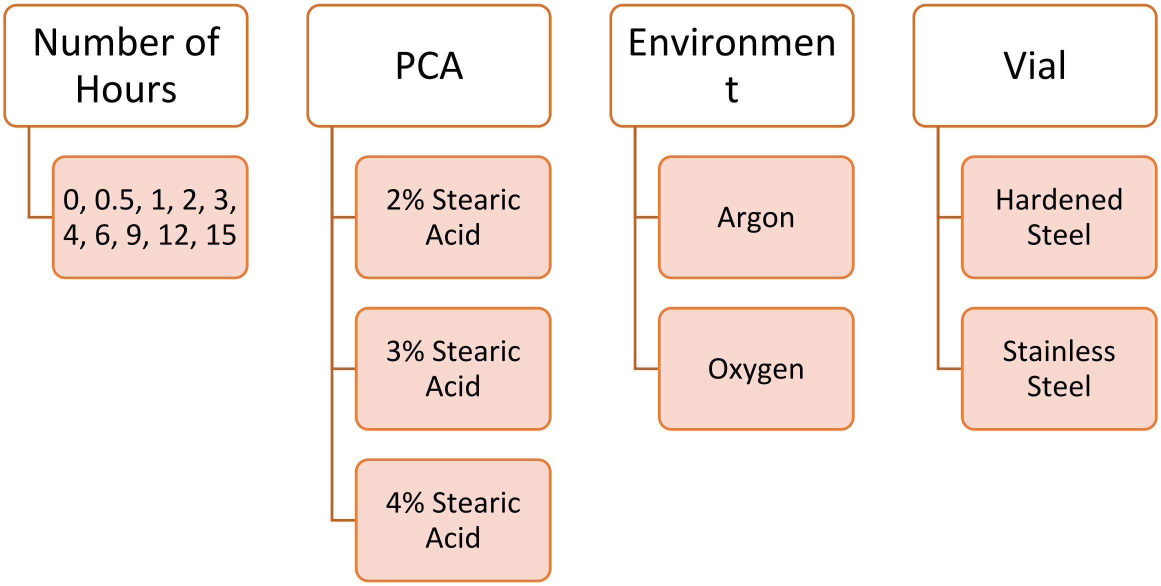

3. Testing and Characterization

3.1 Phase Analysis

Then X-ray diffraction was performed using Rigaku-Miniflex600 X-ray Diffractometer (**Figure 24**) with Ni filter and CuKα radiation in the 2θ range of 20° to 100°. The pattern was then analyzed on ORIGIN PRO software to calculate lattice parameter, crystallite size and strain using Cohen's Least Square method [53]. The lattice parameter correction was performed using the analytical method, and the final value is obtained.

Figure 24. Rigaku-Miniflex600 X-ray Diffractometer

3.2 Particle Size Distribution Analysis

The sample was then loaded into JEOL IT500 Scanning Electron Microscope (**Figure 25)** for EDAX, mapping and images of particle at ≈50µm. ImageJ software was used to analyze the image and calculate the particle size.

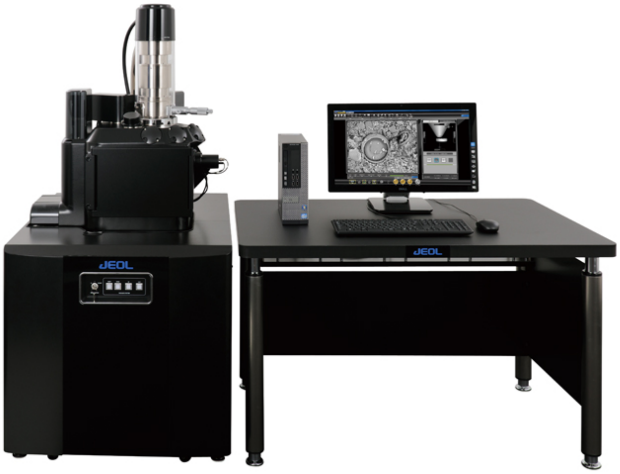

Figure 25. JEOL IT500 Scanning Electron Microscope

3.3 Magnetic Properties

The sample was tested on Quantum Design Versa Lab Vibrating Sample Magnetometer (VSM) (**Figure 26**) for the magnetic properties like saturation magnetization and coercivity. Three tests were carried out on VSM- 1) Room temperature (300K) M vs H curve. 2) Low temperature (300-60K) M vs H curves at every 60K. 3) High temperature (300-885 K) M vs H and M vs T curve at 80 kA/m (1 kOe).

Figure 26. Quantum Design's Versa Lab Vibrating Sample Magnetometer

Chapter 5 RESULTS AND DISCUSSIONS

From the literature survey, it was observed that FeCoNi(AlSi)$_X$ was a good candidate for magnetic alloy. Instead of adding all the 5 elements together, a perfect composition for FeCoNi was planned to be synthesized having best magnetic properties. Once the FeCoNi was ready, the other two elements were added in optimum ratio to obtain 5 element HEA with good magnetic properties.

5.1 Equiatomic Ratio FeCoNi $\Delta S_{mix} \approx 9.1$ J/mol.K (1.1*R*)

33.33 at. wt% of each element was taken and was milled for 0, 0.5, 1, 3, 6, 9, 12, 15 hours and were named as S0, S0.5, S1, S3, S6, S9, S12 and S15 respectively. Three parameters were varied- PCA percentage, environment of milling and vial material. These were varied to get an alloy with best magnetic properties with less milling time and cost. All the variables and element percentages are given down in **Table 3**.

Table 3. Table of Parameters for equiatomic alloys

Hours of Milling	Grinding Media	Environment	PCA Weight%
1	Stainless steel	Argon	3
0.5			3
3			2
3			3
6			2
6			3
9			3
9		Oxygen	3
9	Hardened Steel	Argon	3
12	Stainless Steel		2
12			3
18			3

5.1.1 XRD Analysis

An equiatomic blend of 5 gm of powder was taken for mechanical alloying and 2% of PCA was added to it. The run went for first 3 hours of alloying but after that the balls were getting welded. Because of welding of balls, the MA was getting hindered and we have to stop the process in between to separate the balls and resume alloying. After 3 samples getting welded, 3% PCA was added instead of 2% and the problem was resolved.

However, 3 hours of MA was not enough for all the Fe and Co to go into Ni and form a high-entropy alloy. As show **Figure 27,** XRD for 0, 0.5, 1 and 3 hours sample have Fe and Co peaks. While the 6, 9, 12, 15 hours sample has only Ni peaks, which suggest that all the Fe and Co has fused into Ni lattice and the alloy has formed an FCC structure.

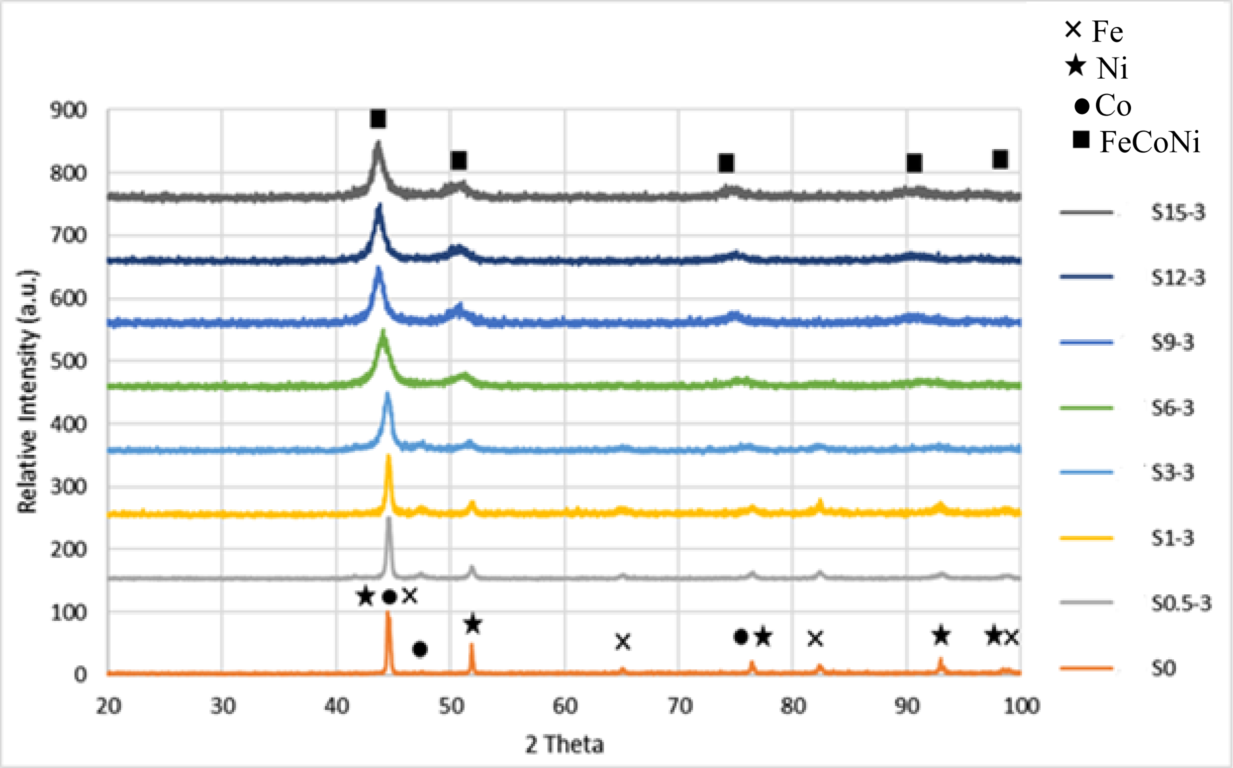

Figure 27 XRD pattern of all the samples with 3% PCA

If we compare the 3% and 2% PCA sample on XRD, it is hard to differentiate between them. As shown in **Figure 28,** XRDs for 3% and 2% PCA seems to be similar. But the upcoming

VSM comparison shows the difference between them and clarifies how much PCA to take for a sample with equiatomic Fe-Co-Ni alloy.

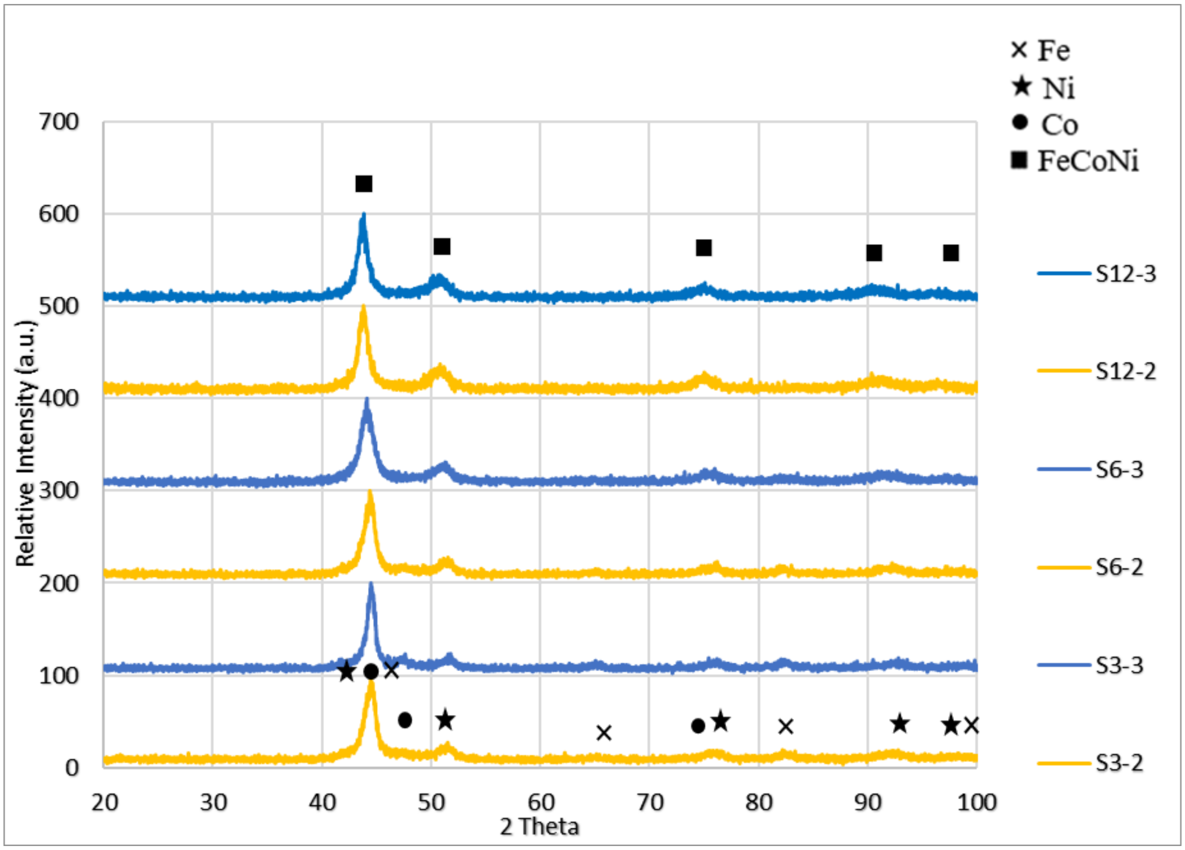

Figure 28. XRD comparison for 3-6-12-hour sample with 3% and 2% PCA

Now it is clear that to get a good sample of Fe-Co-Ni, 3% PCA needs to be added. But to find out the optimum hours for the alloy to form a single-phase FCC structure, the blend went through 0.5, 1, 3, 6, 9, 12 and 15 hours of mechanical alloying and each sample went through XRD.

The XRD results were consistent after 9 hours of alloying. As shown in **Figure 29,** the XRD pattern for 9, 12 and 15 hours of alloying are similar. To figure out the difference between the three alloys, the samples went through Scanning Electron Microscope (SEM) and Vibrating Sample Magnetometer (VSM) testing.

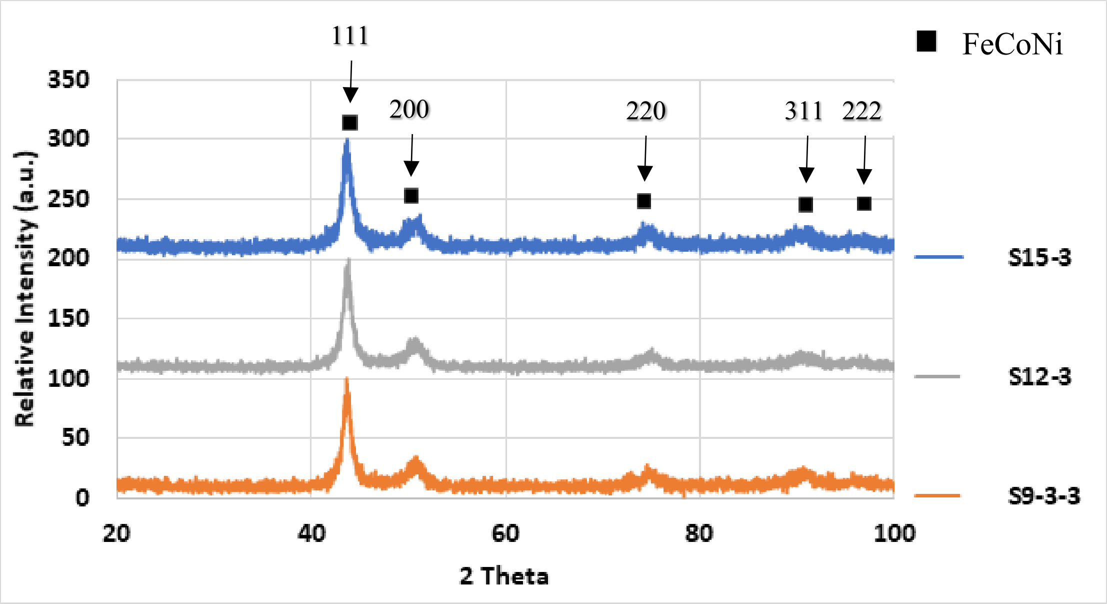

Figure 29.XRD results for 9, 12 and 15 hours sample with 3% PCA

Considering the SEM and VSM results of the three samples, 9 hours of alloying was found to be giving highest saturation magnetization with less coercivity. Thus, S9 was selected to check the variation in behavior of alloy if the material of vial is changed.

Initially all the MA was executed in stainless steel vial but now S9 was synthesized in hardened steel vial. **Figure 30** shows that it does not matter which vial you use; the result will be similar. But looking at the physical condition of the two vials, it was clear that hardened steel vials would last longer as compared to stainless steel vials. The bottom surface of stainless steel vial was having dents while the hardened steel vial surface was all smooth. Considering the cost, hardened steel vials are cost effective and last longer as compared to stainless steel vials.

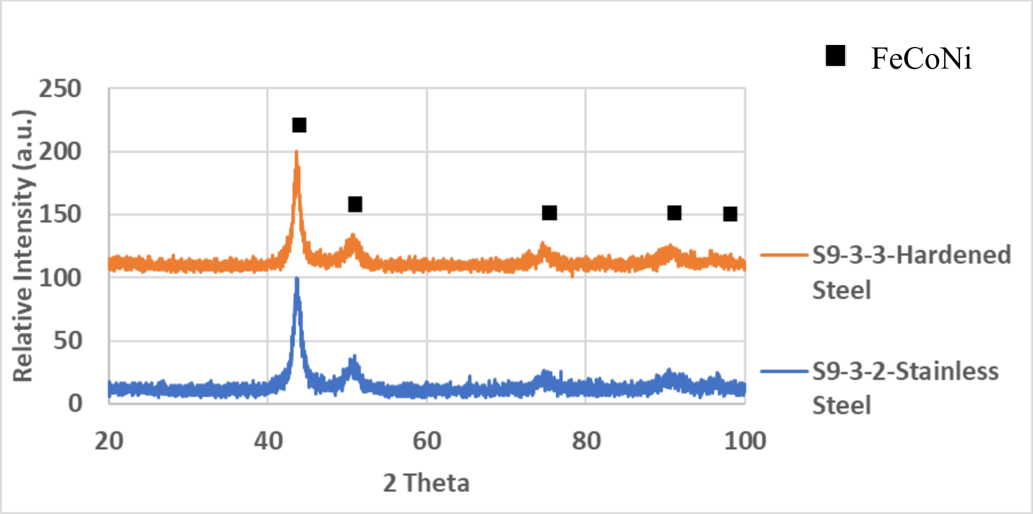

Figure 30. XRD comparison for hardened steel vial and stainless-steel vial

With 3% PCA, and 9 hours of milling in hardened steel vial, we have a single-phase FCC alloy. But closing and opening the vial in argon chamber takes a lot of time and thus a sample was made which was alloyed in oxygen environment. Again, the XRD results of the samples as shown in **Figure 31** are similar but the VSM results and the physical condition of balls were good for comparison. A slight decrease in saturation magnetization and increase in coercivity was observed. However, this small change is negligible if the blend can be milled in oxygen. The balls were also damaged in case of oxygen sample, but again can be avoided to prevent the cost of maintaining argon atmosphere all through milling process.

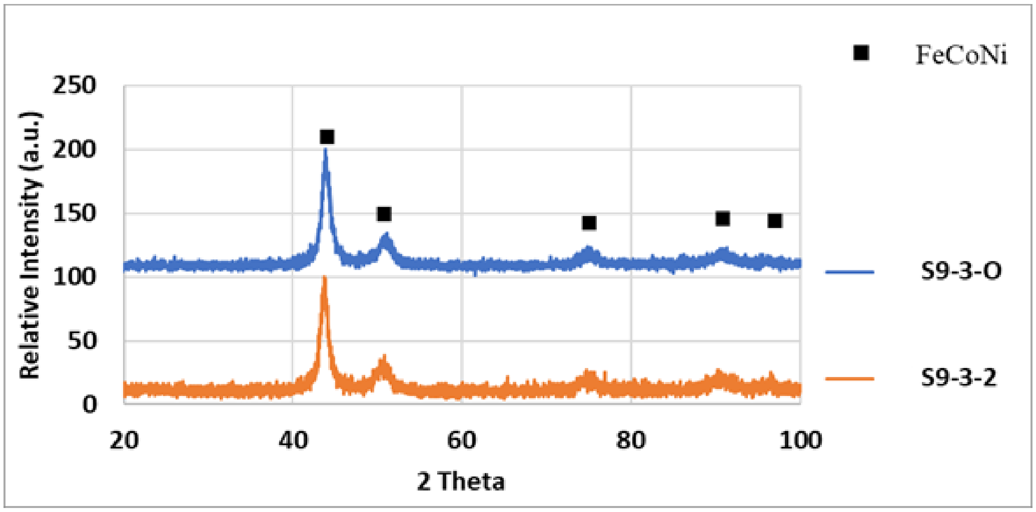

Figure 31. XRD comparison for oxygen sample and argon sample environment

5.1.2 VSM Analysis

The magnetic characterization of the samples was performed on Quantum Design's Vibrating Sample Magnetometer. The magnetic field was applied from -2150 kA/m (-27 kOe) to 2150 kA/m (27 kOe) and the corresponding moment was obtained to find out the saturation magnetization (*Ms*) and coercivity (*Hc*) of the material. **Table 4** is the collection of all the *Ms* and *Hc* of samples with 3% PCA. S6 is having the highest *Ms* but the *Hc* is also high. We need to select a sample with high *Ms* and less *Hc*. S12 is having high *Ms* and less *Hc* but the value of S9 is also similar to that of S12. The difference in the *Ms* and *Hc* of S9 and S12 are not worth of extra 3 hours of milling and thus S9 is selected to be the best sample.

Table 4. Saturation Magnetization and Coercivity of the equiatomic alloy samples

Sample	M_S(Am^2/kg)	*Hc(*kA/m)
S0	145.16 ± 1.13	5.49 ± 0.09
S0.5-3	137.36 ± 0.96	7.32 ± 0.19
S1-3	133.61 ± 0.54	9.35 ± 0.13
S3-3	133.21 ± 1.05	10.87 ± 0.17
S6-3	139.56 ± 0.35	4.54 ± 0.04
S9-3	135.57 ± 2.89	2.37 ± 0.01
S12-3	137.58 ± 0.90	1.87 ± 0
S15-3	129.82 ± 1.48	1.90 ± 0.04

Hysteresis loops were plotted for all the samples from -2150 kA/m (-27 kOe) to 2150 kA/m (27 kOe) , as shown in **Figure 32 and 33.** The value of saturation magnetization and coercivity are taken from these loops and plotted in **Figure 34.** It shows the trend of *Hc* initially increasing because of the grain size going nano. The stress in the particles increases because of the cold welding and plastic deformation during MA which also results in increase in *Hc.* After this, the diffusion of particles or the alloy formation starts which results in increase in grain size and thus decreasing *Hc.* After ≈9 hours of alloying, the particle size becomes constant. In the similar manner *Ms* firstly decreases because of decrease in grain size and then increases with alloy formation.

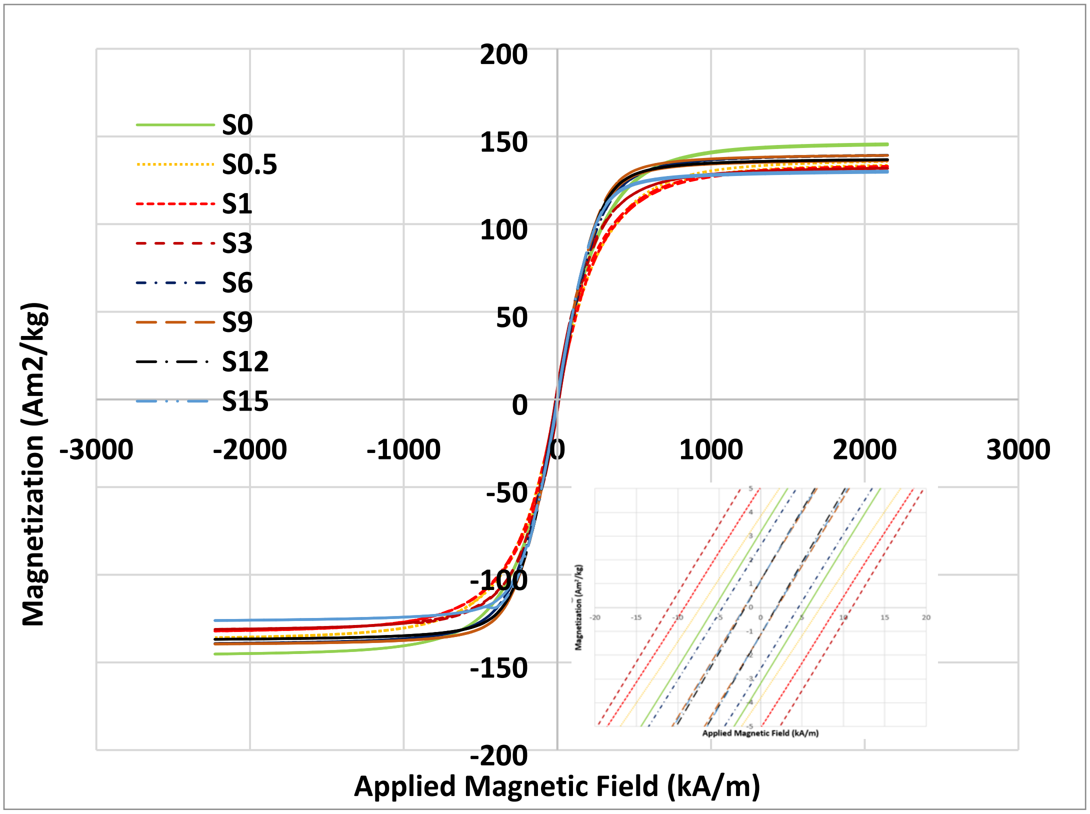

Figure 32. *M-H* curve for all the 3% PCA samples

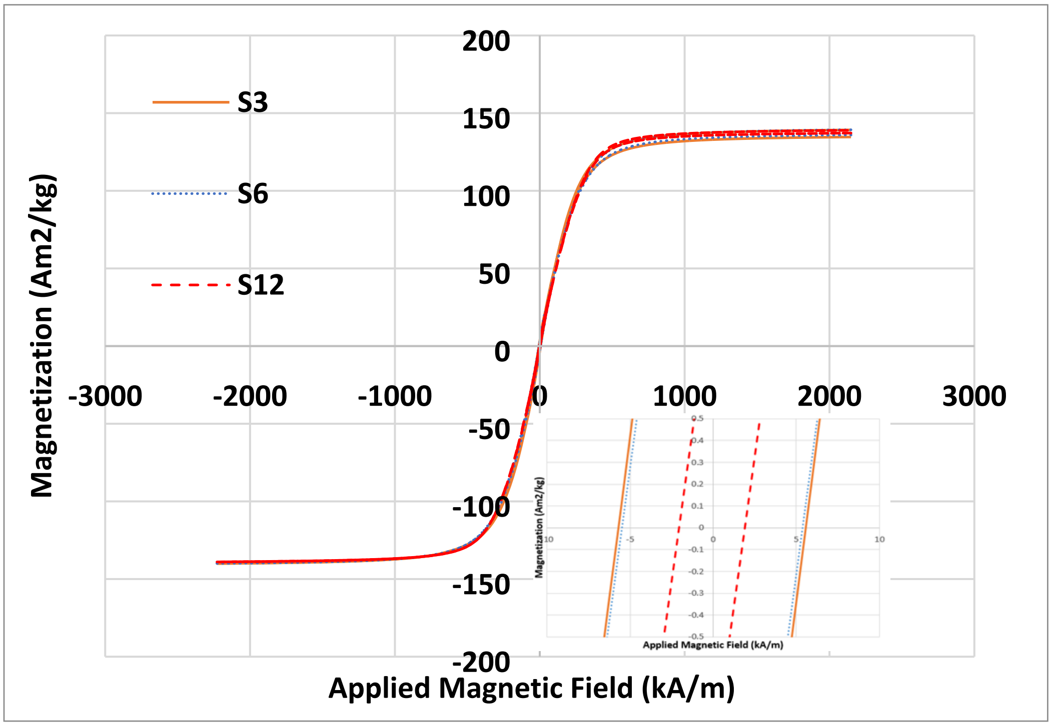

Figure 33. *M-H* curves for all the 2% PCA samples

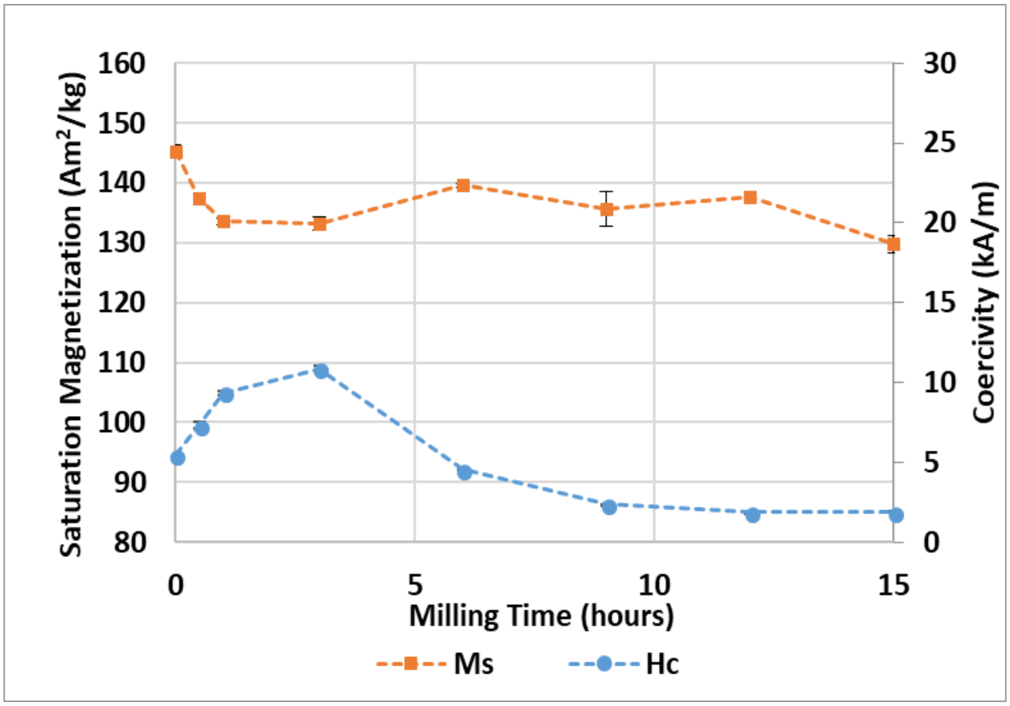

Figure 34. Saturation Magnetization and Coercivity variation with number of hours of milling

The PCA percentage was kept low to prevent contamination. This can be seen from the **Figure 35,** the *Ms* and *Hc* for 3% and 2% PCA are quite similar for 6 hours and 12 hours of MA. However, with 3 hours of alloying there is a noticeable difference between 3% and 2% PCA samples. The *Ms* for 3% PCA is low for 3 hours of MA because of contamination. However, if the run is continued for 6 hours, the PCA gets consumed and we do not have such issue for 6 and 12 hours samples. Thus, for equiatomic alloy sample of FeCoNi, 3% PCA is required for more than 3 hours of MA and it will not cause any contamination issue.

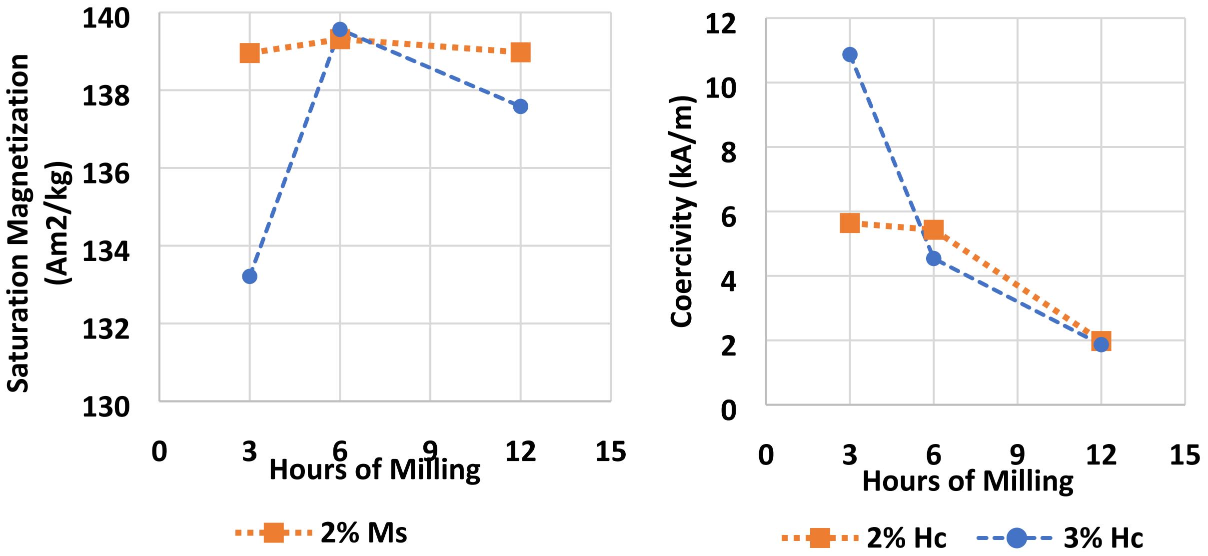

Figure 35 Saturation Magnetization and Coercivity of 3-6-12 hours of milling

After concluding that 3% PCA do not contaminate the alloy and prevents welding, best alloy out of S9, S12 and S15 was to be selected. From **Table 5 and Figure 36,** S15 was competitive in terms of *Hc*, but the *Ms* of S15 was low. S12 had high *Ms* and lowest *Hc* out of three but S9 was having comparable *Ms* and was taking 3 hours lesser to get synthesized as compared to S12. Thus, S9 is selected to be the best equiatomic alloy of FeCoNi.

Table 5. Saturation Magnetization (*Ms*) and Coercivity *(Hc)* of best samples of equiatomic FeCoNi alloy

Sample	*Ms*(Am^2/kg)	*Hc*(kA/m)
S9	135.57 ± 2.89	2.37 ± 0.01
S12	137.58 ± 0.90	2.14 ± 0.00
S15	129.82 ± 1.48	2.59 ± 0.04

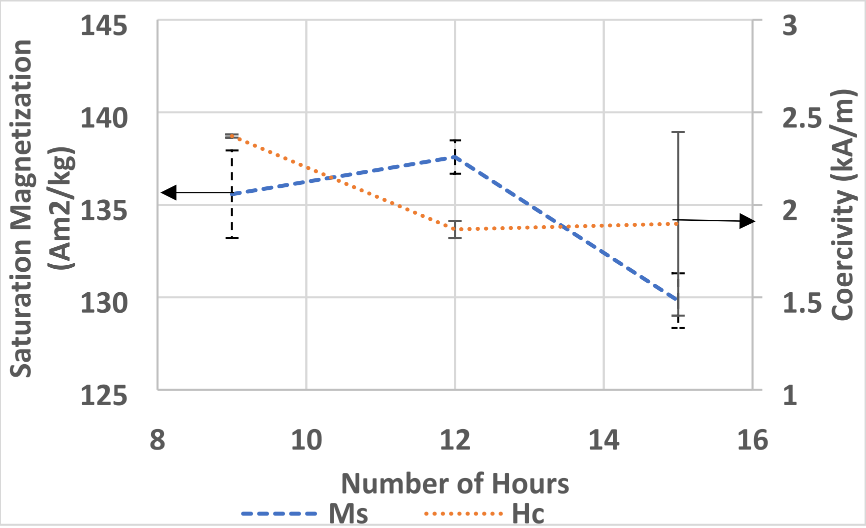

Figure 36. Saturation Magnetization (*Ms*) and Coercivity (*Hc*) of S9, S12 and S15

Now that S9 was found to be the best alloy of all, it was synthesized in a hardened steel vial (S9-3-3) because hardened steel vials last longer as compared to stainless steel vial. Also, to save time, S9 was prepared in oxygen environment. As shown in **Figure 37,** the variation of *Ms* and *Hc* is not much in both the cases. Considering hardened steel vial, the *Ms* is increasing by 1.72% and *Hc* is decreasing by 9.83%. In case of oxygen environment, the *Ms* is decreasing by 2.44% and *Hc* is increasing by 9.15%. As the changes are less than 10% and to save time and money, these changes are bearable. In fact, S9 in hardened steel vial shows better properties than S9 in stainless steel vial. Thus, further testing was performed on hardened steel S9 sample.

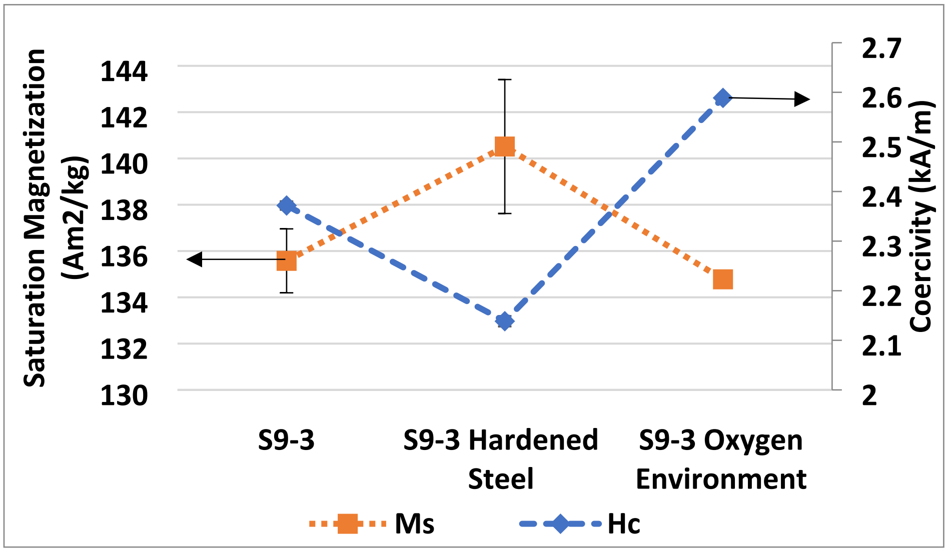

Figure 37. Saturation Magnetization (*Ms*) and Coercivity (*Hc*) of S9 samples in hardened steel vial and oxygen environment

To find the behavior of S9 synthesized in hardened steel vial at high temperature, it went through VSM runs with the temperature rise from 300 K to 852 K at 80 kA/m (1 kOe) magnetic field. As shown in **Figure 38**, the alloy was found to be stable till ≈650K, magnetization going down with increase in temperature. But after that, Fe came out of the Ni lattice and Fe being a ferromagnetic material, magnetization started going up. When the temperature reached ≈785K, the magnetization again started going down till 852K. While going back from 852 K to 300K, the magnetization increased consistently.

Now that the Fe came out of the alloy, the heat-treated went through the same run again. As expected, this time it gave a consistent decrease in magnetization with increase in temperature and vice versa, as shown in **Figure 38.**

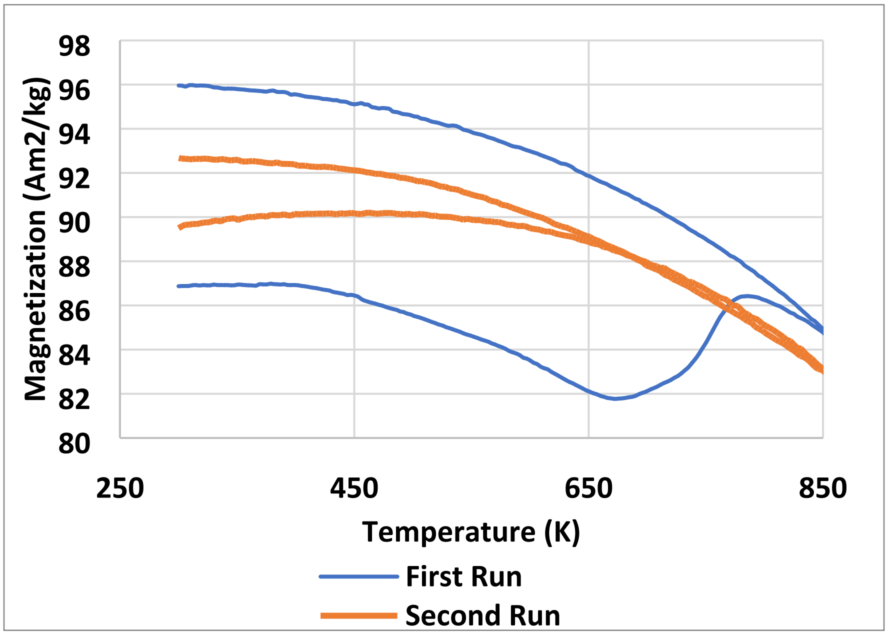

Figure 38. Magnetization vs temperature curve of S9 from 300K-852K

The magnetization was measured continuously with increasing temperature at some applied magnetic field. So, to study the change in *M-T* curve with applied field, the curve was generated at three different fields, 8 kA/m (100 Oe), 80 kA/m (1 kOe) and 800 kA/m (10 kOe). As shown in **Figure 39**, the three graphs follow similar pattern.

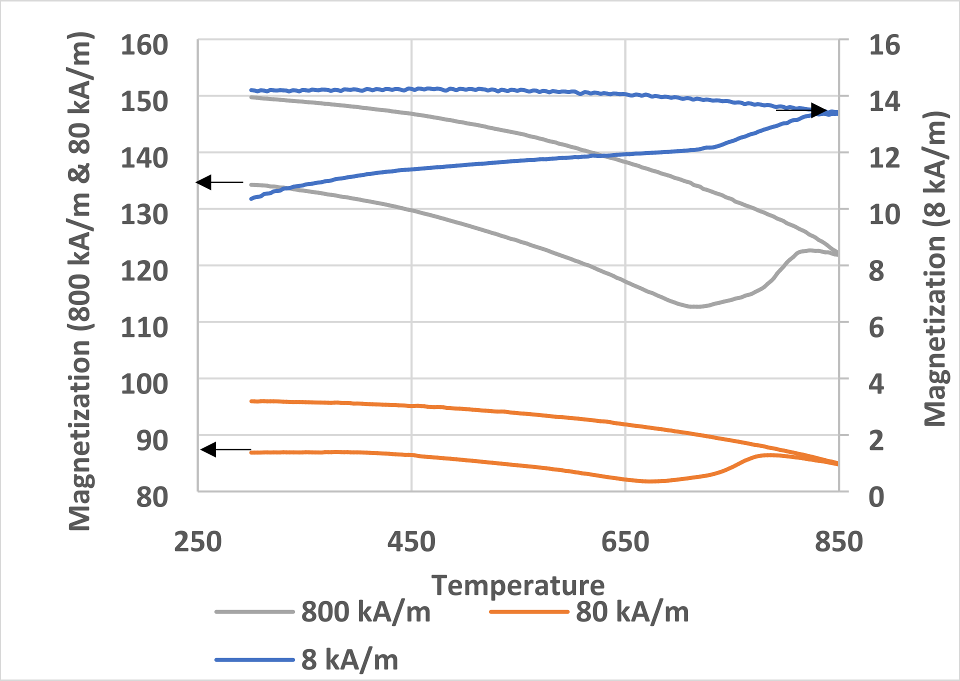

Figure 39. Magnetization vs Temperature curve at different applied field (0.08 kA/m≈1 Oe)

5.1.3 SEM Analysis

All the samples were tested on JEOL IT500 Scanning Electron Microscope for EDAX, mapping and images of particle at ≈50µm. ImageJ software was used to analyze the image and calculate the particle size. **Figure 40** shows the images of all the samples alloyed for 0 to 15 hours with 3% PCA, at 100 µm and 200 µm of resolution.

S0

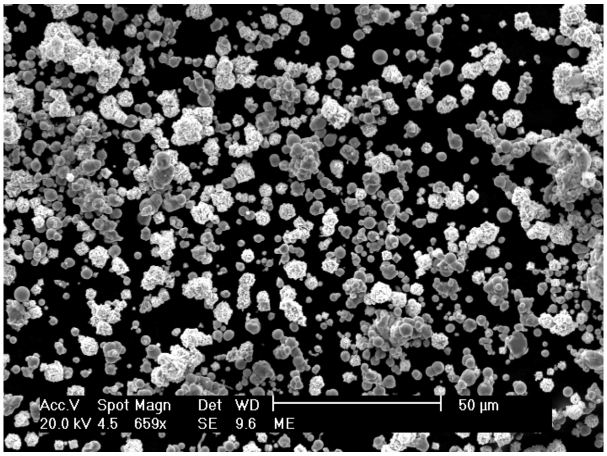

S0.5

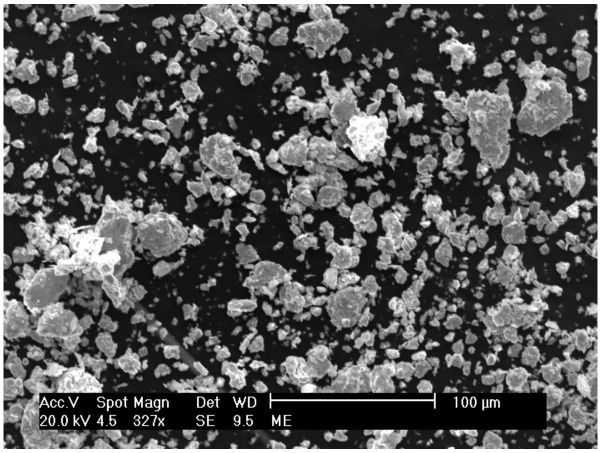

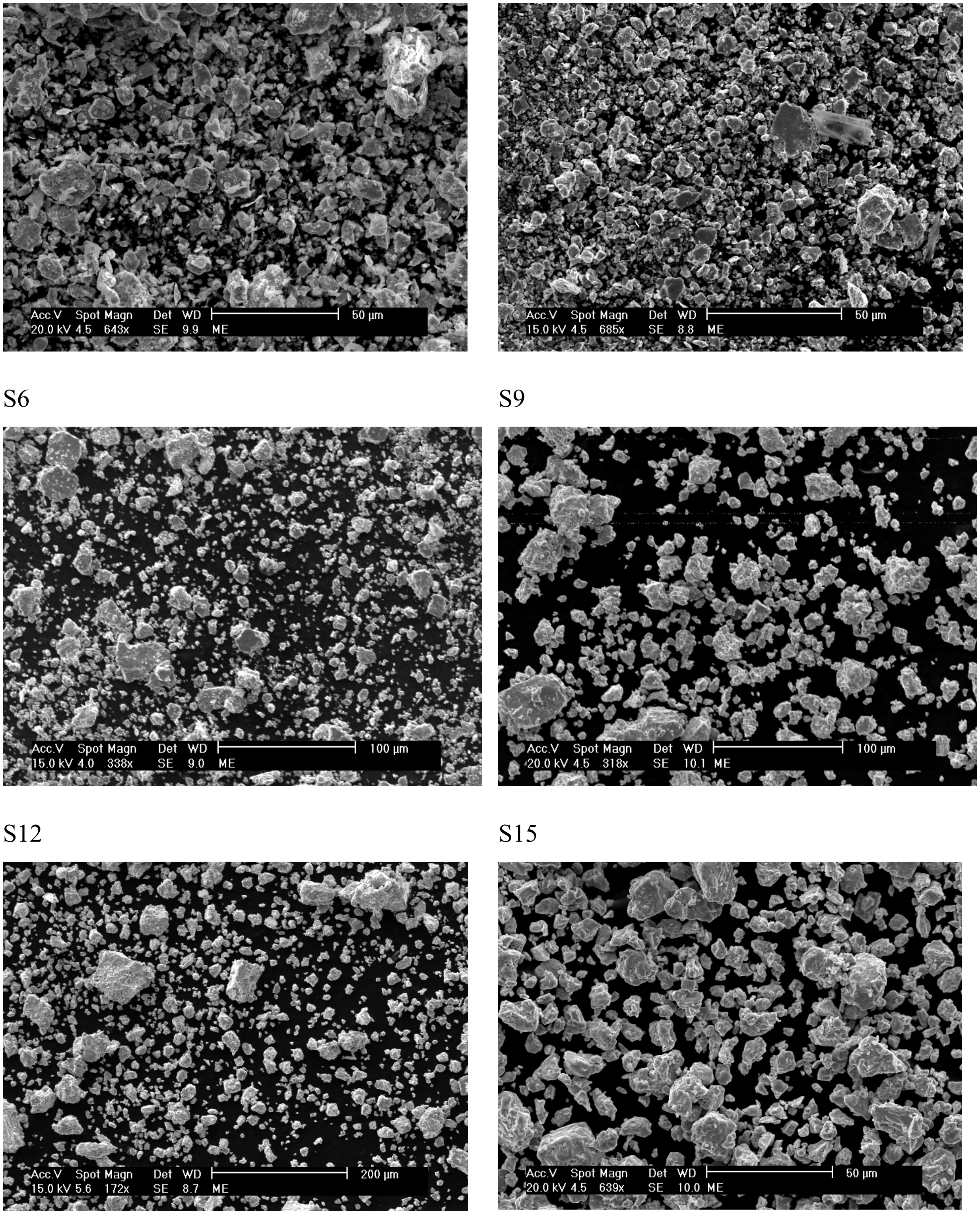
S1 S3 S6 S9 S12 S15

Figure 40. SEM images of samples mechanically alloyed for 0 to 15 hours.

From **Figure 41** and **Figure 42**, the diameter of S0 is least, then it increases with half an hour of alloying but decreases after another half an hour of run. Diameter of S1, S3 and S6 are similar, which then increases at S9 and S12 because of particles getting fused into each other. The alloy has formed by 12 hours of mechanical alloying and now it starts to mill and at S15 the particle size reduces.

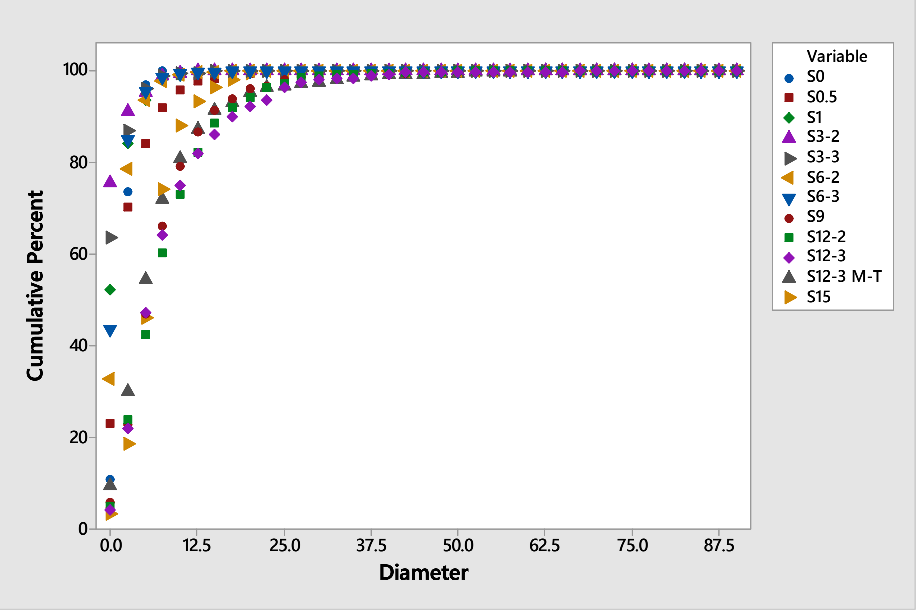

Figure 41. Histogram of Cumulative Diameter of all the samples

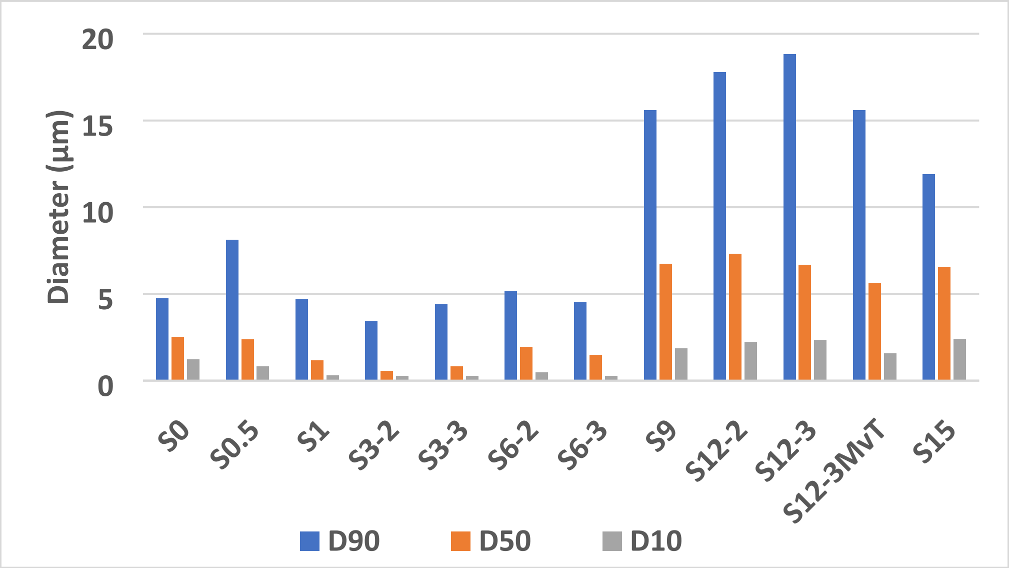

Figure 42. ***D90*, *D50* and *D10* particle diameter of all the mechanically alloyed samples**

With increase in duration of alloying, the atomic percentage of Ni tends to go down and relatively Co percentage increases. The atomic percentage of Fe is quite consistent for all the mechanically alloyed powders, as shown in **Figure 43**. The variation of the atomic percentage of powder from EDAX result versus the percentage taken during synthesis is less than 20%.

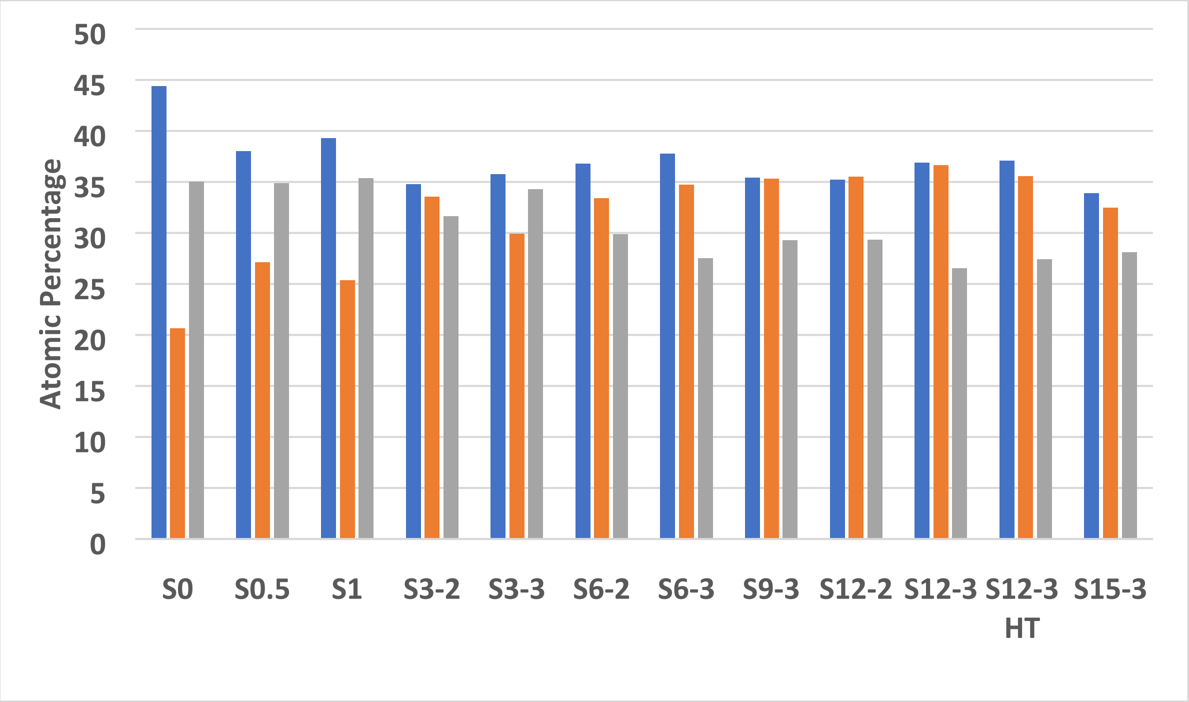

Figure 43. Histogram of atomic percentage of Fe, Co and Ni in all the mechanically alloyed samples

Lattice parameter, strain and crystallite size of the particles obtained after 0.5, 1, 3, 6, 9, 12 and 15 hours of alloying were calculated from the XRD pattern using Cohen's method also known as least squares method. Pseudo Voigt 2 and Lorentz curve fitting functions were used to determine the location of peaks on Origin Pro software.

Lattice parameter correction was performed by analytical approach using the following equations shown below which is explain in the following book [54]

$$\sum \alpha \, Sin^2\theta = A \sum \alpha^2 + C \sum \alpha\delta \qquad (6)$$

$$\sum \delta \, Sin^2\theta = A \sum \alpha\delta + C \sum \delta^2 \qquad (7)$$

With, $\alpha = h^2+k^2+l^2$, $\delta = 10\sin^2 2\theta$, $=\frac{\lambda^2}{4a_0^2}$, $=\frac{D}{10}$

Where λ was the average wavelength of both $K\alpha_1$ and $K\alpha_2$ radiations and 2θ is the corresponding value at each peak, a_0 (nm) is the corrected lattice parameter.

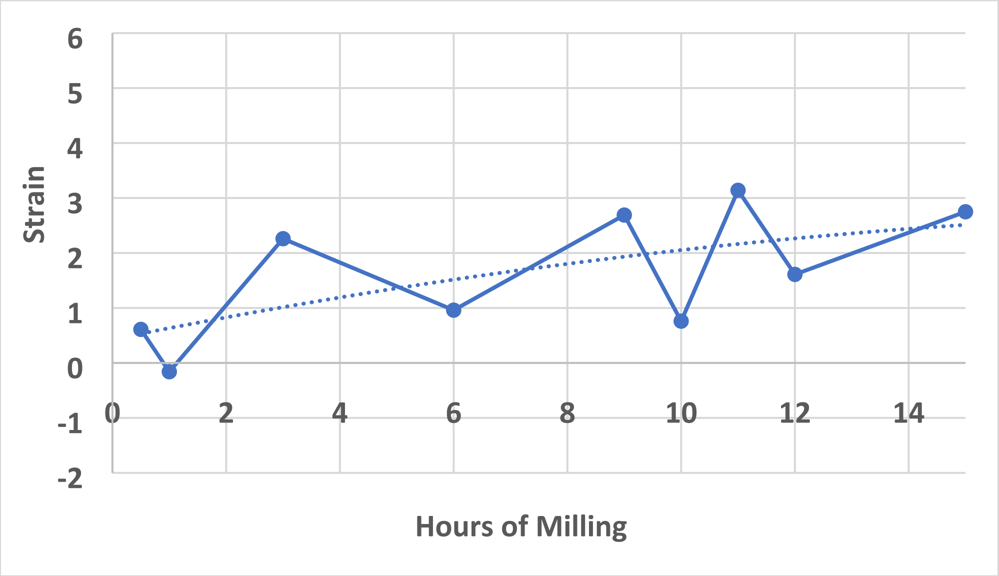

Figure 44. Strain in samples after mechanical alloying (the dotted line shows the general trend)

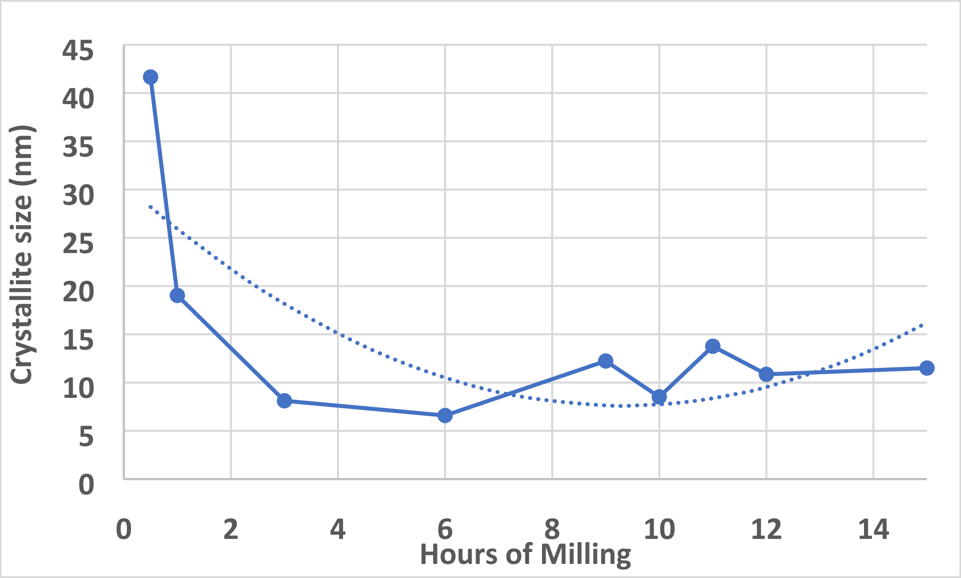

Figure 45. Crystallite size after mechanical alloying (the dotted line shows the general trend)

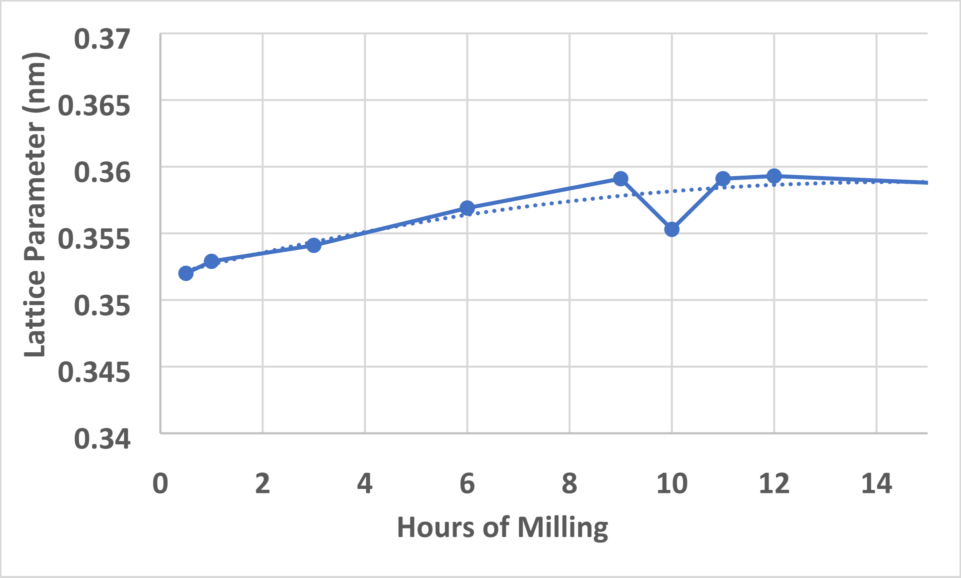

Figure 46. Lattice parameter after mechanical alloying (the dotted line shows the general trend)

5.1.4 Heat Treatment

To check the stability of the equiatomic alloy of FeCoNi S9, the magnetic properties were measured at room temperature after *MvH* curve at respective temperature (~1 hour) in vacuum (<0.01 mTorr). It was heat treated at a range of temperature from 400 K- 882 K. The alloy was found stable till 720 K after which some peaks of Fe were visible at 750 K. The XRD pattern of all the heat-treated samples is shown in **Figure 47**. After the temperature rise to ≈750 K the Fe atom comes out of Ni lattice. It is proved by the magnetics data which shows that after ≈750 K the magnetization increases. Since Fe is ferromagnetic in nature, the magnetization of alloy increases.

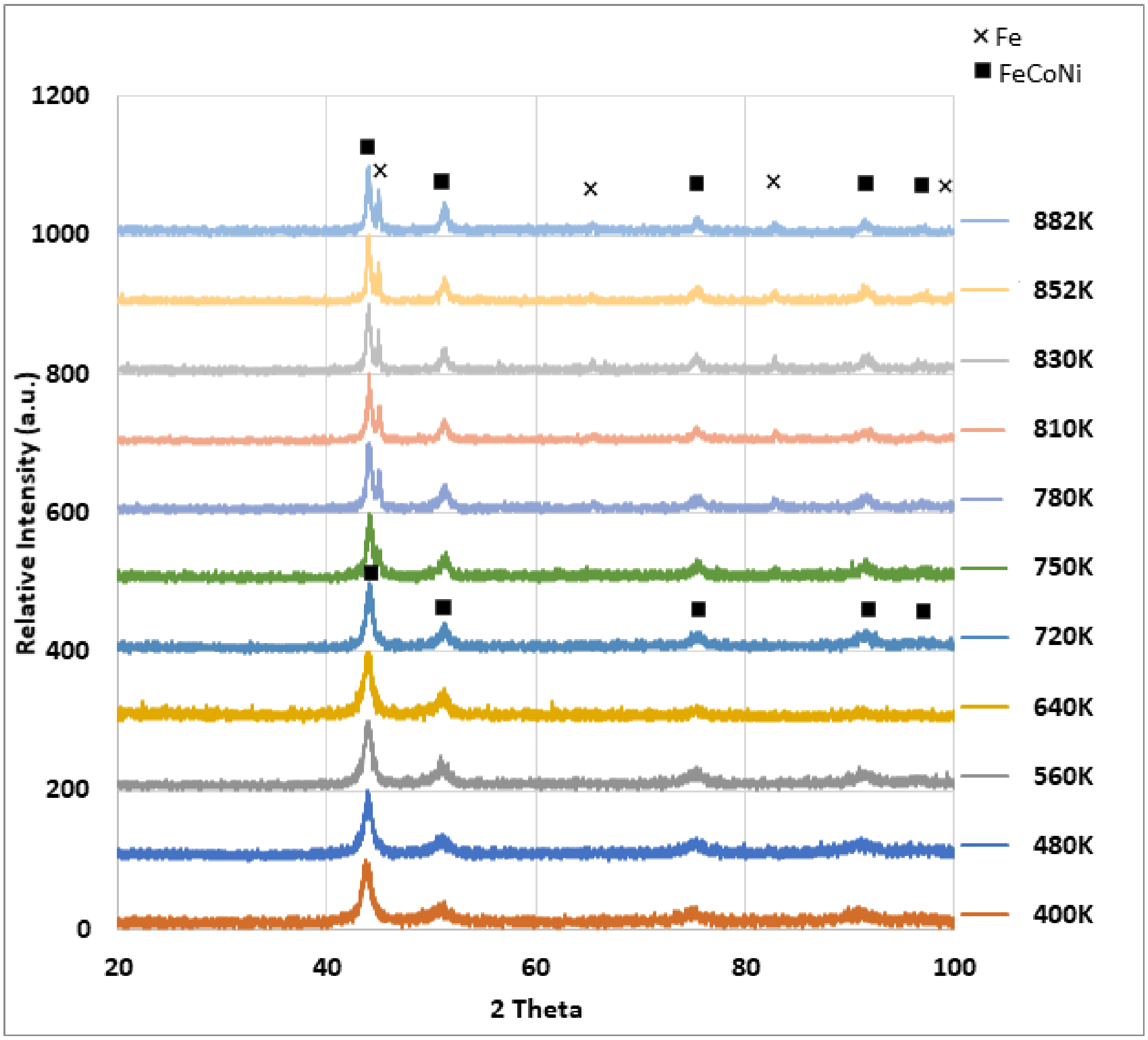

Figure 47. XRD of S9 samples heat treated from 400 K to 882K

Figure 48 shows the *M-H* curves of S9 synthesized in hardened steel vial measured at 400 K to 882 K. **Figure 49** shows the *M-H* curves, measured at 300 K, of S9 synthesized in hardened steel vial after heat treatment.

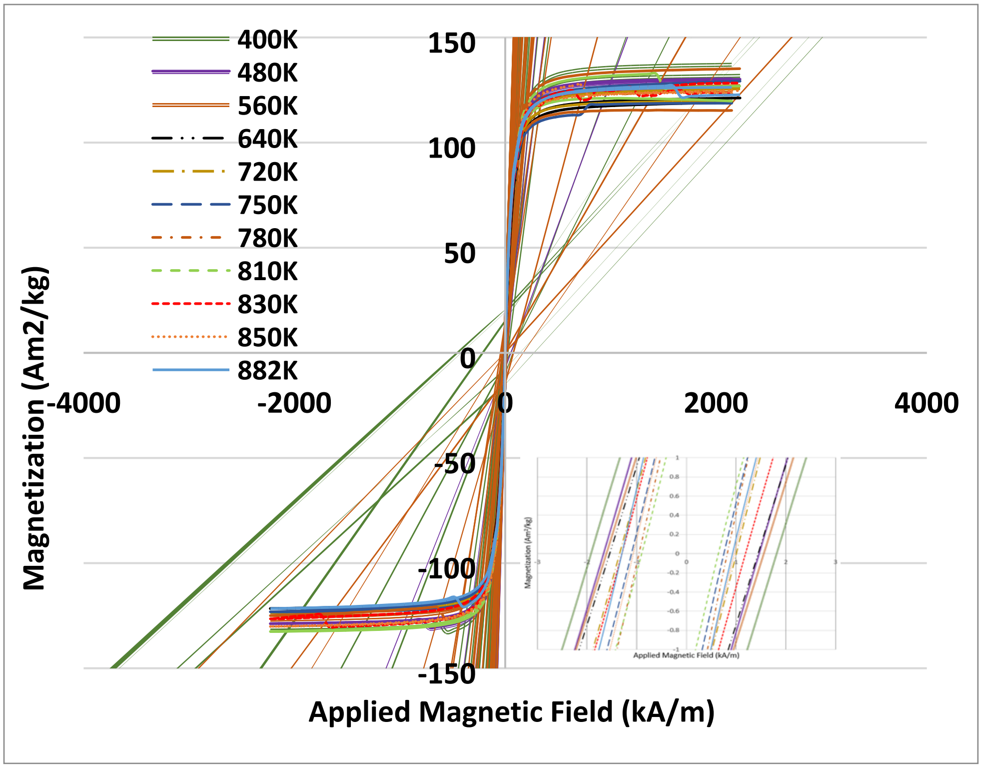

Figure 48. *M-H* curves of S9-Hardened steel measured at high temperature from 400 K to 882 K

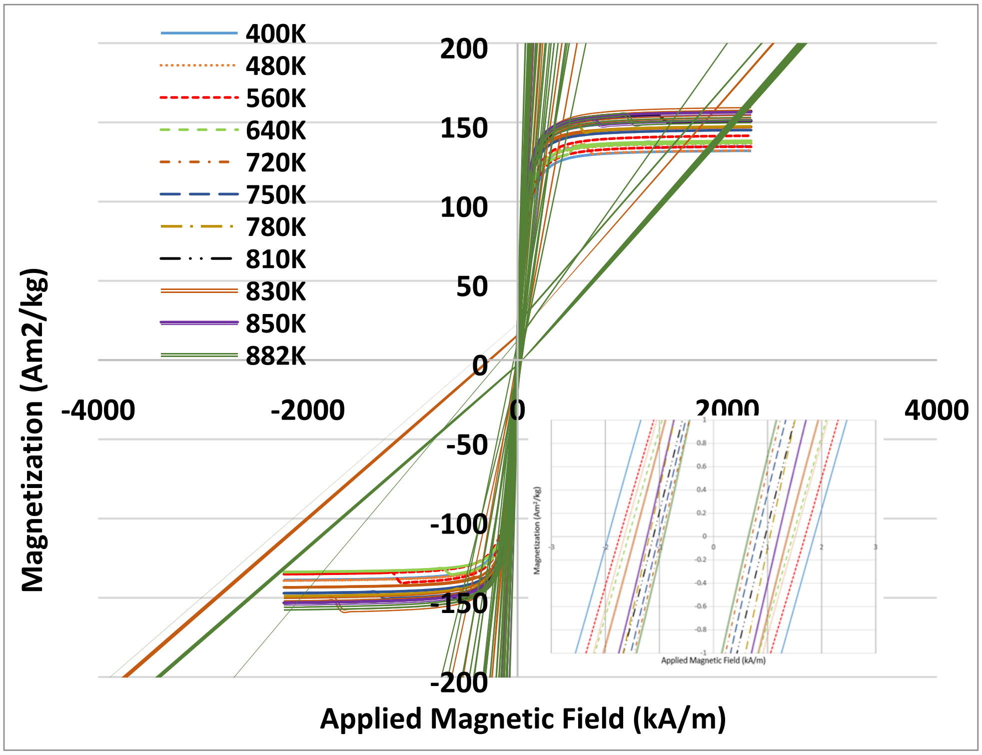

Figure 49. *M-H* curves of S9-Hardened steel measured at room temperature after heat treatment at a range of temperature from 400 K-882 K

Later, the alloy was heat treated for 11 different temperatures between 300 K to 900 K, to figure out the variation in *Ms* and *Hc* of alloy with temperature. *Ms* in **Figure 50** follows the similar pattern as magnetization in **Figure 34.** *Hc* follows reverse pattern as that of *Ms*. The highest *Ms* was154.58 Am^2/kg at 830 K with *Hc* of 1.5 kA/m (18.85 Oe). However, the best combination of *Ms* and *Hc* was obtained at 882K, which was 154.11 Am^2/kg and 0.93 kA/m (11.75 Oe) respectively. But the increase in value of *Ms* after 650 K is because of Fe coming out of Ni lattice. Thus, the best value of *Ms* and *Hc* of heat treated single phase equiatomic FeCoNi alloy is 136.74 Am^2/kg and 1.68 kA/m (21.11 Oe) at 560K.

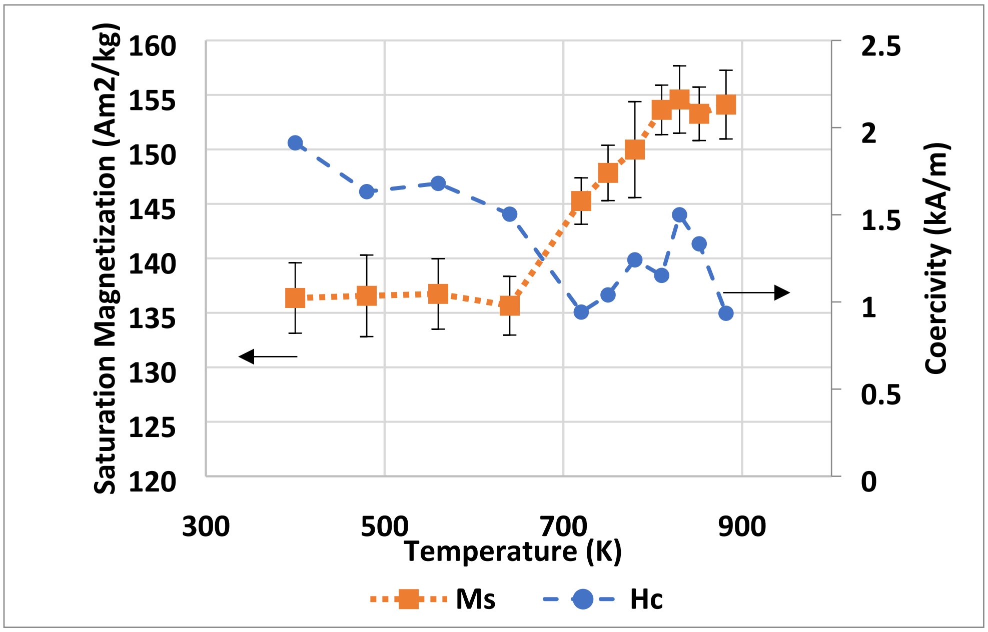

Figure 50. Change in Saturation Magnetization and Coercivity of S9 after Heat Treatment

As shown in **Figure 51,** the 12 hours sample of equiatomic FeCoNi alloy was treated for the magnetization vs temperature curve which plotted for 6 different temperatures between 300 K to 1000 K. The results suggested that, as in case of S9 samples, for S12 samples also Fe was coming out after ≈650 K.

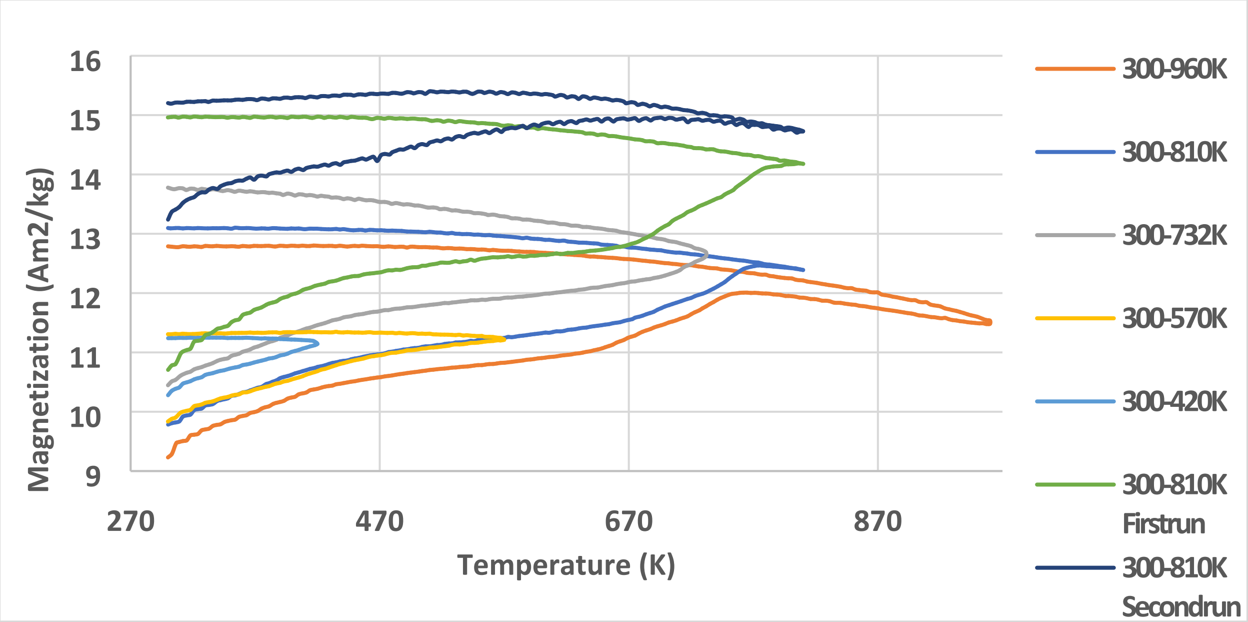

Figure 51. Magnetization vs temperature curve for 6 different temperatures between 300 K to 1000 K

The samples were also cold treated from 300 K to 60 K and *Ms* and *Hc* were calculated after every 60K. As shown in **Figure 52 and 53,** the results are as expected i.e. *Ms* almost remains constant with decrease in temperature and *Hc* increases as the temperature approaches 60 K. **Figure 52** shows that S12, S9 (prepared in oxygen/argon or hardened steel vial/stainless steel vial) all shows similar results at low temperature.

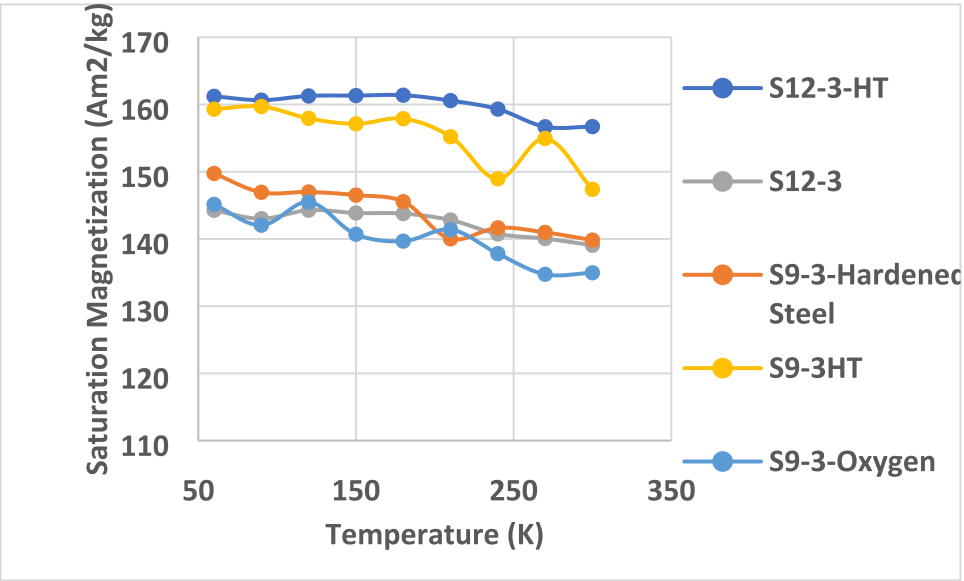

Figure 52. Saturation Magnetization vs Temperature curve for S9 and S12

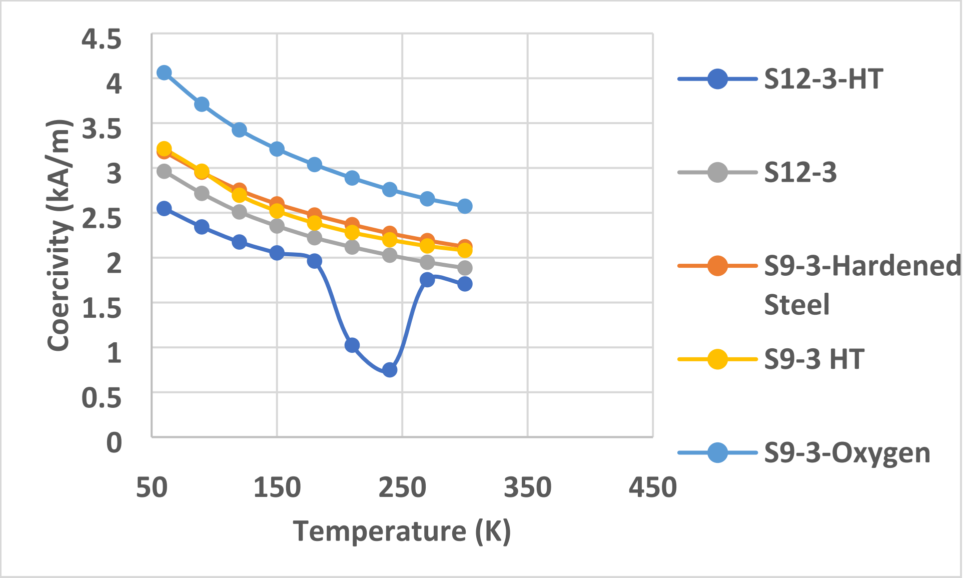

Figure 53. Coercivity vs Temperature for S9 and S12

Figure 54 and 55 shows the change in *Ms* and *Hc* for a wide range of temperature from 60 K to 882 K for S9 prepared in hardened steel vial.

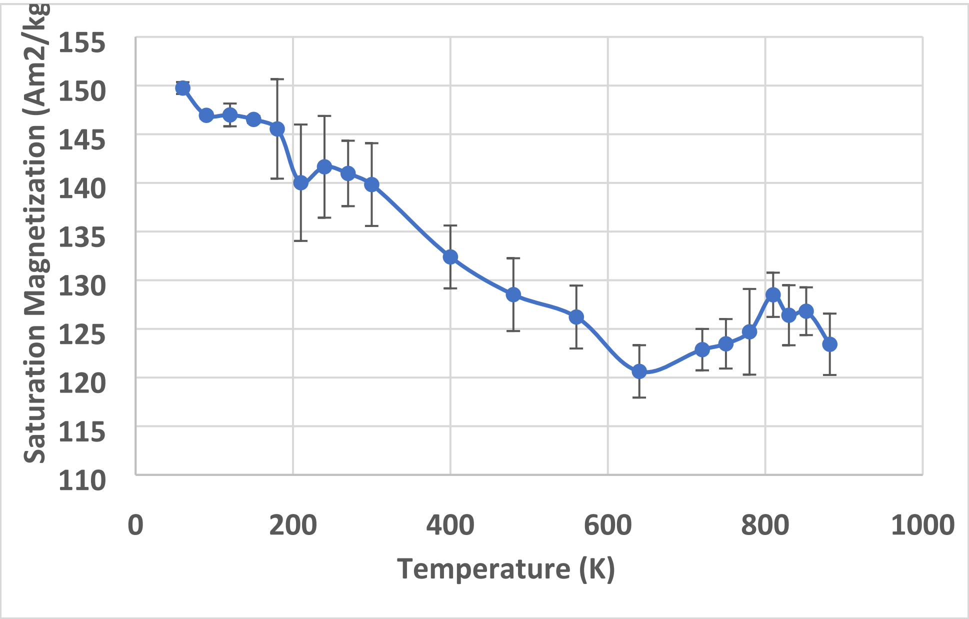

Figure 54. Saturation Magnetization vs Temperature curve for S9-Hardened Steel sample from 60-882K

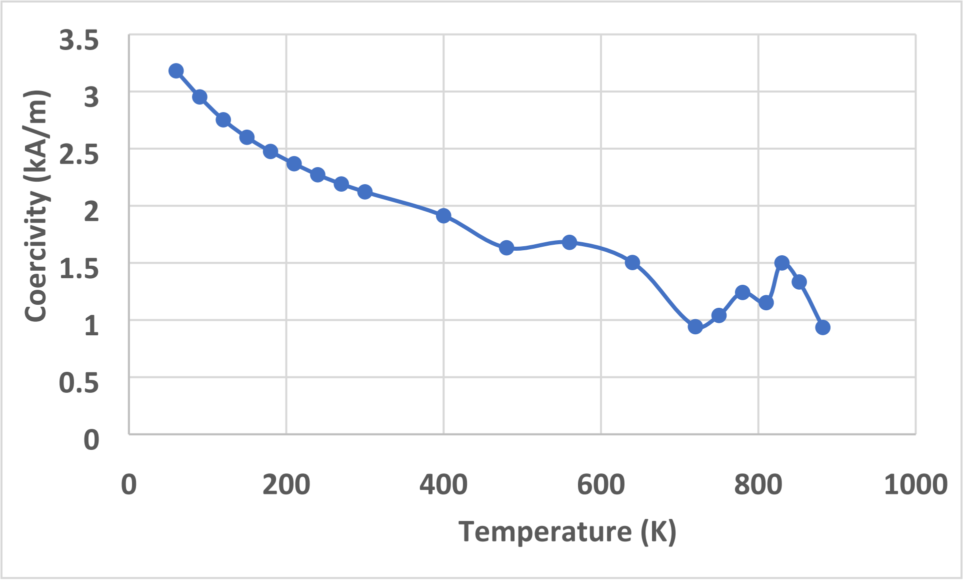

Figure 55. Coercivity vs Temperature curve for S9-Hardened Steel sample from 60-882 K

With heat treatment of the powder, the particle size tends to decrease. The particle size increases when the powder is heated to 560 K, and then with further increase in temperature up to 852 K, the particle size decreases, as shown in **Figure 56** and **Figure 57.**

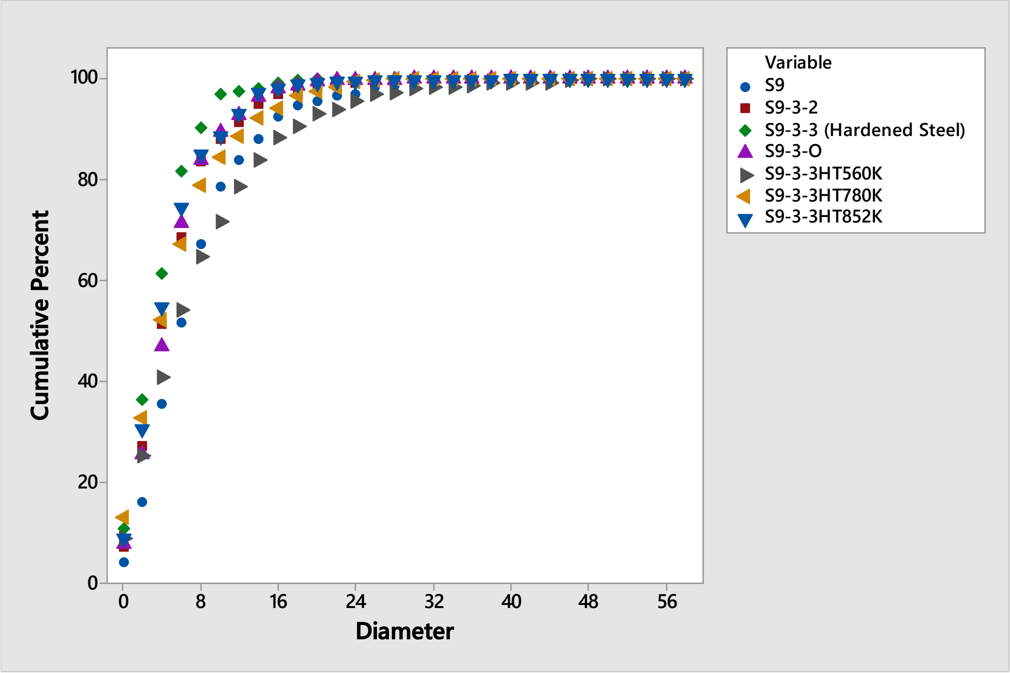

Figure 56. Histogram of cumulative diameter of heat treated S9

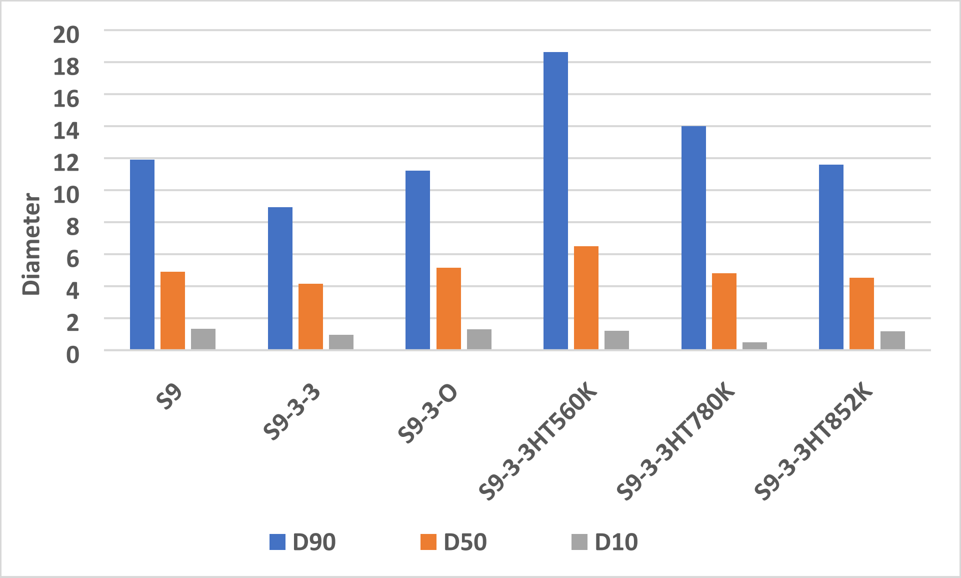

Figure 57. *D90*, *D50* and *D10* particle diameter of S9 sample and its heat-treated samples

Once the sample S9 is heat treated, the strain releases because of which the lattice parameter goes down, as shown in **Figure 58 and 60.** The change in crystallite size is shown in **Figure 59.**

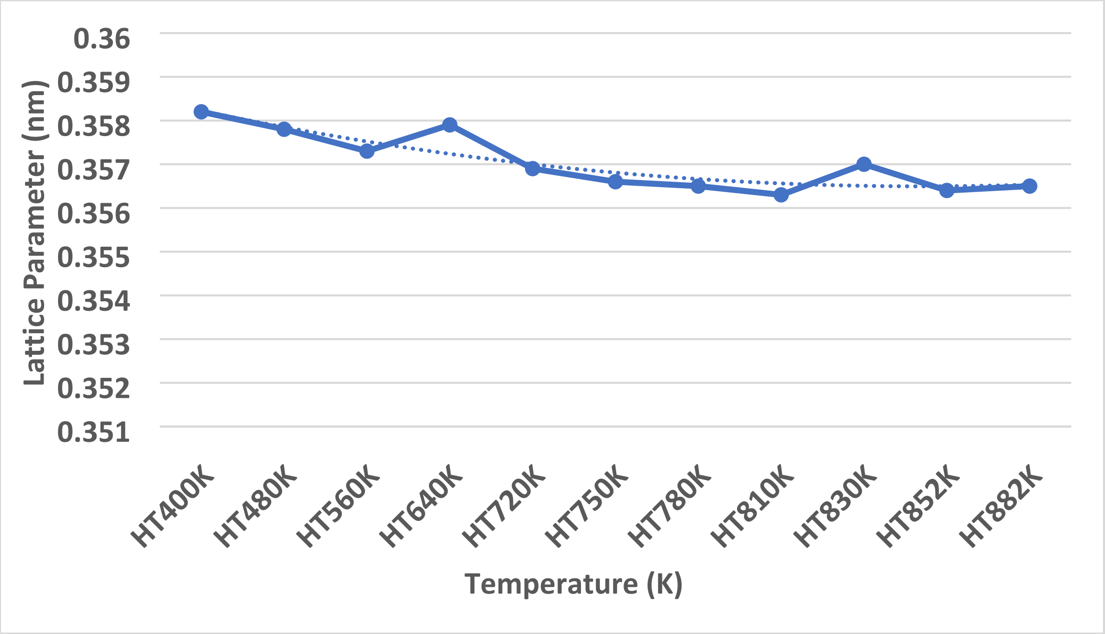

Figure 58. Lattice Parameter of S9 sample with increasing temperature (dotted line shows the trend)

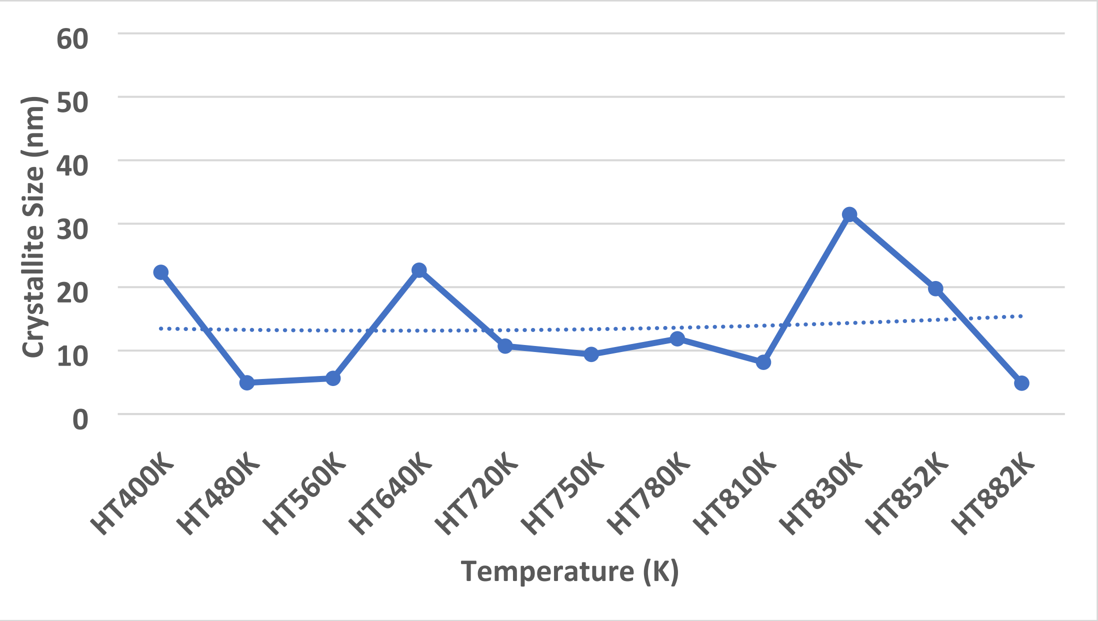

Figure 59. Crystallite size of S9 sample with increasing temperature (dotted line shows the trend)

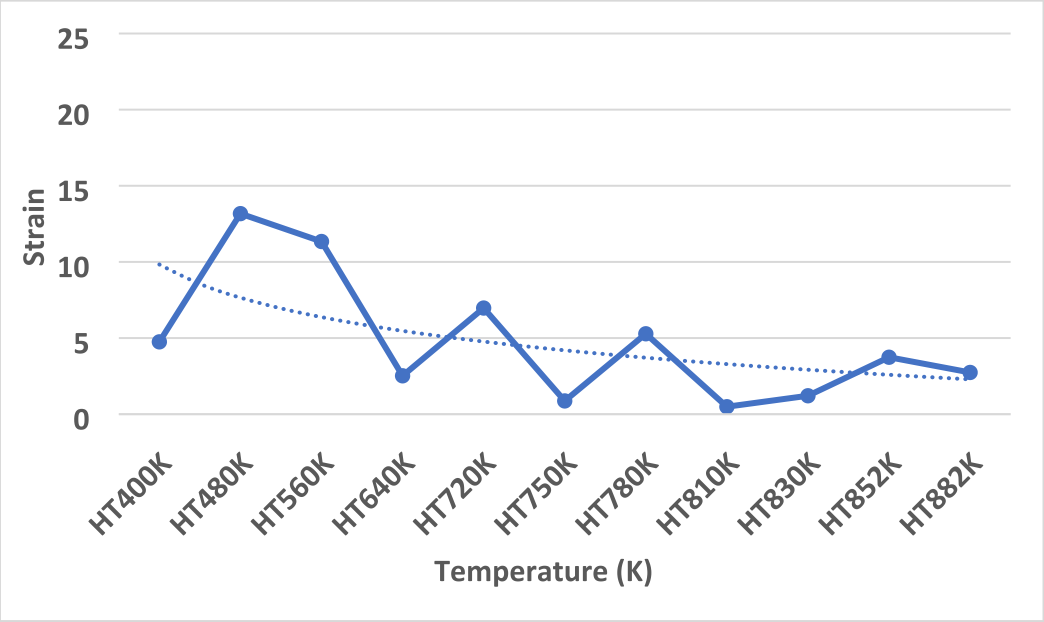

Figure 60. Percentage strain in lattice of S9 sample with increasing temperature (dotted line shows the trend)

In mechanical alloying, the outside temperature of vial can be a factor to check the alloying activity going inside the vial. So, after every specific time period of alloying, temperatures were noted down as shown in **Table 6.** From **Figure 61,** we observe that with increase in duration of alloying the temperature of the vial is going down. This shows that the alloy is getting stable with more alloying. Since alloy formation has stopped, the temperature of vial is going down.

Table 6. Temperature of the vials after alloying for different duration

Hours of Milling	S0.5	S1	S3	S6	S9	S9-HS	S9-SS-O	S12	S15	Mean	Standard Deviation
0	25	25	25	25				25	25	25	
0.5	39.9									39.9	
1		44.9								44.9	
3			41.2	41	44.2	42.6	40.5	46.2	39.6	42.31	2.18
6				41.3	46	42.2	44.1	44.4	41.3	42.99	1.85
9					43.2	46	40.5	41.2	34.6	39.97	4.68
12								39.1	34.3	36.7	3.39
15									33.6	33.6	

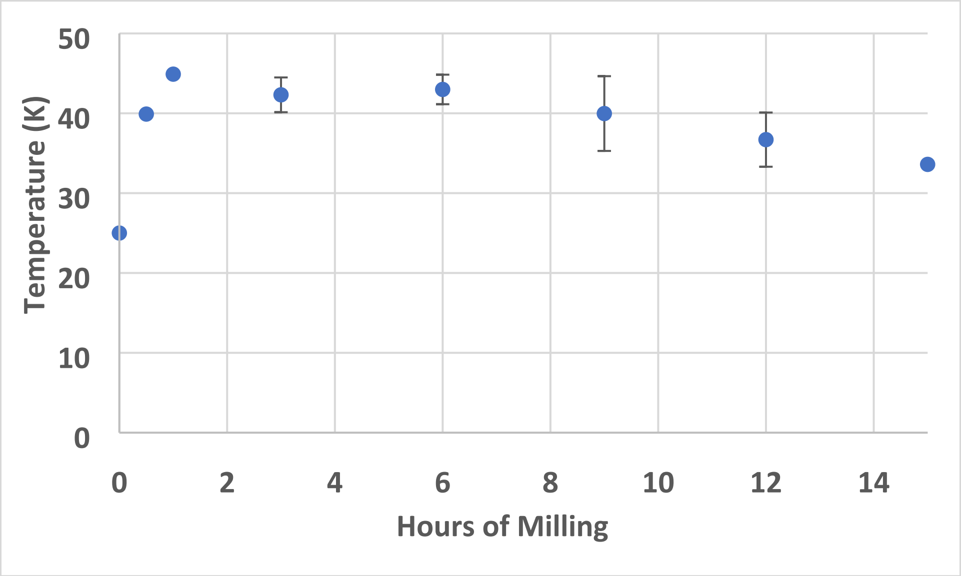

Figure 61. Temperature of vial after alloying for different duration

5.2 Composition considering $\Delta S_{mix} \approx 9$ J/mol.K

Three compositions were synthesized under this category, Ni-rich, Fe-rich and Co-rich, keeping the configuration entropy approximately equal to 9. The composition was kept 40:30:30 and all the three alloys were synthesized in hardened steel vial. The PCA was kept between 3-4% and for every composition 4 samples were prepared according to duration of milling- 3, 6, 9 and 12 hours of milling. Ni-rich, Fe-rich and Co-rich samples were named as HEA-4, HEA-5 and HEA-6 respectively.

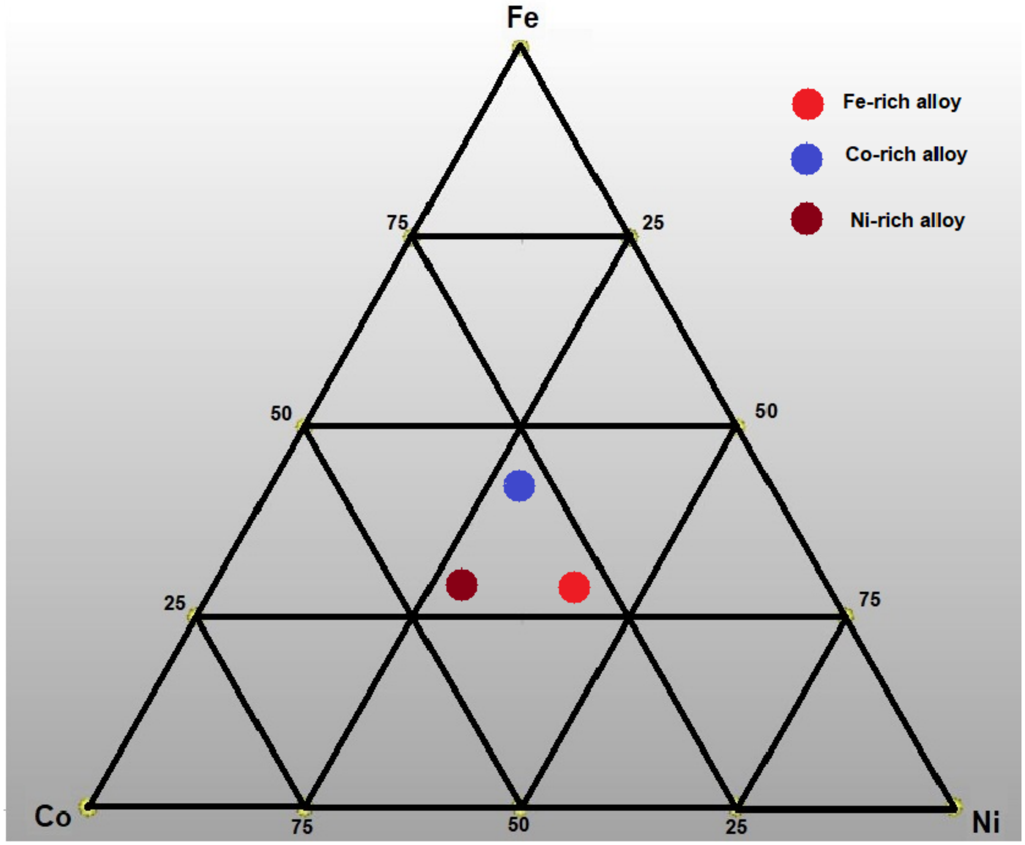

Figure 62. Fe-rich, Co-rich and Ni-rich shown on ternary composition diagram

5.2.1 XRD Analysis

In all the three compositions, Fe and Co goes into the Ni structure and forms single phase FCC alloy. In Ni-rich and Fe-rich alloys, after 6 hours of alloying we do not see any traces of Fe and Co in XRD, as shown in **Figure 63 and 64.** However for Co-rich alloy, we could still see some Co peaks in S6 sample and thus 9 hours of alloying is required for Co-rich sample to form single phase alloy, as shown in **Figure 65**. The XRD depicts the phase transformation occurring in 3 hours of milling to 12 hours of milling.

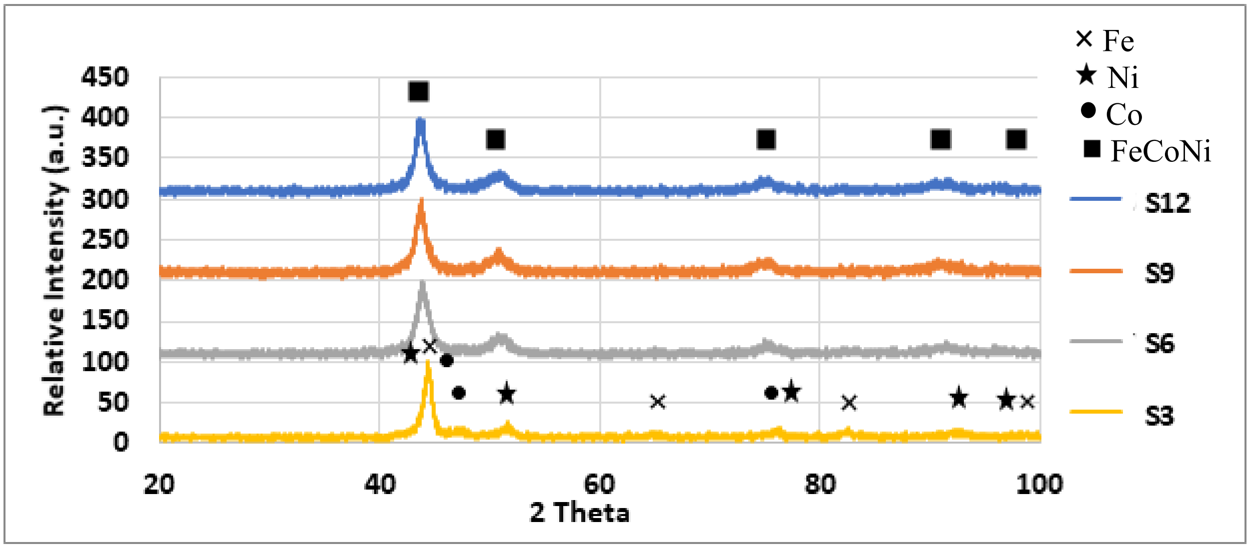

Figure 63. XRD pattern for Ni-rich alloy

In the **Figure 63, 64 and 65,** the peak gets broader with increase in hours of milling. This indicates increasing strain in structure and grain size getting finer. Also, with more hours of milling, the peak is shifting towards left, which means increase in lattice parameter. It can be proved by the Braggs Law,

$$n\lambda=2d\sin\vartheta \qquad (1)$$

where *n* is a positive integer and *λ* is the wavelength of the incident wave.

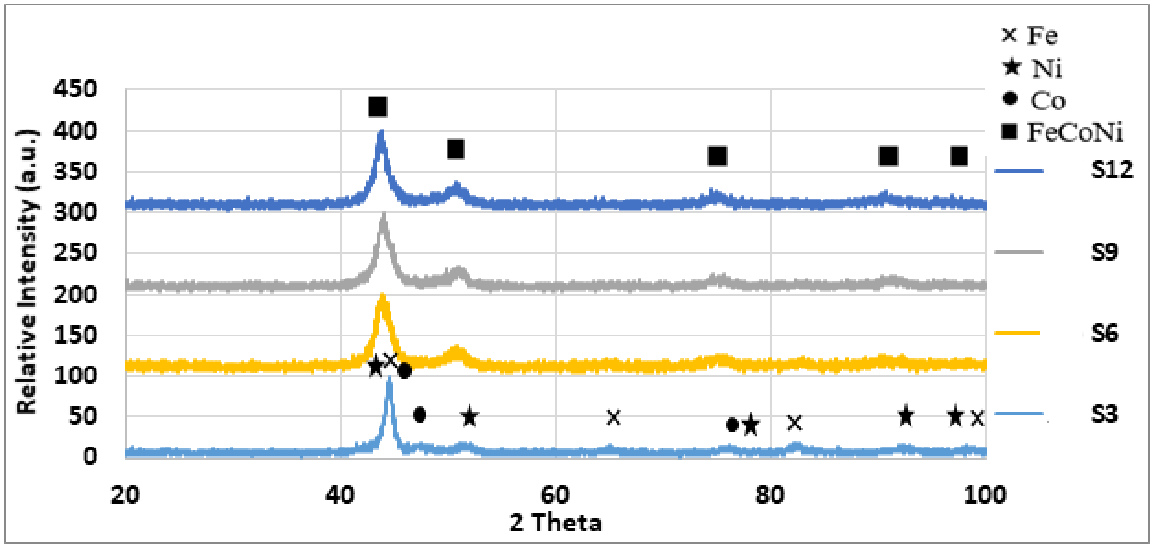

Figure 64. XRD pattern for Fe-rich alloy

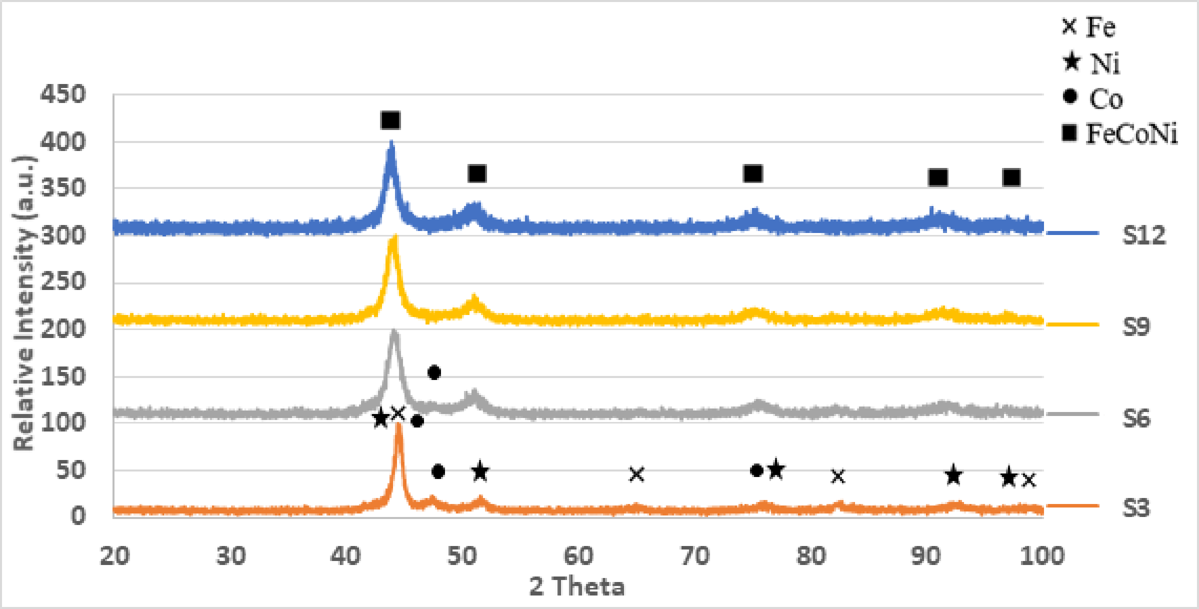

Figure 65. XRD pattern for Co-rich alloy with Cu source

Due to issue of fluorescence, the Co particles were reflecting most of the light from the cathode and was hard to detect the Co particles. So, just to reassure that all the Co has gone into Ni lattice, all the Co-rich samples were examined under Co source XRD. As shown in **Figure 66,** there are no Co peaks in S9 or S12 samples which is the same as with the Cu source XRD.

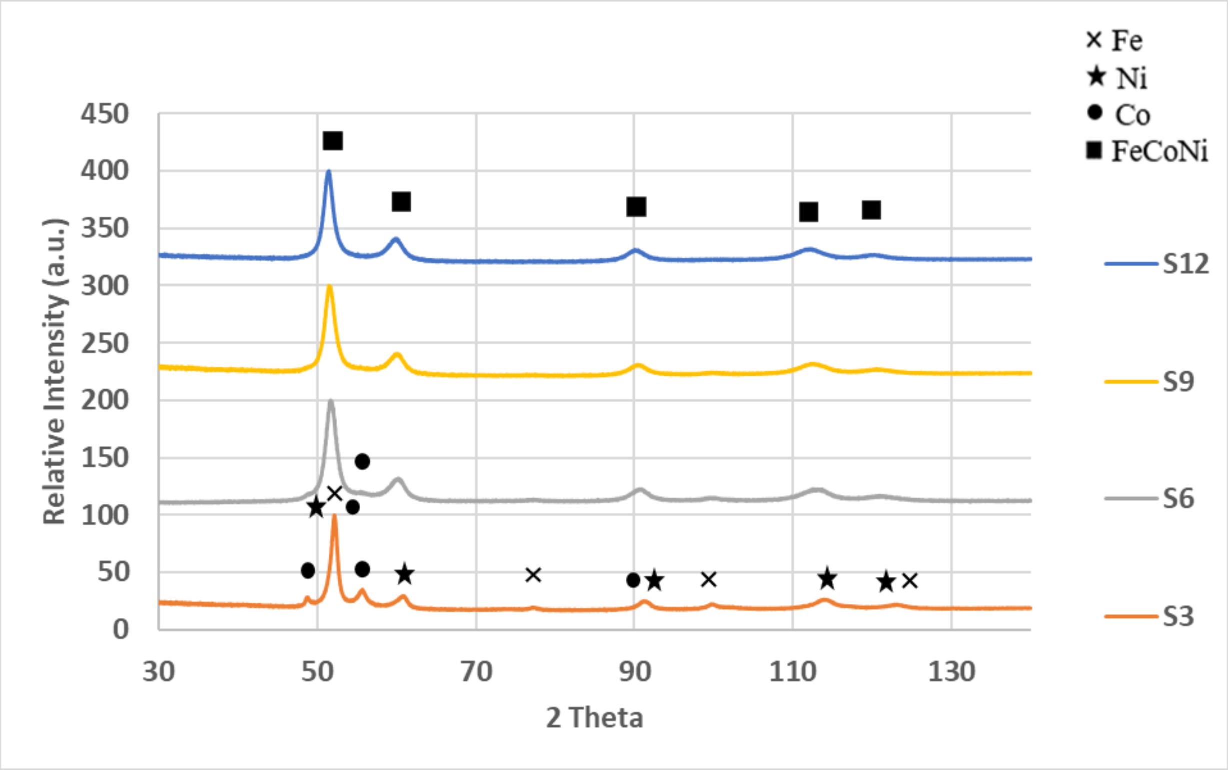

Figure 66. XRD pattern for Co-rich alloy with Co source

5.2.2 VSM Analysis

Magnetic Characterization of all the alloys were performed on Quantum Design's Vibrating Sample Magnetometer (VSM). The magnetic field of -2150 kA/m (-27 kOe) to 2150 kA/m (27 kOe) were applied and the consequent change in magnetization were recorded, as shown in **Figure 67, 68 and 69.** The hysteresis loops prove the alloy to be ferromagnetic. It can also be observed from the figures that with more alloying, the coercivity is decreasing because of particle size getting nanostructured. Also, saturation magnetization is increasing because with more alloying, more Fe is going into the structure to form single phase FCC alloy. This variation can also be seen in the **Figure 70 and 71.**

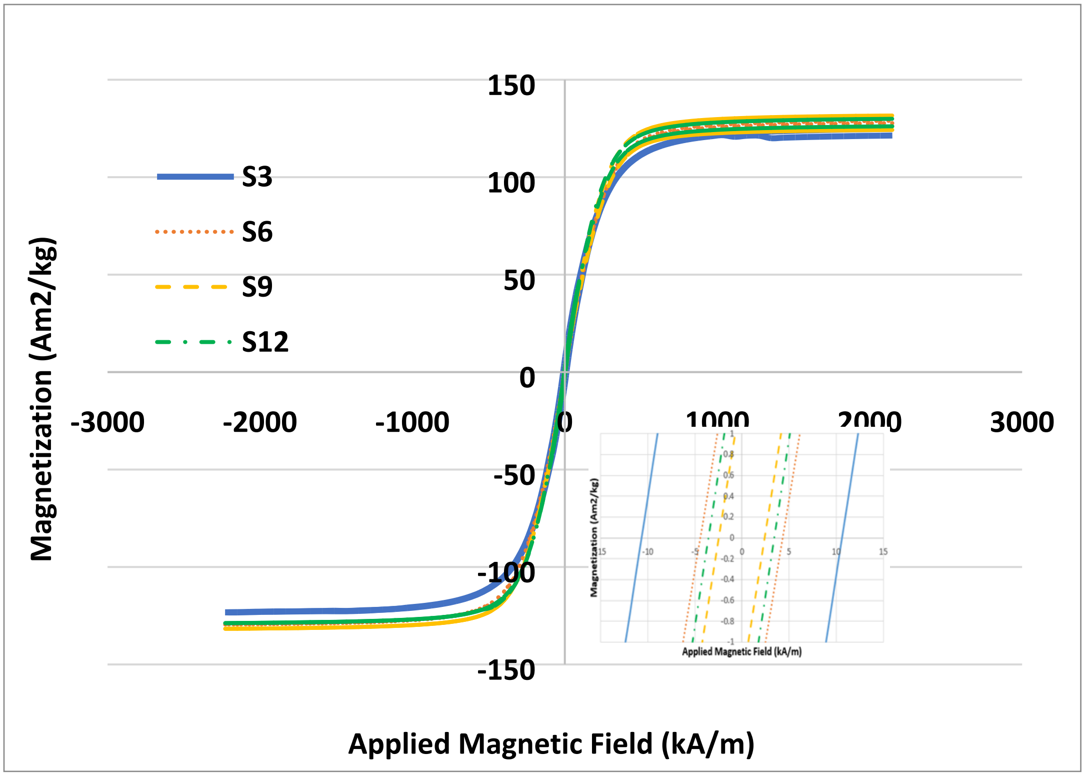

Figure 67. *M-H* curves for Ni-rich alloy milled for 3, 6, 9 and 12 hours

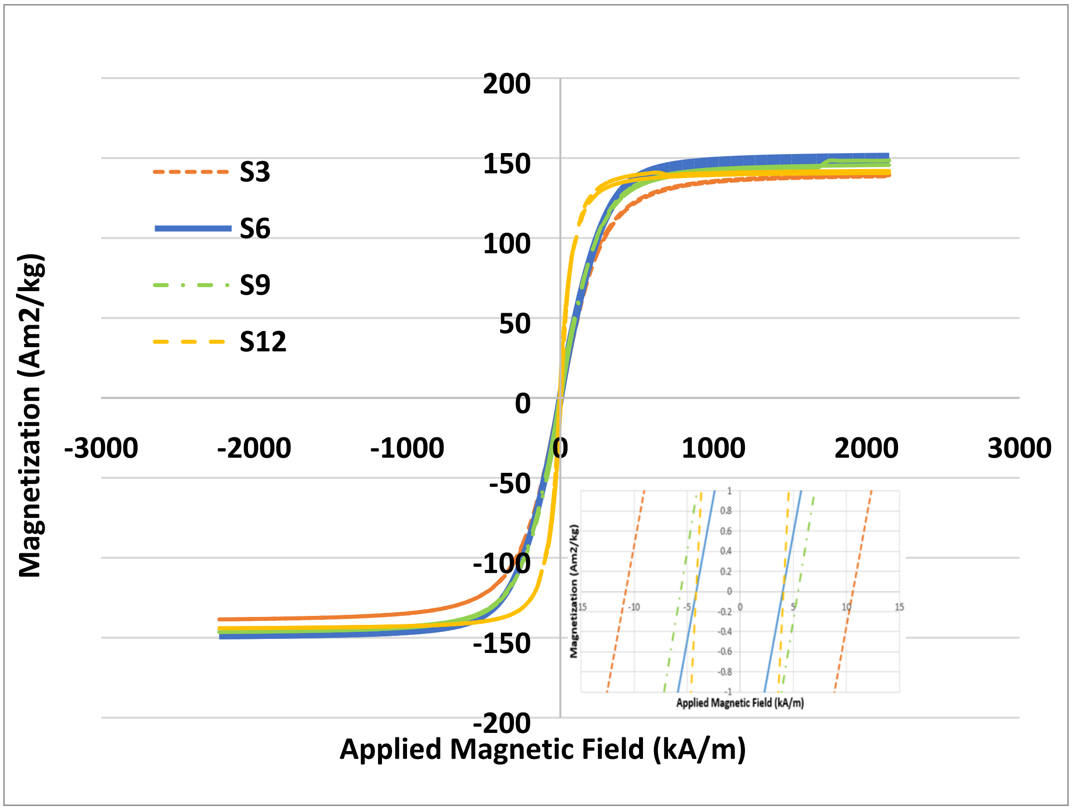

Figure 68. *M-H* curves for Fe-rich alloy milled for 3, 6, 9 and 12 hours

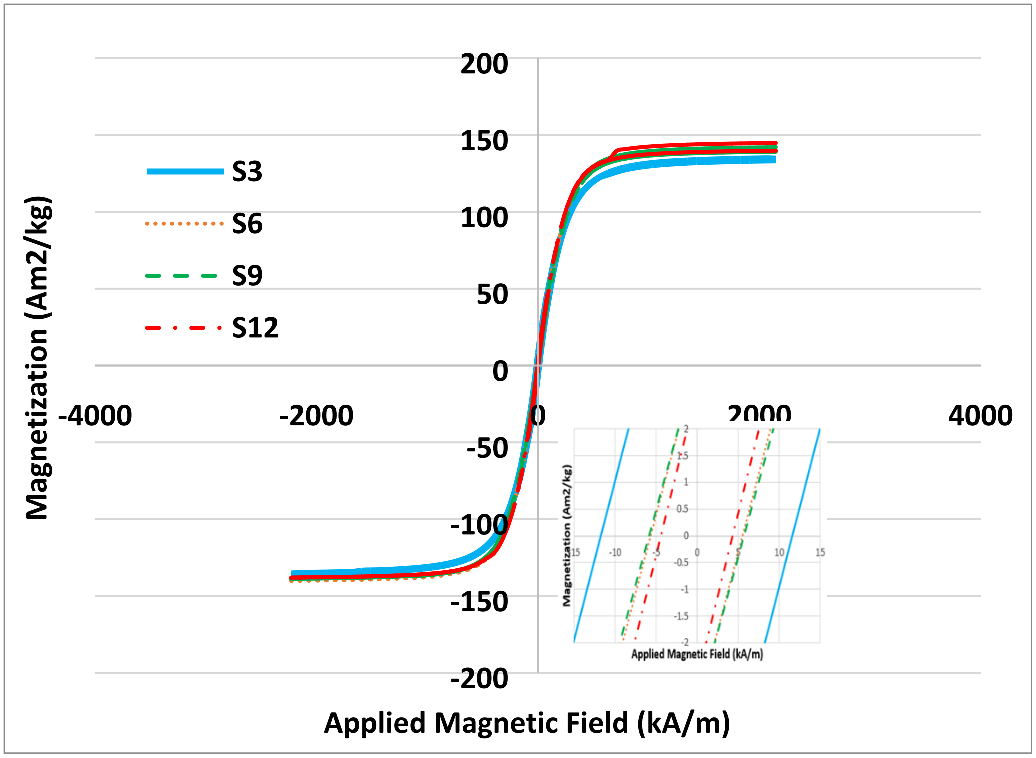

Figure 69. ***M-H*** **curves for Co-rich alloy milled for 3, 6, 9 and 12 hours**

For saturation magnetization (M_S), the magnetization is recorded at 1989.44kA/m (25 kOe) and then divided by mass of sample. The coercivity is the magnitude of negative magnetic field applied to bring the magnetization in the material to zero and is denoted by H_C. **Figure 70 and 71,** shows the variation of *Ms* and H_C with increase in duration of alloying. Fe is the ferromagnetic material and thus Fe-rich alloy shown the highest M_S as compared to Ni-rich and Co-rich samples. Ni-rich alloy shows the least coercivity since with addition of Ni coercivity decreases. Coercivity is also inversely proportional to crystallite size, which we can see from **Figure 81**, crystallite size increasing as we go from S3 to S12 and coercivity decreasing from S3 to S12.

Table 7.Saturation magnetization and coercivity of all the samples

	S6		S9		S12	
Alloy	*Ms* (Am^2/kg)	*Hc* (kA/m)	*Ms* (Am^2/kg)	*Hc* (kA/m)	*Ms* (Am^2/kg)	*Hc* (kA/m)
HEA-4	128.83 ± 1.99	4.36 ± 0.06	130.11 ± 1.02	2.39 ± 0.08	128.42 ± 0.49	3.49 ± 0.07
HEA-5	148.05 ± 1.41	4.07 ± 0.02	146.13 ± 2.56	5.47 ± 0.09	147.50 ± 2.56	4.26 ± 0.13
HEA-6	139.87 ± 0.48	5.63 ± 0.09	139.81 ± 0.58	5.70 ± 0.08	140.91 ± 2.18	4.31 ± 0.06

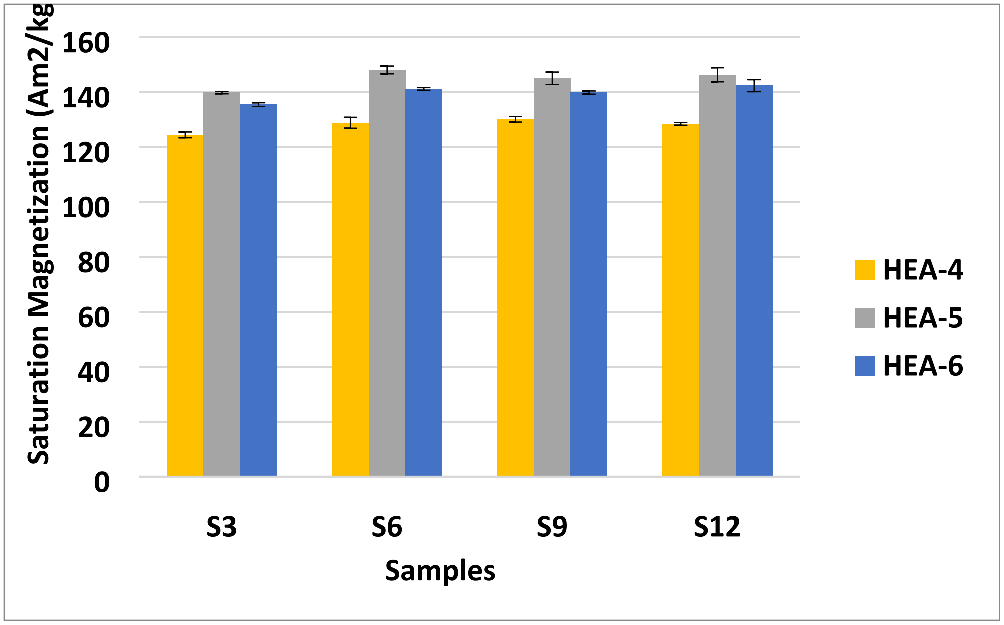

Figure 70. Saturation Magnetization (M_S) of all the samples with 3, 6, 9 and 12 hours of alloying

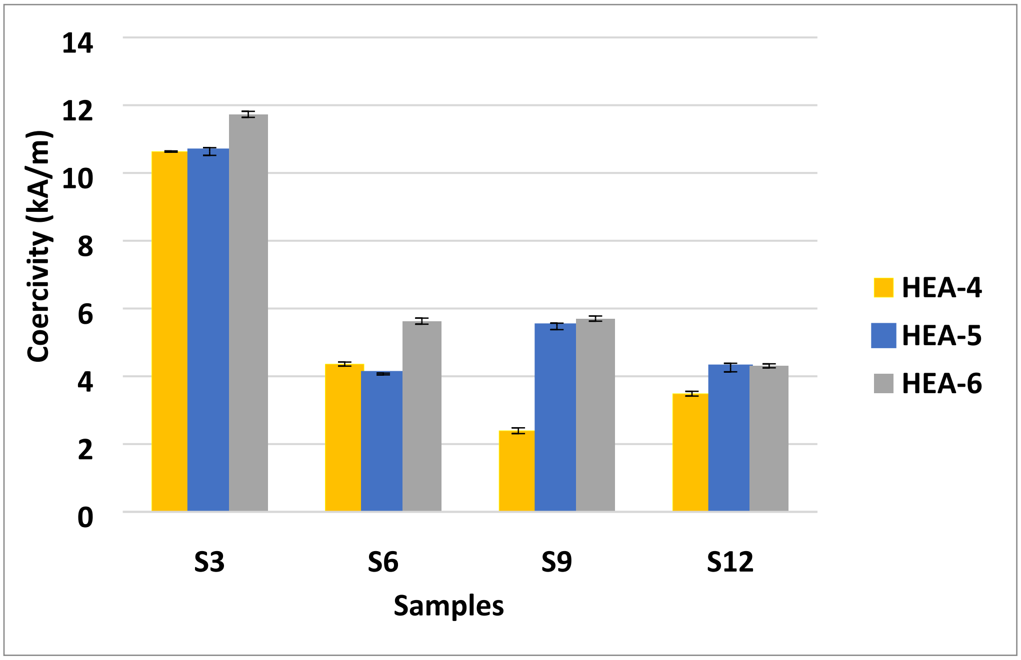

Figure 71. Coercivity (H_C) of all the samples with 3, 6, 9 and 12 hours of alloying

5.2.3 SEM Analysis

A SEM and EDAX analysis were performed for each sample with different magnification and the results are shown in **Figure 72, 73 and 74.**

S3  100 µm	S6 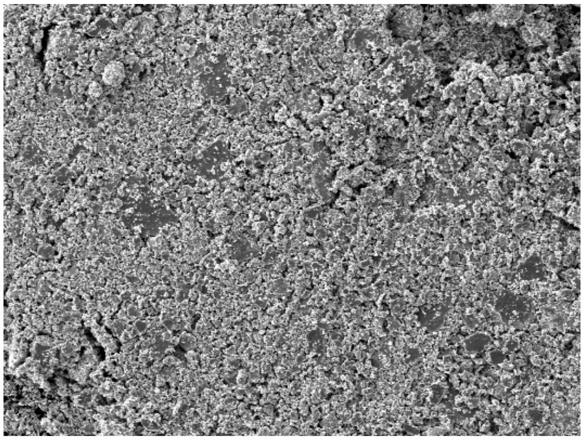 100 µm
S9 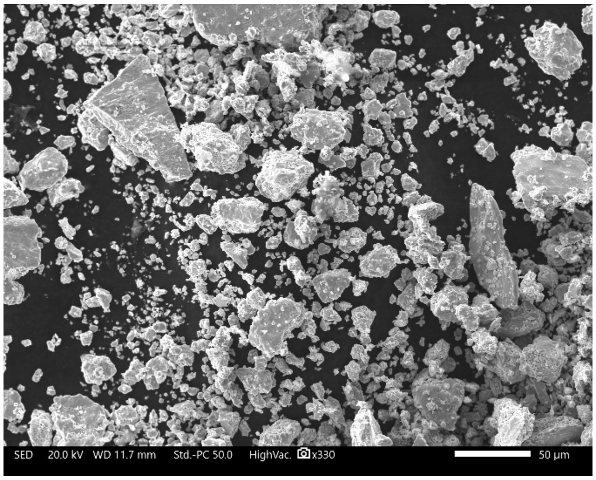 50 µm	S12 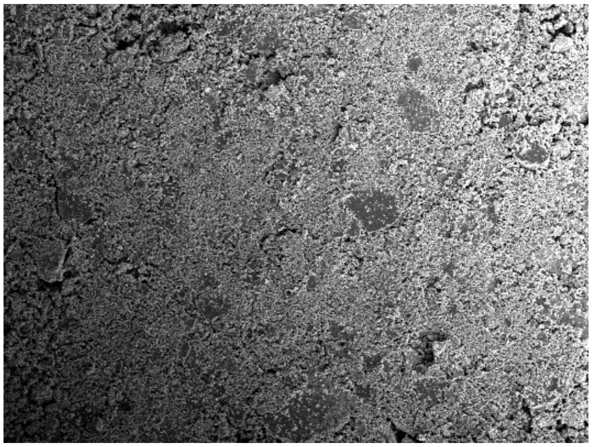 100 µm

Figure 72. SEM images of all the Ni-rich sample at 100 µm resolution

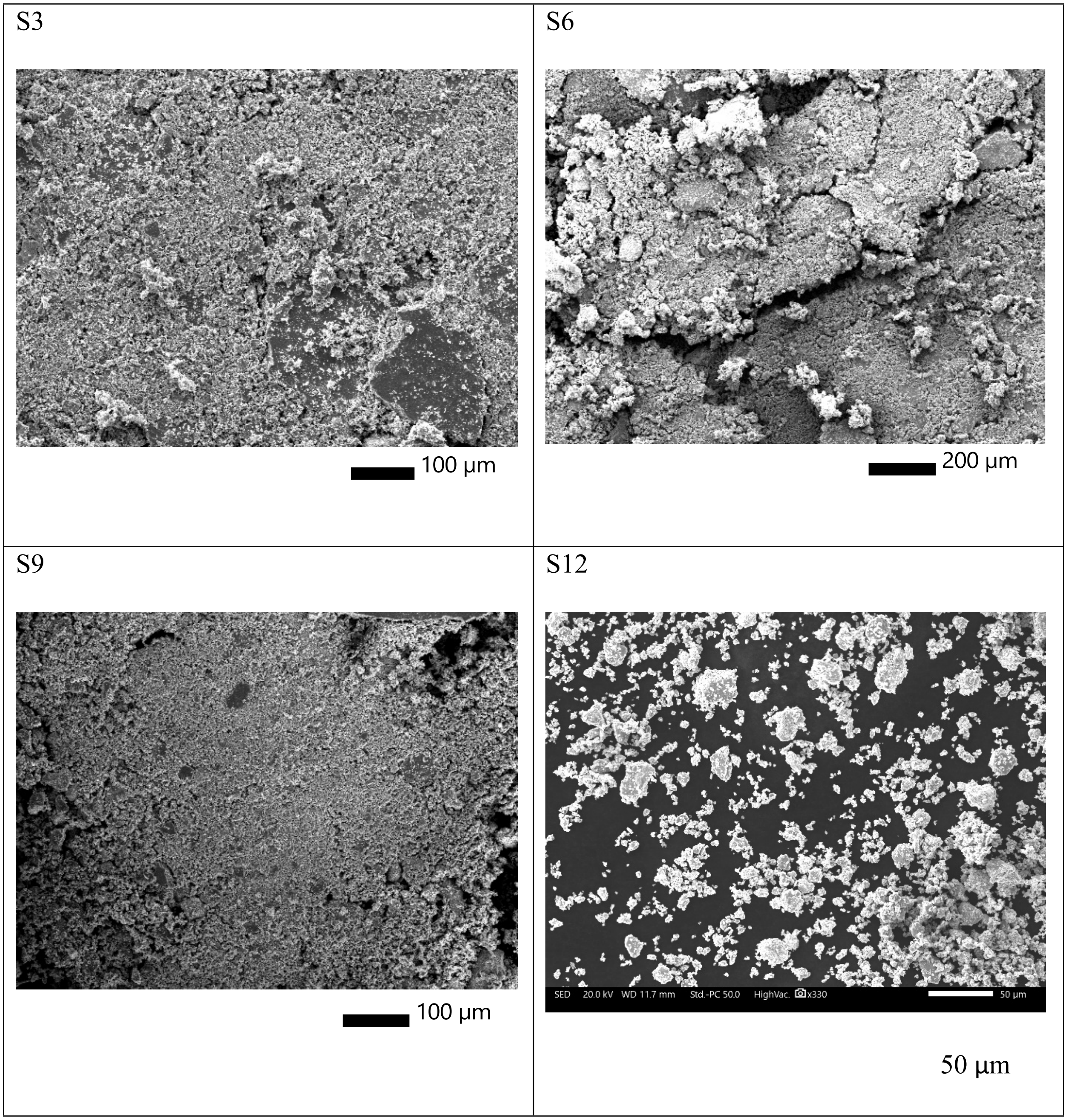

Figure 73. SEM images of all the Fe-rich sample at 100 µm and 200 µm resolution

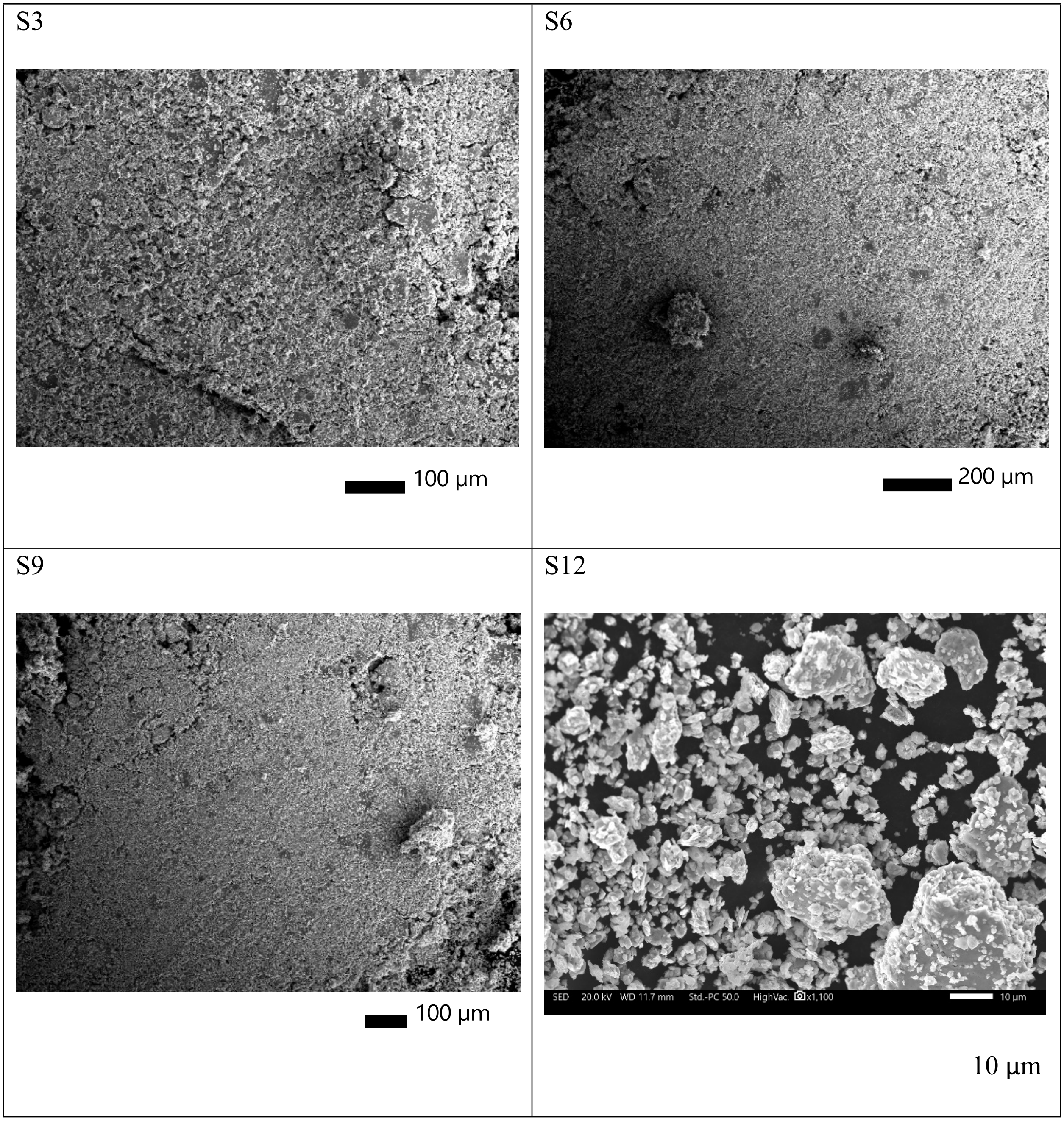

Figure 74. SEM images of all the Co-rich sample at 100 µm and 200 µm resolution

The atomic percentage of Fe-Co-Ni is shown in **Figure 12.** The atomic ratio was 40:30:30. HEA-4 was having 40 atomic percent Ni, HEA-5 was having 40 atomic percent Fe and HEA-6 was having 40 atomic percent Co. It was found that atomic percentage of Ni was getting less with increase in duration of alloying and to compensate, Fe and Co percentage were rising. From the EDAX result, as shown in **Figure 12,** the ratio is not always 40:30:30 but the element that is rich in the alloy is always relatively more than the other two elements.

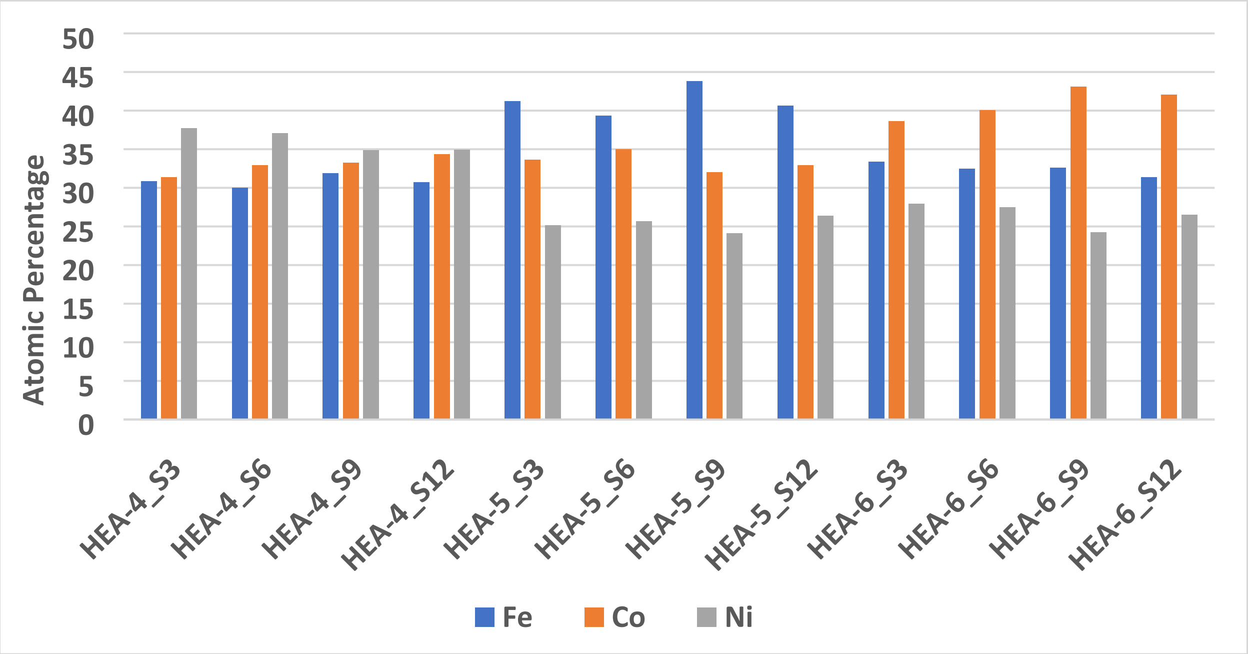

Figure 75. EDAX result for all the samples with 3, 6, 9 and 12 hours of alloying

In Ni-rich alloy, till 6 hours of milling the diameter was almost consistent at ~4.33 µm. After 3 more hours of alloying, due to particles fusing into each other, it increased to ~11.49 µm. After 12 hours of alloying, the particle size reduced to ~9.75 µm because of milling, as shown in **Figure 76.**

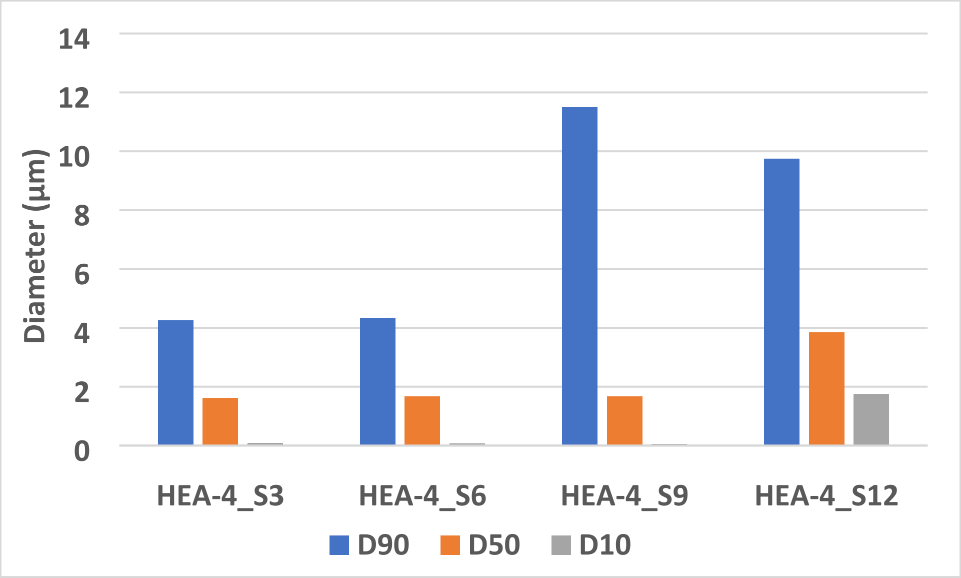

Figure 76 *D90*, *D50*, and *D10* particle size diameters of HEA-4 samples

In Fe- rich alloy, fusion started at 6 hours and thus the particle size reached ~11.52 µm after 6 hours of milling. After that, due to milling, the particle size started reducing and at S12 it reached ~5.54 µm, as shown in **Figure 77.**

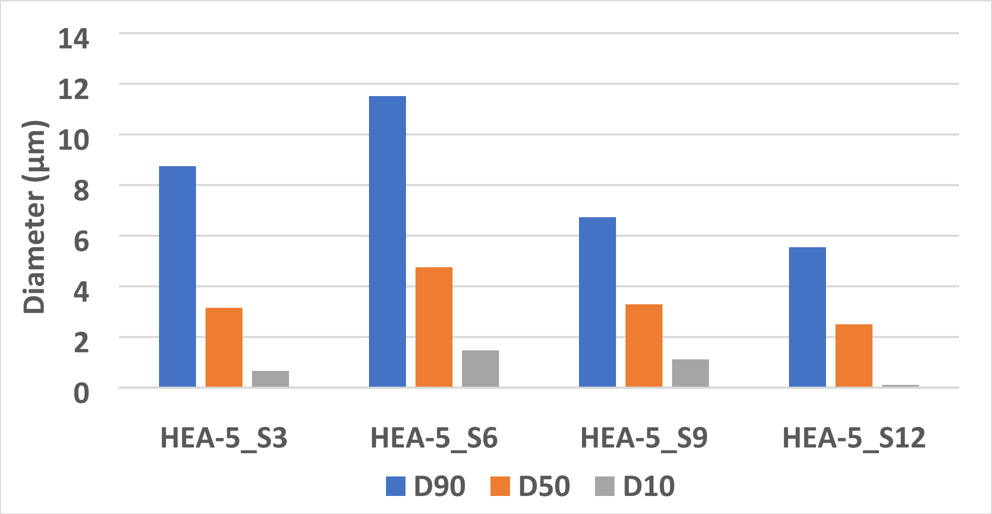

Figure 77. ***D90*, *D50*, and *D10* particle size diameters of HEA-5 samples**

In Co-rich alloy also, we have similar observations. The particle size changed due to fusion and milling. It started from ~3.64 µm in S3 sample and ended at ~7.16 µm in S12 sample, as shown in **Figure 78.**

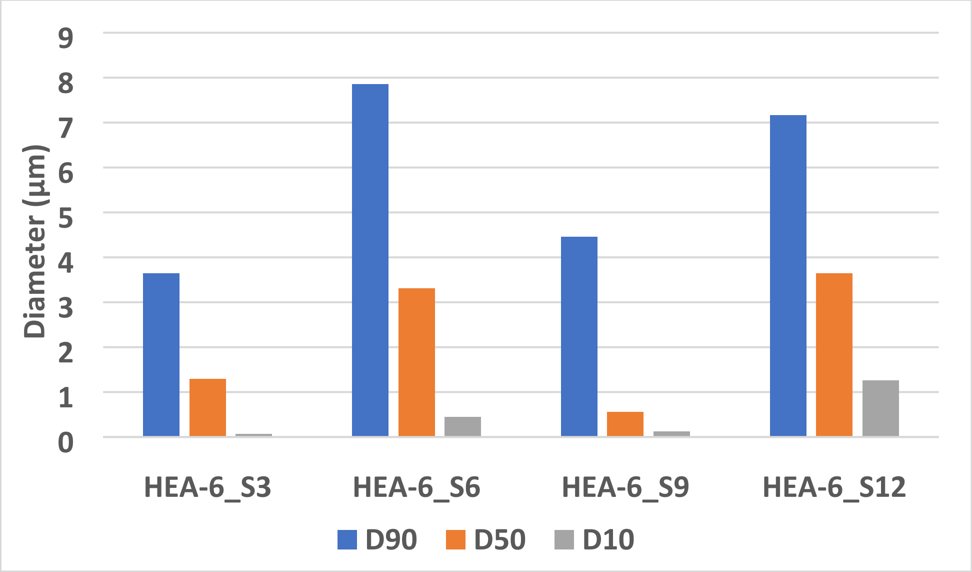

Figure 78. ***D90*, *D50*, and *D10* particle size diameters of HEA-6 samples**

As explained earlier, with induced strain from S6 to S12 sample, the lattice parameter increases, as shown in **Figure 79 and 80**. Also, with more hours of alloying, the crystallite size also increases, as shown in **Figure 81.** The crystallite size increases from ~2.39 nm to ~16.94 nm in case of Ni-rich alloy. In case of Fe-rich alloy, it does not change much and just increases by ~1.03 nm from S3 to S12. The Co-rich crystallite size has a big jump of ~32.26 nm, from ~3.59 nm to ~35.85 nm.

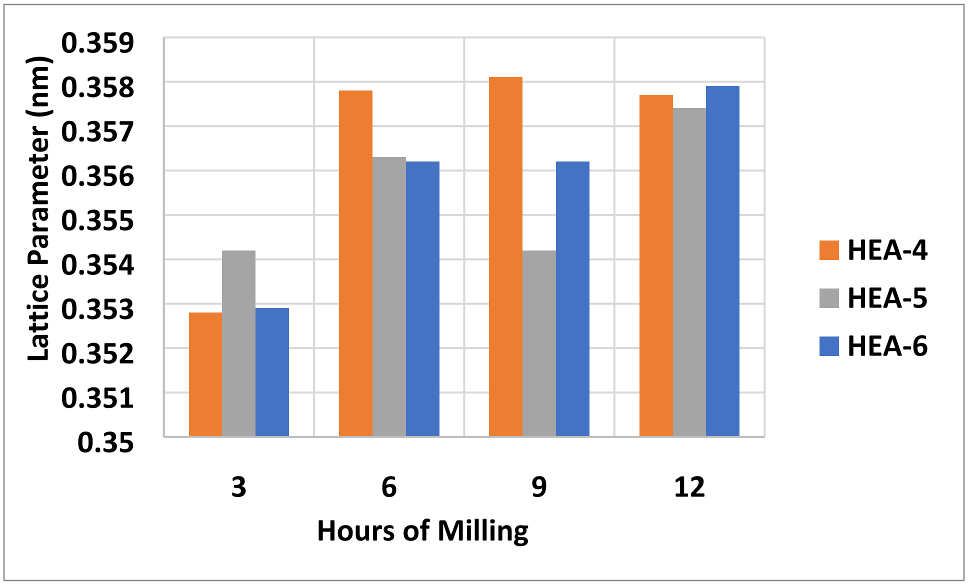

Figure 79. Lattice parameter of all the samples milled for 3, 6, 9 and 12 hours

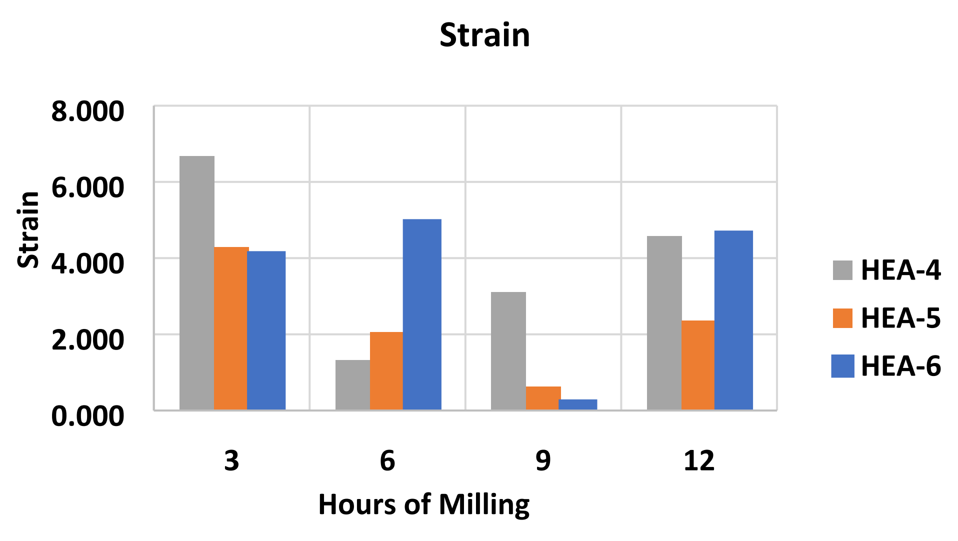

Figure 80. Strain of all the samples milled for 3, 6, 9 and 12 hours

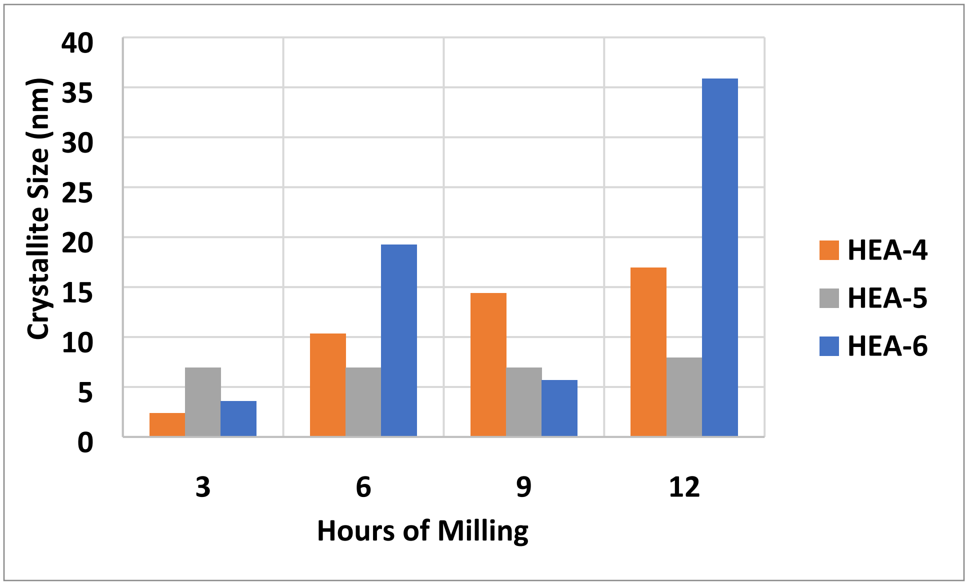

Figure 81. Crystallite size of all the samples milled for 3, 6, 9 and 12 hours

5.2.4 Synthesis in oxygen environment

As seen in the above results, Fe-rich samples gave the highest saturation magnetization 148.05 Am^2/kg and Ni-rich gave the lowest coercivity of 2.39 kA/m (30.08 Oe). Since a good soft magnetic alloy has high M_S and low H_C, thus S12 sample of Fe-rich alloy was the best candidate among all. It was having the best combination of M_S (146.29 Am^2/kg) and H_C (4.26 kA/m). The XRD also confirmed it to be the single face FCC alloy.

Once the best sample was selected, it was synthesized in oxygen environment (S12-O). Preparing the sample in argon environment requires lots of efforts and careful handling of alloy once it has been synthesized. Thus, by preparing in oxygen we can save time, efforts and manpower.

XRD, in **Figure 82,** shows that S12-O does not form any oxides even after 12 hours of alloying. XRD is similar to S12 prepared in argon and S12-O is also single-phase FCC structure.

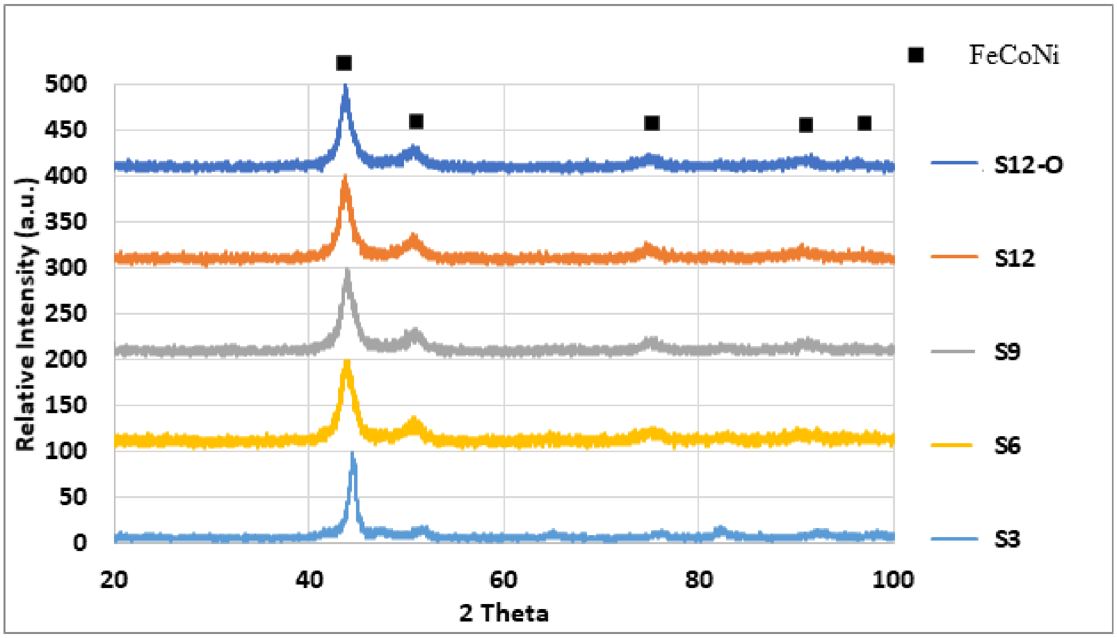

Figure 82. XRD of Fe-rich S12 sample prepared in oxygen compared with all the Fe-rich sample

From the hysteresis loop as shown in **Figure 83**, M_S and H_C is calculated. It is found that M_S decreases by ~6% ($M_S = 137.35$ Am^2/kg) and H_C increases by ~20% ($H_C = 5.14$ kA/m), as shown in **Figure 84 and 85**. These variations are acceptable if we get rid of the 'argon environment' hassle.

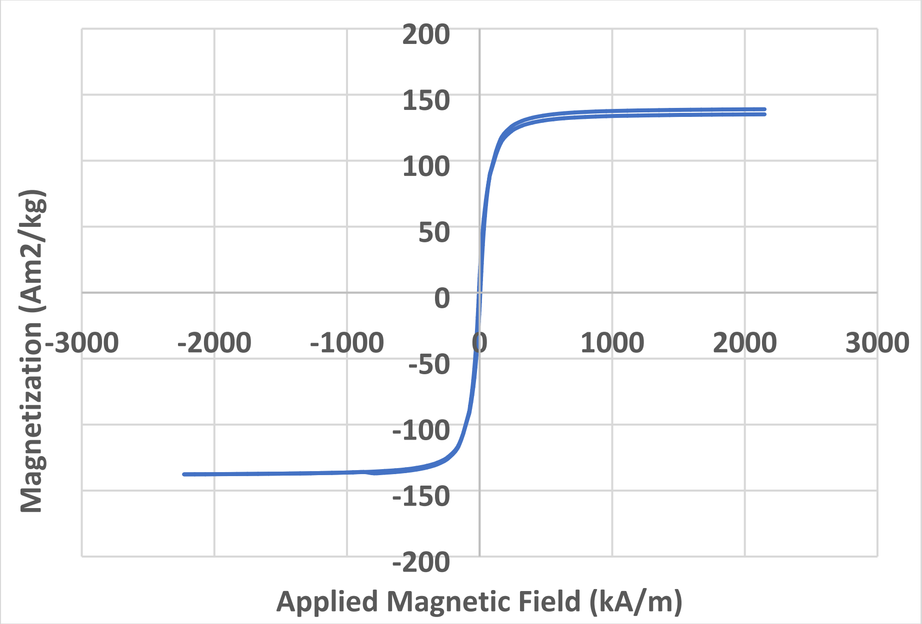

Figure 83. Hysteresis loop of Fe-rich S12 sample prepared in oxygen

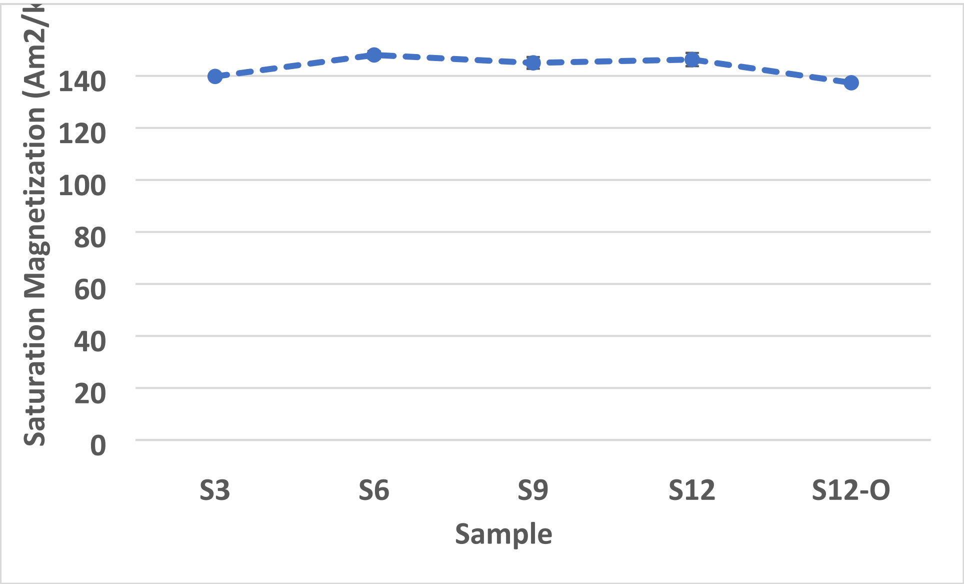

Figure 84. M_S **of Fe-rich S12 sample prepared in oxygen compared with all the Fe-rich sample**

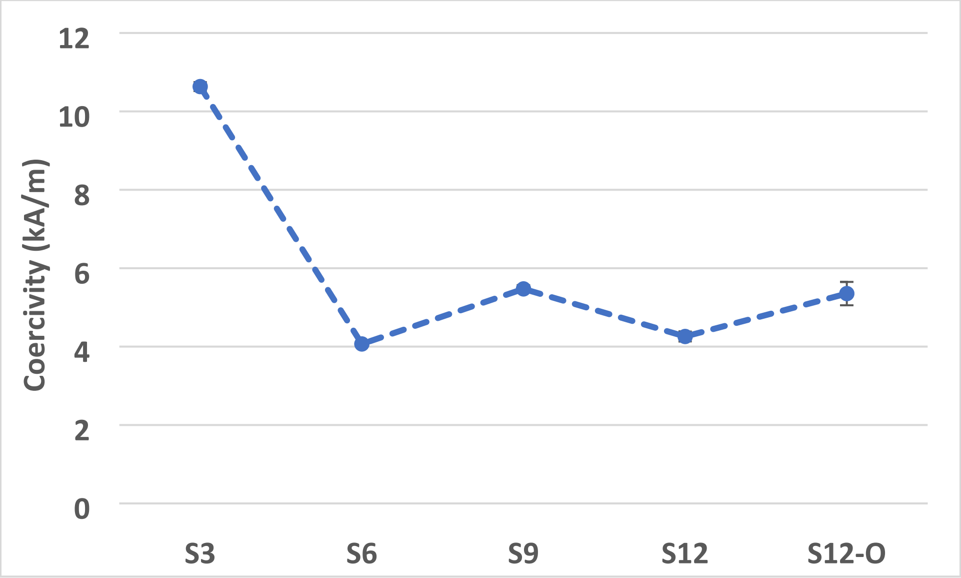

Figure 85. H_C **of Fe-rich S12 sample prepared in oxygen compared with all the Fe-rich sample**

As shown in **Figure 86,** the particle diameter of S12-O increases by ~0.5% as compared to S12 prepared in argon. Since both the samples are milled for the same time, the particle diameter is expected to be similar.

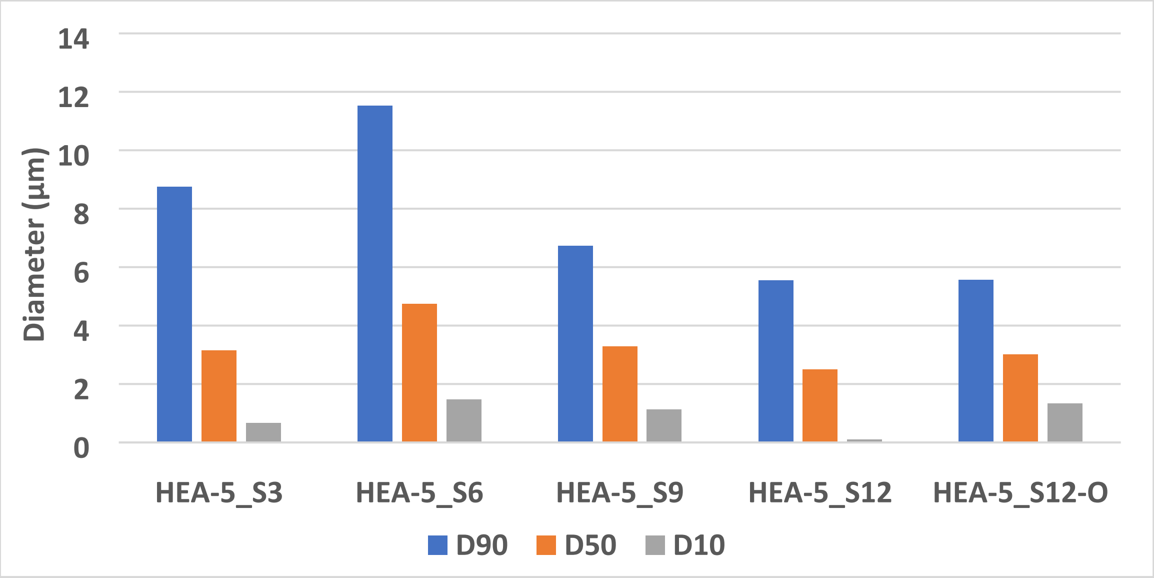

Figure 86. ***D90***, ***D50***, **and** ***D10*** **of Fe-rich S12 sample prepared in oxygen compared with all the Fe-rich sample**

The lattice parameter of S12-O increases by ~0.4% and crystallite size decreases by ~13%, as shown in **Figure 87 and 89.** The strain increases in S12-O by ~575%, as shown in **Figure 88**. As it is known that strain increases with increase in milling energy, which is achieved by higher ball to mass ratio or increased milling speed, can also be achieved by flammable oxygen environment.

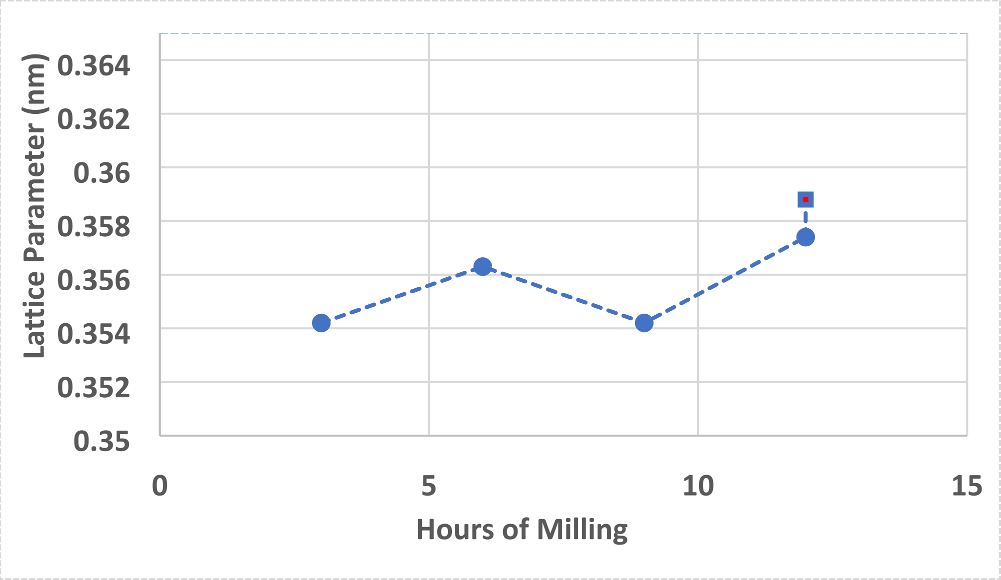

Figure 87. Lattice parameter of Fe-rich S12 sample prepared in oxygen compared with all the Fe-rich sample

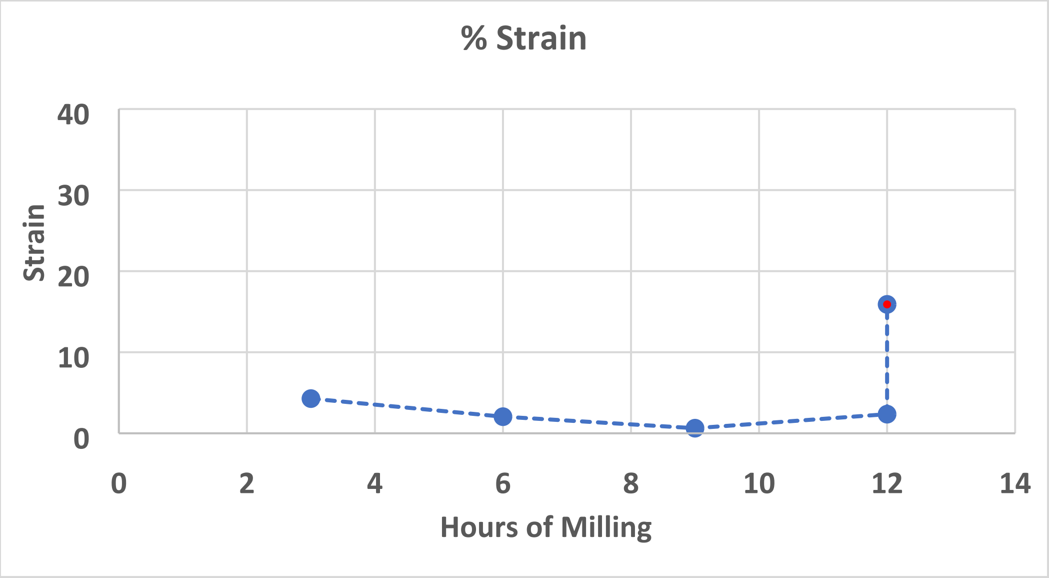

Figure 88. Strain of Fe-rich S12 sample prepared in oxygen compared with all the Fe-rich sample

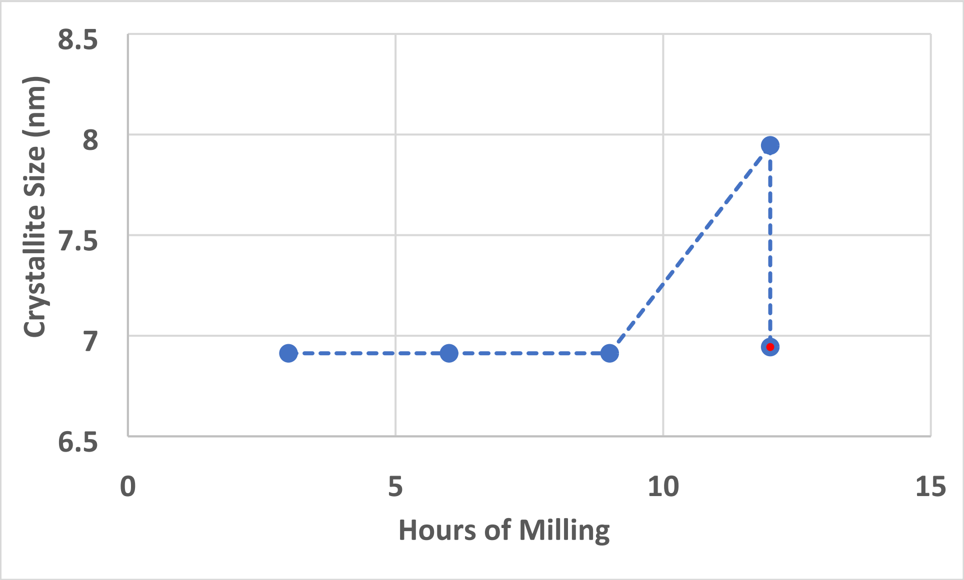

Figure 89. Crystallite size of Fe-rich S12 sample prepared in oxygen compared with all the Fe-rich sample

5.2.5 Heat Treatment

After the samples were tested at room temperatures, they were heat treated (as stated in section 5.1.4) at a temperature more than 850 K to determine the change in properties. S3 was not considered for heat treatment since there were some Fe peaks in XRD, which meant the powders were not completely alloyed. The magnetization vs. temperature curve was plotted for all the three samples at 80 kA/m (1 kOe). As shown in **Figure 90, 91 and 92,** the magnetization decreases with increase in temperature, but at ≈650 K the magnetization starts rising. This increase in magnetization is because of ferromagnetic behavior of Fe which has escaped the HEA lattice due to thermal vibrations. Between 750 K to 800 K, the thermal energy starts dominating ferromagnetic effect of Fe and the magnetization starts going down. To check the behavior of new two phase HEA alloy, another *M*v*T* curve was plotted for as-annealed S6 sample. As shown in **Figure 90,** it follows the curie law and there is no trough in crest in the graph.

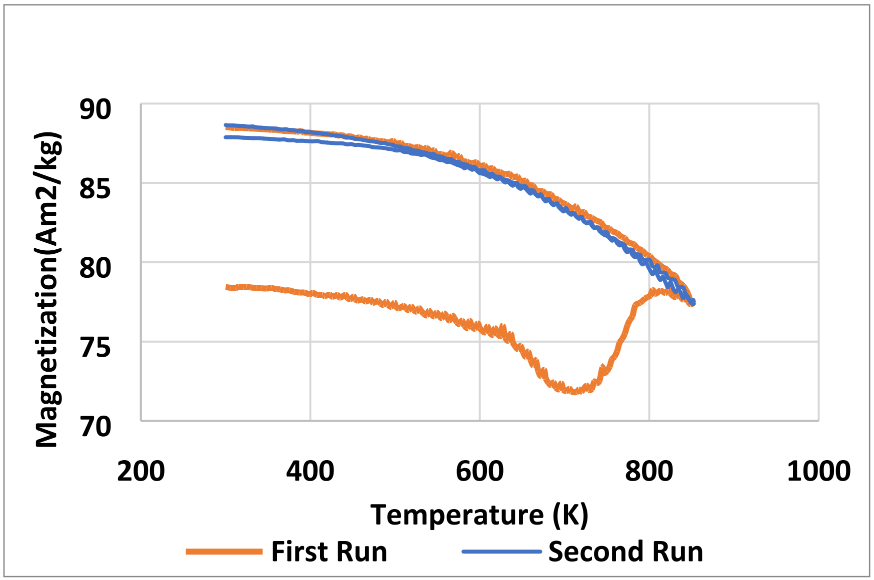

Figure 90. Magnetization vs temperature curve of Ni-rich S6 sample

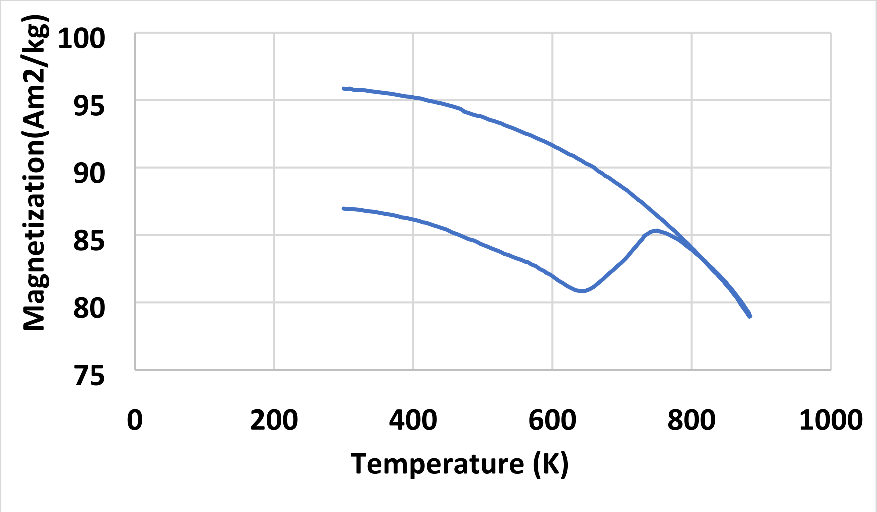

Figure 91. Magnetization vs temperature curve of Ni-rich S9 sample

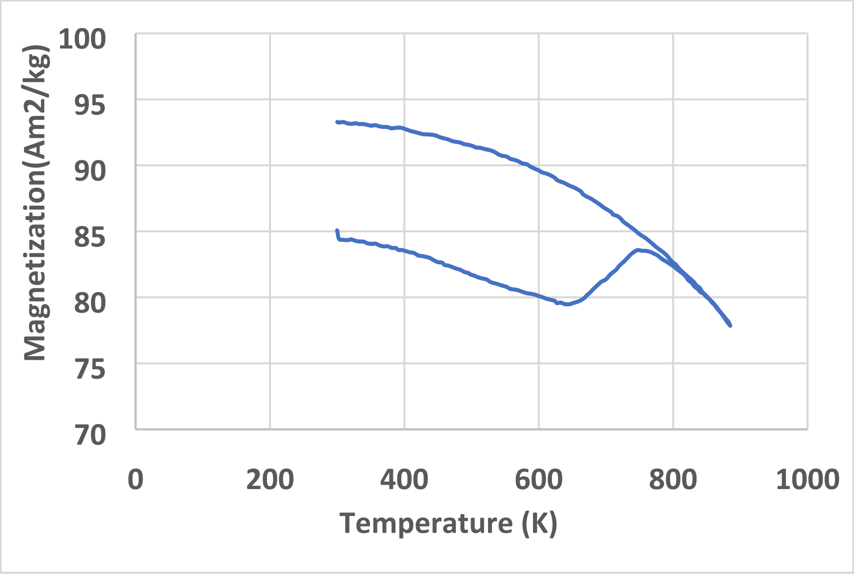

Figure 92. Magnetization vs temperature curve of Ni-rich S12 sample

The XRD for all the heat-treated samples were plotted. In all the samples there were Fe peaks along with HEA which confirms the Fe atoms leaving the HEA lattice, as shown in **Figure 93, 94 and 95.**

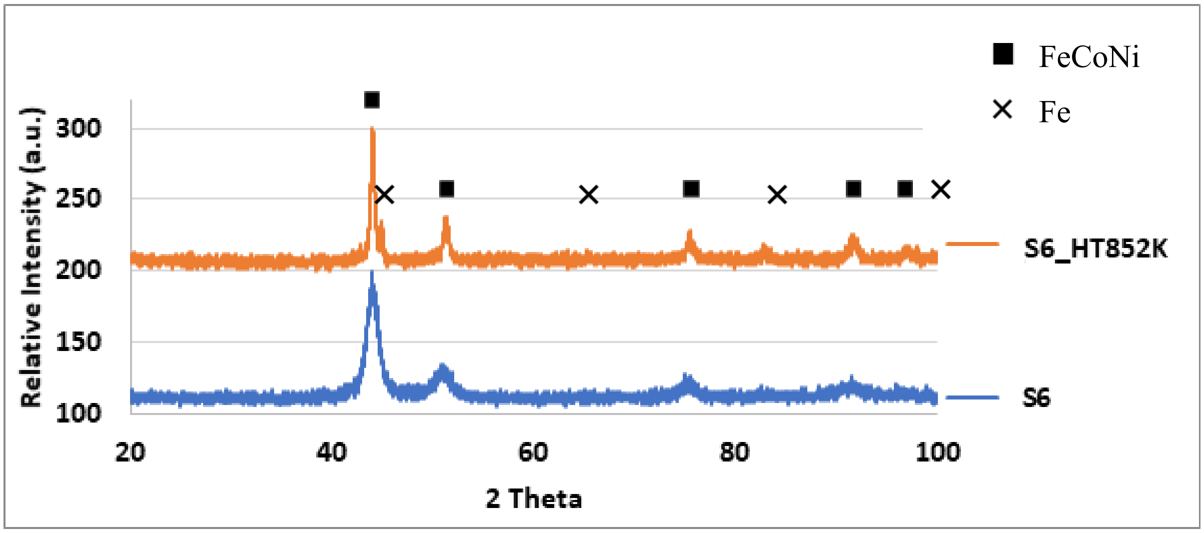

Figure 93. Comparison of XRD of heat treated Ni-rich S6 sample vs as-prepared sample

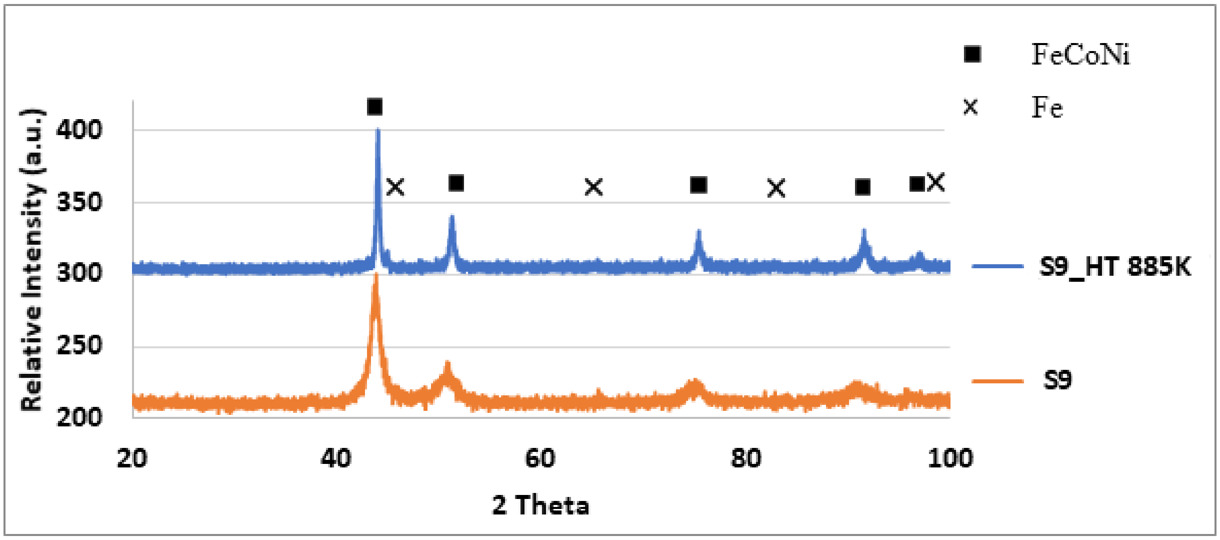

Figure 94. Comparison of XRD of heat treated Ni-rich S9 sample vs as-prepared sample

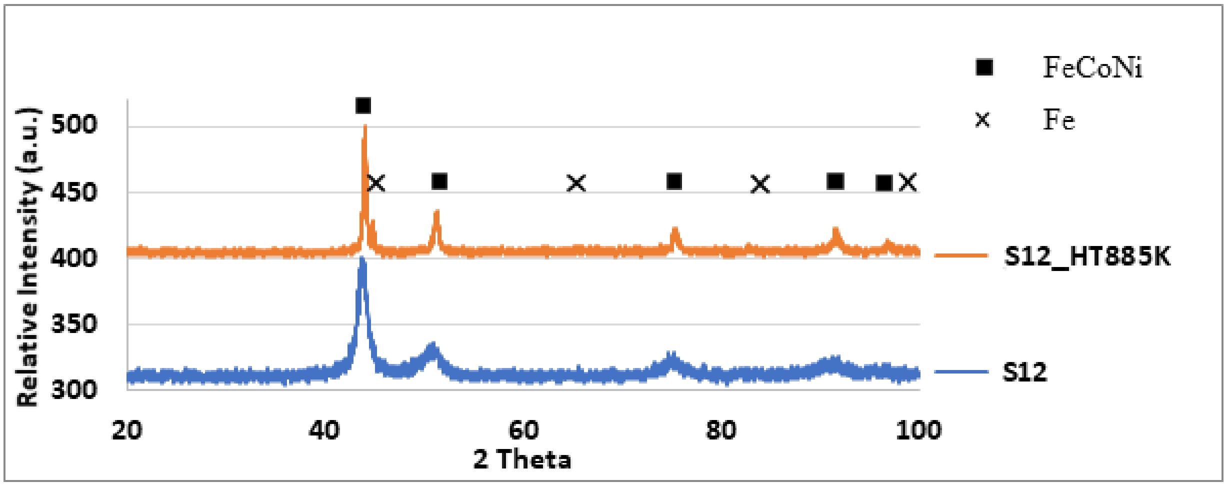

Figure 95. Comparison of XRD of heat treated Ni-rich S12 sample vs as-prepared sample

As shown in **Figure 96,** the saturation magnetization of alloy increases with decreasing temperature. The reason is because lower the temperature, lesser is the thermal vibrations. Increase in temperature causes dipole misalignment even if there is an external magnetic field present. This ultimately brings M_S to zero at a temperature known as Curie temperature (T_C).

From **Figure 97,** we see the coercivity increases with decreasing temperature. It can be explained by the following Neel Brown equation [55]

$$H_C = H_0 \left[1 - \left[\frac{k_B T}{\Delta E_0} ln\left(\frac{f_0 t_0}{ln\,(2)}\right)\right]^{1/n}\right] \qquad (8)$$

where f_0 is the attempt frequency, k_B (J/K) the Boltzmann constant ΔE_0 the energy barrier separating the two stable states at zero field, H_0 (kA/m) the zero-temperature coercive field and T (K) the temperature. So, with decrease in temperature, the coercivity increases.

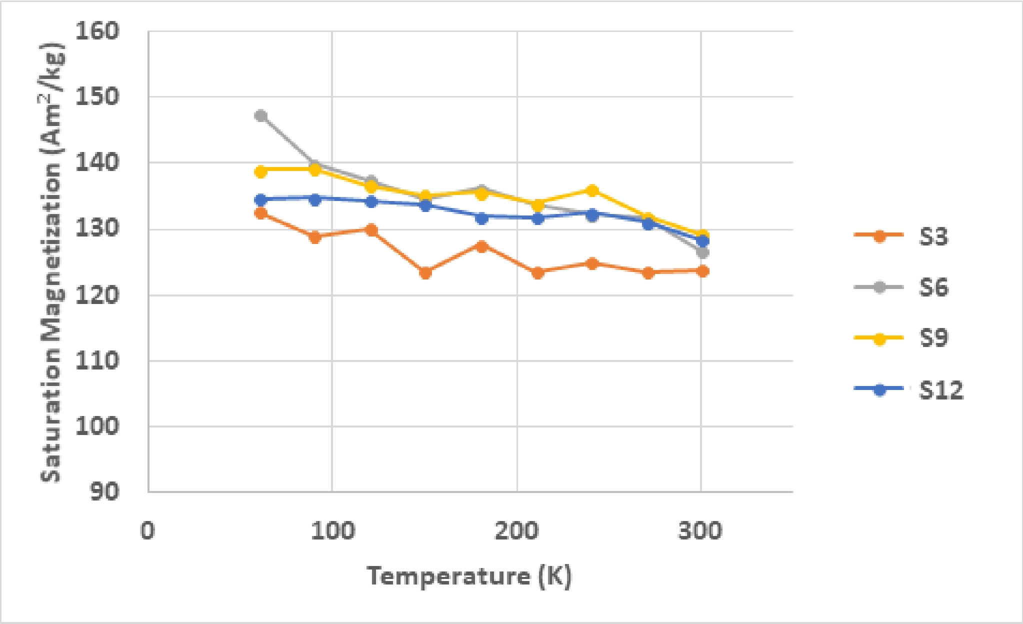

Figure 96. Saturation magnetization of all Ni-rich alloy from 60K-300K

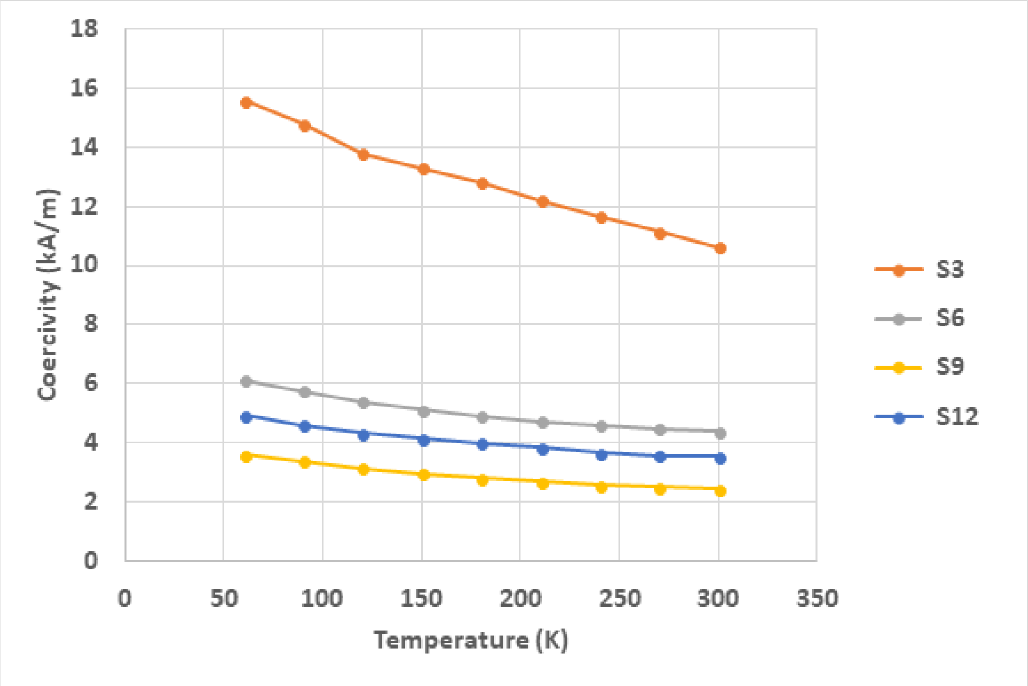

Figure 97. Coercivity of all Ni-rich alloy from 60K-300K

The XRD and *MvT* curves for S6, S9 and S12 are similar but from the *Ms* and *Hc* values from **Table 7,** S9 seems to be the best sample in Ni-rich alloy. So, Ni-rich S9 was heat treated from 300 K-840 K at every 90 K difference. From **Figure 98, 99 and 100,** at high temperature the M_S and H_C are going down. However, in as-annealed sample the M_S increases while H_C decreases with increase in temperature, as shown in **Figure 101.**

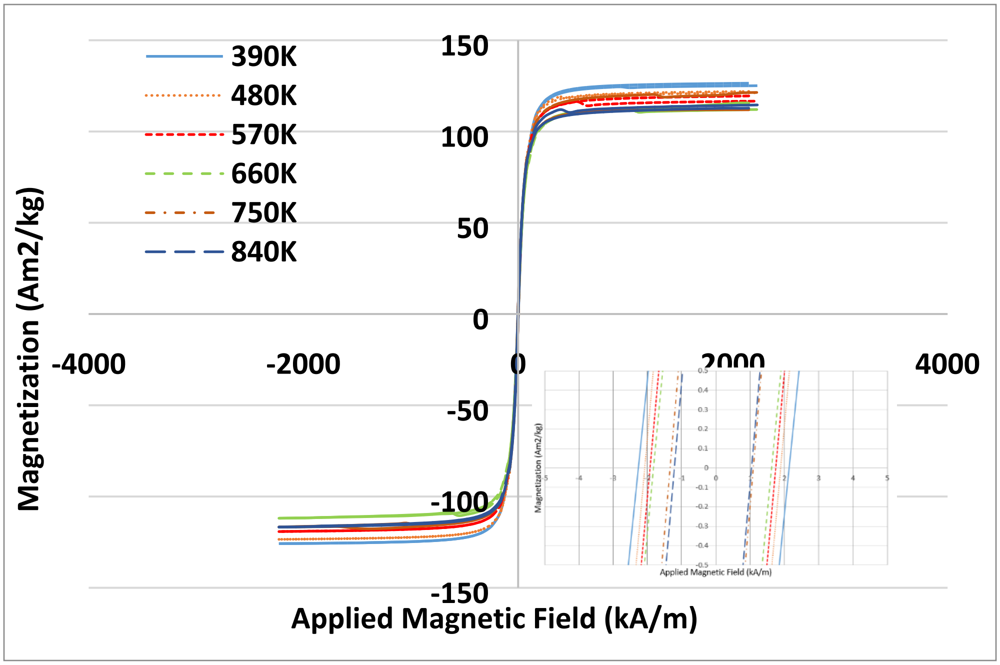

Figure 98. *M-H* curve of Ni-rich S9 sample measured at high temperature

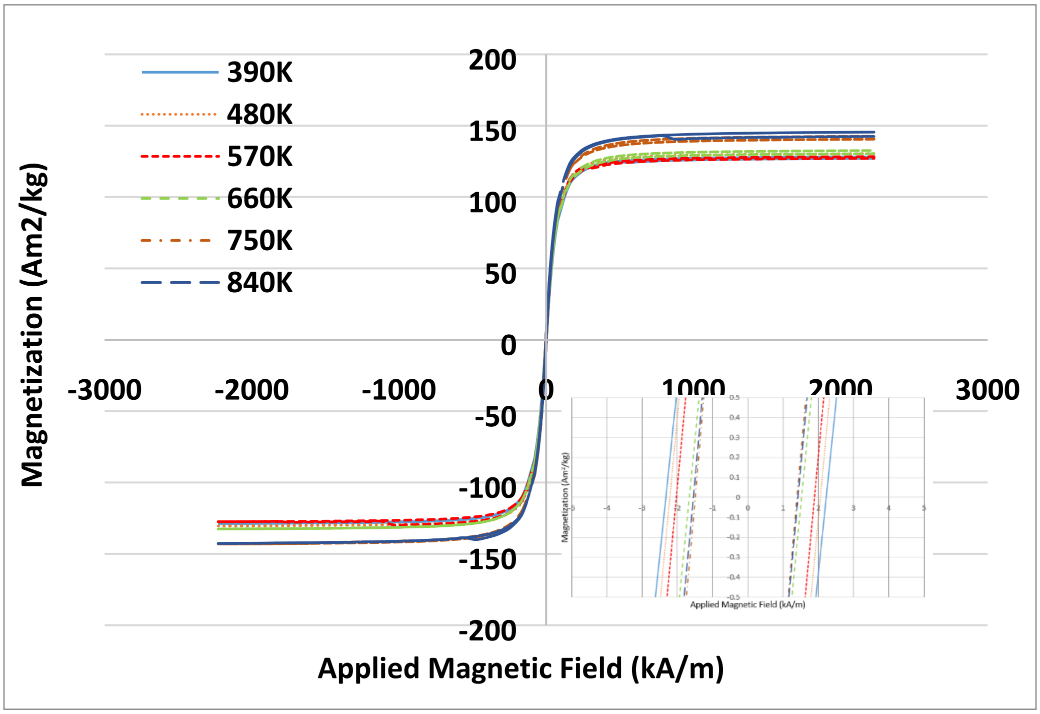

Figure 99. *M-H* curve of as-annealed Ni-rich S9 sample measured at 300 K

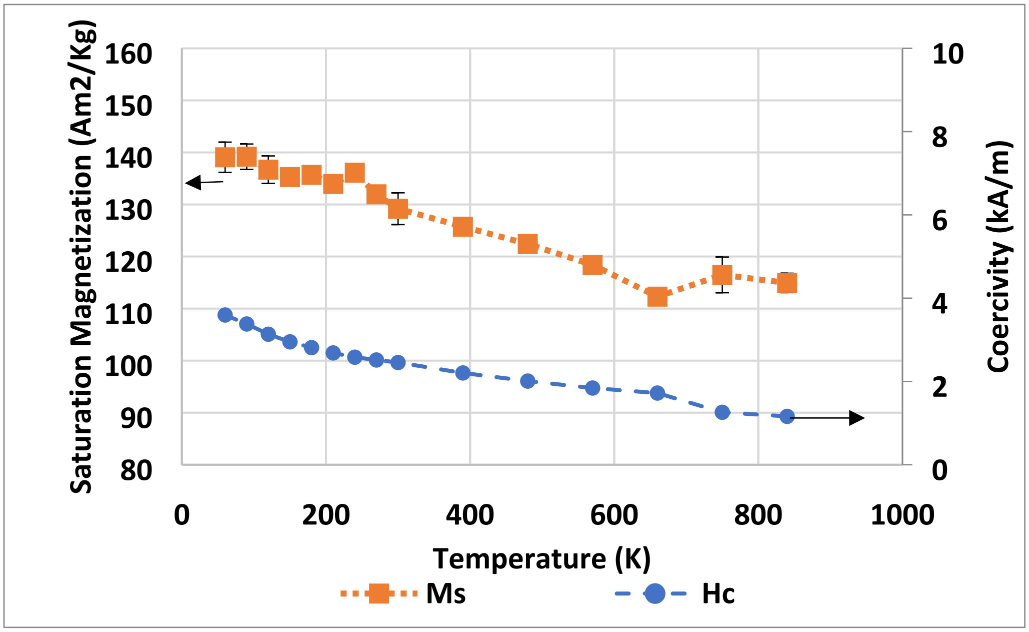

Figure 100. Change in saturation magnetization and coercivity of Ni-rich S9 sample with increasing temperature

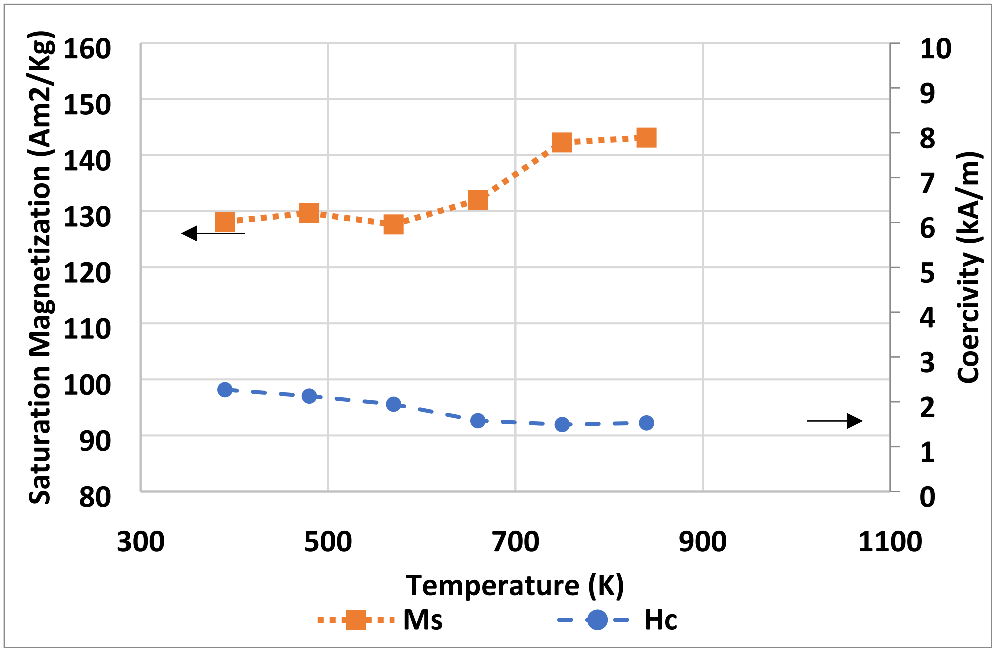

Figure 101. Saturation magnetization and coercivity vs temperature of as annealed Ni-rich S9 sample

As shown in **Figure 102,** we see a Fe peak in 750 K heat treated sample and this match with the above *MvT* curve, in **Figure 91,** in which the magnetization starts going up after ≈660 K.

Since the amount of Ni is more in the alloy, the Fe peak in XRD is relatively small. It gets higher in Co-rich alloy and goes beyond the HEA peak in Fe-rich alloy.

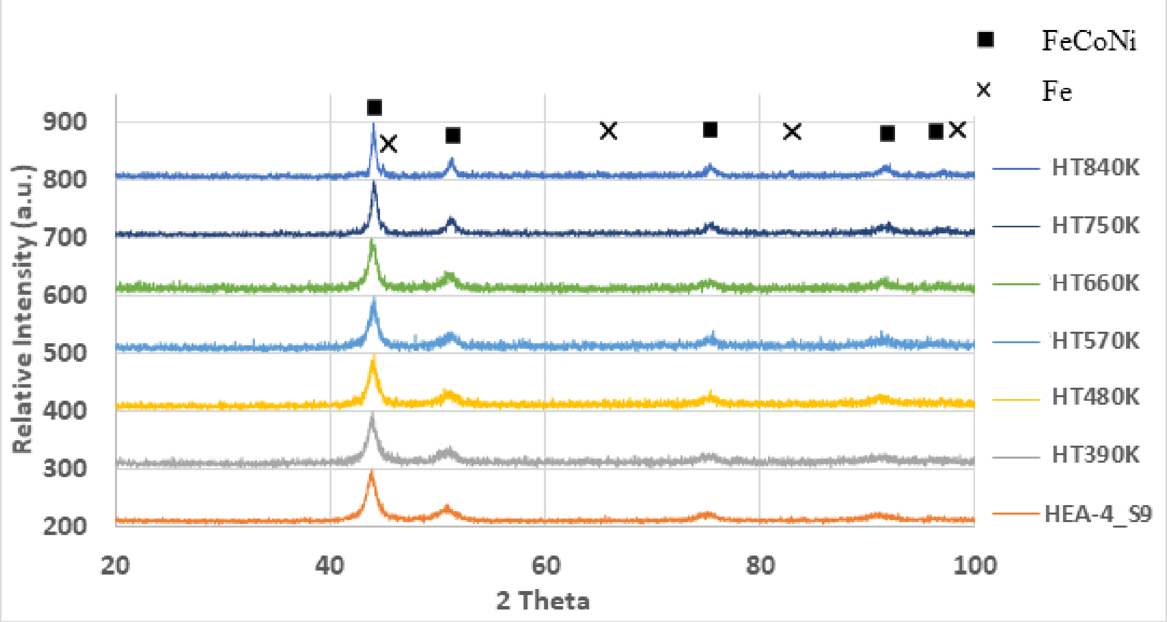

Figure 102. Heat treatment of Ni-rich S9 sample

As shown in **Figure 103 and 104,** the particle size increases and get maximum at 660 K due to release of strain during heat treatment. After that the Fe atoms comes out of HEA lattice and the particle size decreases.

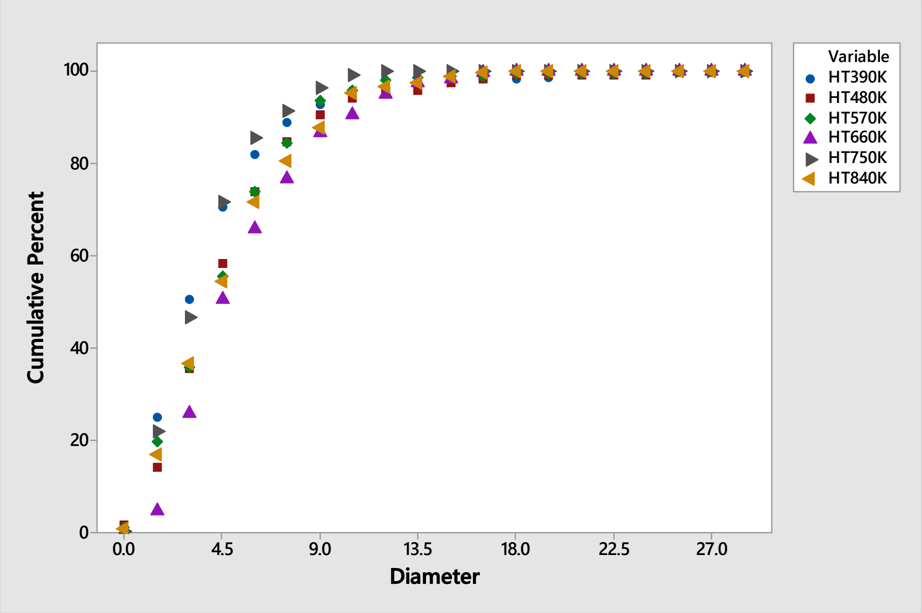

Figure 103. Cumulative particle size of as-annealed Ni-rich S9 sample

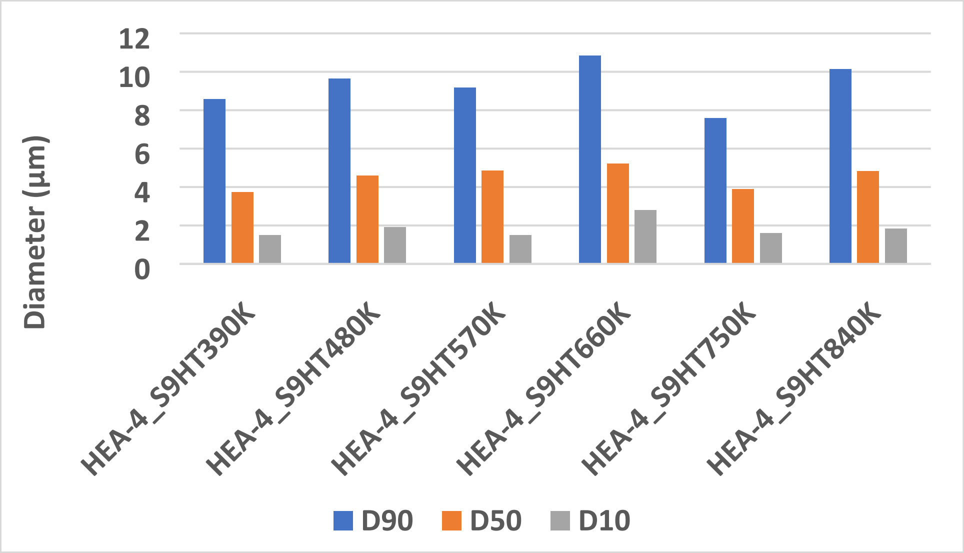

Figure 104. *D90*, *D50*, and *D10* particle size diameters of as-annealed Ni-rich S9 samples

After testing Ni-rich alloys, Fe-rich were heat treated at a temperature ≈850 K to determine the change in properties. S3 was not considered for heat treatment for Fe-rich alloys too, since the powders were not completely alloyed. The magnetization vs. temperature curve was plotted for all the three samples at 80 kA/m (1 kOe). As shown in **Figure 105, 106 and 107**, the magnetization decreases with increase in temperature, but at ≈650 K the magnetization starts rising. This increase in magnetization is because of ferromagnetic behavior of Fe which evaded the HEA lattice due to thermal vibrations. Between 750 K to 800 K, the thermal energy starts dominating ferromagnetic effect of Fe and the magnetization starts going down.

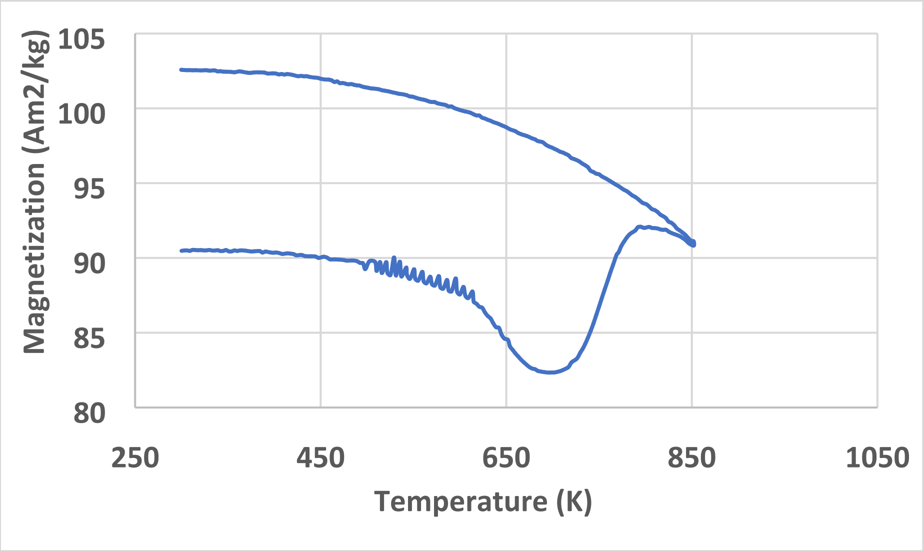

Figure 105. Magnetization vs temperature curve of Fe-rich S6 sample

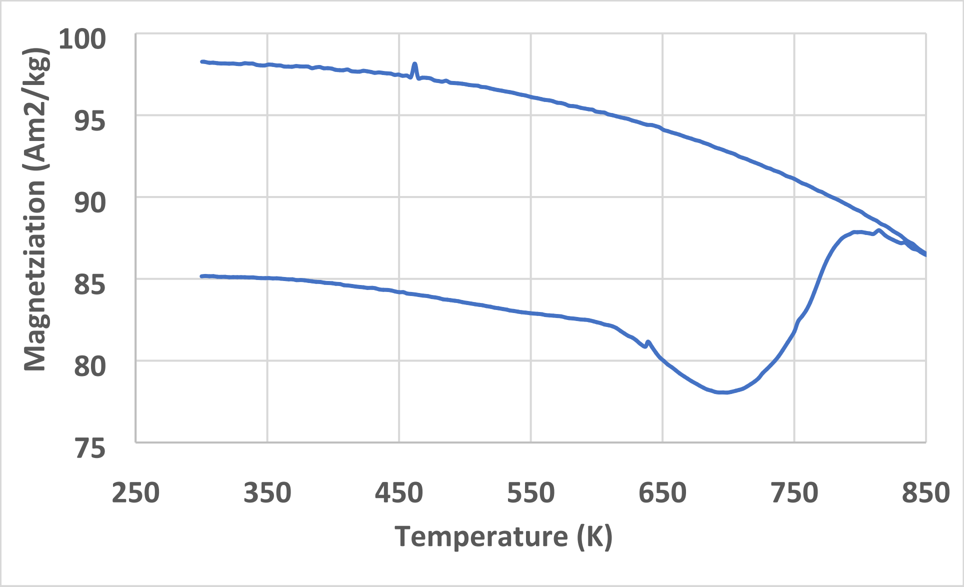

Figure 106. Magnetization vs temperature curve of Fe-rich S9 sample

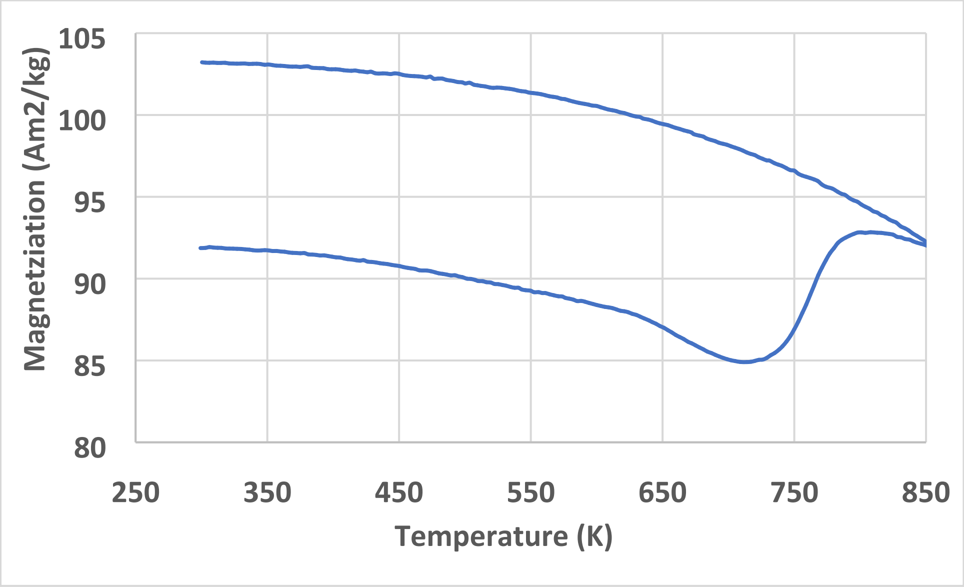

Figure 107. Magnetization vs temperature curve of Fe-rich S12 sample

The XRD for all the heat-treated samples were plotted. The Fe peaks along with HEA peaks in the XRD confirmed that the Fe atoms left HEA lattice at ≈650K, as shown in **Figure 108, 109 and 110.**

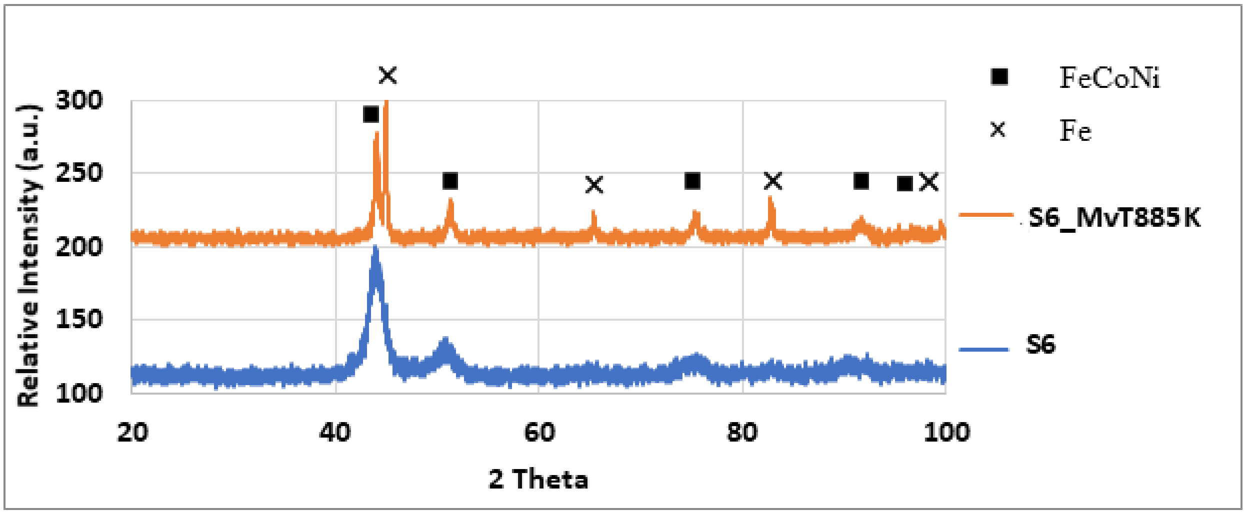

Figure 108. Comparison of XRD of heat treated Fe-rich S6 sample vs as-prepared sample

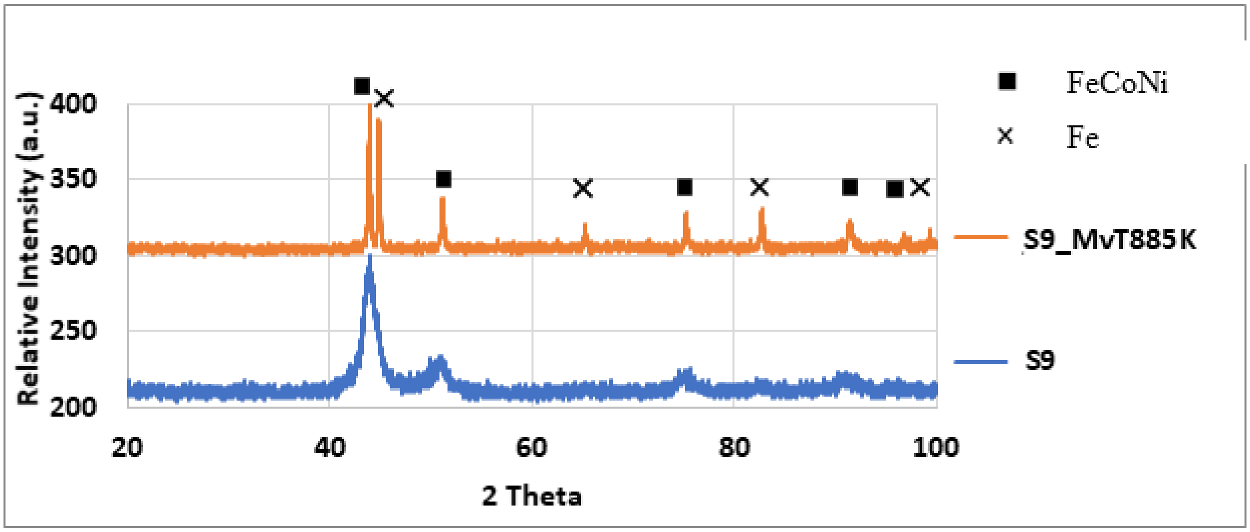

Figure 109. Comparison of XRD of heat treated Fe-rich S9 sample vs as-prepared sample

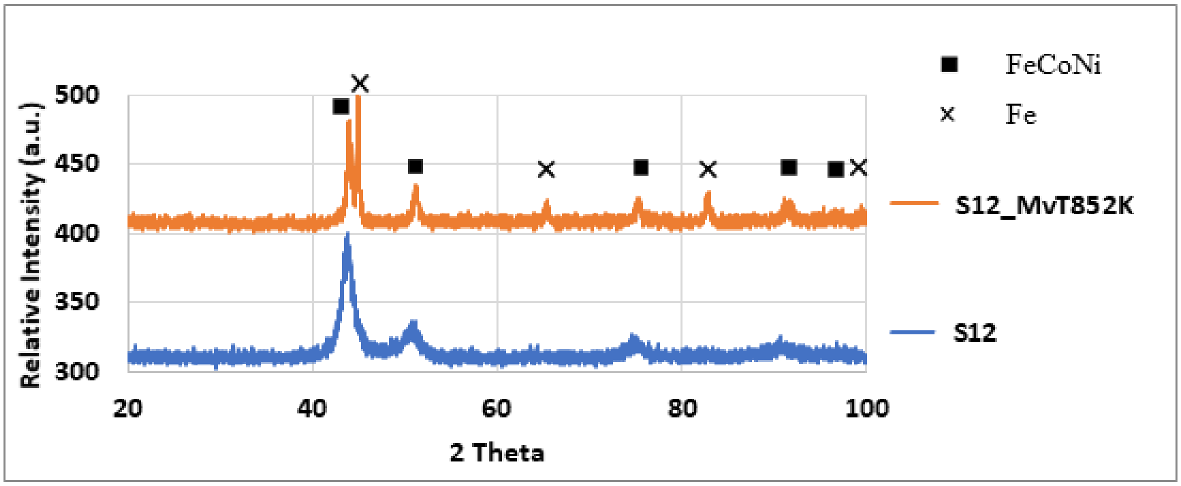

Figure 110. Comparison of XRD of heat treated Fe-rich S12 sample vs as-prepared sample

Saturation magnetization and coercivity follows the same trend as Ni-rich alloy. S12-O stands for the Fe-rich S12 sample made in oxygen environment since Fe-rich S12 is best sample of all the alloys, as shown in **Figure 111 and 112**. This will be explained in coming sections.

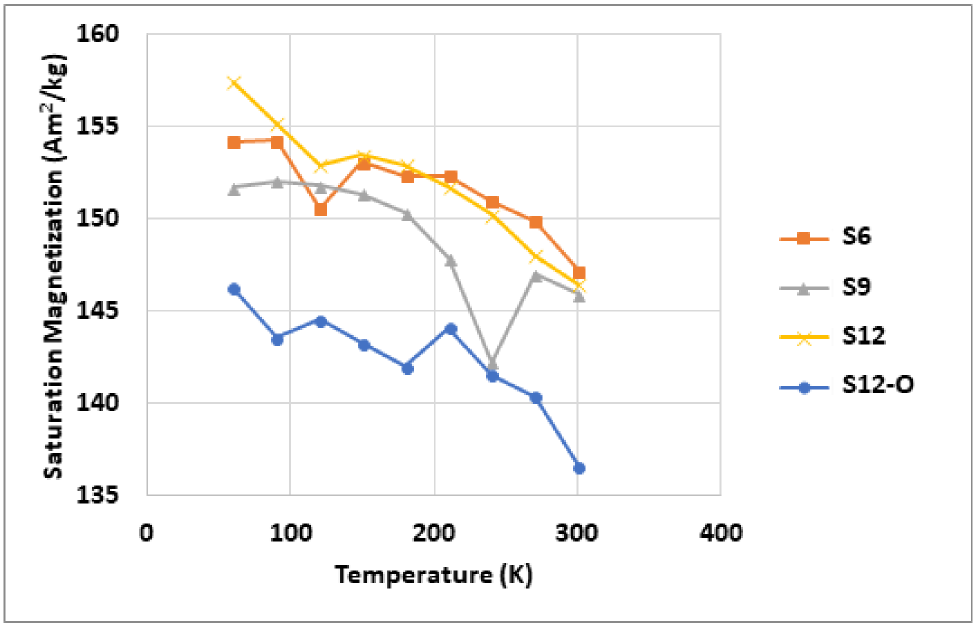

Figure 111. Saturation magnetization of all Fe-rich alloy from 60 K-300 K

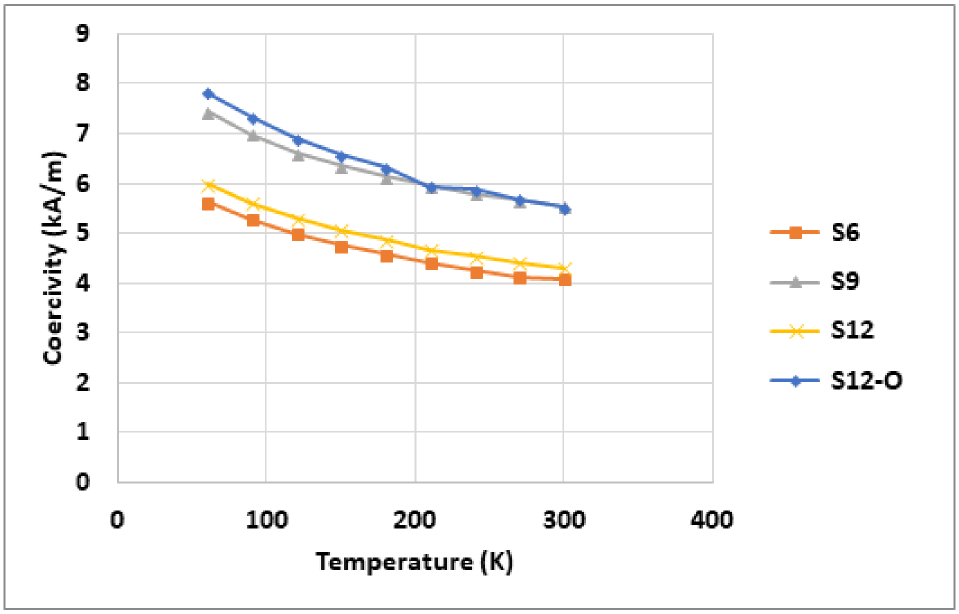

Figure 112. Coercivity of all Fe-rich alloy from 60 K-300 K

The XRD and *MvT* curves for S6, S9 and S12 are similar but from the *Ms* and *Hc* values from **Table 7,** S12 seems to be the best sample in Fe-rich alloy. So, Fe-rich S12 was heat treated from 300 K-840 K at every 90 K difference. From **Figure 113, 114 and 115,** at high temperature the M_S and H_C are going down. However, in as-annealed sample the M_S increases while H_C decreases with increase in temperature, as shown in **Figure 116.**

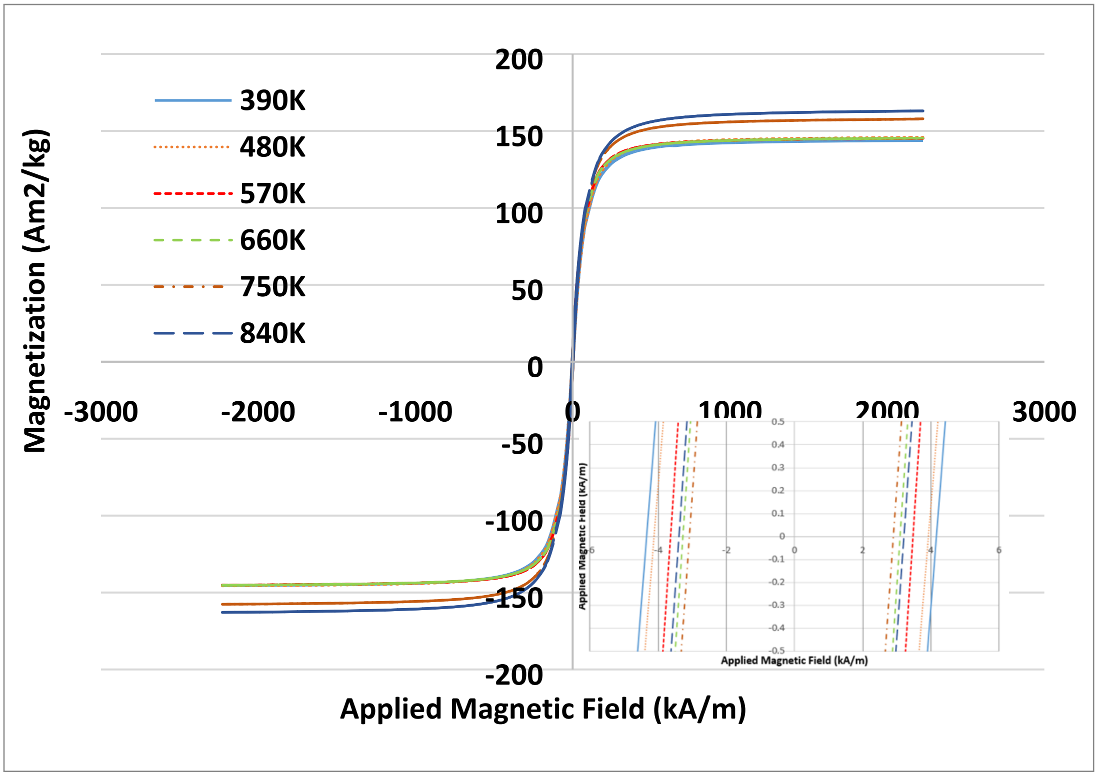

Figure 113. *M-H* curve of Fe-rich S12 sample measured at high temperature

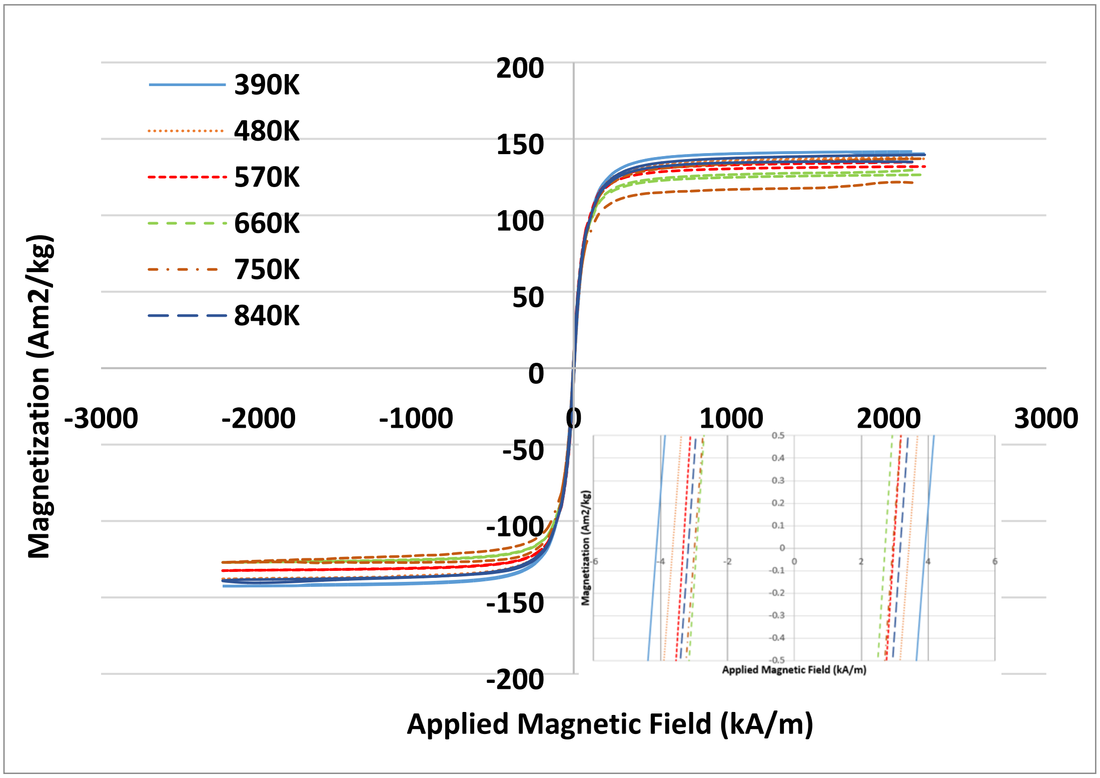

Figure 114. *M-H* curve of as-annealed Fe-rich S12 sample measured at high temperature

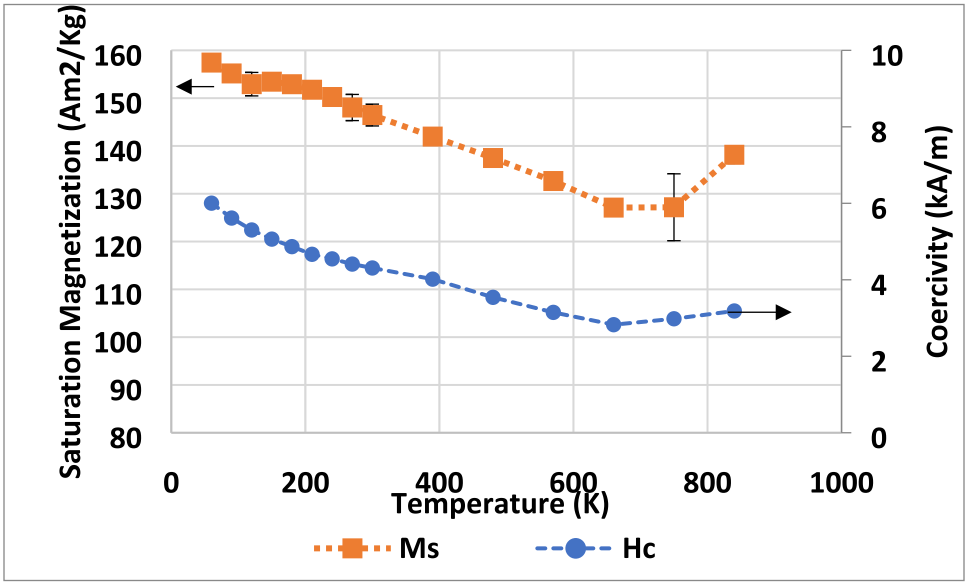

Figure 115. Change in saturation magnetization and coercivity of Fe-rich S12 sample with increasing temperature

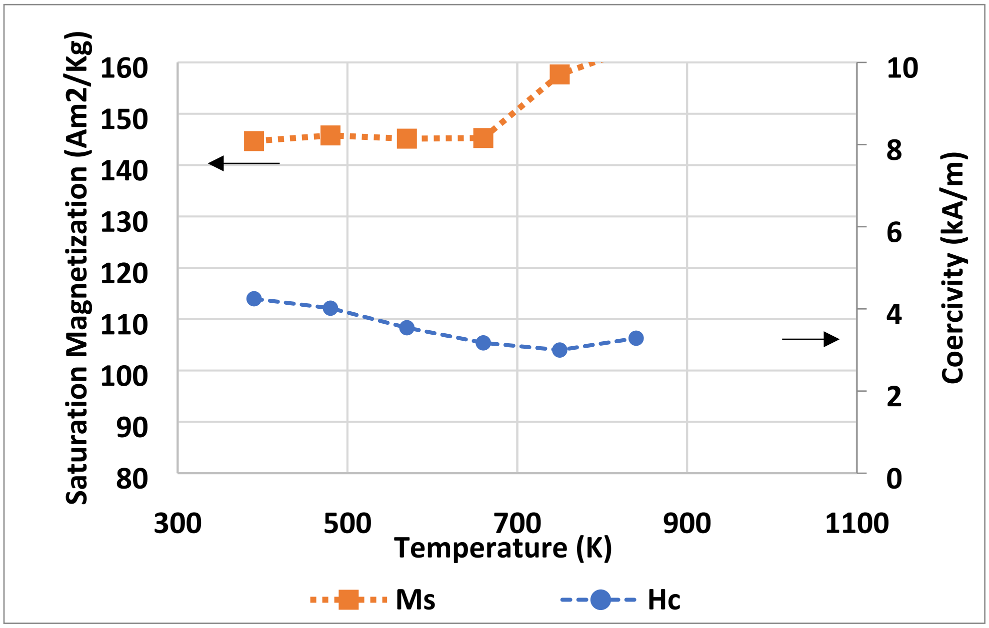

Figure 116. Saturation magnetization and coercivity vs temperature of as annealed Fe-rich S12 sample

As shown in **Figure 117,** we see a Fe peak in 750 K heat treated sample and this match with the above *MvT* curve, in **Figure 107,** in which the magnetization starts going up after ≈660 K. As expected, since the Fe content is more in this alloy, the Fe peak is higher than the HEA peak.

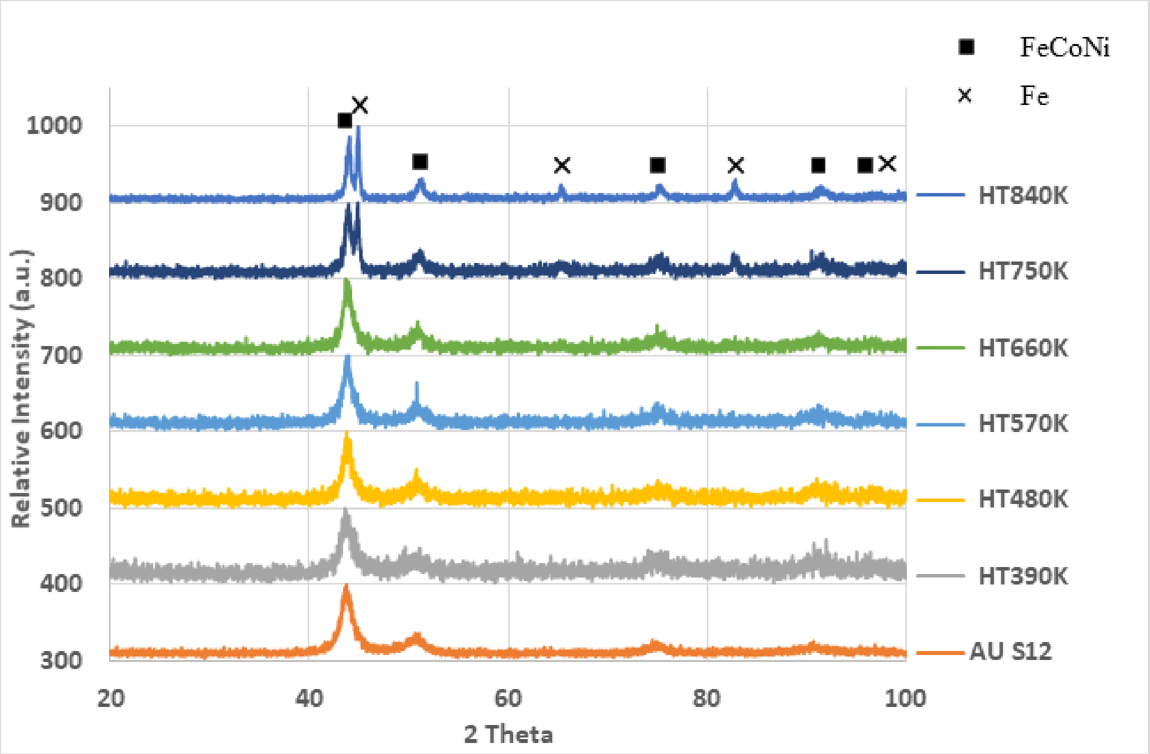

Figure 117. XRD of heat treated Fe-rich S12 sample

As shown in **Figure 118 and 119,** the particle size decreases and get minimum at 570 K. After that the Fe atoms comes out of HEA lattice and the particle size increases.

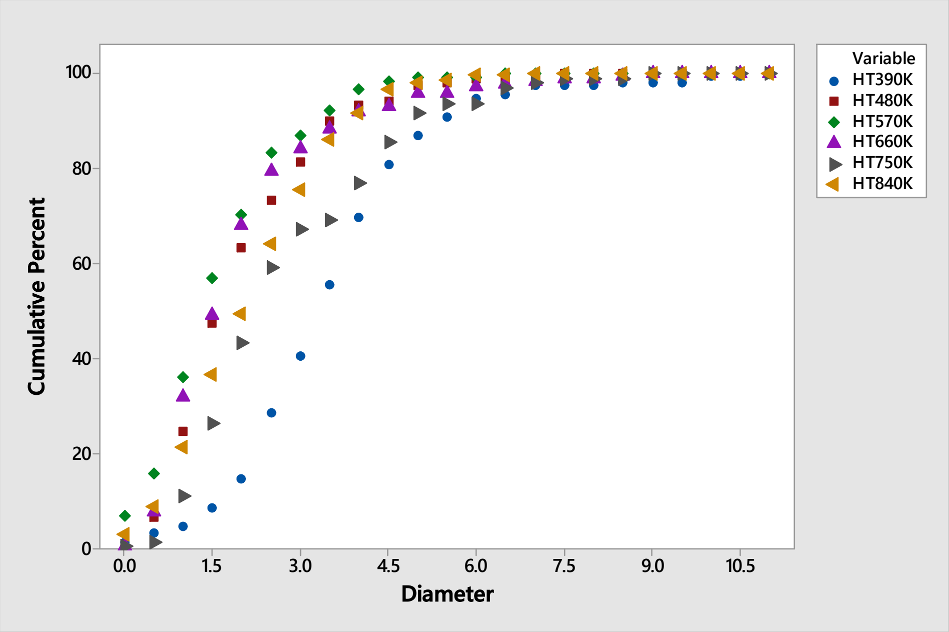

Figure 118. Cumulative particle size of as-annealed Fe-rich S12 sample

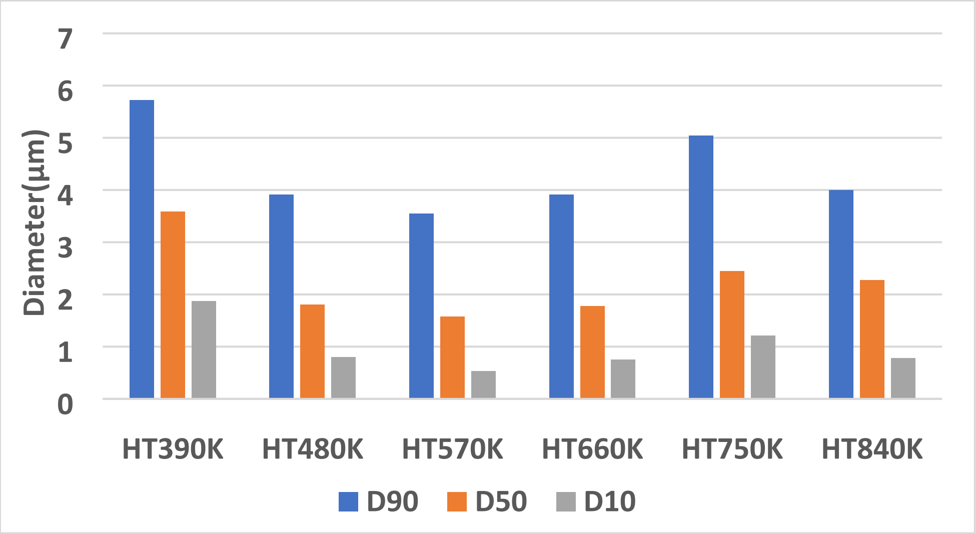

Figure 119. ***D90*, *D50*, and *D10* particle size diameters of as-annealed Fe-rich S12 samples**

The Fe-rich S12 sample prepared in oxygen was also heat treated from 300 K-840 K at every 90 K difference. From **Figure 120, 121 and 122,** at high temperature the M_S and H_C are going down. However, in as-annealed sample the M_S increases while H_C decreases with increase in temperature, as shown in **Figure 123.** The behavior of HEA prepared in argon environment and oxygen environment is similar, with a slight decrease in value of M_S and H_C.

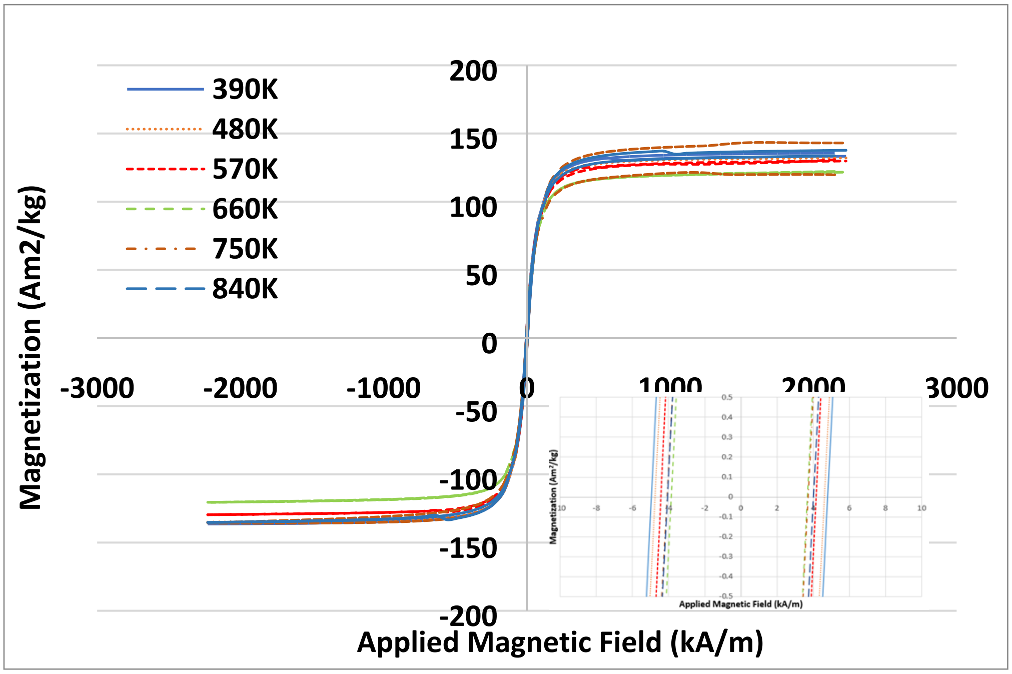

Figure 120. ***M-H*** **curve of Fe-rich S12 sample prepared in oxygen measured at high temperature**

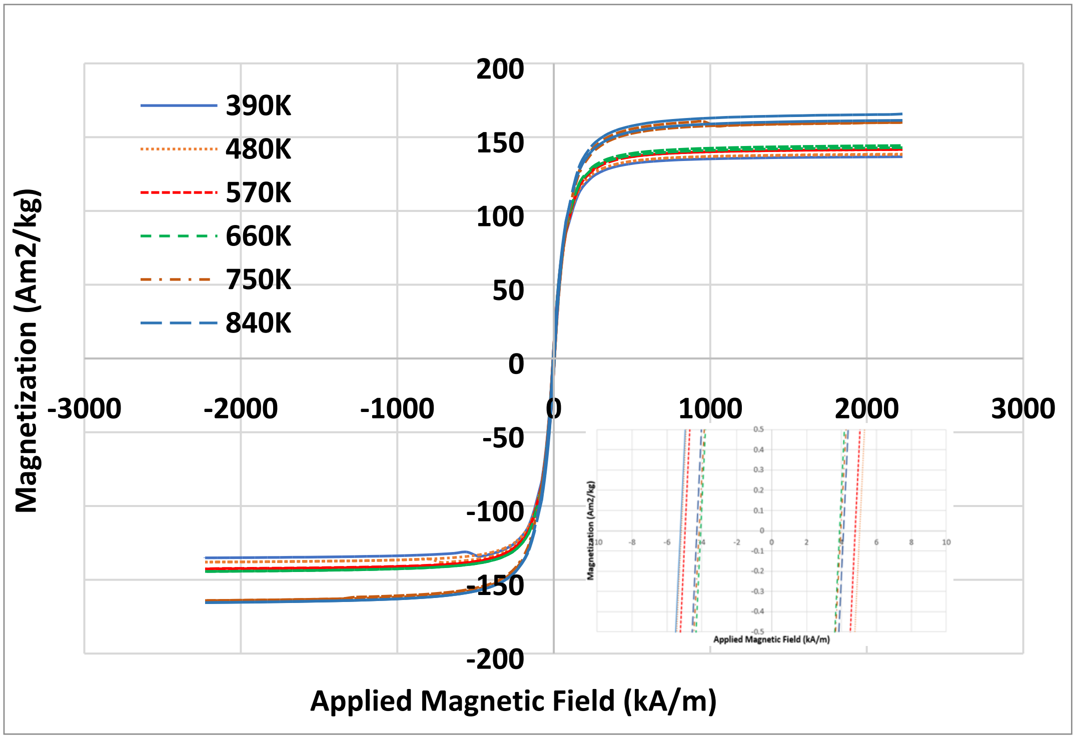

Figure 121. *M-H* curve of as-annealed Fe-rich S12 sample prepared in oxygen measured at 300K

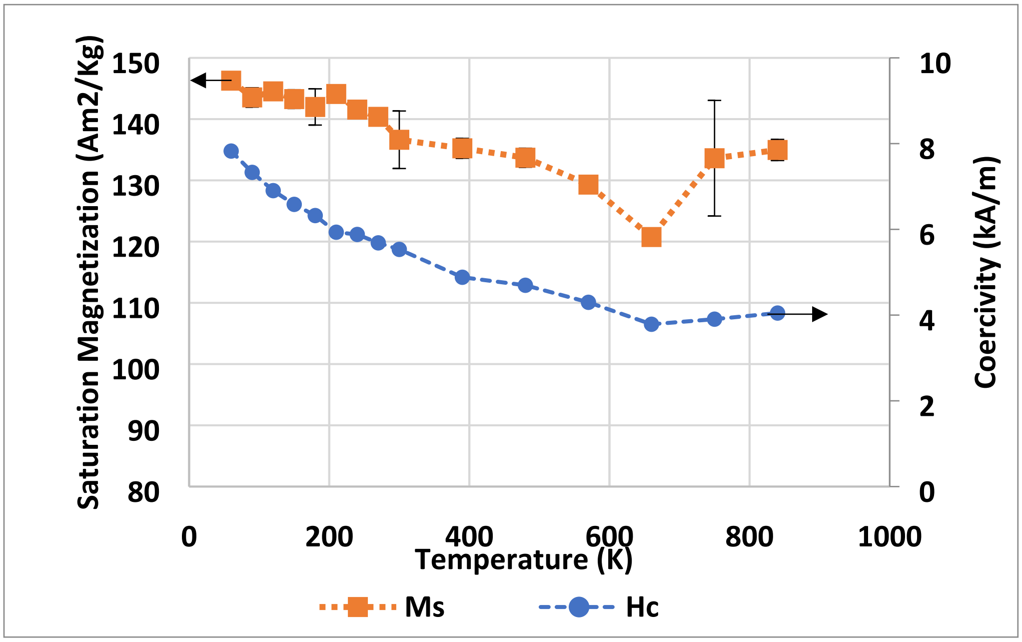

Figure 122. Change in saturation magnetization and coercivity of Fe-rich S12 sample prepared in oxygen with increasing temperature

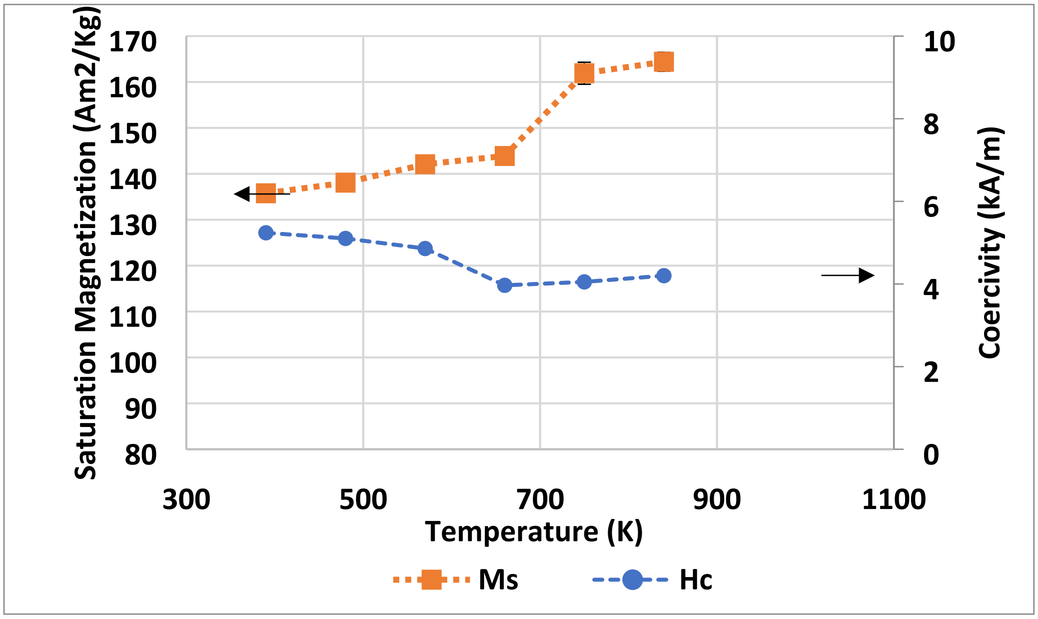

Figure 123. Saturation magnetization and coercivity vs temperature of as annealed Fe -rich S12 sample prepared in oxygen

In oxygen sample also, the Fe peak comes up after 660K, as shown in **Figure 124.** This explains the rise of magnetization with temperature in *MvT* curve in **Figure 107** of Fe-rich S12 sample prepared in oxygen environment. Since the Fe content is more in this alloy, the Fe peak is higher than the HEA peak.

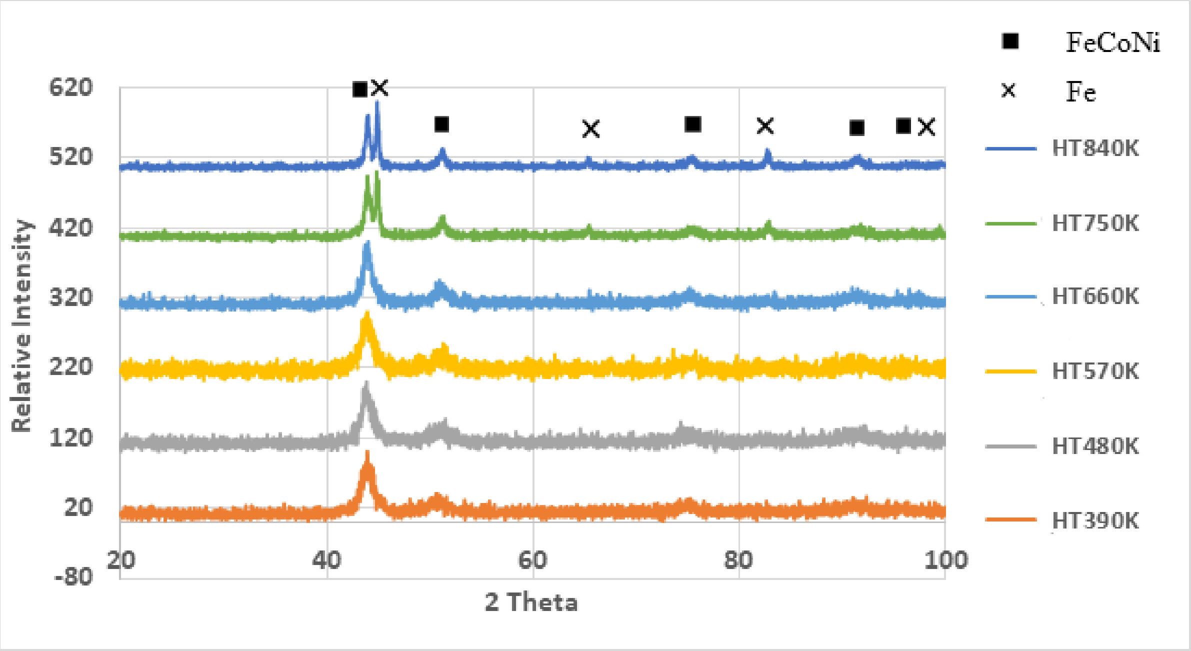

Figure 124. XRD of heat treated Fe-rich S12 sample prepared in oxygen

As shown in **Figure 125 and 126,** the particle size is almost consistent throughout the heat treatment.

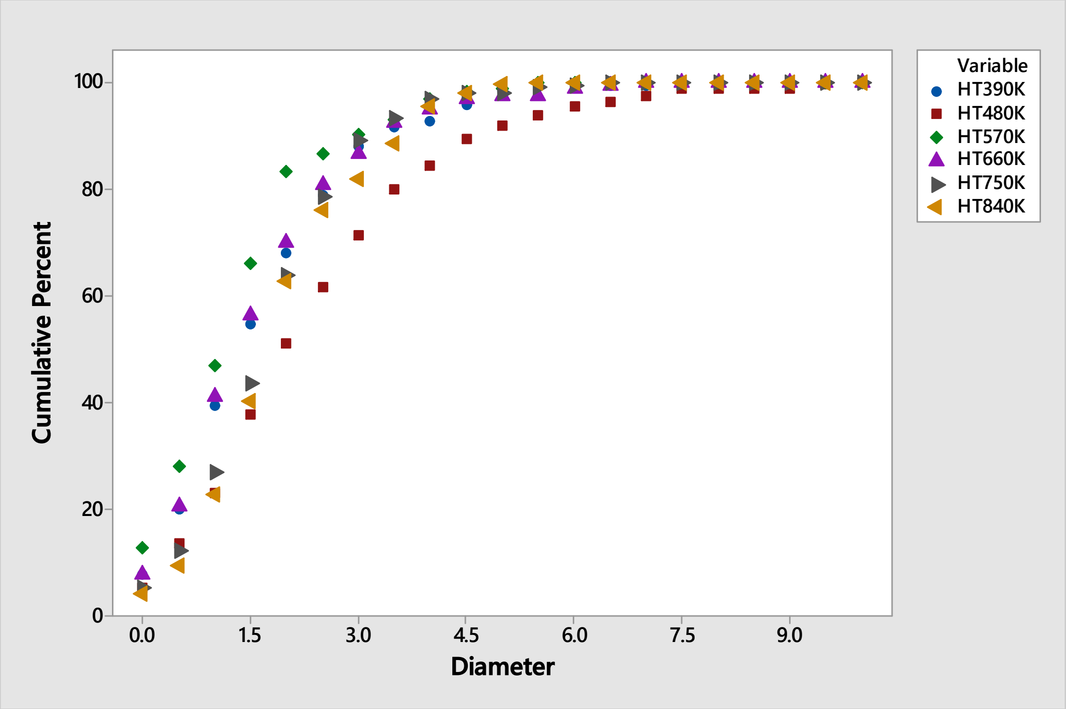

Figure 125. Cumulative particle size of as-annealed Fe-rich S12 sample prepared in oxygen

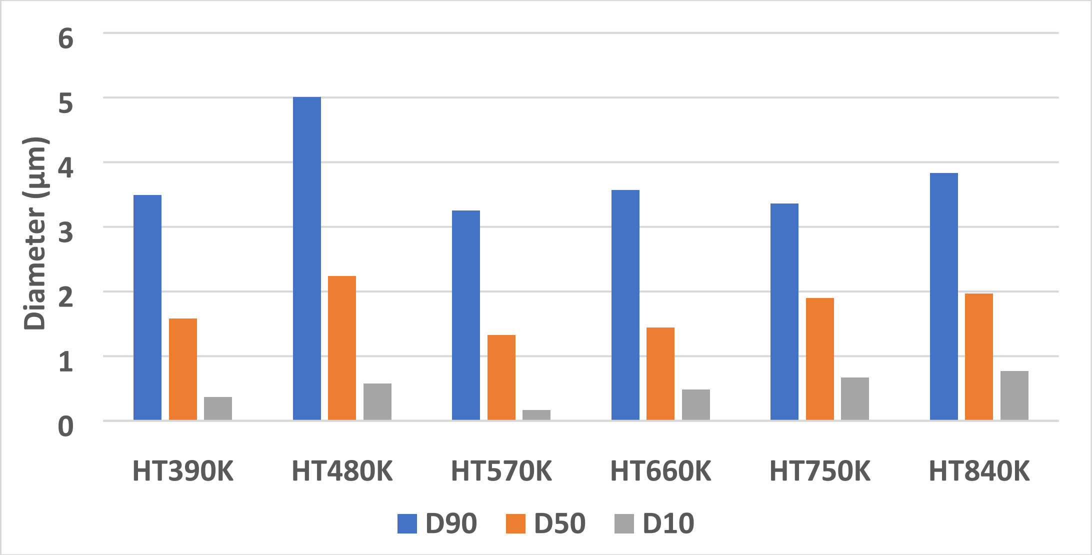

Figure 126. *D90*, *D50*, and *D10* particle size diameters of as-annealed Fe-rich S12-oxygen samples

As the Ni-rich and Fe-rich were heat treated, S6, S9 and S12 of Co-rich alloys were also heat treated at ≈850 K. The magnetization was measured at 80 kA/m (1 kOe) for a temperature range of 300 K to 852K. As shown in **Figure 127, 128 and 129,** the magnetization decreases with increase in temperature up to ≈650 K. After that due to thermal vibrations Fe comes out of the Ni lattice and because of its ferromagnetic behavior, magnetization starts rising. At ≈800 K, the thermal vibration dominates the ferromagnetic behavior and the magnetization again drops down.

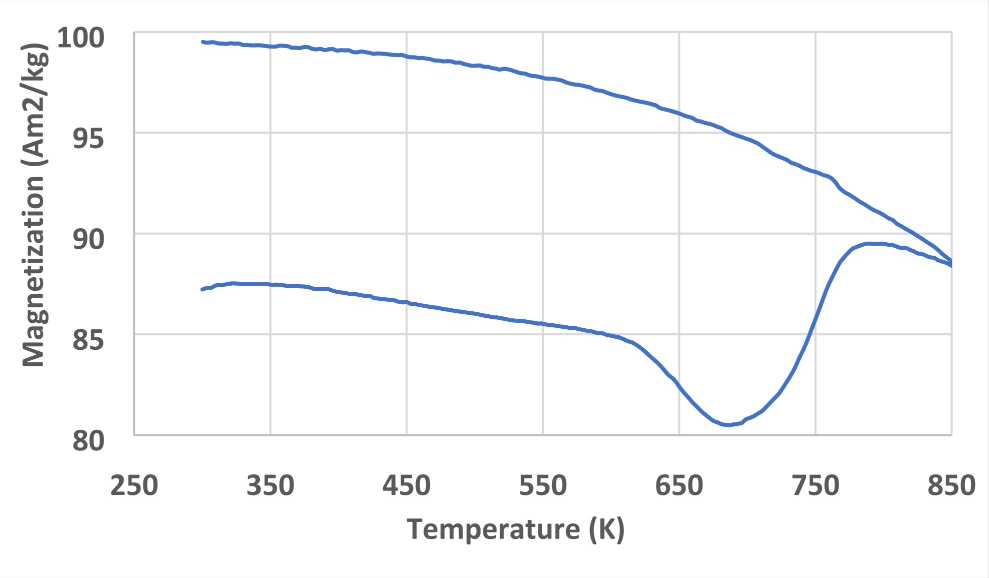

Figure 127. Magnetization vs temperature curve of Co-rich S6 sample

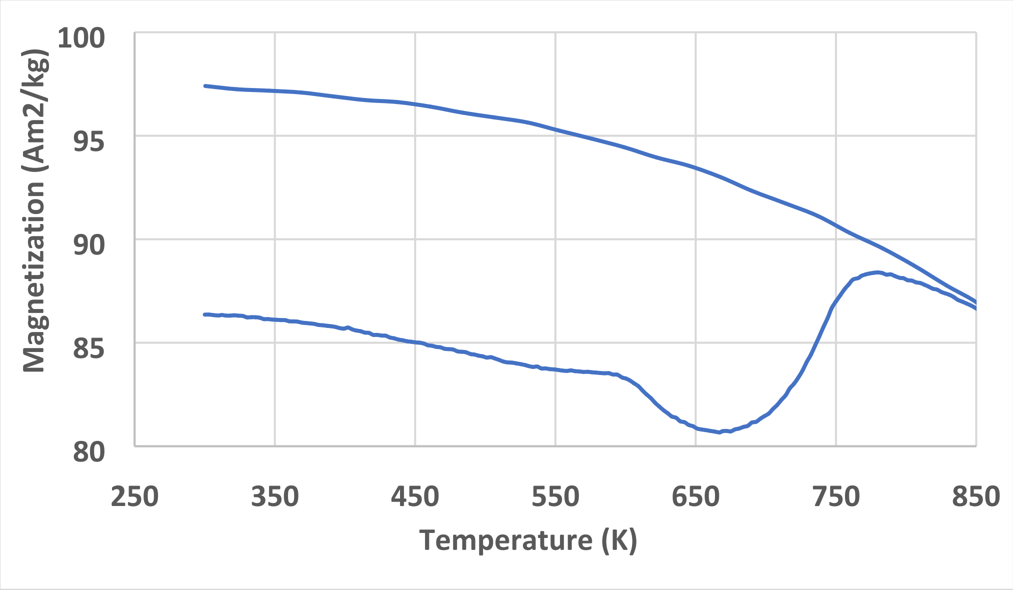

Figure 128. Magnetization vs temperature curve of Co-rich S9 sample

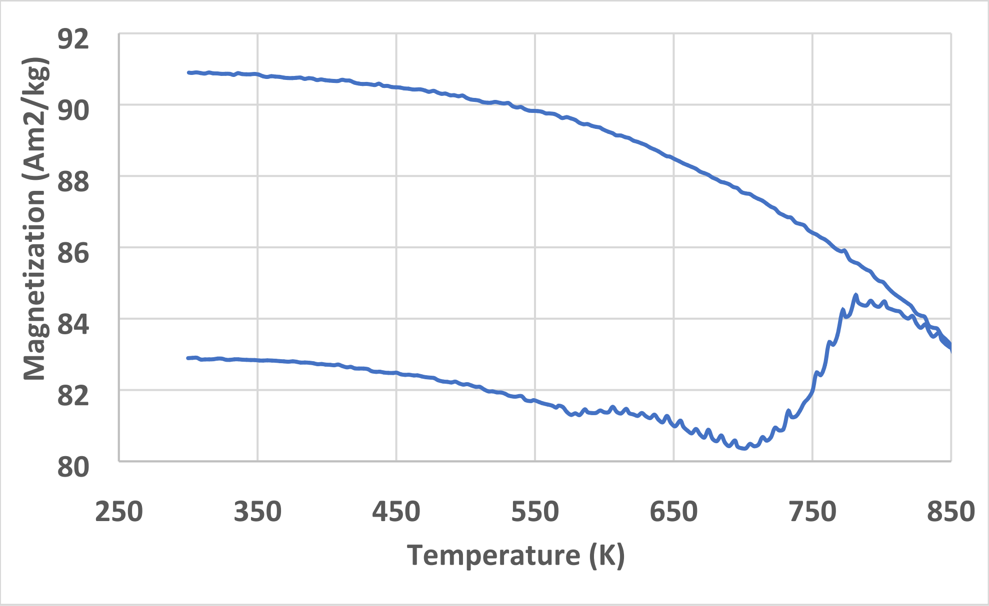

Figure 129. Magnetization vs temperature curve of Co-rich S12 sample

Figure 130, 131 and 132 shows the XRD of heat treated sample and as-milled sample for S6, S9 and S12 samples. The Fe peak in heat treated XRD proves that the change in *MvT* curve is due to Fe coming out at ≈650 K.

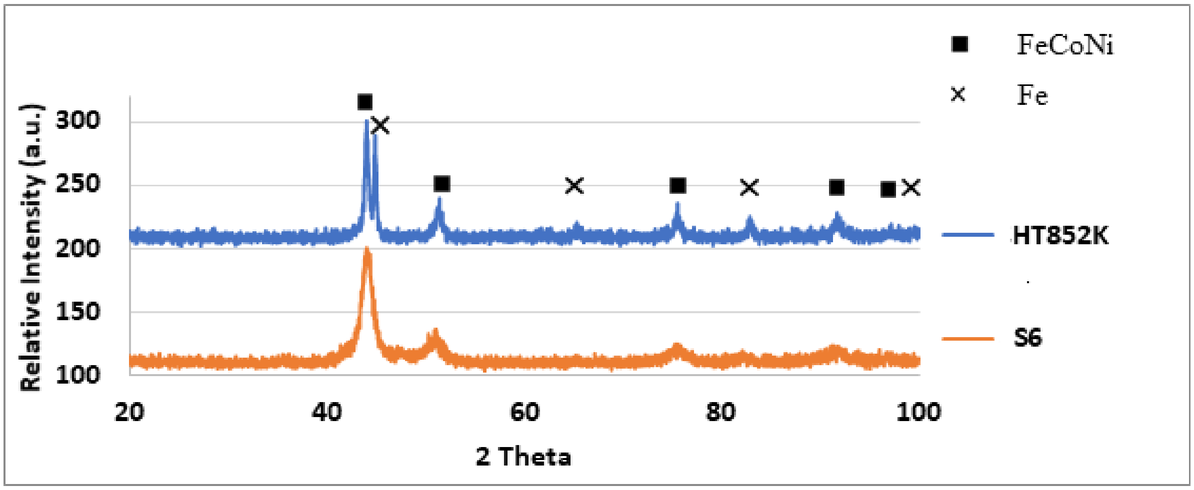

Figure 130. Comparison of XRD of heat treated Co-rich S6 sample vs as-prepared sample

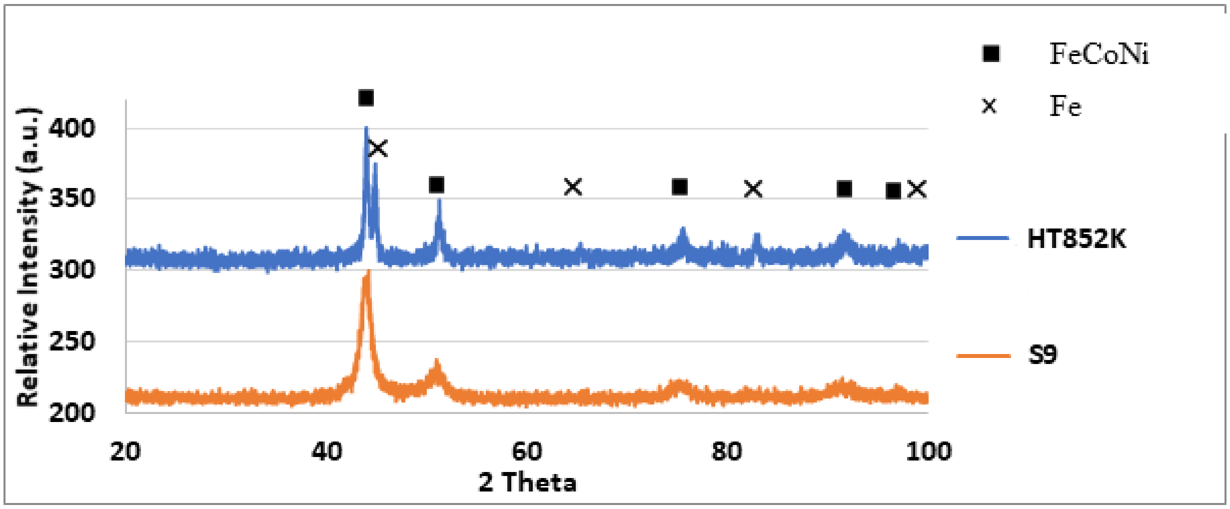

Figure 131. Comparison of XRD of heat treated Co-rich S9 sample vs as-prepared sample

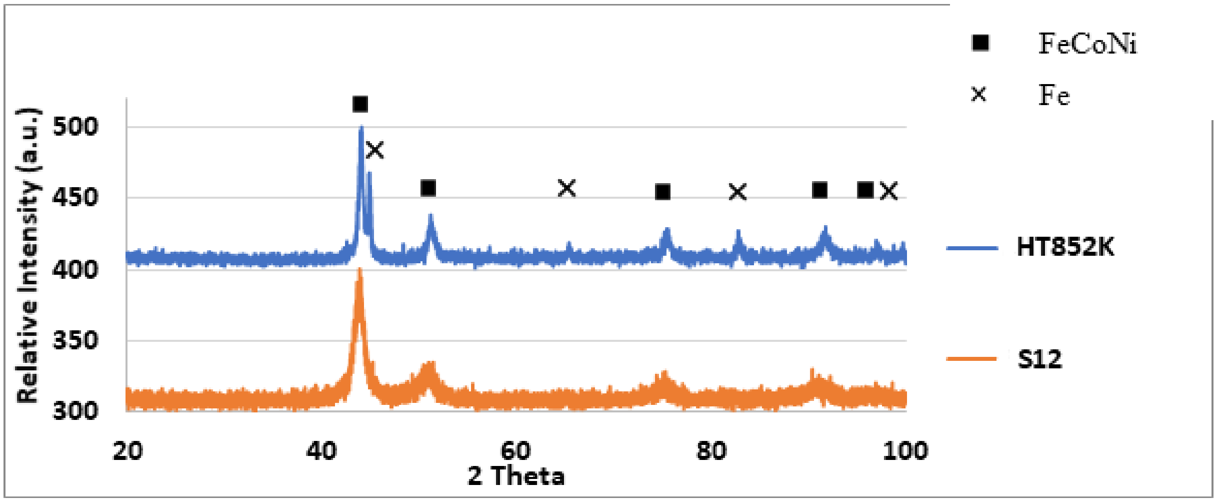

Figure 132.Comparison of XRD of heat treated Co-rich S12 sample vs as-prepared sample

The saturation magnetization and coercivity follows the same trend for all the samples of Ni-rich, Fe-rich and Co-rich, as shown in **Figure 133 and 134.**

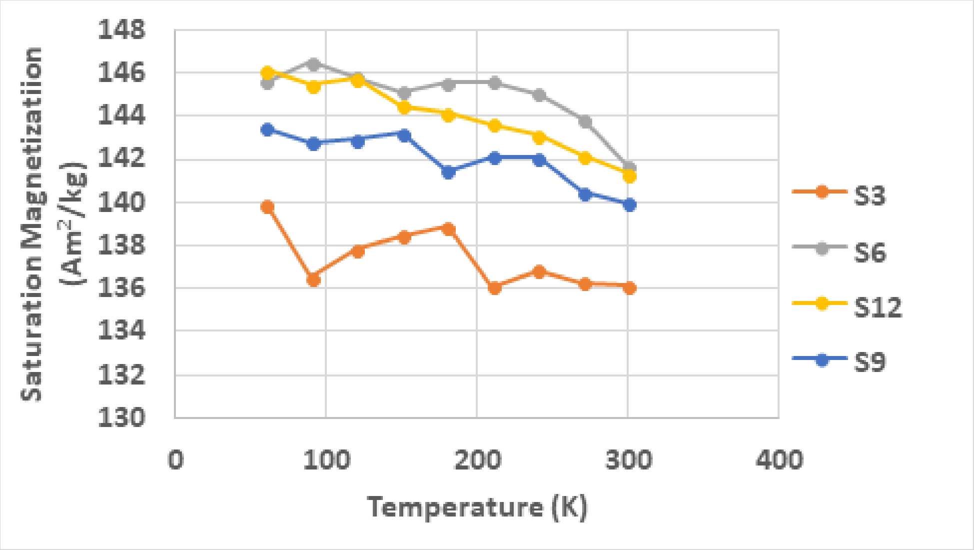

Figure 133. Saturation magnetization of all Co-rich alloy from 60 K-300 K

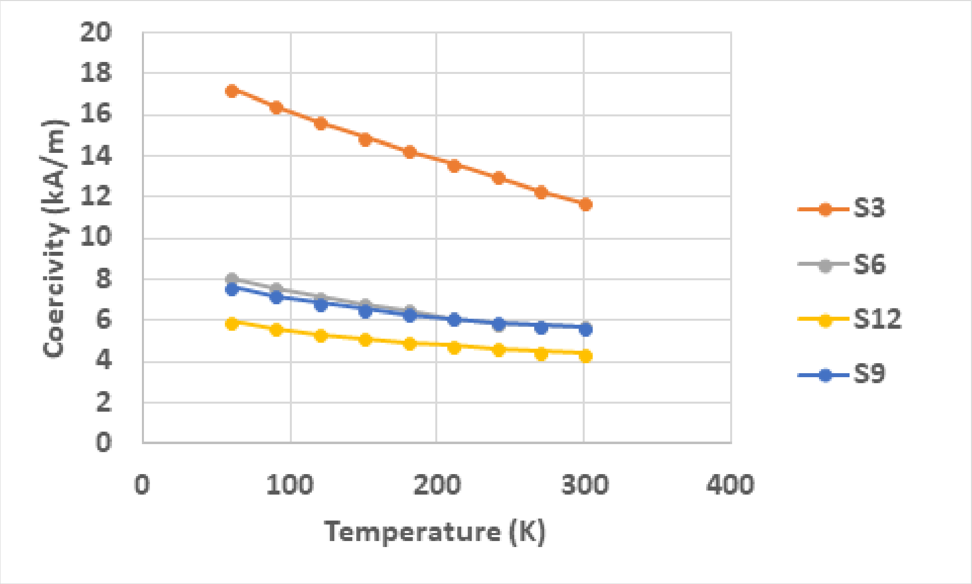

Figure 134. Coercivity of all Co-rich alloy from 60 K-300 K

To figure out the best sample of Fe-rich sample, we need to check the value of *Ms* and *Hc* since the XRD and *MvT* results for all the samples are similar. Thus, from **Table 7**, S12 seems to be the best sample for Co-rich alloy. The S12 sample of Co-rich alloy was heat treated from 300 K-840 K at every 90 K temperature difference. With increase in temperature, *Ms* and *Hc* decreases as shown in **Figure 135, 136, and 137.** However, in as-annealed sample the M_S increases while H_C decreases with increase in temperature, as shown in **Figure 138.**

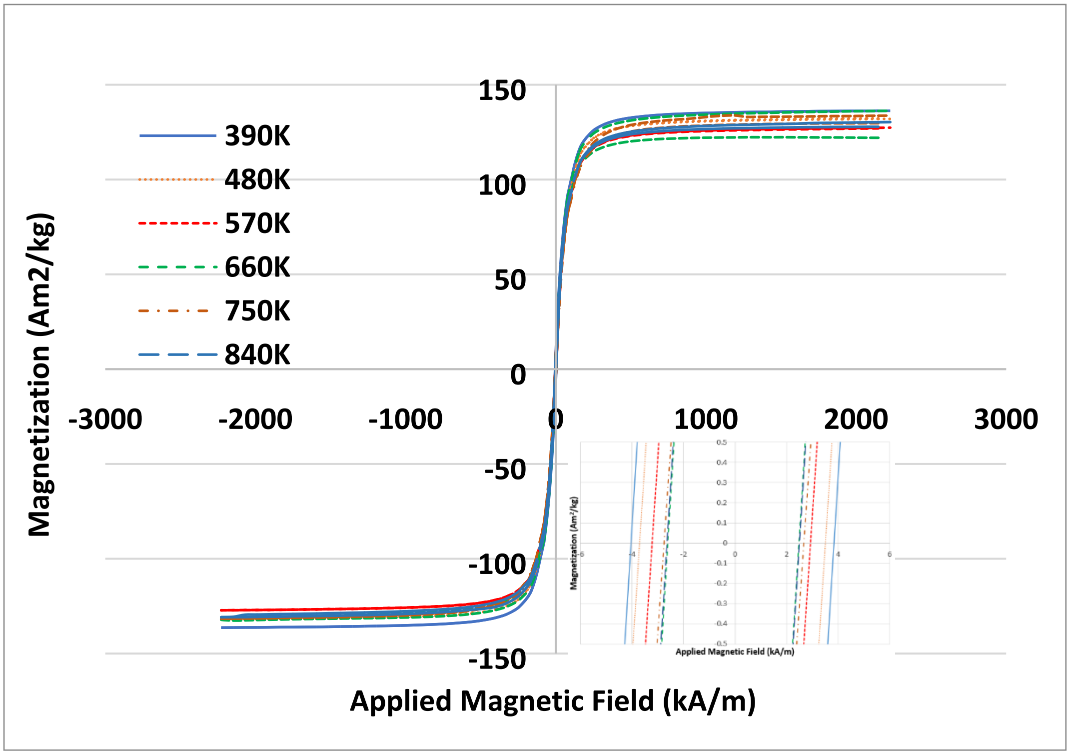

Figure 135. *M-H* curve of Co-rich S12 sample measured at high temperature

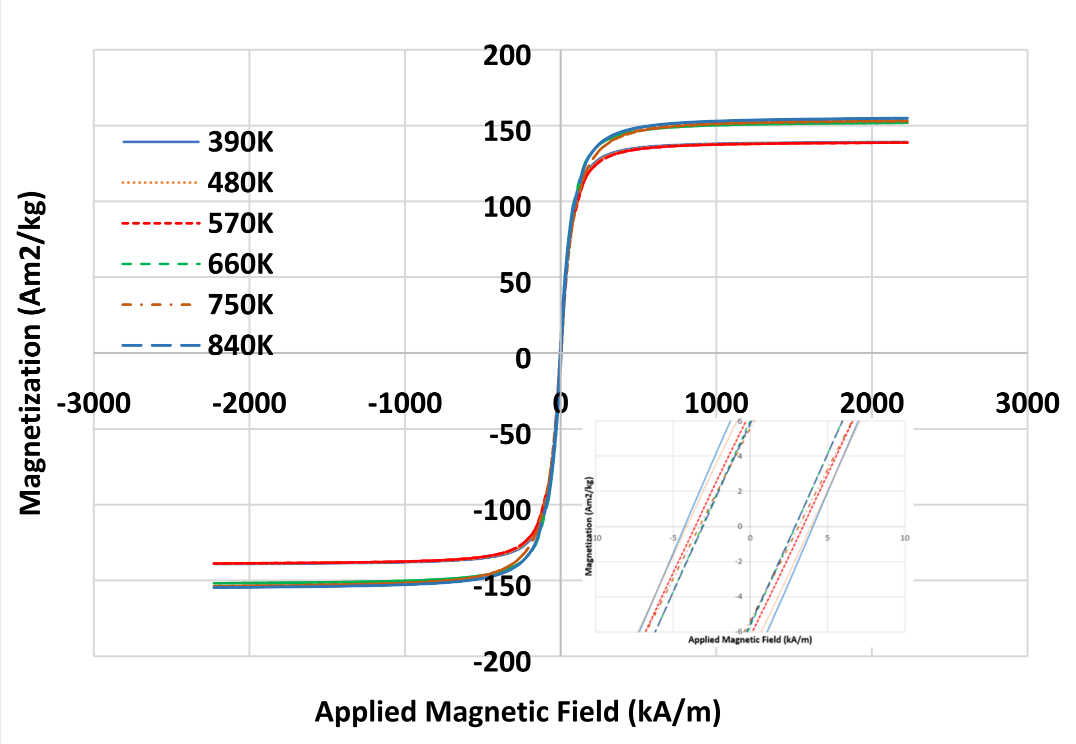

Figure 136. *M-H* curve of as-annealed Co-rich S12 sample measured at 300K

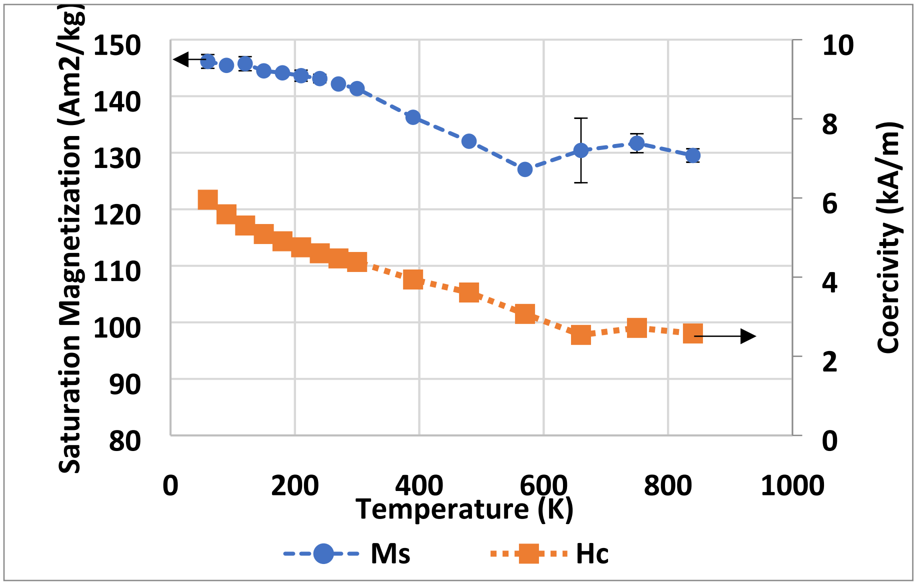

Figure 137. Change in saturation magnetization and coercivity of Co-rich S12 sample with increasing temperature

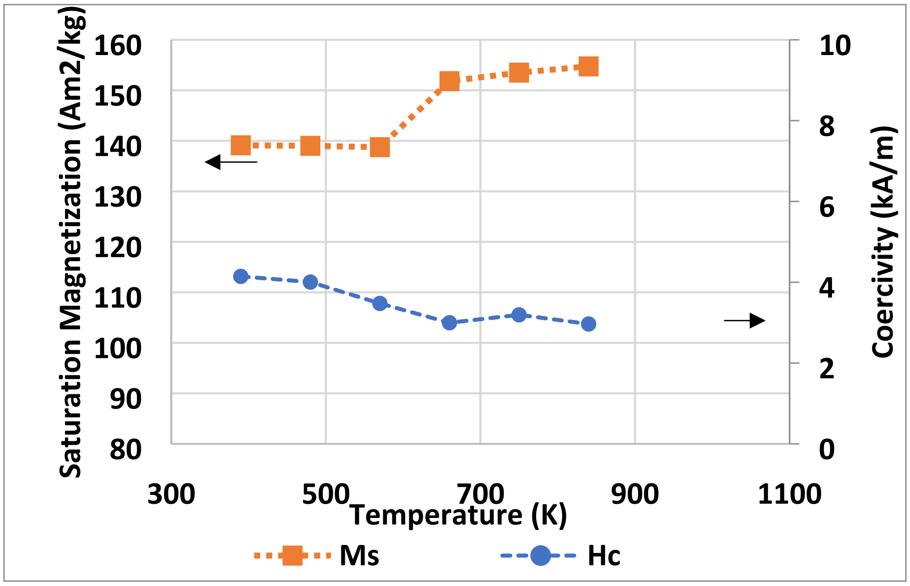

Figure 138. Saturation magnetization and coercivity vs temperature of as annealed Co-rich S12 sample

Figure 139 shows the XRD of all the as-annealed sample from 300 K-840 K. The Fe peaks can be seen when the sample is heat treated at 660 K.

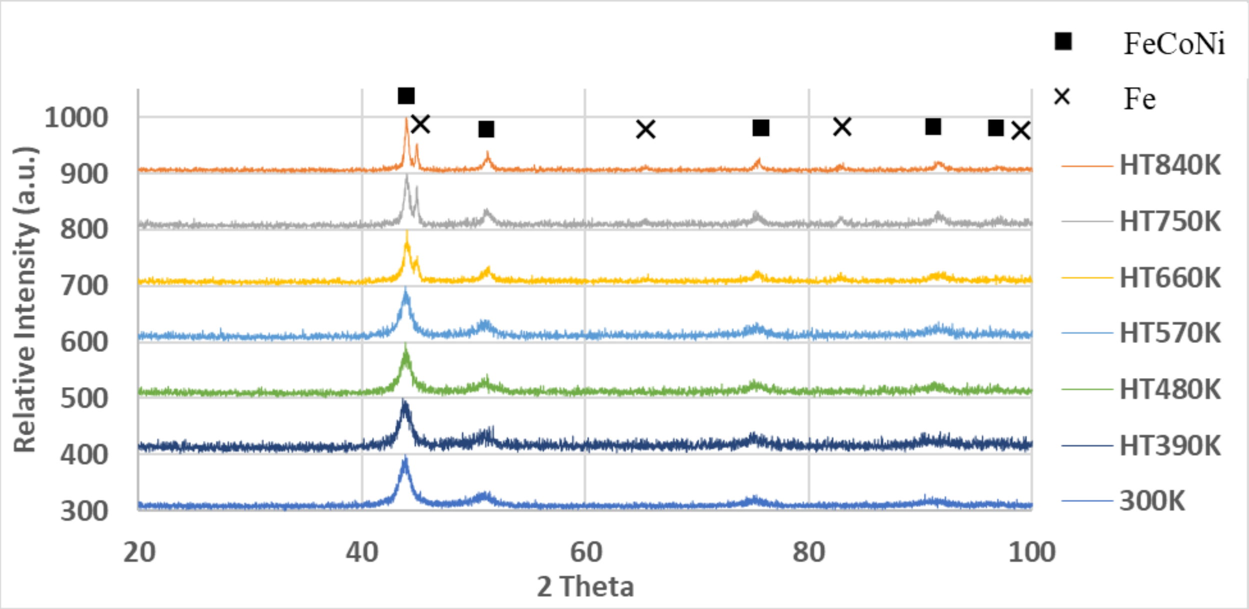

Figure 139. Heat treatment of Co-rich S12 sample

As shown in **Figure 140 and 141,** the particle size increases and get maximum at 660 K due to release of strain during heat treatment. After that the Fe atom comes out of HEA lattice and the particle size decreases at 750 K. Then further heating releases strain and particle size increases at 840 K.

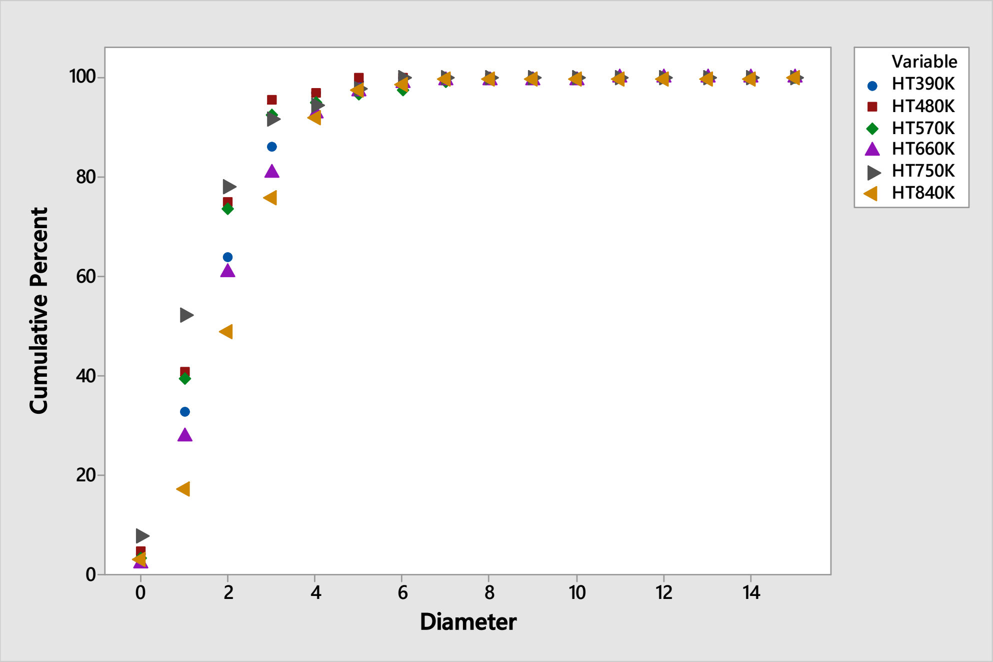

Figure 140. Cumulative particle size of as-annealed Co-rich S12 sample

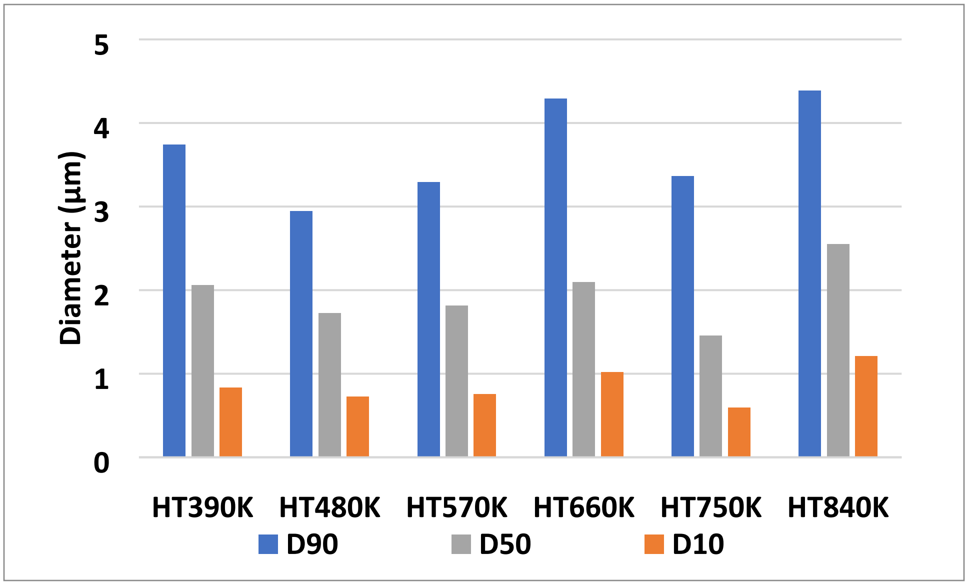

Figure 141. ***D90***, ***D50***, **and** ***D10*** **particle size diameters of as-annealed Co-rich S12 samples**

Figure 142, 143 and 144 shows the changing lattice parameter, strain and crystallite size for Ni-rich, Fe-rich and Co-rich samples with increasing temperature from 390 K to 840 K.

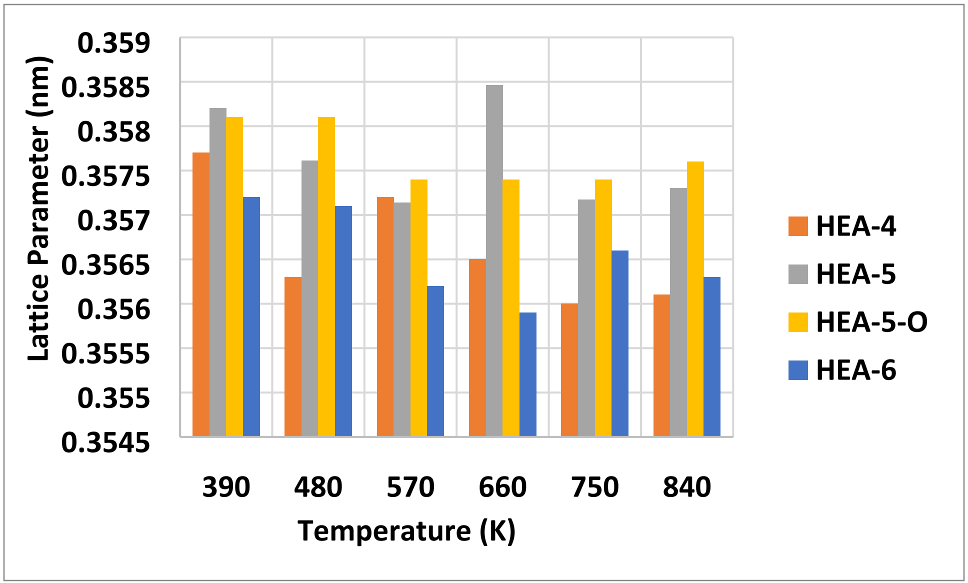

Figure 142. Change in lattice parameter with increase in temperature

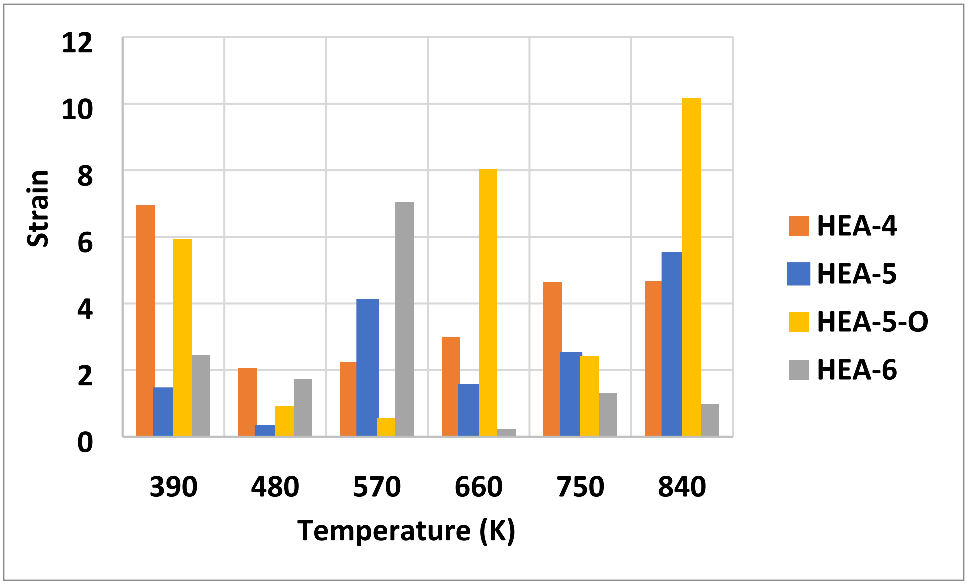

Figure 143. Change in strain with increase in temperature

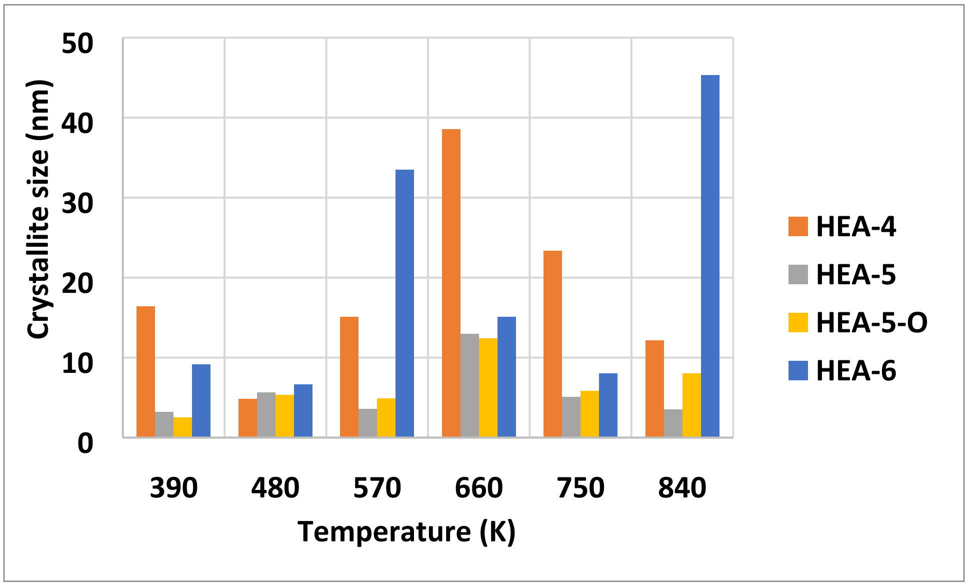

Figure 144. Change in crystallite size with increase in temperature

5.3 Composition considering ≈ 8.7 J/mol.K

The configurational entropy for equiatomic alloy was 9.13 J/mol.K, which can be reduced to as low as 8.4 J/mol.K to keep the alloy high entropy. Thus, the next alloy, named HEA-3, had a composition of Fe:Co:Ni as 46:34:20. By increasing the quantity of Fe, saturation magnetization increased and the composition of Ni in alloy assured lower coercivity. The configurational entropy is 8.70 J/mol.K, still less than 8.4. There was only one sample prepared for HEA-3 using mechanical milling for 9 hours.

5.3.1 XRD Analysis

The XRD for HEA-3 at 300 K showed the structure was amorphous, as shown in **Figure 145.** The reason being lesser amount of Ni resulting in lesser space for Fe and Co atoms to fit in, to form an FCC structure. Even after the heat treatment till 660 K , the structure was amorphous. But, once it was heat treated till 840 K, the same phenomenon of Fe leaving the Ni lattice occurs as explained in equiatomic alloys. This creates more space for Co atoms to get into Ni lattice and form a dual phase FCC and BCC alloy. The height of Fe peak, surpassing the alloy peak, shows the high amount of Fe.

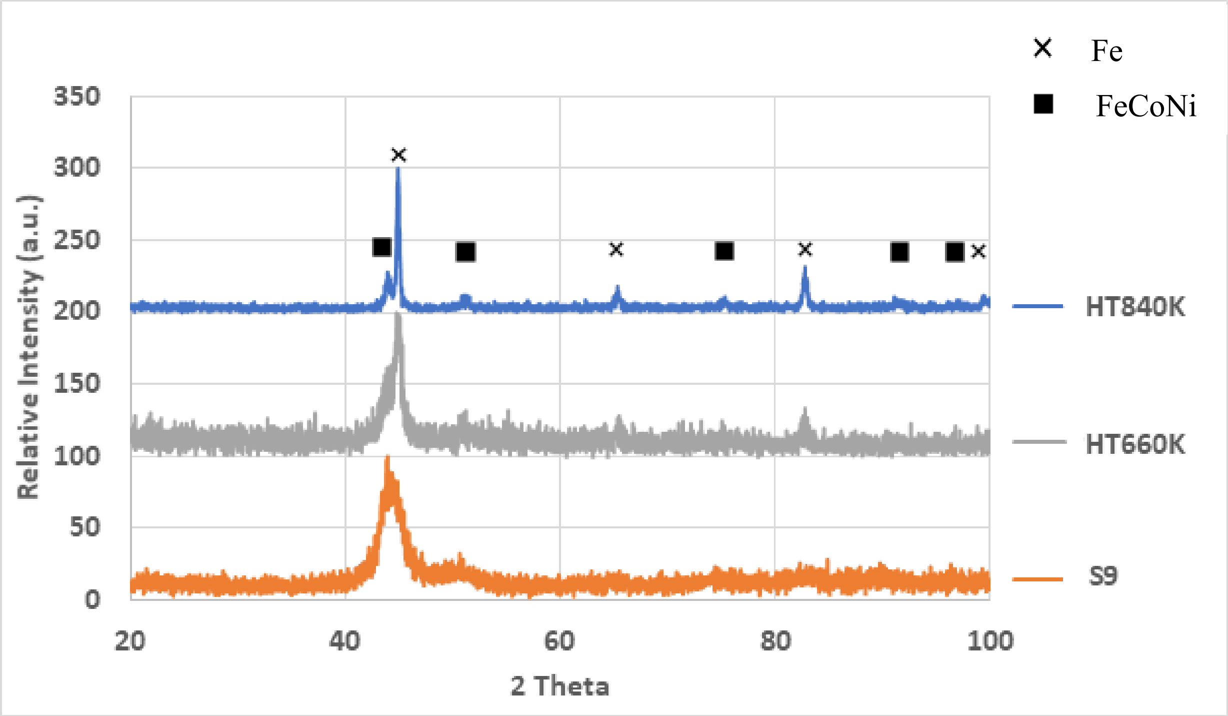

Figure 145. XRD for as-alloyed and heat treated HEA-3

5.3.2 VSM Analysis

For magnetic characterization of HEA-3 as-milled and as-annealed samples, Quantum Design’s Vibrating Sample Magnetometer (VSM) was used. Change in magnetization was recorded while applying magnetic field from -2150 kA/m (-27 kOe) to 2150 kA/m (27 kOe) . **Figure 146** shows the hysteresis loops of as-milled sample measured at different temperature. **Figure 147** shows the hysteresis loops of as-milled and as-annealed sample. After the heat treatment (as stated in section 5.1.4) of alloy, the *Ms* increases while *Hc* decreases, as shown in **Figure 147** and **Table 8.** The area of the hysteresis loop is very small which suggests that the alloy is ferromagnetic.

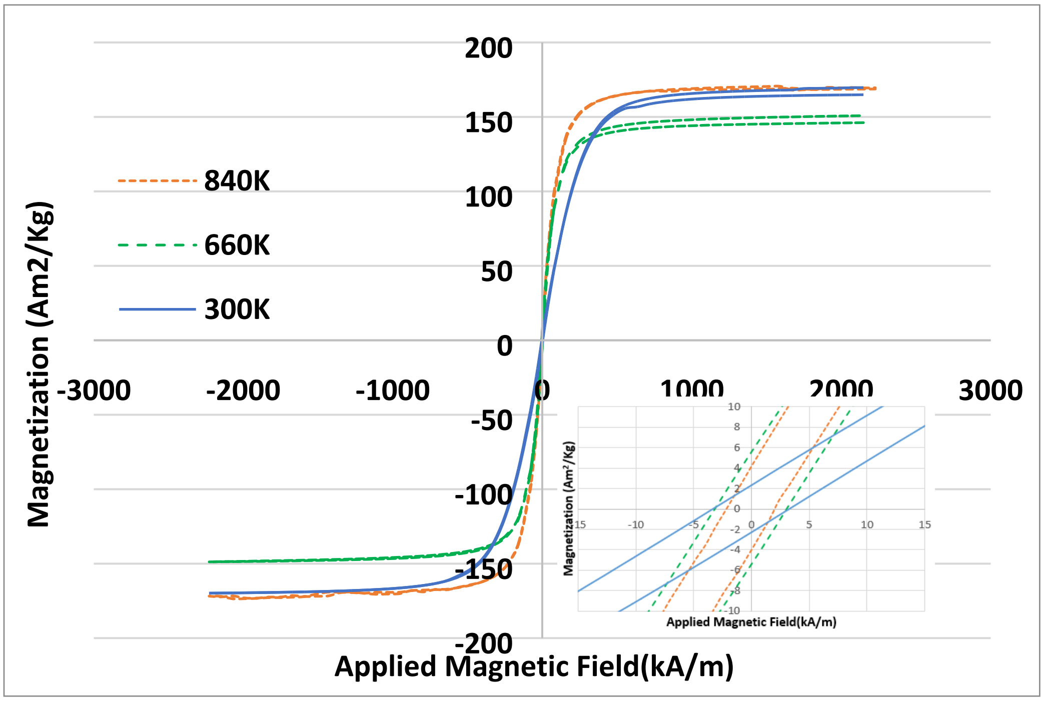

Figure 146. ***M-H*** **curves of HEA-3 at room temperature and high temperature**

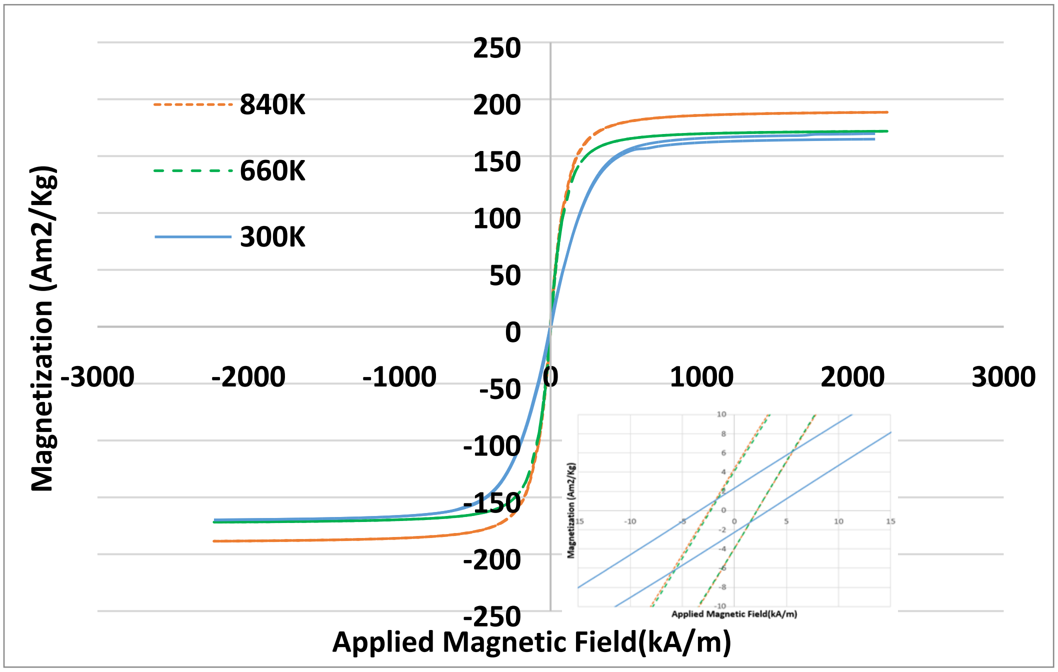

Figure 147. ***M-H*** **curves of as-milled and as-annealed HEA-3**

Table 8. Saturation magnetization and coercivity of HEA-3

Sample	*Ms*(Am^2/kg)	*Hc*(kA/m)
S9	167.12 ± 2.35	3.25 ± 0.01

The saturation magnetization decreases with increase in temperature, which can be seen in **Figure 148.** The reason for this drop is thermal vibrations due to increase in temperature. The change in coercivity can be explained by Neel Brown equation, which will be explained later.

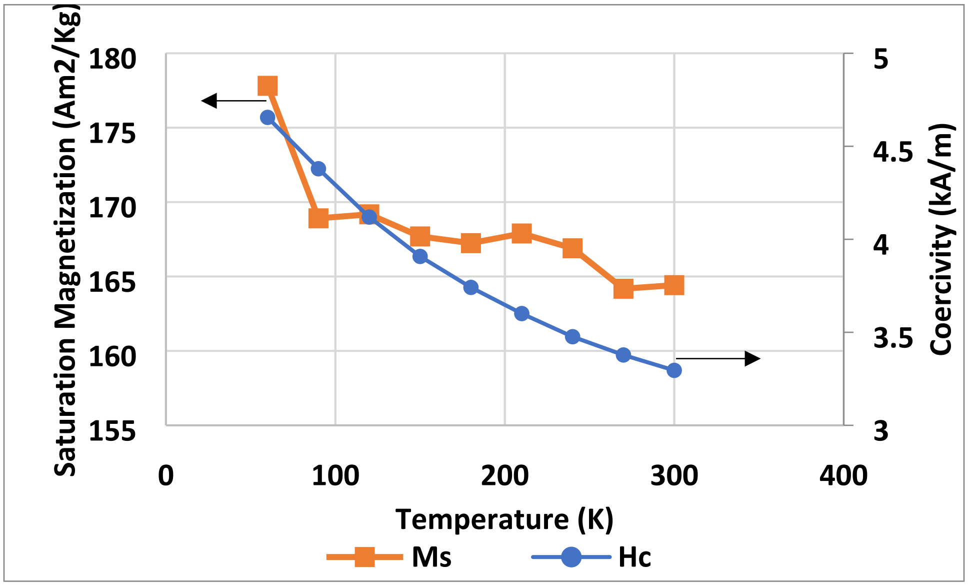

Figure 148. Change in saturation magnetization and coercivity at low temperature of HEA-3

HEA-3 is examined for magnetization vs temperature curve from 300 K to 852 K at 8 kA/m (100 Oe). As shown in **Figure 149,** the curve is similar to the equatomic alloy i.e. the same phenomenon of Fe leaving Ni lattice after 650 K is confirmed from this curve. Thus, in **Figure 150,** *Ms* decreases till 660 K but after that when Fe comes out, *Ms* increases. The disturbance in the curve from 800 K to 852 K is because of instrument issue. **Figure 151** shows the as-annealed sample in which *Ms* always increases with increase in temperature.

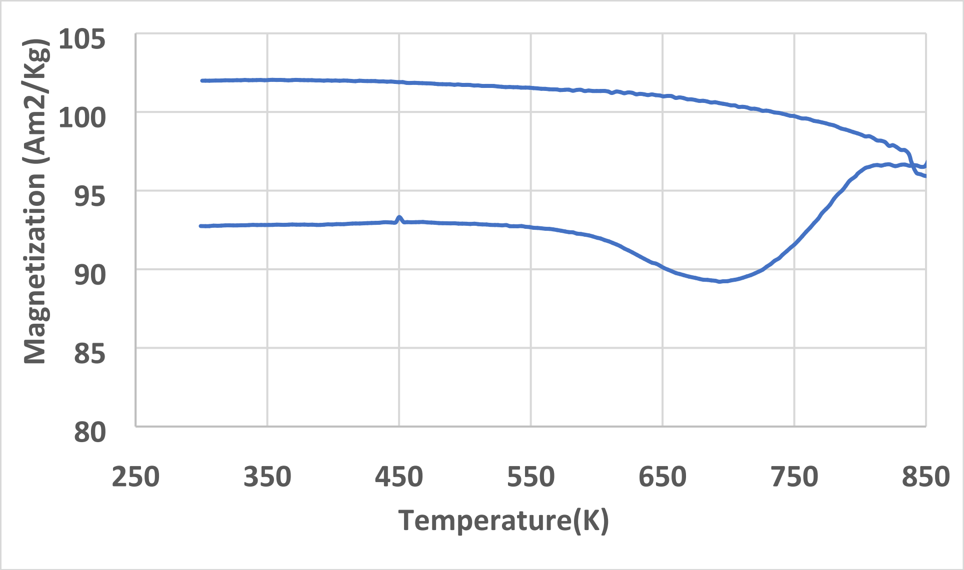

Figure 149. Magnetization vs temperature of HEA-3

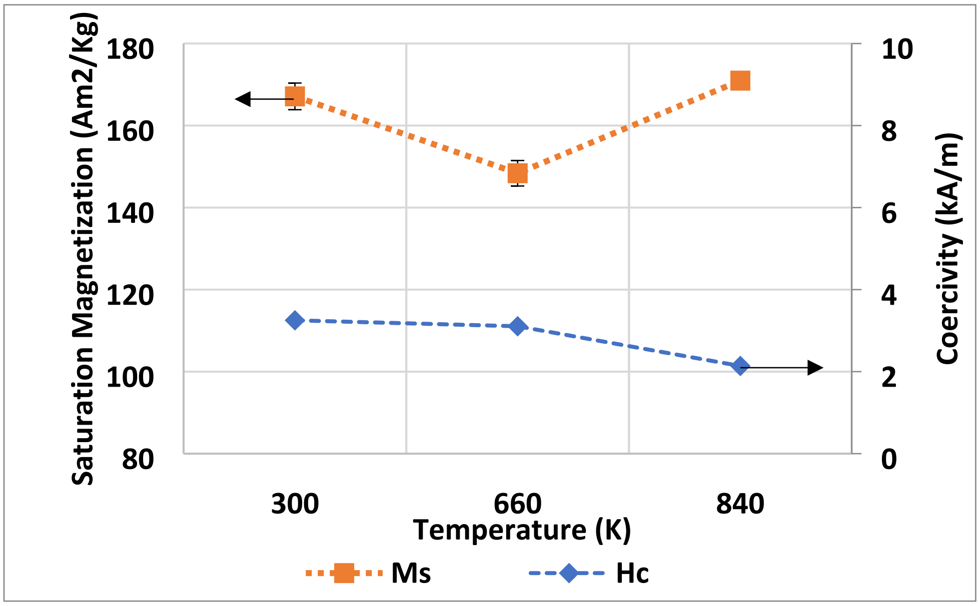

Figure 150. Change in saturation magnetization and coercivity of HEA-3 with increasing temperature

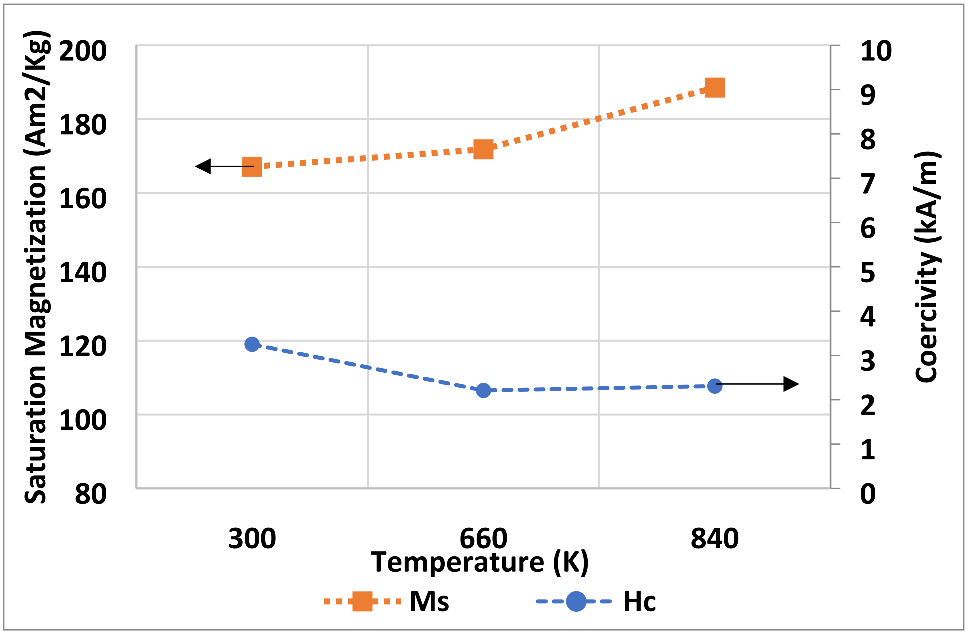

Figure 151. Saturation magnetization and coercivity vs temperature of as annealed HEA-3

5.3.3 SEM Analysis

Figure 152 shows the SEM image of HEA-3 alloy at a resolution of 100 μm. **Figure 153** shows the cumulative diameter of the particles in HEA-3 alloy. From this data, 90, 50 and 10 percentile diameters were extracted and shown in **Figure 154.**

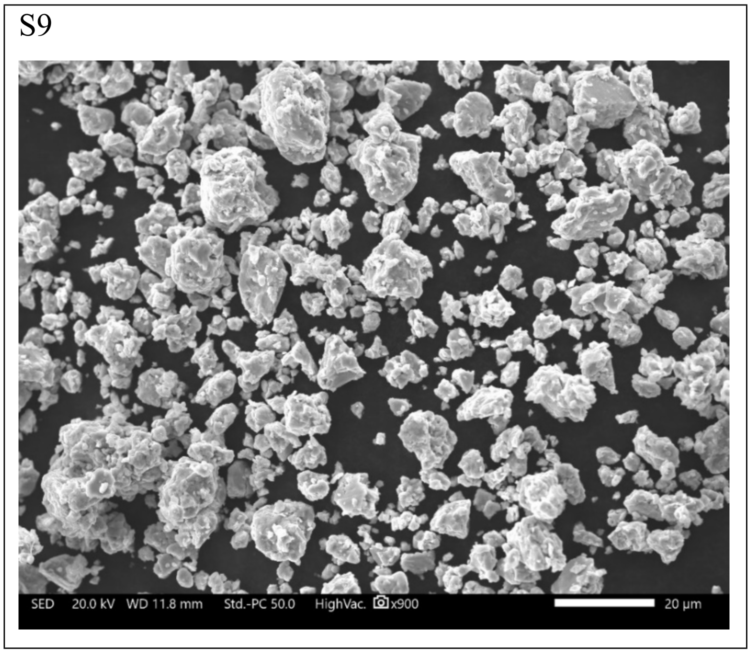

Figure 152. SEM images of the HEA-3 at 100 μm resolution

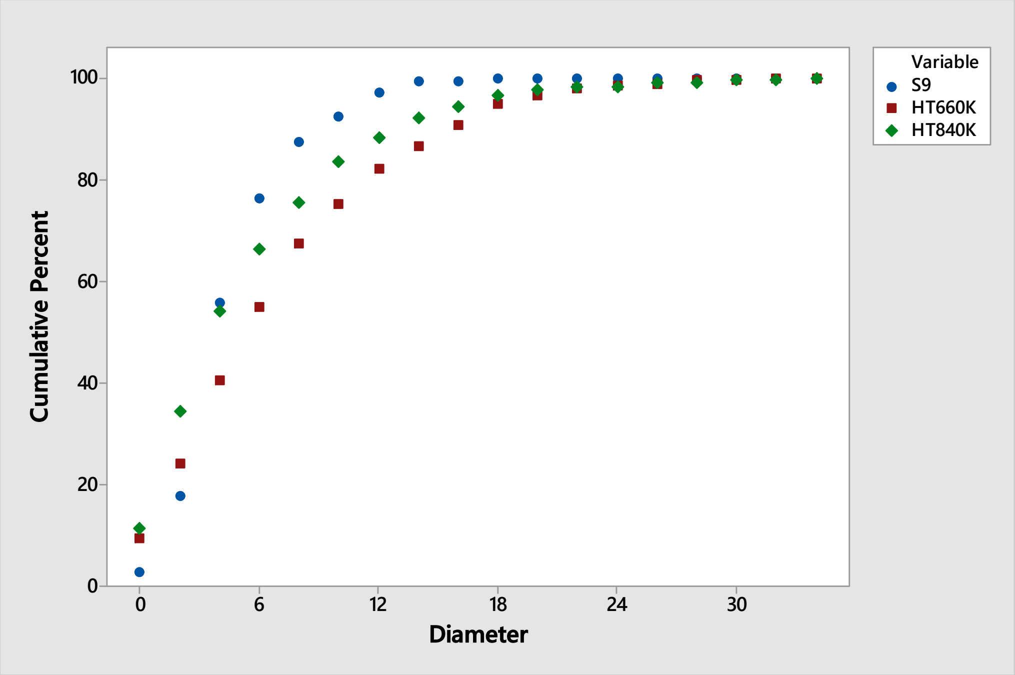

Figure 153. Cumulative particle size of HEA-3 alloy

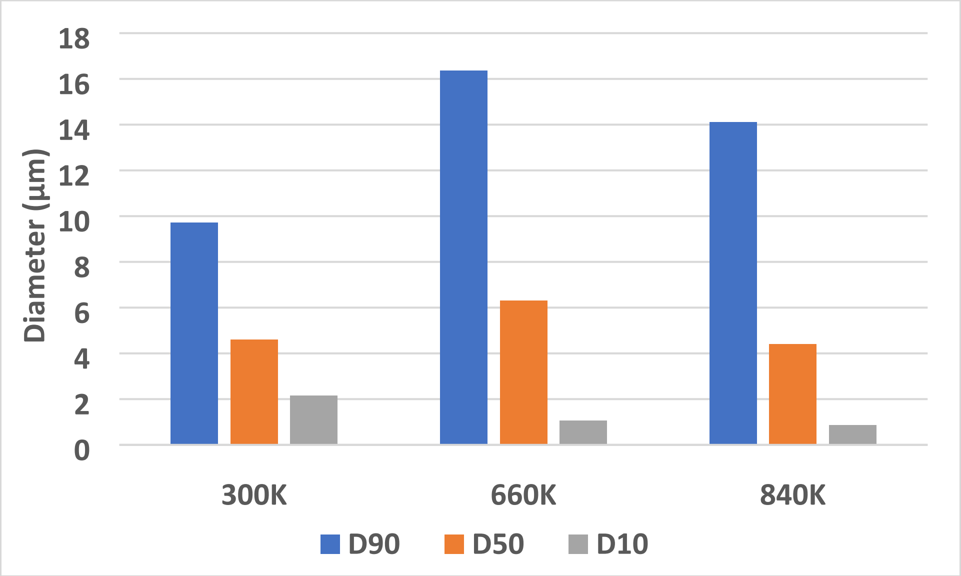

Figure 154. 90, 50 and 10 percentile particle size diameters of HEA-3

The comparison lattice parameter, strain and crystallite size of as-milled and as-annealed is shown in **Figure 155, 156 and 157** respectively.

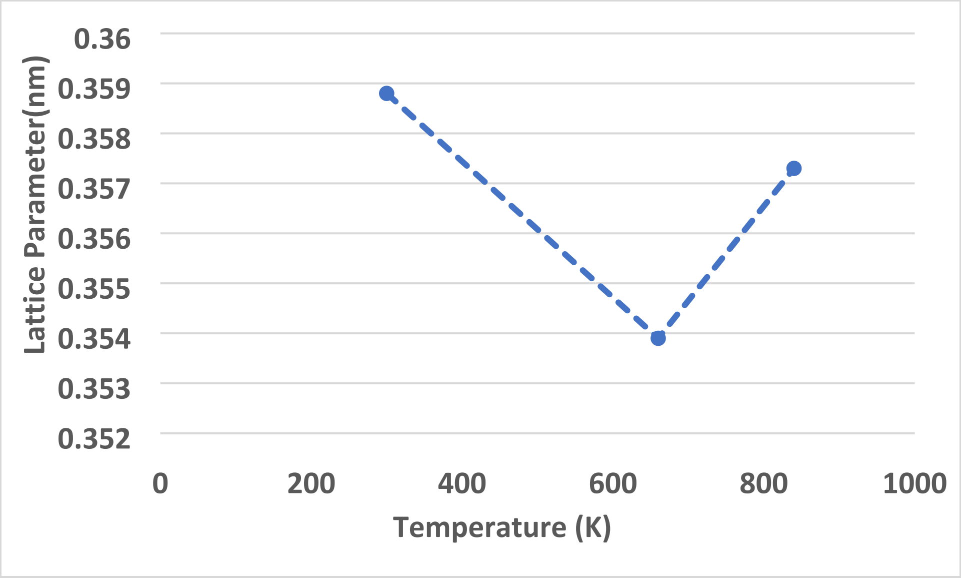

Figure 155. Lattice parameter of HEA-3 alloy at room temperature and after heat treatment

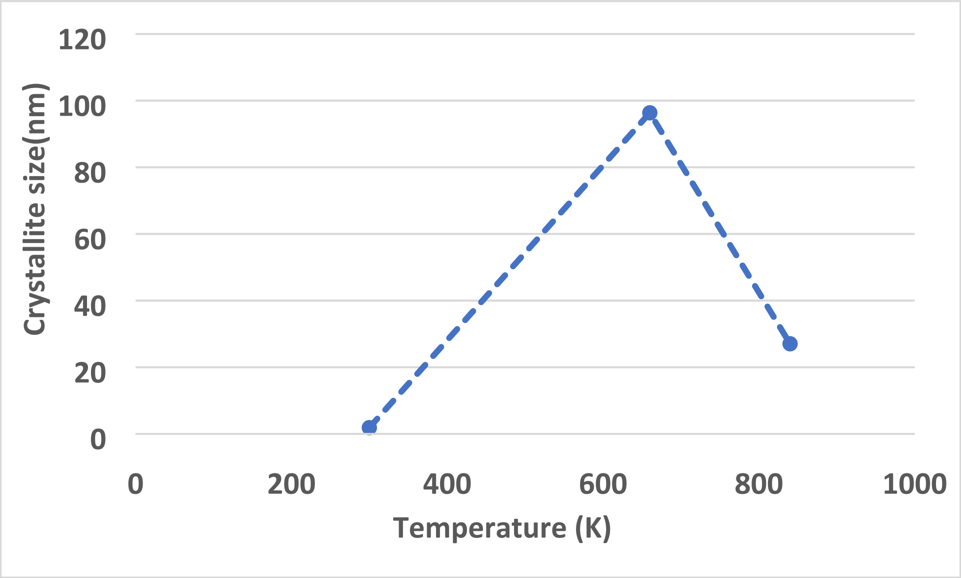

Figure 156. Crystallite size of HEA-3 alloy at room temperature and after heat treatment

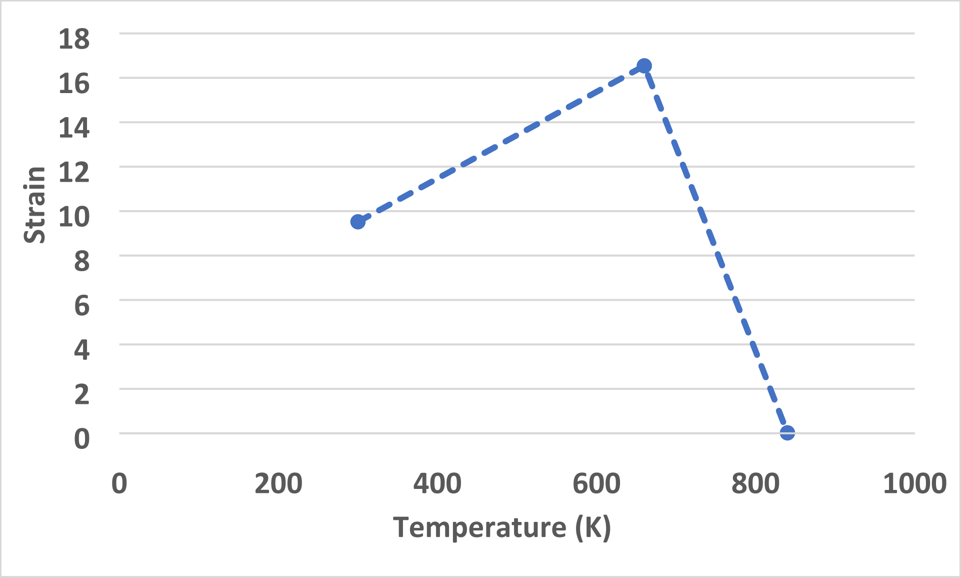

Figure 157. Strain in HEA-3 alloy at room temperature and after heat treatment

5.4 Composition considering $\Delta S_{mix} \approx 10.12$ J/mol.K

Fe-rich alloy mechanically milled for 9 hours is the best alloy in terms of high *Ms* and low *Hc*. The Fe-rich alloy is again prepared the same way by milling it for 9 hours. After preparation of FeCoNi alloy, silicon, as fourth element, is added to increase the configurational entropy and decrease coercivity. Also, the quantity of Si is kept very less so as to maintain high saturation magnetization. The atomic ratio of FeCoNi:Si is taken as 95.8:4.2, thus 4.9 gm of FeCoNi alloy is mixed with 0.1 gm of Si. This 5 gm of sample (HEA-7) is mechanically milled for 1 hour (S1) without any further addition of stearic acid, in oxygen. The sample was tested for XRD, VSM and SEM and then same sample(≈5gm) is again put together in hardened steel vial. Keeping the mass ratio of ball to powder as 8:1, the sample is milled for another 2 hours (S3) in oxygen.

5.4.1 XRD Analysis

1 hour of alloying was thought to be enough for the fusion of such a small amount of Si into FeCoNi alloy but the XRD of S1 shows Si peak, as shown in **Figure 158.** The reason for this can be the difference in the particle size of alloyed FeCoNi and Si. Thus, it will take some more time for the Si particles to get smaller and then get alloyed with FeCoNi. However, when the vial of S3 was opened the sample started burning and fumes started coming out. This means that the sample was oxidized which can be confirmed from the XRD in **Figure 158.** The PDF suggests that the new peak is a FeCoNi oxide.

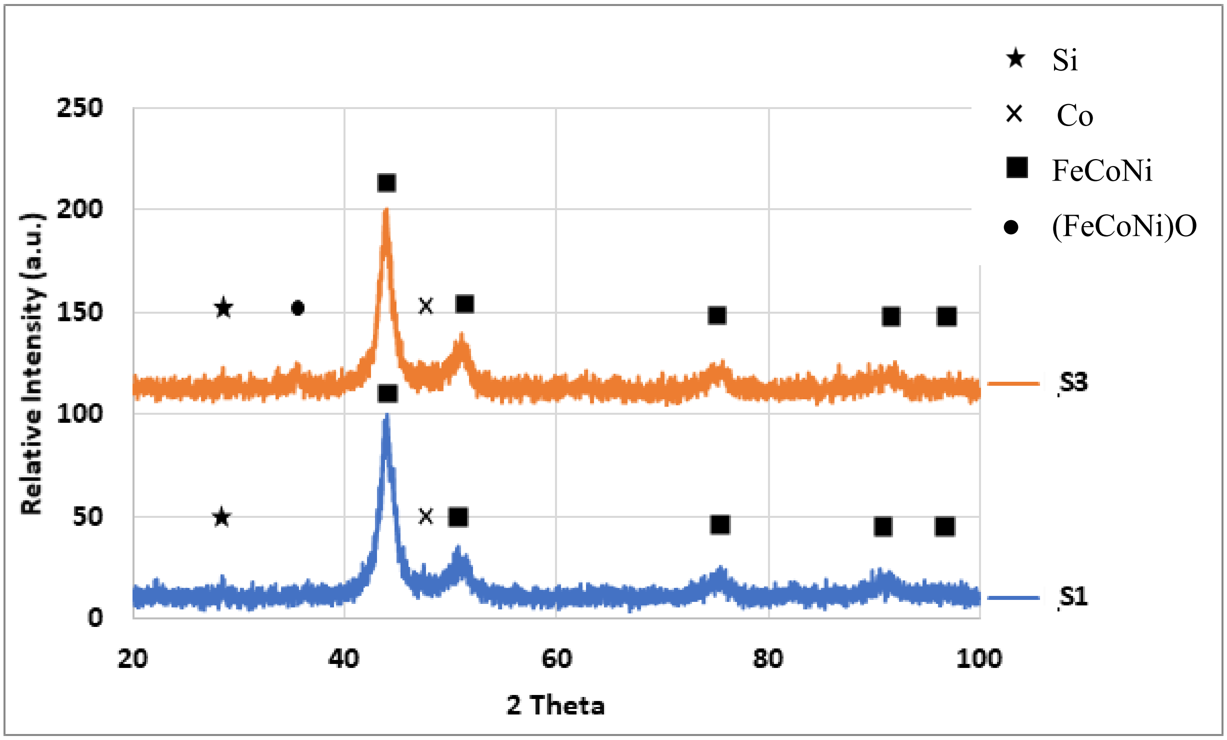

Figure 158. XRD for HEA-7 milled for 1 hour and 3 hours

5.4.2 VSM Analysis

The magnetic characterization was performed on Quantum Design's Vibrating Sample Magnetometer (VSM). An external magnetic field of -2150 kA/m (-27 kOe) to 2150 kA/m (27 kOe) is applied and the change in magnetization of the sample is recorded. **Figure 159** shows the hysteresis loop for S1 and S3. Since the alloy is not completely formed in S1, thus the *Hc* of the sample increases because of dual phase. Also, with addition of a diamagnetic material the *Ms* also decreases in S1 and S3, as shown in **Table 9.**

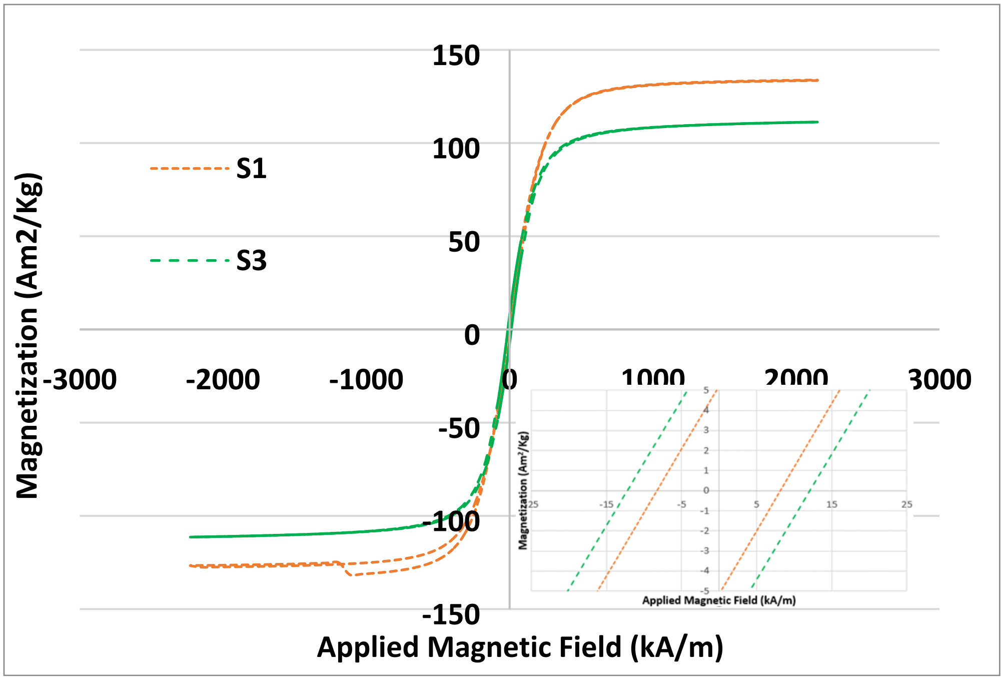

Figure 159. ***M-H*** **curves of as-prepared HEA-7 milled for 1 hour and 3 hours**

Table 9. Saturation magnetization and coercivity of HEA-7

Sample	*Ms*(Am^2/kg)	*Hc*(kA/m)
S1	130.83	8.22
S3	111.17	12.16

5.4.3 SEM Analysis

Figure 160 shows the SEM image of S1 and S3. The bigger particles that can be seen in S1 are the Si particles that have not been alloyed with FeCoNi.

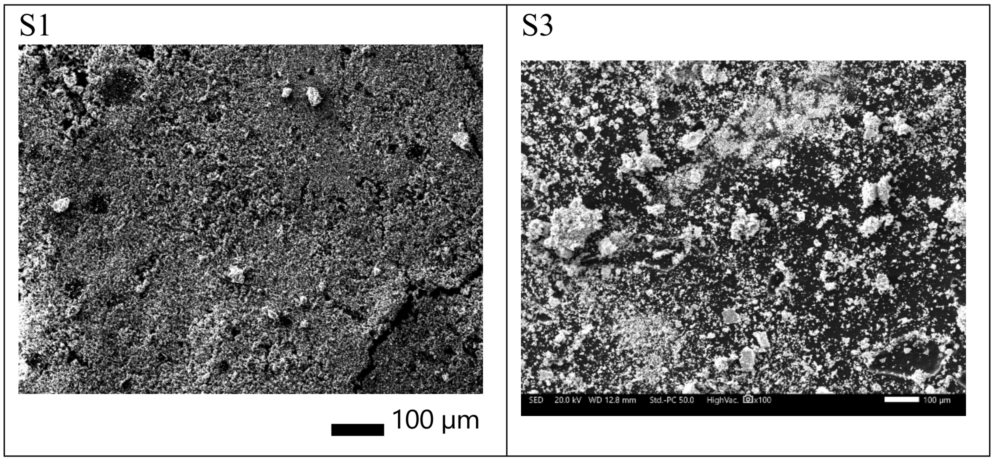
S1
S3

Figure 160. SEM images of the HEA-7 at 100 µm resolution

The comparison lattice parameter, strain and crystallite size of as-milled and as-annealed is shown in **Figure 161, 162 and 163** respectively.

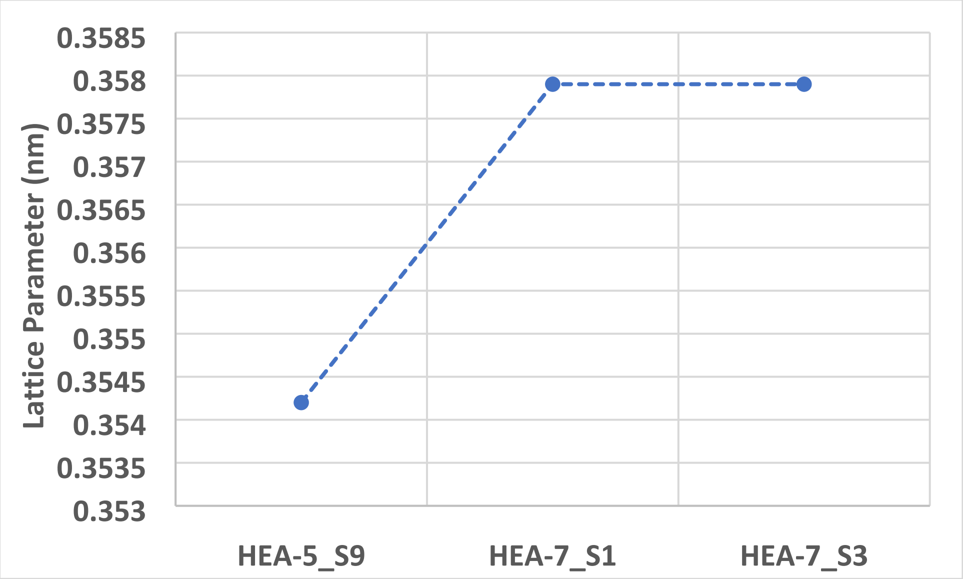

Figure 161. Lattice parameter of Fe-rich and HEA-7 alloy

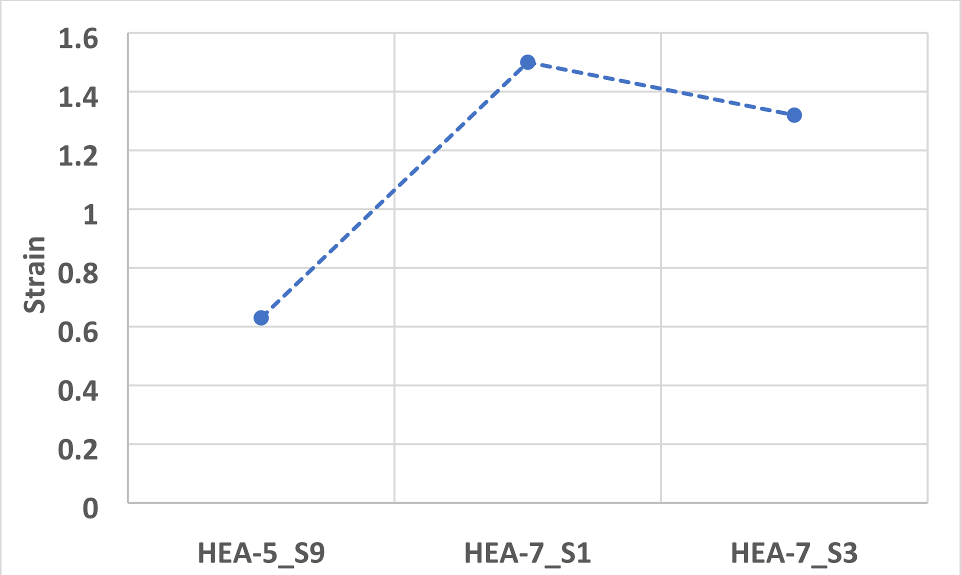

Figure 162. Strain of Fe-rich and HEA-7 alloy

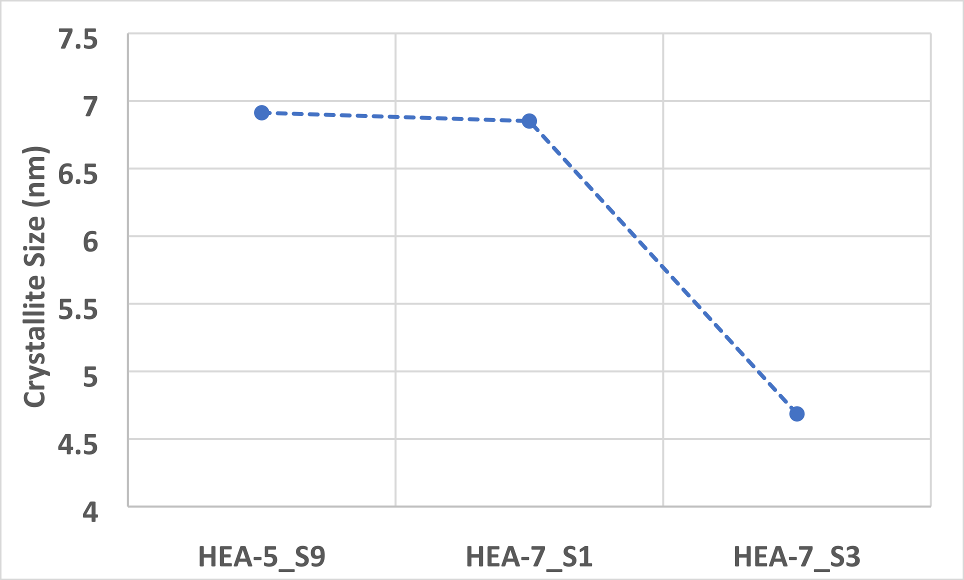

Figure 163. Crystallite Size of Fe-rich and HEA-7 alloy

5.5 Composition considering $\Delta S_{mix} \approx 10.85$ J/mol.K

Since in HEA-7 more hours of alloying were required, thus now the powder is alloyed for 9 hours and also the amount of Si has also been increased to increase the configurational entropy. Now the FeCoNi:Si atomic percent ratio has changed to 90:10 which has increased configurational entropy to 10.85 J/molK. It is synthesized the same way as HEA-7 is produced. Fe-rich alloy is prepared first and then according to at.%, it is mixed with Si to make a 5 gm sample (HEA-8). Keeping the ball to powder ratio as 8:1, it is alloyed for 9 hours (S9) with 1% stearic acid in hardened steel vial.

5.5.1 XRD Analysis

The XRD in **Figure 164** shows that at 300 K , HEA-8 is still having some Si particles that has not yet been alloyed. There are two possible reason, either the alloying duration was not enough, or the amount of Ni is not enough to amalgamate Fe, Co and Si together into itself. This as-annealed sample behaved the similar way as the previous alloys. Till 660 K there was not much difference in XRD, however when the sample was annealed at 840 K the Fe atoms came out of Ni lattice and resulted in a dual phase alloy.

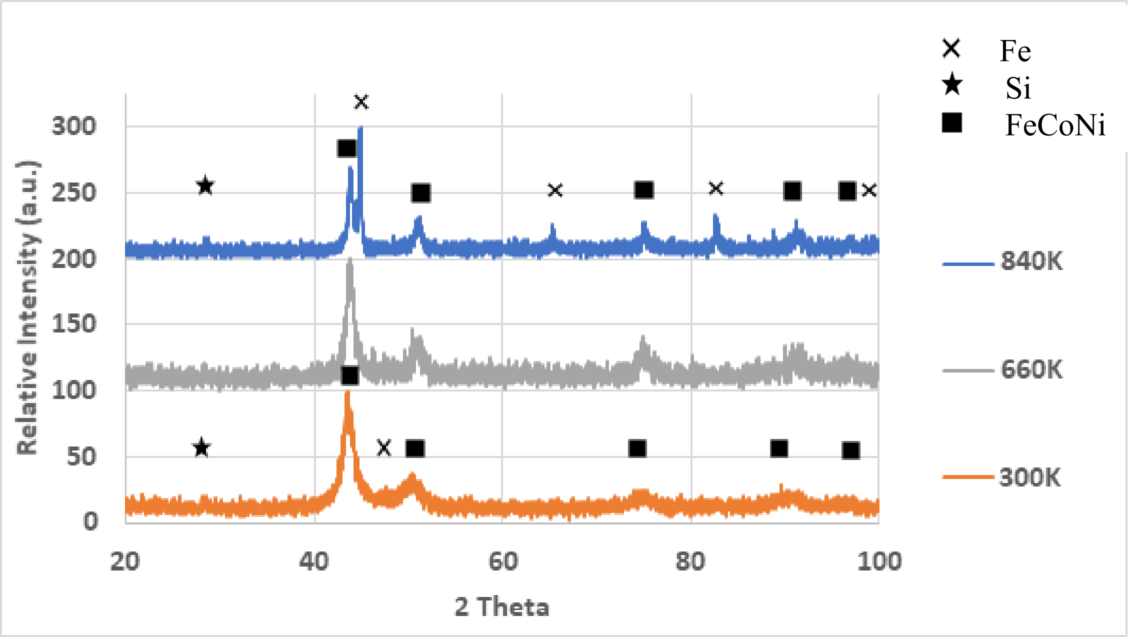

Figure 164. XRD for HEA-8 and heat treated HEA-8

5.5.2 VSM Analysis

The magnetic characterization of HEA-8 of as-milled and as-annealed samples was performed in Quantum Design's Vibrating Sample Magnetometer (VSM). Change in magnetization was recorded while applying magnetic field from -2150 kA/m (-27 kOe) to 2150 kA/m (27 kOe) . **Figure 165** shows the hysteresis loops of as-milled sample at 3 different temperature of 300 K , 660 K and 840 K . **Figure 166** shows the hysteresis loops of as-milled and as-annealed samples. **Figure 166 and Table 10** shows that the heat treatment (as stated in section 5.1.4) of alloy increases *Ms* and decreases *Hc.* The reason being the changing grain size and the strain relieving with increasing temperature. Also, as explained earlier, the sudden increase in *Ms* is because of Fe coming out of the Ni lattice. The ferromagnetic behavior of Fe increases *Ms.*

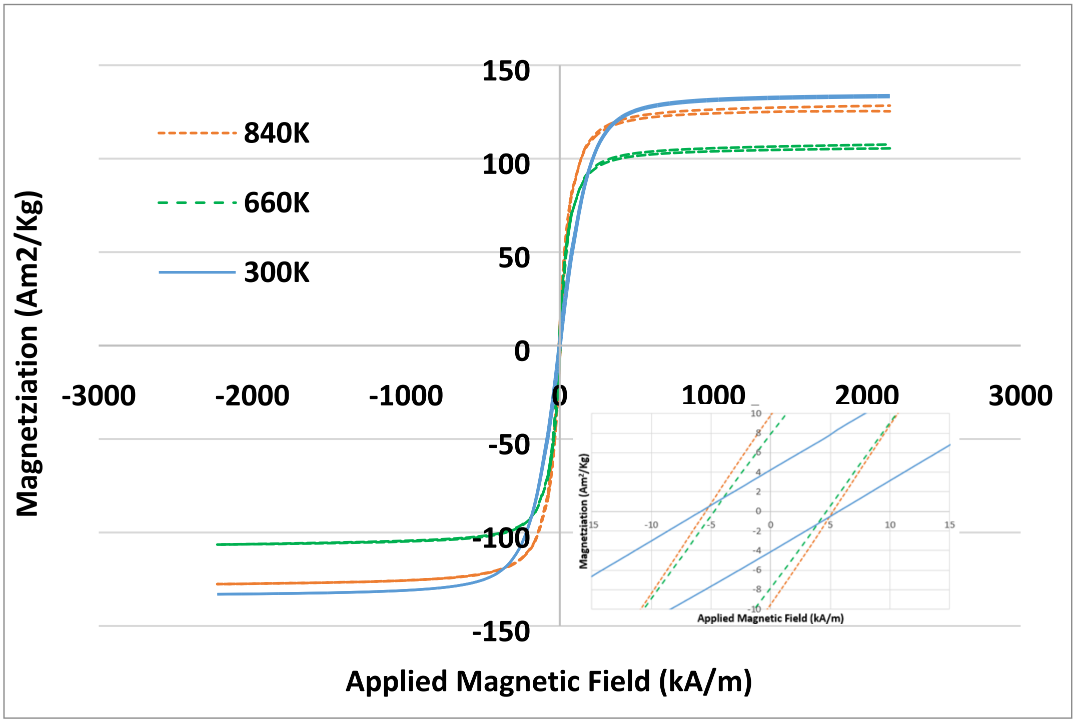

Figure 165. *M-H* curves of HEA-8 at room temperature and high temperature

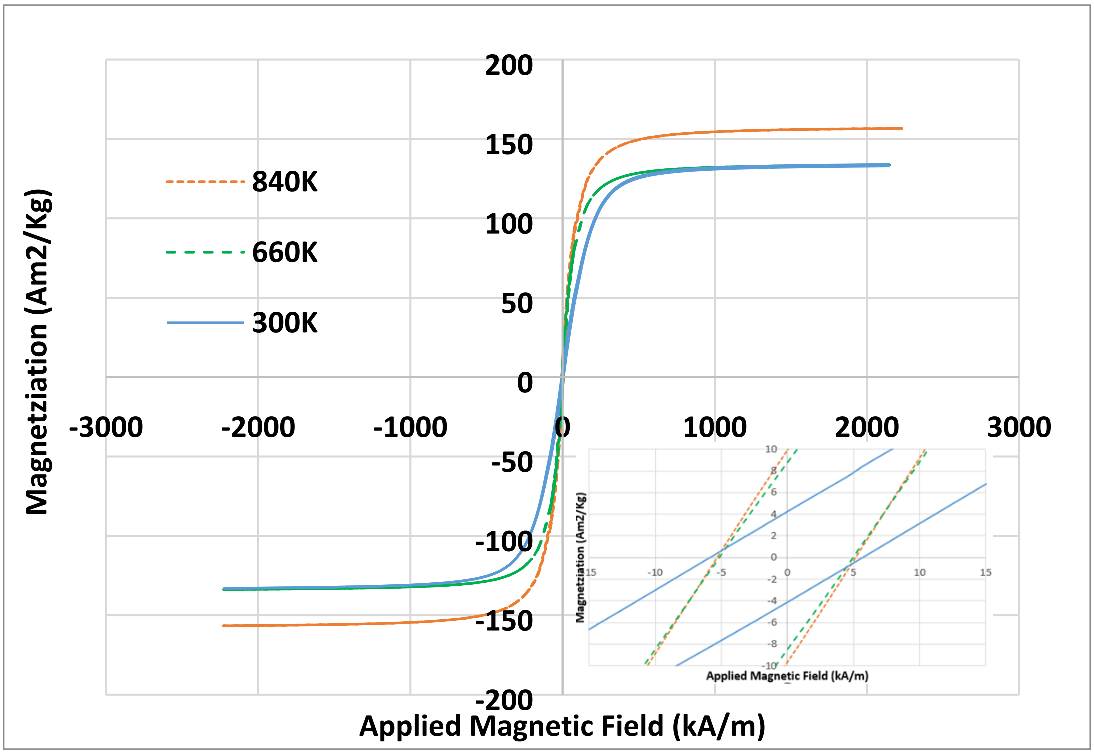

Figure 166. *M-H* curves of as-milled and as-annealed HEA-8

Table 10. Saturation magnetization and coercivity of HEA-8

Sample	*Ms*(Am^2/kg)	*Hc*(kA/m)
S9	132.23 ± 1.15	5.82 ± 0.06

With the decrease in temperature, *Ms* and *Hc* increases which can be seen in **Figure 167.** The increase in magnetization is due to the decrease in thermal vibrations with lowering temperature. The variation in coercivity has been explained earlier with the help of Neel Brown equation.

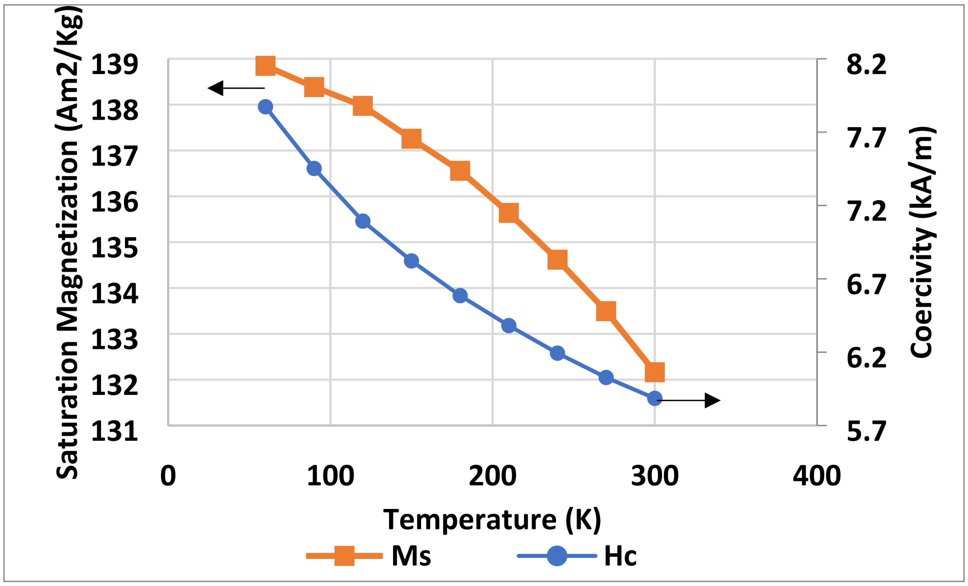

Figure 167. Change in saturation magnetization and coercivity at low temperature of HEA-8

The magnetization vs temperature curve of HEA-8 confirms that Fe atoms comes out between a temperature range of 650 K to 750 K because after that the magnetization starts rising, as shown in **Figure 168. Figure 169 and 170** confirms the change in *Ms* and *Hc* after heat treatment. Between 780 K and 800 K, the magnetization again starts going down because the thermal vibration starts dominating the ferromagnetic behavior of Fe atoms which jumped out of Ni lattice.

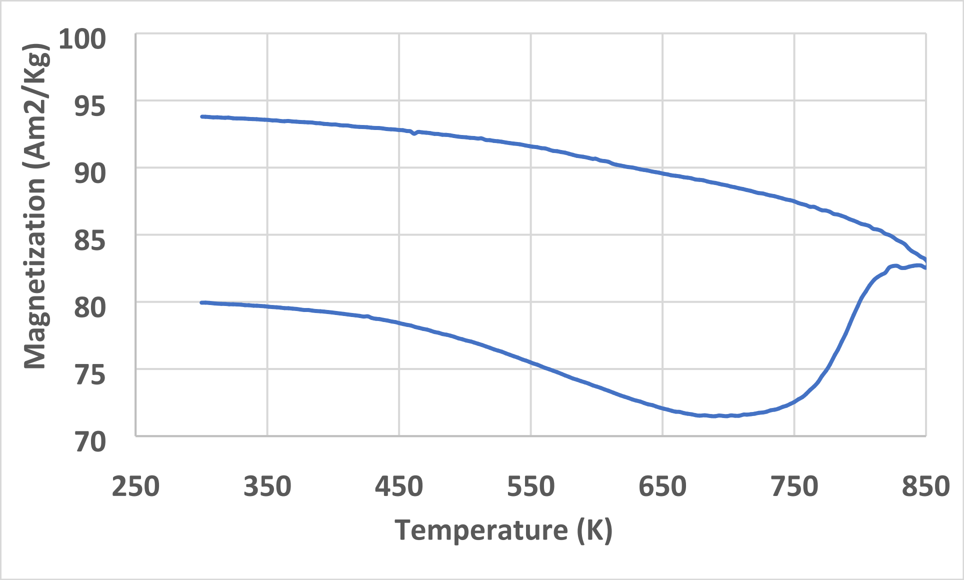

Figure 168. Magnetization vs temperature of HEA-8

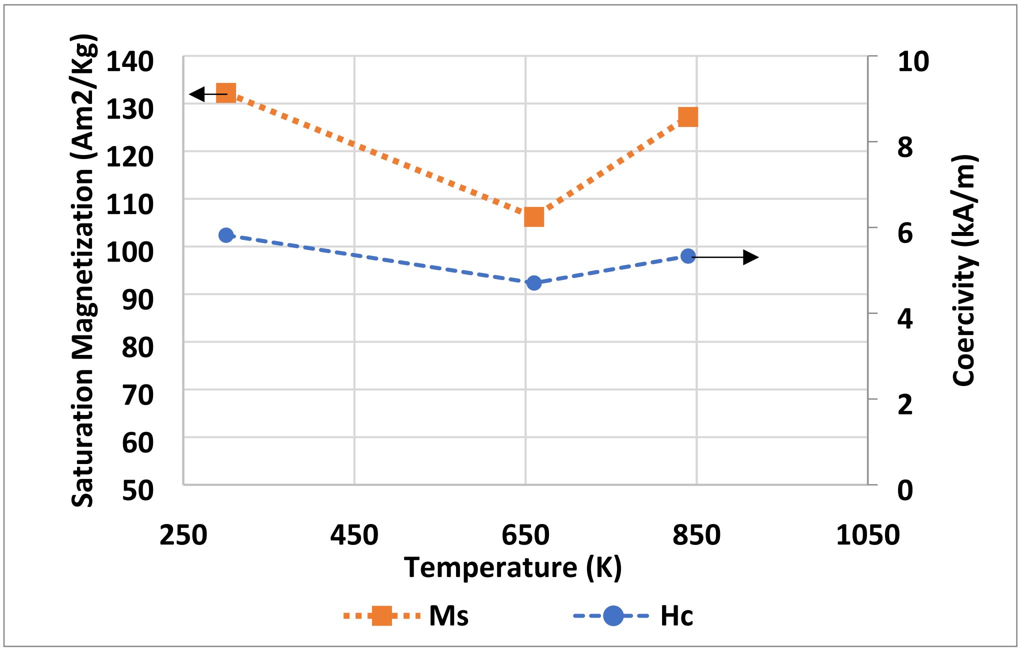

Figure 169. Change in saturation magnetization and coercivity of HEA-8 with increasing temperature

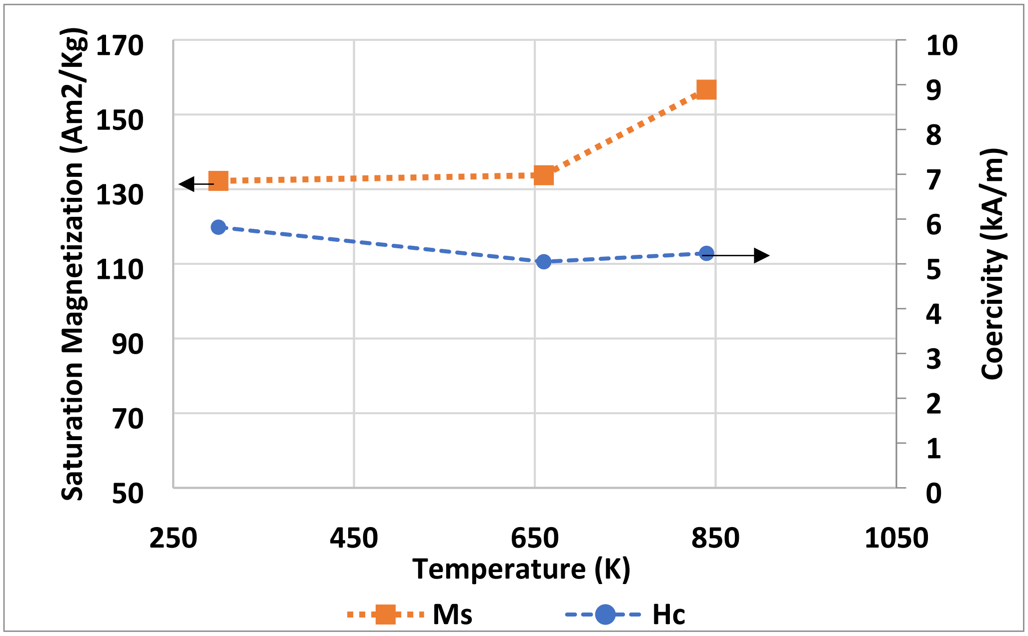

Figure 170. Saturation magnetization and coercivity vs temperature of as annealed HEA-8

5.5.3 SEM Analysis

The SEM image of HEA-8 shows that the particle size has immensely gone down as in 50 µm resolution also it is hard to distinguish between individual particles as compared to HEA-7, as shown in **Figure 171**. Cumulative diameter is shown in the **Figure 172** using which 90, 50 and 10 percentile diameters are plotted in **Figure 173.**

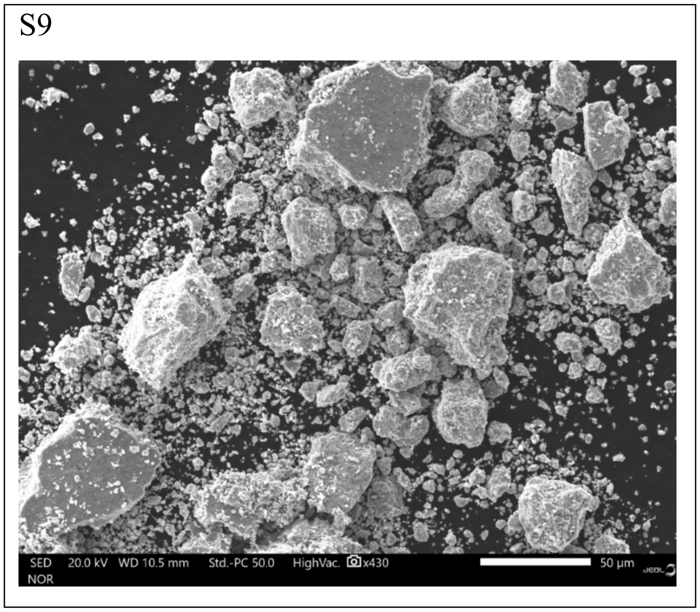

Figure 171. SEM images of the HEA-8 at 50 µm resolution

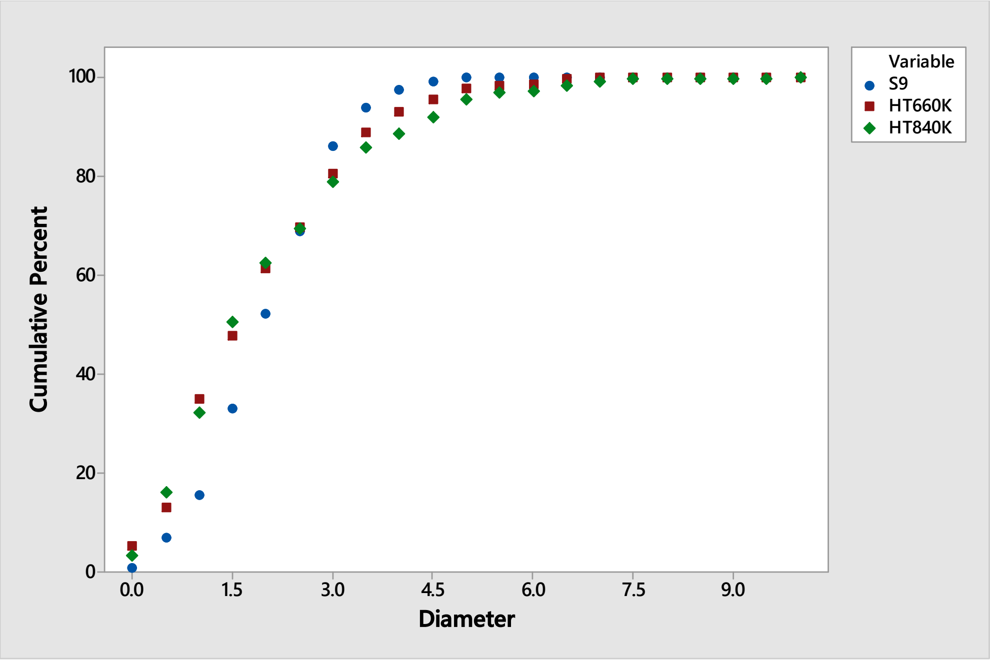

Figure 172. Cumulative particle size of HEA-8 alloy

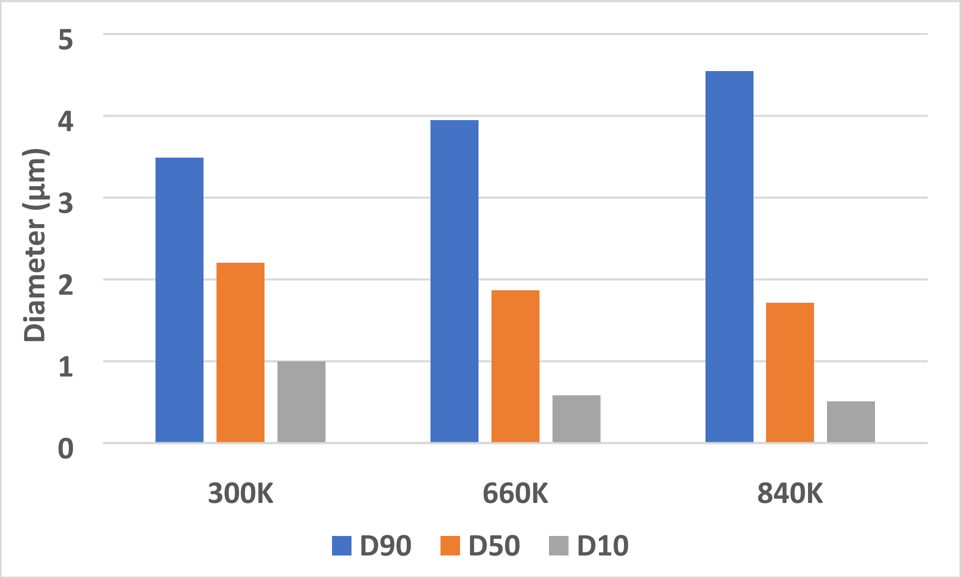

Figure 173. *D90*, *D50*, and *D10* particle size diameters of HEA-8

The comparison lattice parameter, strain and crystallite size of as-milled and as-annealed is shown in **Figure 174, 175 and 176** respectively.

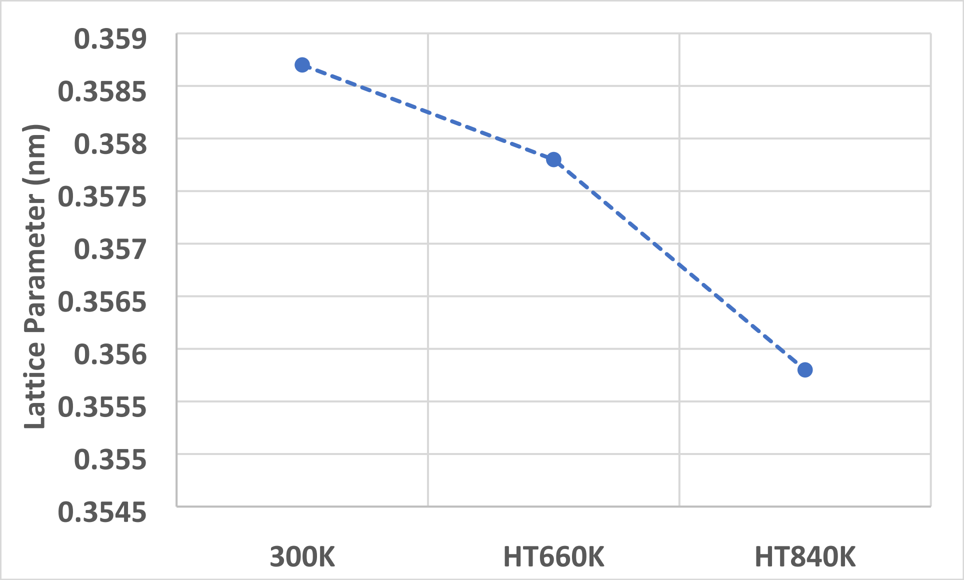

Figure 174. Lattice parameter of HEA-8 alloy at room temperature and after heat treatment

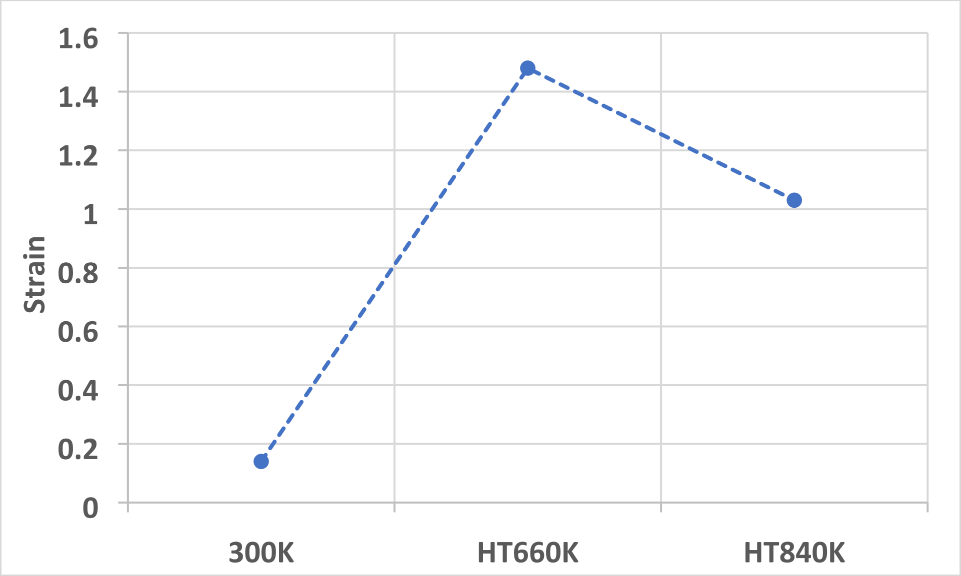

Figure 175. Strain of HEA-8 alloy at room temperature and after heat treatment

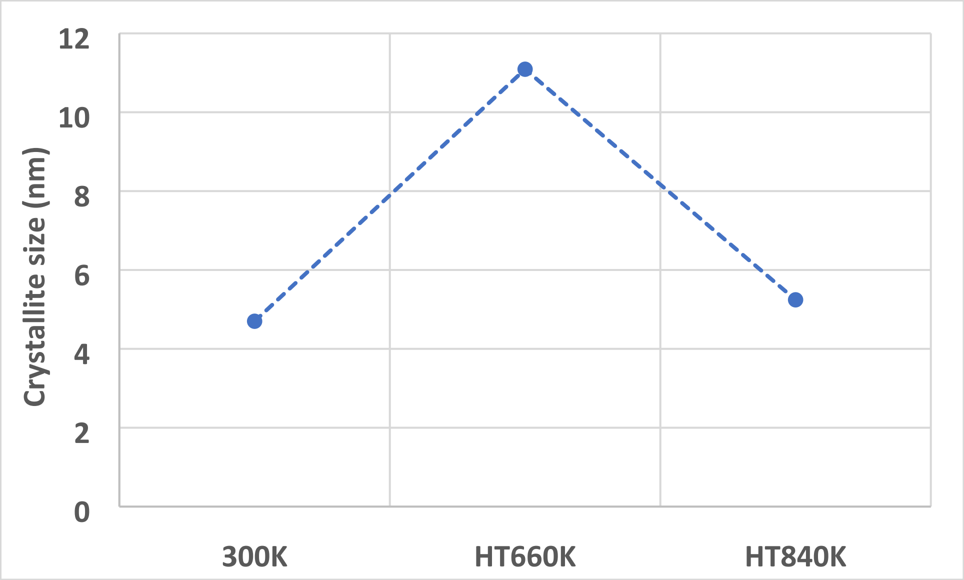

Figure 176. Crystallite size of HEA-8 alloy at room temperature and after heat treatment

The magnetic properties of the alloys successfully synthesized in this thesis work is summarized in **Figure 177**. To provide a perspective, a commercial alloy—permendur alloy (Fe-Co-V alloy)—that has a wide range of applications is also included.

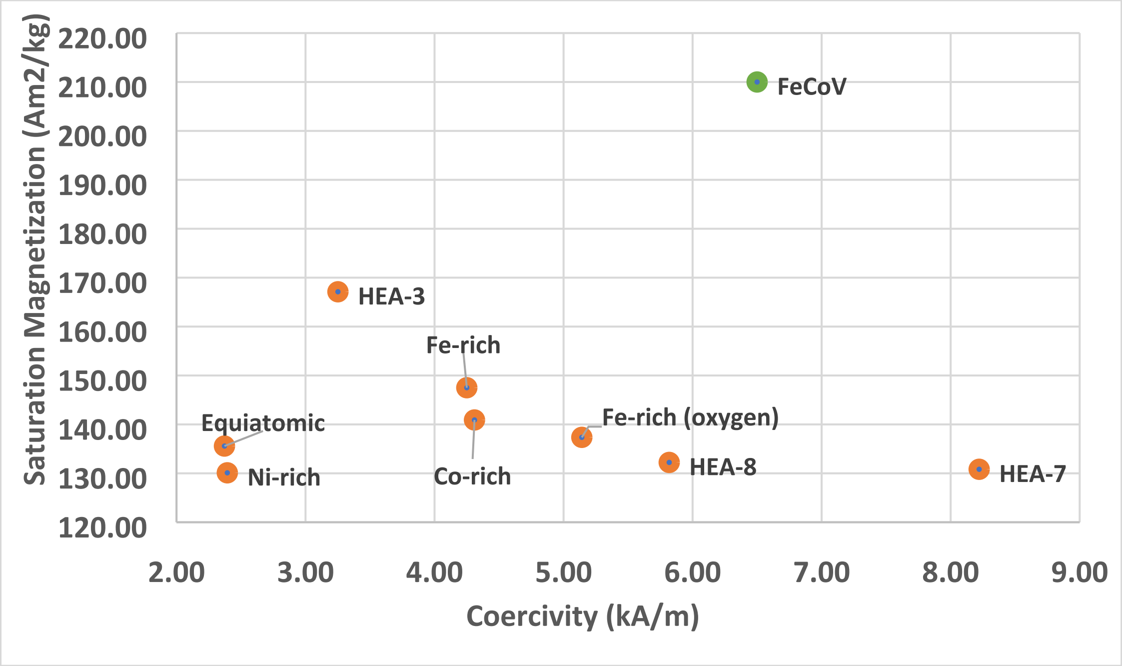

Figure 177. All the magnetic composition synthesized in *Ms* vs *Hc* plot

Chapter 6 CONCLUSION

1. Successfully synthesized ternary iron-cobalt-nickel alloys ($Fe_{33.33}Co_{33.33}Ni_{33.33}$, $Ni_{40}Co_{30}Fe_{30}$, $Fe_{40}Co_{30}Ni_{30}$, $Co_{40}Fe_{30}Ni_{30}$, and $Fe_{46}Co_{34}Ni_{20}$) and the quaternary iron-cobalt-nickel-silicon alloys $(Fe_{40}Co_{30}Ni_{30})_{0.9}Si_{0.1}$ by mechanical alloying and, investigated the phase evolution during synthesis and thermal treatments.
2. This was followed by structural characterization of phase evolution by x-ray diffraction (XRD), scanning electron microscopy (SEM) and magnetic characterization by magnetometry.
3. The equiatomic alloy- $Fe_{33.33}Co_{33.33}Ni_{33.33}$ (HEA-2) mechanical alloyed for 9 hours in argon atmosphere with hardened steel as grinding media showed relatively better magnetic properties. The as-prepared powder had FCC structure with crystallite size of ~12 nm, lattice strain of ~3% and lattice parameter of ~0.3591 nm. The D_{90}, D_{50} and D_{10} of the powders were estimated to be ~15.9 μm, ~6.8 μm, ~1.9 μm respectively. The as-prepared powder exhibited a decent magnetic property with a saturation magnetization (*Ms*) of 136 ± 3 Am^2/kg and coercivity (*Hc*) of ~2.4 kA/m. After heat treatment at 882 K , *Ms* increased by 15% to 154 Am^2/kg and *Hc* decreased by 60% to 0.9 kA/m. Thermally treated powder comprised of FCC+BCC structure with crystallite size, lattice strain and lattice parameter also decreased to ~5 nm, ~2.7% and ~0.3565 nm respectively.
4. Amongst the $Ni_{40}Co_{30}Fe_{30}$, $Fe_{40}Co_{30}Ni_{30}$, $Co_{40}Fe_{30}Ni_{30}$ alloys, Fe-rich alloy milled for 12 hours showed the best magnetic properties with *Ms* of 148 ± 3 Am^2/kg and *Hc* of 4.3 kA/m. For as-prepared powder (FCC), the crystallite size, lattice strain and lattice parameter were ~8 nm, ~2.4% and ~0.3574 nm respectively and after heat treatment at 840 K they changed to ~3.5 nm, ~5.5% and ~0.3573 nm respectively. Heating the alloy beyond 660 K transforms the FCC structure to FCC+BCC alloy. The D_{90}, D_{50} and D_{10} of the as-prepared powders were estimated to be ~5.5 μm, ~2.5 μm, ~0.1 μm respectively. After thermal treatment at 840 K the *Ms* increased by 10% to 163 Am^2/kg and *Hc* dropped down by 25% to 3.3 kA/m.

5. The $Fe_{46}Co_{34}Ni_{20}$ has the *Ms* of 167 ± 2 and *Hc* is 3.3 kA/m . The as-prepared powder had crystallite size of < ~10 nm, lattice parameter ~0.3588 nm, and lattice strain ~9.5%. After thermal treatment at 840 K, the values of crystallite size, lattice parameter and strain changed to ~27 nm, ~0.3573 nm and 0.02% respectively. The D_{90}, D_{50} and D_{10} of the as-prepared powders were estimated to be ~9.7 µm, ~4.6 µm, ~2.2 µm respectively.
6. After addition of 10 at.% Si to Fe-rich alloy ($(Fe_{40}Co_{30}Ni_{30})_{0.9}Si_{0.1}$) and milling it for 9 hours made FCC alloy with Si not blended completely. The *Ms* decreased by 10% to 132 ± 1 Am^2/kg and *Hc* increased by 40% to 5.8 kA/m . For as-prepared powder, the crystallite size, lattice strain and lattice parameter were ~4.7 nm, ~0.1% and ~0.3587 nm respectively and after thermal treatment at 840 K they changed to ~5.2 nm, ~1.0% and ~0.3558 nm respectively. The D_{90}, D_{50} and D_{10} of the as-prepared powders were estimated to be ~3.5 µm, ~2.2 µm, ~1.0 µm respectively

REFERENCES

[1] J. William D. Callister, Material Science and Engineering, John Wiley & Sons, Inc., 2007.

[2] J. A. Maurer, Introduction to Molecular Magnetism and Crystal Engineering.

[3] "Wikipedia," 2 1 2018. [Online]. Available: https://en.wikipedia.org/wiki/Magnet. [Accessed 1 2 2018].

[4] D. Jiles, "Recent advances and future directions in magnetic materials," *Acta Materialia,* no. 51, pp. 5907-5939, 2003.

[5] X. Xu, "Magnetic properties of nano-composite particles," Tuscaloosa, 2015.

[6] C.-W. Chen, Magnetism and Metallurgy of Soft Magnetic Materials, 1986.

[7] J.-W. Yeh, "Recent progress in high-entropy alloys," *European General of Control,* 2006.

[8] D. Miracle and O. Senkov, "A critical review of high entropy alloys and related concepts," *Acta Materialia,* vol. 122, pp. 448-511, 2017.

[9] J.-Y. Yeh, S.-K. Shen, S.-J. Lin, J.-Y. Gan and T.-S. Shin, "Nanostructured Jigh=-Entropy Alloys with Multiple Principal Elements: Novel Alloy Design Concepts and Outcomes," *Advanced Engineering Materials,* vol. 5, no. 6, pp. 299-303, 2004.

[10] Y. Ye, Q. Wang, J. Lu, C. Liu and Y. Yang, "High-entropy alloy: challenges and prospects," *Materials Today,* vol. 19, no. 6, pp. 349-362, 2016.

[11] Y. Zhang, T. T. Zuo, Z. Tang, M. C. Gao and K. A. Dahmen, "Microstructures and properties of high-entropy alloys," *Progress in Materials Science,* vol. 61, pp. 1-93, 2014.

[12] H. Diao, R. Feng, K. Dahmen and P. Liaw, "Fundamental deformation behavior in high-entropy alloys: An overview," *Current Opinion in Solid State and Materials Science,* vol. 21, pp. 252-266, 2017.

[13] Z. Lu, H. Wang, M. Chen, I. Baker, J. Yeh, C. Liu and T. Nieh, "An assessment on the future development of high-entropy alloys: Summary from a recent workshop," *Intermetallics,* vol. 66, pp. 67-76, 2015.

[14] A.Gali and E.P.George, "Tensile properties of high- and medium-entropy alloys," *Intermetallics,* vol. 39, pp. 74-78, 2013.

[15] P. Koželj, S. Vrtnik, A. Jelen, S. Jazbec, Z. Jagličić, S. Maiti, M. Feuerbacher and J. D. W. Steurer, "Discovery of a Superconducting High-Entropy Alloy," *PHYSICAL REVIEW LETTERS,* vol. 114, 2014.

[16] Y. &. Z. Zhang, T. &. Cheng, Y. &. Liaw and Peter., "High-entropy Alloys with High Saturation Magnetization, Electrical Resistivity, and Malleability," *Scientific reports,* 2013.

[17] X. F. Wang, Y. Zhang, Y. Qiao and G. Chen, "Novel microstructure and properties of multicomponent CoCrCuFeNiTix alloys," *Intermetallics,* vol. 15, pp. 357-362, 2017.

[18] K. Zhanga, Z. Fua, J. Zhanga, J. Shib, W. Wanga, H. Wanga, Y. Wanga and Q. Zhanga, "Annealing on the structure and properties evolution of the CoCrFeNiCuAl high-entropy alloy," *Journal of Alloys and Compounds,* vol. 502, pp. 295-299, 2010.

[19] Y.-F. Kao, S.-K. Chen, T.-J. Chen, P.-C. Chu, J.-W. Yeha and S.-J. Lina, "Electrical, magnetic, and Hall properties of AlxCoCrFeNi high-entropy alloys," *Journal of Alloys and Compounds,* vol. 509, pp. 1607-1614, 2011.

[20] M. S. Lucas, L. Mauger, J. A. Mun˜oz, Y. Xiao, A. O. Sheets, S. L. Semiatin, J. Horwath and Z. Turgut1, "Magnetic and vibrational properties of high-entropy alloys," *JOURNAL OF APPLIED PHYSICS ,* vol. 109, 2011.

[21] T. Zuo, M. C. Gao, L. Ouyang, X. Yang and Y. Cheng, "Tailoring magnetic behavior of CoFeMnNiX (X ¼ Al, Cr, Ga, and Sn) high entropy alloys by metal doping," *Acta Materialia,* vol. 130, pp. 10-18, 2017.

[22] Y. Li, W. Zhang and T. Qi, "New soft magnetic Fe25Co25Ni25(P, C, B)25 high entropy bulk metallic glasses with large supercooled liquid region," *Journal of Alloys and Compounds,* vol. 693, pp. 25-31, 2017.

[23] L. Liu, J. B. Zhu, J. C. Li and Q. Jiang, "Microstructure and Magnetic Properties of FeNiCuMnTiSnx," *Advanced Engineering Materials,* vol. 14, pp. 919-922, 2012.

[24] J. Wang, Z. Zheng, J. Xu and Y. Wang, "Microstructure and magnetic properties of mechanically alloyed FeSiBAlNi(Nb) high entropy alloys," *Journal of Magnetism and Magnetic Materials,* vol. 355, pp. 58-64, 2014.

[25] Q. Zhang, H. Xu, X. Tan, X. Hou, S. Wu, G. Tan and L. Yu, "The effects of phase constitution on magnetic and mechanical properties of FeCoNi(CuAl)x (x ¼ 0e1.2) high-entropy alloys," *Journal of Alloys and Compounds,* vol. 693, pp. 1061-1067, 2017.

[26] R. Kulkarni, B.S.Murty and V.Srinivas, "Study of microstructure and magnetic properties of AlNiCo(CuFe) high entropy alloy," *Journal of Alloys and Compounds,* vol. 746, pp. 194-199, 2018.

[27] P. Li, A. Wang and C. Liu, "Composition dependence of structure, physical and mechanical properties of FeCoNi(MnAl)x high entropy alloys," *Intermetallics,* vol. 87, pp. 21-26, 2017.

[28] R. Wei, H. Sun, C. Chen, J. Tao and F. Li, "Formation of soft magnetic high entropy amorphous alloys composites containing in situ solid solution phase," *Journal of Magnetism and Magnetic Materials,* no. 449, pp. 63-67, 2018.

[29] S.-M. Na, J.-H. Yoo, P. K. Lambert and N. J. Jones, "Room-temperature ferromagnetic transitions and the temperature dependence of magnetic behaviors in FeCoNiCr-based high-entropy alloys," *American Institute of Physics,* vol. 8, 2018.

[30] Y. Xua, Y. Lia, Z. Zhub and W. Zhang, "Formation and properties of Fe25Co25Ni25(P, C, B, Si)25 high-entropy bulk metallic glasses," *Journal of Non-Crystalline Solids,* pp. 60-64, 2018.

[31] Z. Li, H. Xu, Y. Gu, M. Pan, L. Yu and X. Tan, *Journal of Alloys and Compounds,* pp. 285-291, 2018.

[32] B. Zhang, Y. Duan, Y. Cui, G. Ma, T. Wang and X. Dong, "A new mechanism for improving electromagnetic properties based on tunable crystallographic structures of FeCoNiSixAl0.4 high entropy alloy powders," *RSC Advances,* vol. 8, pp. 14936-14946, 2018.

[33] Z. N. Kayani, S. Riaz, S. Iram and S. Naseem, "Structural and magnetic properties of nano-crystalline FeCoNiN thin films," *Journal of Saudi Chemical Society,* 2018.

[34] Z.Wu, H.Bei, F.Otto, G.M.Pharr and E.P.George, "Recovery, recrystallization, grain growth and phase stability of a family of FCC-structured multi-component equiatomic solid solution alloys," *Intermettalics,* vol. 46, pp. 131-140, 2014.

[35] Y. Wu, W. H. Liu, X. L. Wang, D. Ma, A. D. Stoica, T. G. Nieh, Z. B. He and Z. P. Lu, "In-situ neutron diffraction study of deformation behavior of a multi-component high-entropy alloy," *Applied Physics Letters,* vol. 104, no. 5, 2014.

[36] B.Ren, Z.X.Liu, B.Cai, M.X.Wang and L.Shi, "Aging behavior of a CuCr2Fe2NiMn high-entropy alloy," *Material and Design,* vol. 33, pp. 121-126, 2012.

[37] Shin-TsungChen, Wei-YehTang, Yen-FuKuo, Sheng-YaoChen, Chun-HueiTsau, Tao-TsungShun and Jien-WeiYeh, "Microstructure and properties of age-hardenable AlxCrFe1.5MnNi0.5 alloys," *Materials Science and Engineering: A,* vol. 527, pp. 5818-5825, 2010.

[38] K. V. Nagesha, R. M and D.Shivappa, "A Review On Mechanical Alloying," *International Journal of Engineering Research and Applications,* vol. 3, no. 3, pp. 921-924, 2013.

[39] H. Li and R. Ramanujan, "Micro structural evolution and nanocrystalline formation kinetics in FeCo based alloys during mechanical alloying," *Journal of Metastable and Nanocrystalline Materials,* vol. 23, 2005.

[40] Y. Yuanzheeng, M. Xueming and D. Yizhen, "The Nano- structuctuer of Iron Formed by Mechanical Grinding, Institute of Solid state Physics," *Hefei.,* vol. 9, no. 5, p. 266, 1992.

[41] R. Hamzaoui, F. M. S. Guessasma, A. Bennabi and J. Guillin, "Structural and thermal behavior of proclay kaolinite using high energy ball milling process," *Powder Technology,* vol. 271, pp. 228-237, 2015.

[42] C. Suryanarayana, "Mechanical alloying and milling," *Progress in Materials Science,* vol. 46, pp. 1-184, 2001.

[43] S. C, I. E, N. R, C. MA and M. JJ., *J Mater Res,* vol. 14, pp. 3777-83, 1999.

[44] C. B-L, C. C-C and P. T-P., *Metall Trans,* vol. A23, pp. 2105-2110, 1992.

[45] L. JM, L. TS and e. Merrick HF. In: Meyerhoff RW, "Manufacture of superconducting materials," *Materials Park, OH: ASM International,* pp. 155-63, 1977.

[46] B. A, D. GK, H. AJ, B. DK and B. S., *Mater Res,* vol. 11, pp. 599-607, 1996.

[47] G. D, V. O, S. WJD, I. P. A and S. K, "Proc. Inter. Conf.," *ICCM-10,* vol. 3, p. 11, 1995.

[48] T. L and P.-H. M., *Appl Phys,* vol. 75, pp. 5864-5866, 1994.

[49] C. Z-H and P. T-P., *Mater Sci Forum,* vol. 121, no. 6, pp. 235-238, 1997.

[50] Kis-Varga and B. DL., *Mater Sci Forum,* vol. 465, no. 70, pp. 225-227, 1996.

[51] I. PK, C. N, S. I, C. G, E. S and B. L., *Mater Sci and Engng,* vol. 859, no. 62, p. A134, 1991.

[52] H. LB, B. C and F. B., *Nanostructured Mater,* vol. 4, pp. 949-56, 1994.

[53] D. L. Dorset, "X-ray Diffraction: A Practical Approach," *Microsc. Microanal.,* vol. 4, no. 5, pp. 513-515, 1998.

[54] C. Suryanarayana and M. G. Norton, X-Ray Diffraction: A Practical Approach, Plenum Publishing Corporation, 1998.

[55] D. Suess, L. Breth, J. Lee, M. Fuger, C. Vogler, F. Bruckner, B. Bergmair, T. Huber and J. Fidler, "Calculation of coercivity of magnetic nanostructures at finite temperatures".

[56] P. Li, A. Wang and C. Liu, "A ductile high entropy alloy with attractive magnetic properties," *Journal of Alloys and Compounds,* vol. 694, pp. 55-60, 2017.

[57] D. H. Tarling and F. Hrouda, Magnetic Anisotropy of Rocks, Champman and Hall, 1993.